Green Energy and Technology

Md. Rabiul Islam
Faz Rahman
Wei Xu *Editors*

Advances in Solar Photovoltaic Power Plants

Iran Solar Magazine

Springer

Green Energy and Technology

Climate change, environmental impact and the limited natural resources urge scientific research and novel technical solutions. The monograph series Green Energy and Technology serves as a publishing platform for scientific and technological approaches to "green"—i.e. environmentally friendly and sustainable—technologies. While a focus lies on energy and power supply, it also covers "green" solutions in industrial engineering and engineering design. Green Energy and Technology addresses researchers, advanced students, technical consultants as well as decision makers in industries and politics. Hence, the level of presentation spans from instructional to highly technical.

More information about this series at http://www.springer.com/series/8059

Md. Rabiul Islam · Faz Rahman · Wei Xu
Editors

Advances in Solar Photovoltaic Power Plants

Springer

Editors
Md. Rabiul Islam
Rajshahi University of Engineering and Technology
Rajshahi
Bangladesh

Wei Xu
Huazhong University of Science and Technology
Wuhan, Hubei
China

Faz Rahman
University of New South Wales (UNSW)
Sydney, NSW
Australia

ISSN 1865-3529 ISSN 1865-3537 (electronic)
Green Energy and Technology
ISBN 978-3-662-50519-9 ISBN 978-3-662-50521-2 (eBook)
DOI 10.1007/978-3-662-50521-2

Library of Congress Control Number: 2016939060

Printed on acid-free paper

This Springer imprint is published by Springer Nature
The registered company is Springer-Verlag GmbH Berlin Heidelberg

Contents

About the Editors

Md. Rabiul Islam (M' 14, SM' 16, IEEE) received the B.Sc. and M.Sc. degree from Rajshahi University of Engineering and Technology (RUET), Rajshahi, Bangladesh, in 2003 and 2009, respectively, both in electrical and electronic engineering (EEE); and the Ph.D. degree from University of Technology Sydney (UTS), Sydney, Australia, in 2014, in electrical engineering.

In 2005, he was appointed as a Lecturer in the department of EEE, RUET where he was promoted as an Assistant Professor in 2008 and currently he is an Associate Professor of the department. From 2013 to 2014, he was a Research Associate with the School of Electrical, Mechanical and Mechatronic Systems, UTS. He has authored and coauthored more than 60 technical papers, a book (Springer) and three book chapters (Springer and IET). His research interests are in the fields of power electronic converters, renewable energy technologies, and smart grid.

Dr. Islam is a Senior member of the Institute of Electrical and Electronic Engineers (IEEE), and member of Institution of Engineers, Bangladesh (IEB), and the Australian Institute of Energy (AIE), Australia. He received the University Gold Medal and Joynal Memorial Award from RUET for his outstanding academic performance while pursuing the B.Sc. engineering degree. He also received the Best Paper Awards at IEEE PECon-2012, ICEEE 2015, and ICCIE 2015. He acts as a reviewer for several prestigious international journals.

Faz Rahman (M'79-SM'96-F2012, IEEE) received the B.S. degree in electrical engineering from Bangladesh University of Engineering and Technology (BUET), Dhaka, Bangladesh, in 1972 and the Master's and Ph.D. degrees from the University of Manchester, Manchester, UK, in 1975 and 1978, respectively.

For 2 years, he was a Systems Design Engineer with the General Electric Projects Co. of UK at Rugby, before joining the National University of Singapore, Singapore, in 1980. In 1988, he joined the University of New South Wales, Sydney, Australia, as a Senior Lecturer. He is currently a professor and Head of the Energy Systems Group with the School of Electrical Engineering and Telecommunications. His research interests include power electronics, motor drives, design of electrical machines with PM excitation, and motion control systems.

Wei Xu (SM'2014, IEEE) received the double B.E. degree from Tianjin University (TJU), China, in July 2002, and M.E. degree from TJU in March 2005, and the Ph.D. degree from Institute of Electrical Engineering, Chinese Academy of Sciences (IEECAS), in July 2008, respectively, all in electrical engineering.

From 2008 to 2011, he had been a Postdoctoral Research Fellow with the School of Electrical, Mechanical and Mechatronic Systems, Faculty of Engineering and Information Technology, University of Technology, Sydney (UTS), Australia. From 2011 to 2013, Dr. Xu had been appointed as one Royal Melbourne Institute of Technology (RMIT) University Vice Chancellor Research Fellow with School of Electrical and Computer Engineering in RMIT University. Since 2013, Dr. Xu has joined Huazhong University of Science and Technology (HUST), China as a professor.

In May 2015, he was awarded as China Thousand Talent Program for Young Outstanding Scientists. Till now, he has been one Regular Reviewer for more than eight IEEE Journals, and Session Chair for more than 15 IEEE Conferences. He has 22 China Patents and more than 35 internationally recognized Journal papers (in which have more than 25 IEEE Transactions Journal papers). His current research interests mainly include design and control for drive system, especially on linear machines and novel structure PMSMs.

Acronyms

μF	Microfarad
μm	Micrometre
μs	Microsecond
3L	Three level
3PI-P&O	3-point incremental perturb and observe
7122-RC	Model of inductor
A	Ampere
ABB	ASEA Brown Boveri
AC	Alternating current
ADC	Analog to digital converter
AESC	Adaptive extremum seeking control
AFD	Active frequency drift
AFDPF	Active frequency drift with positive feedback
Ag	Silver
Al	Aluminium
ANFIS	Adaptive neuro-fuzzy
ANN	Artificial neural network
ARC	Anti-reflection coating
As_2O_3	Arsenic trioxide
a-Si	Amorphous silicon
a-Si/μc-Si	Amorphous and micromorph silicon multi-junction
BDTk	Bangladesh taka
BST	Bisection search theorem
BST	Binary signal transfer
BZO	Boron-doped zinc oxide
CAES	Compressed air energy storage
CCL	Ceiling concentration limit
Cd	Cadmium
$CdCO_3$	Cadmium carbonate
CdS	Cadmium sulfide

$CdSO_4$	Cadmium sulfate
CdTe	Cadmium telluride
cf	Chopping fraction
CG	Centralized generator
CGH_2	Compressed gaseous hydrogen
CI[G]S	Copper–indium–[gallium]–[di]-sulphide
CIGS	Copper indium gallium selenide
cm	Centimetre
CMV	Common-mode voltage
CO_2	Carbon dioxide
CPF	Continuation power flow
CPV	Concentrator photovoltaic
CSC	Current source converter
c-Si	Crystalline silicon
CVD	Chemical vapor deposition
CVS	Controllable voltage source
CVT	Constant-voltage tracing method
DC	Direct current
DC-AC	Direct current to alternating current
DC-DC	Direct current to direct current
DCI	Double capacitor interface
DFACTS	Distributed FACTS
DG	Distributed generator
DGs	Distributed generation
DHESS	Distributed HESS
DHHS	United States Department of Health and Human Services
DL	Distribution line
DLC	Distribution line carrier
DS1104	Model of dSPACE research & development controller board
DSMES	Distributed SMES
e^-	Electron
ECA2DHG3R3	Model of capacitor
EDLC	Electrical double-layer capacitor
EDLC	Electrochemical double-layer capacitor
EES	Electrical energy storage
EMI	Electromagnetic interference
ENPH	Enphase
EPA	United States Environmental Protection Agency
EPIA	European PV Industry Association
ESC	Extremum seeking control
ESS	Energy storage system
EV	Electric vehicle
EVA	Ethylene vinyl acetate
FACTS	Flexible AC transmission system
FC	Fuel cell

FCL	Fault current limiting
FCV	FC vehicle
FES	Flywheel energy storage
FLC	Fuzzy logic controller
FRT	Fault ride through
FulCurvE	Full curve estimation
G	Solar irradiance
g	Gram
Ga	Gallium
$Ga(NO_3)_3$	Gallium nitrate
GaInP	Gallium indium phosphide
GaN	Gallium nitride
Ge	Germanium
GHG	Green house gas
GMPP	Global maximum power point
GMPPT	Global maximum power point tracking
GP	Global peak
GPO	Generalised perturb and observe
GUI	Graphical user interface
GW	Gigawatt
GW_P	Gigawatt-peak
H_2	Hydrogen
H_2O	Water
H_2SO_4	Sulfuric acid
HBZVR-D	H-bridge zero voltage rectifier diode
HC	Hill climbing
HCPL3120	Model of gate drive optocoupler
HCPSO	Hybrid Chaotic PSO
HERIC	Highly efficient and reliable inverter concept
HESS	Hybrid energy storage system
HEV	Hybrid electric vehicle
HF	High frequency
HIT	Heterojunction with intrinsic thin layer
HNO_3	Nitric acid
HS300 33RJ	Model of resistor
HTS	High temperature superconducting
HVAC	High-voltage alternating current
HVDC	High-voltage direct current
HY5P	Model of current transducer
Hz	Hertz
IARC	International Agency for Research on Cancer
IBC	Interdigitated back contact
IC	Incremental conductance
IEC	International Electrotechnical Commission
IEDs	Intelligent Electronics Devices

IEEE	Institute of Electrical and Electronics Engineers
IGBT	Insulated-gate bipolar transistor
In	Indium
INC	Incremental conductance method
IncCond	Incremental conductance
InGaP	Indium gallium phosphide
IRF1640G	Model of MOSFET
I–V	Current–Voltage
K_2TeO_3	Potassium tellurite
kg	Kilogram
kHz	Kilohertz
KOH	Potassium hydroxide
kV	Kilovolt
kW	Kilowatt
kWh	Kilowatt hour
LED	Light-emitting diode
LF	Low frequency
LH_2	Liquid hydrogen
LIB	Lithium-ion battery
LP	Local peak
LV	Low voltage
LV25P	Model of voltage transducer
LVDC	Low-voltage direct current
m^2	Square meter
MABE	Mean absolute bias error
MAPE	Mean absolute percentage error
MBE	Mean bias error
MCL	Maximum contaminant level
mg/kg	Microgram per kilogram
mg/L	Microgram per litre
mH	Milli Henry
MLP	Maximum loading point
mm	Millimetre
MMA	Methylmethacrylate
Mo	Molybdenum
MOCVD	Metal organic chemical vapor deposition
Mono-c-Si	Monocrystalline silicon
MOSFET	Metal oxide semiconductor field effect transistor
MPa	Megapascal
MPC	Model predictive control
MPE	Mean percentage error
MPP	Maximum power point
MPPE	Maximum power point estimation
MPPT	Maximum power point tracking
MSE	Mean squared error

MTOE	Million tons of oil equivalent
Multi-c-Si	Multi crystalline silicone
MV	Medium voltage
MW	Megawatt
MW_p	Megawatt-peak
MWT	Metal wrap through
Na_2CO_3	Sodium carbonate
Na_2SO_4	Sodium sulfate
NB	Negative big
NDZ	Non-detected Zone
NM	Negative medium
NO_2	Nitrogen dioxide
NPC	Neutral point clamped
NS	Negative small
OFP	Over frequency protection
OP	Operating point
OVP	Over voltage protection
P&O	Perturbation and observation method
PB	Positive big
PCC	Point of common coupling
PCL	Pollutant concentration limit
PCS	Power conditioning system
PCU	Power conditioning unit
P-D	Power duty cycle
PERC	Passivated emitter rear cells
PET	Polyethylene terephthalate
PH	Numeric scale used to specify the acidity or alkalinity
PHEV	Plug in electric vehicle
PHS	Pumped hydro storage
PI	Proportion integration
PID	Proportional–integral–derivative
PJD	Phase jump detection
PLCC	Power-line carrier communication
PM	Positive medium
PMMA	Poly-methyl-methacrylate
POI	Potentially optimal interval
POT	Power operating triangle
ppmw	Parts per million weight
PS	Positive small
PSAT	Power system analysis toolbox
PSCs	Partially shaded conditions
PSO	Particle swarm optimisation
pu	Per unit
PV	Photovoltaic
P–V	Power–Voltage

PVAS	PV array simulator
PVF	Polyvinyl fluoride
PWM	Pulse width modulation
Q factor	Quality factor
R	Receiver
RAM	Random access memory
RCC	Ripple correlation control
RCMU	Residual current monitor unit
RH	Relative humidity
RMSE	Root-mean-square error
RTI	Real-time interface
S	Sulphur
SA	Simulated annealing
SC	Superconducting cable
SCADA	Supervisory control and data acquisition
SE	Selective emitter
SFS	Sandia frequency shift
SHS	Solar home system
Si	Silicon
SiC	Silicon carbide
SiN_x	Silicon nitride
SiO_x	Silicon oxide
SISO	Single input single output
SM	Superconducting magnet
SMC	Sliding mode control
SMEE	Superconducting magnetic energy exchange
SMES	Superconducting magnetic energy storage
SnO_2	Tin oxide
SO_2	Sulfur dioxide
SPD	Signal produced by disconnect
SSSC	Static synchronous series compensator
STATCOM	Static synchronous compensator
SVS	Sandia voltage shift
T	Transmitter
TCO	Transparent conducting oxide
Te	Tellurium
$Te(SO_4)_2$	Tellurium sulfate
TeO_2	Tellurium dioxide
TF	Thin film
THD	Total harmonic distortion
TL	Transmission line
TNB	Tenaga nasional berhad
TTZ	Threshold tracking zone
U.S.	United States
U.S.EIA	U.S. Energy Information Administration

UFP	Under frequency protection
UK	United Kingdom
UL	Underwriters Laboratories
UPFC	Unified power flow controller
UPS	Uninterrupted power supply
USA	United States of America
USD	United state dollar
USD/kg	United States dollar per kilogram
UV	Ultraviolet
UVP	Under voltage protection
V	Volt
VAR_C	Capacitive load
VAR_L	Inductive load
VFP	Voltage protection and frequency protection
VSC	Voltage source converter
VWS	Voltage window search
W	Watt
W/m^2	Waat per meter squared
Wh	Watt hour
WS	Wind speed (m/s)
WSCC	Western system coordinating council
wt%	Percentage by weight
ZE	Zero
ZnS	Zinc sulfide

Symbols

$\%$	Percentage
^{o}C	Degree Celsius
V_{DC}	DC link voltage (V)
V_{AN}, V_{BN}	Phase voltages of converter
P	Positive terminal of the DC link
N	Negative terminal of the DC link
A, B	Terminals of single-phase system
C_{PV}	Stray capacitance (F)
L_1, L_2	Filter inductors (H)
I_L	Leakage current (A)
R_G	Ground resistor (Ω)
V_{CM}	Common-mode voltage (V)
V_{DM}	Differential-mode voltage (V)
V_{ECM}	Equivalent common-mode voltage (V)
I_{ph}	PV generated current (A)
I_0	PV cell reverse saturation current (A)
q	Electronic charge of an electron (1.6×10^{-19}C)
T	Temperature of the PV cell (°C)
S	Solar radiation intensity (W/m^2)
K	Boltzmann's constant (1.38×10^{-23} J/K)
A	Constant factor (1.2 for Si-mono)
i	PV cell output current (A)
u	PV cell output voltage (V)
R_s	PV array series resistance (Ω)
R_{sh}	PV array shunt resistance (Ω)
I_{sc}	Short-circuit current of PV array (A)
U_{oc}	Open-circuit voltage of PV array (V)
U_m	MPP's voltage for PV model (V)
I_m	MPP's current for PV model (A)
$P(u)$	Function of PV output power (W)

I_{SCref}	Current under standard conditions (A)
U_{OCref}	Open-circuit voltage under standard conditions (V)
U_{mref}	MPP's voltage under standard conditions (V)
I_{mref}	MPP's current under standard conditions (A)
R_{opt}	Ratio of U_{mpp} and I_{mpp}
ΔI_0	Current error of inverter output (A)
I_{ref}	Instantaneous current reference of inverter output (A)
i_g	Instantaneous value of grid current (A)
U_{ref}	Voltage reference of PV operating point (V)
U_{PV}	Output voltage sample value of PV cells (V)
C	Capacitor
D	Diode
L	Inductor
e	Slope value of the continuous sampling points of attachment
Δe	Change in unit time slope on the PV cells P-U curve
$P(k)$	PV power for the k sampling times (W)
$I(k)$	PV current for the k sampling times (A)
$U(k)$	PV voltage for the k sampling times (V)
dU	Difference of voltage $U(k)$
P_{mpp}	Power of Maximum power point (W)
U_i	Corresponding voltage of language variable (V)
i, j	The subscripts
U_{dc}	Voltage of DC bus (V)
T_p	Time constant for neural network (s)
$O_i(k)$	Activation function
$\lambda_{\mathrm{i}}(k)$	Input signal of neural network
W_{ij}	Weight between neurons i and j
N	Total number of training samples
$t(k)$	Desired output
$O(k)$	Actual output
M	Total number of samples within a day
$P_{\mathrm{MPP}}(k)$	Measured maximum power (W)
$I_{\mathrm{MPP}}(k)$	Corresponding current of $P_{\mathrm{MPP}}(k)$ (A)
$U_{\mathrm{MPP}}(k)$	Corresponding voltage of $P_{\mathrm{MPP}}(k)$ (V)
E_p	Total average error of maximum power within a day
E_i	Total average error of $I_{\mathrm{MPP}}(k)$
E_u	Total average error of $U_{\mathrm{MPP}}(k)$
P_{day}	Total maximum power (W)
I_{day}	Total optimal current (A)
U_{day}	Total average optimal voltage (V)
$P'(u)$	Slope of the PV P-U curve
$P''(u)$	Step change rate
k	Number of cycle
α	Scaling factor
θ	Contingence angle

u_L	$0.02*U_{OC}$ (V)
u_R	$0.98*U_{OC}$ (V)
$D(u)$	Step size
$N_L(u)$	Scaling factor
$H_L(u)$	Left tangent line through point (u_L, $P(u_L)$) of *P-U* curve
$H_R(u)$	Right tangent line through point (u_R, $P(u_R)$) of *P-U* curve
δ	Value of threshold
L_i	Scaling factor
X	Input sets
Y	Output sets
f	Distribution function
R_{pm}	Equivalent load
V_{mpp}	Voltage at MPP (V)
V_{oc}	Open-circuit voltage (V)
k_1	Constant of proportionality for fractional open-circuit voltage method
I_{mpp}	Current at MPP (A)
I_{sc}	Short-circuit current (A)
k_2	Constant of proportionality for fractional short-circuit current method
ΔI	Change in current (A)
M	Scaling factor
dP	Change in power (W)
dV	Change in voltage (V)
$dP_{0.5}$	Change in power due to MPP perturbation and environmental change (W)
dP_1	Change in power due to irradiance change (W)
$P(k)$	Power at sample k (W)
α_1	Scaling factor for Generalised Perturb and Observe
β	Variable for Beta method
I_{pv}	Measured photovoltaic current (A)
V_{pv}	Measured photovoltaic voltage (V)
c	Constant for Beta method
q	Electron charge (1.6×10^{-19} C)
A	Diode ideality factor
k	Boltzmann constant (1.38×10^{-23} J/K)
T	Temperature (K)
N_s	Number of series connected cells
P_1	Power sample for parabolic curve prediction (W)
P_2	Power sample for parabolic curve prediction (W)
P_3	Power sample for parabolic curve prediction (W)
δ_1	Duty cycle sample for parabolic curve prediction
δ_2	Duty cycle sample for parabolic curve prediction
δ_3	Duty cycle sample for parabolic curve prediction
x_i^k	Previous particle position (V)

x_i^{k+1}	New particle position (V)
Φ_i^{k+1}	Particle new velocity
ω_i	Inertia weight
$c_1,\ c_2$	Acceleration coefficients
$r_1,\ r_2$	Random numbers
$P_{\text{best},i}$	Power at best position of particle i (W)
G_{best}	Power at global best position (W)
P_k	Power at candidate voltage (W)
P_i	Power at reference voltage (W)
T_k	Temperature of the search (°C)
Pr	Acceptance probability
M	Number of particles
v_i^k	Velocity vector
v_i^{k+1}	New velocity vector
S_i^k	Current position
S_i^{k+1}	New position
p_{besti}	Previous best position
g_{best}	Global best position
w	Initial weight
c_1	Cognitive coefficient
c_2	Social coefficient
$r_1,\ r_2$	Random parameter
I_{PV}	PV current
I_{SC}	Short-circuit current
P_{PV}	Maximum PV power
I_c	Initial PV current
ΔP	Change of PV power
Q	Switch
R_{load}	Resistive load
f_s	Switching frequency
I_{PSO}	PV current generated by PSO
e	Error signal
k_p	Proportional constant
k_i	Integral constant
k_d	Derivative constant
V_{OC}	Open-circuit voltage
$P_{\max}$	Maximum power
V_{DS}	Drain-source voltage
V_{sensor}	Voltage sensing subsystem
I_{sensor}	Current sensing subsystem
$I_{\text{sensor\_out}}$	Value subtracted by the current value from the current sensing block
$P_{\text{PSO-ANN}}$	Power generated by PSO-ANN
E	Tracking efficiency
P_{mppt}	Power generated by MPPT

$E_{\text{PSO-ANN}}$	Tracking efficiency for PSO-ANN
E_{PSO}	Tracking efficiency for PSO
H	Monthly mean daily global horizontal irradiance (kWh/m^2/day)
H_0	Monthly mean daily extraterrestrial irradiance (kWh/m^2/day)
a	Empirical constant for the existing or the proposed empirical model
b	Empirical constant for the existing or the proposed empirical model
S	Monthly mean daily sunshine hour (h)
S_0	Maximum possible monthly average daily sunshine hour (h)
c	Empirical constant for the existing or the proposed empirical model
d	Empirical constant for the existing or the proposed empirical model
$T_{\max}$	Maximum ambient temperature (^{o}C)
$T_{\min}$	Minimum ambient temperature (^{o}C)
ΔT	Temperature difference
P	Precipitation data (mm)
δ	Declination angle in degree (^{o})
T_{so}	Soil temperature (^{o}C)
T_a	Monthly mean daily ambient temperature (^{o}C)
P_v	Water vapour pressure (Pa)
T_m	Monthly mean daily module temperature (^{o}C)
L	Latitude of the location (degree (^{o}))
D_n	nth day of the year
h	Hours
ω_s	Hour angle (degree (^{o}))
R^2	Regression coefficient
Z	Zenith angle (degree (^{o}))
α	Solar altitude angle (degree (^{o}))
ϕ	Longitude of a location (degree (^{o}))
e	Empirical constant for the existing or the proposed empirical model
f	Empirical constant for the existing or the proposed empirical model
T_s	Temperature of the sun (degree (^{o}))
N	Number of training data sets
E_{dc}	Monthly average daily DC energy generated (W)
E_{ac}	Monthly average daily AC energy generated (W)
η_{pv}	Monthly average daily PV module efficiency (%)
η_{inv}	Monthly average daily inverter efficiency (%)
U	Overall heat transfer coefficient (W/m^2 °C)
A	Area of the PV module or array (m^2)
h_c	Conductive heat transfer coefficient (W/m^2 °C)
v_s	Wind speed (m/s)

Ex_{th}	Thermal exergy loss (W)
Hz	Hertz
I_{PV_inv}	Inverter's output current
km	Kilometre
km^2	Square kilometre
kVA	Kilovolt-amps
kWh	KiloWatt hour
kWp	KiloWatt peak
mH	Millihenry
Mtoe	Tonne of oil equivalent
MW	MegaWatt
MWp	MegaWatt-peak
π	pi
Q_f	Quality factor
TWh	TeraWatt hour
V	Voltage
VAR_C	Reactive power consume by capacitive loads
VAR_L	Reactive power consume by inductive loads
V_{PCC}	Inverter's terminal voltage
W	Watt
Wh/m^2	Watt-hours per square metre
δ1	Acceptable variance
ΔP	Reactive power variation
ΔQ	Real power variation
μF	Microfarad
Ω	Ohm
t	Time
s	Second
R	Resistance
X	Reactance
B	Susceptance
δ	Rotor angle
Ω_b	Base frequency
ω	Rotor speed
P_m	Input mechanical power
P_e	Output electrical power
D	Damping constant
M	Machine inertia
e'_d	d-axis transient voltage
e'_q	q-axis transient voltage
f_s	System frequency
X_d	d-axis synchronous reactance
X_q	q-axis synchronous reactance
X'_d	d-axis transient reactance
X'_q	q-axis transient reactance

i_d	d-axis stator current
i_q	q-axis stator current
E_f	Field voltage
T'_{d0}	d-axis rotor open-circuit time constant
T'_{q0}	q-axis rotor open-circuit time constant
v_d	d-axis stator voltage
v_q	q-axis stator voltage
r_a	Stator resistance
V	Bus voltage
θ	Bus angle
P_{ref}	Real power reference
Q_{ref}	Reactive power reference
V_{ref}	Voltage reference
V_{pcc}	Voltage at the point of common coupling
T_p, T_q	Converter time constants
s	Laplace operator
P	Real power
Q	Reactive power
i_{dref}	d-axis reference current of PV converter
i_{qref}	q-axis reference current of PV converter
S_i	Nominal power of generator i
H_i	Inertial constant of generator i
H_{sys}	Average inertia constant of the system
V	Voltage
I	Current
L	Inductance
K	Kelvin
E	Energy
C	Capacitance
U	Output voltage from a controllable voltage source (V)
R_{line}	Power-line resistance (Ω)
R_{load}	Power-load resistance (Ω)
$U_R(t)$	Transient voltage across the power-load resistor (V)
U_r	Rated voltage (V)
U_{min}	Minimum reference voltage (V)
U_{max}	Maximum reference voltage (V)
$I_L(t)$	Transient current through the superconducting magnet (A)
$I(t)$	Transient current through the power-line resistor (A)
$I_R(t)$	Transient current through the power-load resistor (A)
$I_C(t)$	Transient current through the DC-link capacitor (A)
U_0	Initial voltage across the power-load resistor (V)
I_0	Initial current through the superconducting magnet (A)
L	Inductance of the superconducting magnet (H)
C	Capacitance of the DC-link capacitor (F)
R_{SC}	Equivalent lossy resistance (Ω)

I_c	Critical current (A)
I_{Lr}	Rated current (A)
N_{layer}	Number of the coil layer
I_{dc}	Magnitude of the DC coil current (A)
I_m	Magnitude of the AC coil current (A)
f	Frequency of the AC coil current (Hz)
$S(t)$	Current changing rate (A/s)
P_{hys}	Hysteresis loss (W)
P_{flow}	Flux flow loss (W)
P_{coup}	Coupling current loss (W)
P_{eddy}	Eddy current loss (W)
P_{ac}	AC loss (W)
Q_{hys}	Energy consumption from hysteresis loss (J)
Q_{flow}	Energy consumption from flux flow loss (J)
Q_{coup}	Energy consumption from coupling current loss (J)
Q_{eddy}	Energy consumption from eddy current loss (J)
$B_{\perp}$	Perpendicular magnetic flux density (T)
$B_{//}$	Parallel magnetic flux density (T)
V_{DSmax}	Drain-source breakdown voltage (V)
R_{on}	Turn-on resistance (Ω)
R_{esr}	Equivalent series resistance (Ω)
P_{swell}	Mean surplus power (W)
P_{short}	Mean shortfall power (W)
T_{abs}	Power absorption time duration (s)
T_{com}	Power compensation time duration (s)
η_{total}	Charge–discharge efficiency
$I_{\mathrm{fault}}(t)$	Transient fault current through the superconducting cable (A)
$R(t)$	Transient resistance from the superconducting cable (Ω)
R_{m}	Maximum resistance from the superconducting cable (Ω)
τ_1	Time constant of the quench period (ms)
τ_2	Time constant of the recovery period (ms)
N	Number of the coil turns
r_{inner}	Inner radius of the coil unit (m)
r_{outer}	Outer radius of the coil unit (m)
h	Height of the coil unit (m)
S_{tape}	Tape usage of the coil unit (m)
U_{sc}	Fault current-dependent increased voltage (V)
I_A, I_B	Load voltage-dependent decreased currents (A)
U_{bus}	DC bus voltage (V)
$U_{\mathrm{load}}(t)$	Transient load voltage (V)
n-Si	N-type silicon
p-Si	P-type silicon
n+	Extrinsic doped n-type
n++	Heavy doped n-type
p+	Extrinsic doped p-type

List of Figures

Introduction

Photovoltaic Inverter Topologies for Grid Integration Applications

Advanced Control Techniques for PV Maximum Power Point Tracking

Maximum Power Point Tracking Methods for PV Systems

Photovoltaic Multiple Peaks Power Tracking Using Particle Swarm Optimization with Artificial Neural Network Algorithm

Empirical-Based Approach for Prediction of Global Irradiance and Energy for Solar Photovoltaic Systems

A Study of Islanding Mode Control in Grid-Connected Photovoltaic Systems

Stability Assessment of Power Systems Integrated with Large-Scale Solar PV Units

Energy Storage Technologies for Solar Photovoltaic Systems

Superconducting Magnetic Energy Storage Modeling and Application Prospect

Recycling of Solar Cell Materials at the End of Life

List of Tables

Introduction

Advanced Control Techniques for PV Maximum Power Point Tracking

Photovoltaic Multiple Peaks Power Tracking Using Particle Swarm Optimization with Artificial Neural Network Algorithm

Empirical-Based Approach for Prediction of Global Irradiance and Energy for Solar Photovoltaic Systems

A Study of Islanding Mode Control in Grid-Connected Photovoltaic Systems

Stability Assessment of Power Systems Integrated with Large-Scale Solar PV Units

Energy Storage Technologies for Solar Photovoltaic Systems

Superconducting Magnetic Energy Storage Modeling and Application Prospect

Recycling of Solar Cell Materials at the End of Life

Introduction

Md. Rabiul Islam

Abstract Energy and environment are two foremost areas of global crisis. The world's energy demand is growing remarkably which is not only diminishing the reserve of fossil fuels, but also affecting the environment. In 2014, the global primary energy consumption was 12,928.4 million tons of oil equivalent (MTOE) which generates about 10,000 million tons of carbon during the burning of fossil fuels. It is more and more broadly recognized that renewable energy, especially solar energy, can offer effective solutions to these gigantic challenges. Now, renewable energy contributes around 3 % of the world's energy needs. By the end of 2014, a total of 187.24 GW solar photovoltaic (PV) power capacity had been installed in the world. The annual installation of new PV systems rose from 47.60 GW in 2014 to 58.10 GW in 2015, and in 2010, it was only 17.06 GW. Up to 2014, about 1600 installations worldwide were PV power plants larger than 4 MW. Of which 60 plants in Spain and 50 in Germany generating an output of more than 10 MW. A 10 MW solar PV power plant may save about 15,000 tons of CO_2 emissions per annum. In order to push this emerging technology, more research is needed. The book provides a consistent compilation of fundamental theories, a compendium of current research and development activities in the field of solar PV technologies. In this chapter, the development of solar PV technologies is presented in the Preface section. This introductory chapter also presents the objectives and the organization of the whole book.

Keywords Solar photovoltaic power plants · Energy and environment · Power converter topologies · Maximum power point tracking · Grid integration · Stability · Energy storages · Recycling of solar PV modules · Module cost · Land use · Historical development · Recycling of solar cell materials

M.R. Islam (✉)
Department of Electrical and Electronic Engineering,
Rajshahi University of Engineering and Technology, Rajshahi 6204, Bangladesh
e-mail: Rabiulbd@hotmail.com

M.R. Islam et al. (eds.), *Advances in Solar Photovoltaic Power Plants*,
Green Energy and Technology, DOI 10.1007/978-3-662-50521-2_1

1 Preface

The world's energy demand is growing remarkably due to the strong growth of population and economy in the developing countries [1–3]. Figure 1 shows the world population with projections to 2050 [4]. Almost a constant growth rate has been observed during 1950–2015 and predicted same growth rate until 2050. The increasing energy demand is not only diminishing the reserve of fossil fuels, but also affecting the environment. Carbon dioxide (CO_2) gas is generated from burning of fossil fuels, which significantly contributes to the increase of average global temperatures, i.e., global warming. Figure 2 shows the global CO_2 emission form fossil fuel burning and average global temperature [4, 5]. Scientists worldwide are now seeking solutions to these two enormous challenges (energy and environment) from renewable energy sources, which are richly available in almost every country. Many countries have set targets for renewable power generation resulting in much higher average annual growth rates of renewable power generation than those of conventional power generation in recent years [6–8]. Over the decades, a good

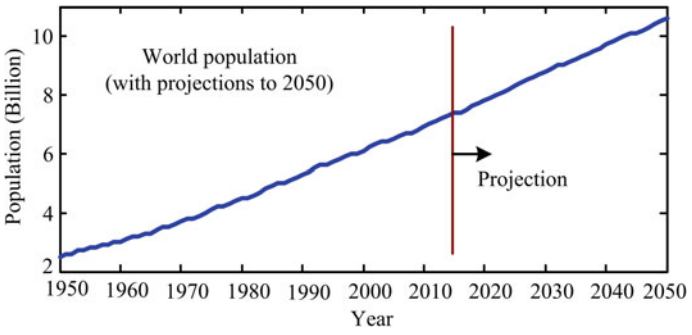

Fig. 1 World population in billion with projections to 2050

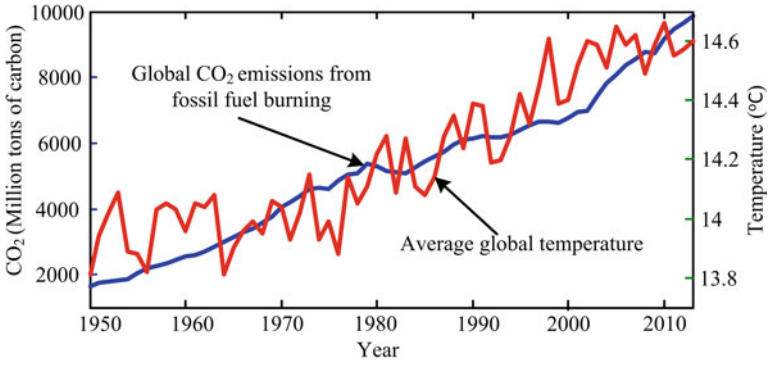

Fig. 2 Global CO_2 emissions from fossil fuel burning and average global temperature

number of countries have implemented specific policies and incentives to support the development of solar PV program, which has led to a rapid increase in the total installed capacity. Solar photovoltaic (PV) represents the highest growth rate due to its abundant source and technological development of PV cells, e.g., fast reduction of PV module cost. Figure 3 shows the world annual growth of energy use by source [4]. The cost of solar PV panels has declined 99 % over the last four decades. Average module cost was USD 74/W in 1972 and reduced to less than USD 0.70/W by 2014. In 2012, Chinese made thin-film (TF) PV modules with an average module cost of USD 0.75/W. It is forecasted that more than 40 % reduction of PV module cost is likely to occur by 2020. In 2012, the cost of small PV systems in Germany was just USD 2200/kW. In 2012, the European PV Industry Association (EPIA) also forecasted that small-scale rooftop PV system and large-scale PV projects cost could decline to between USD 1750–2400/kW and USD 1300–1900/kW, respectively, by 2020 [9]. Due to the fast reduction of module cost as well as the reduction of difference between the cost of renewable power generation and the cost of conventional power generation, the installation of solar PV systems has been gaining interest specially in the energy starved countries in the world. The EPIA projected that PV power may contribute up to 4.9–9.1 and 17–21 % of the global electricity generation by 2030 and 2050, respectively. Currently, there are over 1000 vendors worldwide have been producing PV cells and modules, most of them are in the US, Japan, Europe, and China.

At present in Bangladesh, the cost of diesel-based electric power generation is about BDTk 15.80/kWh [10]. The PV is now becoming competitive with power generated from diesel-based systems. The solar home system (SHS) of Bangladesh is one of the fastest growing solar PV power promotion program in the world. In average 2000 SHSs are installing every day in Bangladesh. Beside a number of

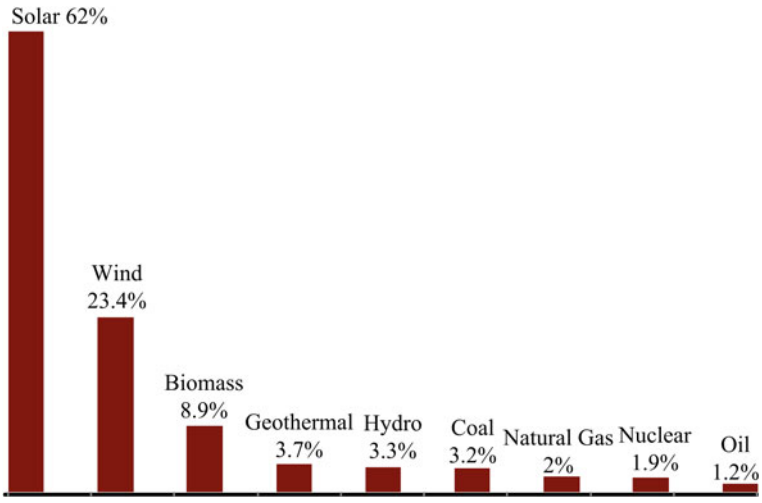

Fig. 3 World annual growth of energy use by source (2008–2013)

developed countries many developing countries have also set their target to generate electricity from renewable sources. The developing country, Bangladesh has set a target to generate 10 % of their total electricity from renewable energy sources by 2020, which is in terms of capacity of 2000 MW.

The first 1 MW_p PV power station was installed in 1982 at California by Arco Solar. In 1984, a 5.2 MW_p PV power plant was installed in Carrizo Plain. Since then, multimegawatt PV power plants have attracted great attention and now power plants of more than 500 MW_p in capacity have thereby become a reality. As of 2015, the Charanka Solar Park, Gujarat is one of the world's largest operating PV power plant and having a capacity of 600 MW_p. Italy, Germany, China, the US, France, and Japan are the leading countries in terms of installation of PV modules and systems. Up to 2014, about 1600 installations worldwide with a combined capacity of 22,500 MW_{AC} were PV power plants larger than 4 MW. Of these plants, several hundred plants have been installed in Germany and Spain, each plant generating an output of more than 1 MW_p. Of which 60 plants in Spain and 50 in Germany generating an output of more than 10 MW_p. Figure 4 shows the world cumulative and annual solar photovoltaic installations [4]. The number of PV power plants will continue to rise. Several hundred PV power plants will be installed within the next few years. Future PV power plants will have higher power capacity. Indeed, some of them will exceed 1000 MW. More than 90 % of the installed capacity consists of grid-connected systems.

The module efficiency is one of the important factor in selecting solar PV technology for installation. Crystalline silicon (c-Si) and the thin-film (TF) technologies dominate the global PV market. There are three types of c-Si-based solar PV technology, i.e., monocrystalline silicon (mono-c-Si), multicrystalline silicone (multi-c-Si), and ribbon-sheet grown silicon. Currently, crystalline silicon PV

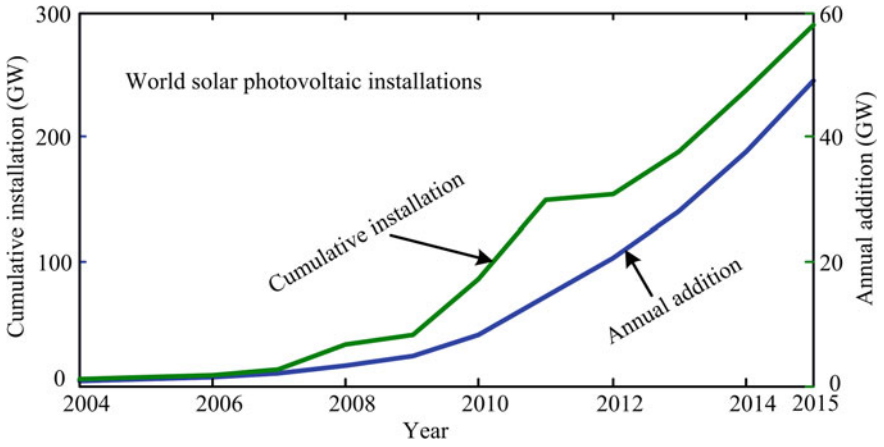

Fig. 4 World cumulative and annual solar photovoltaic installations

Table 1 Performance of commercial solar PV technologies

PV technology		Module effic. (%)	Record lab effic. (%)	Record commercial effic. (%)	Area/kW (m^2/kW)	Lifetime (Years)
c-Si	Mono-c-Si	13–19	24.7	22	7	25
	Multi-c-Si	11–15	–	20.3	8	25
TF	a-Si	4–8	10.4	7.1	15	25
	a-Si/μc-Si	7–9	13.2	10	12	25
	CI[G]S	7–12	20.3	12.1	10	25
	CdTe	10–11	16.5	11.2	10	25

technology dominates about 85 % of the PV market share. Although, TF solar PV is cheaper than c-Si-based solar PV, but TF solar PV is significantly less efficient and requires more surface area for the same power output. The TF solar PV technology can also be divided into four basic types, i.e., amorphous silicon (a-Si), amorphous and micromorph silicon multi-junction (a-Si/μc-Si), copper-indium-[gallium]-[di]-sulfide (CI[G]S), and cadmium telluride (CdTe). Crystalline silicon (c-Si) cells have reached a record efficiency of around 25 %. The highest efficiency of commercial modules recorded at 20 % with a lifetime of about 25 years. Maximum 12 % efficiency recorded for commercial TF modules. It is predicted that the maximum efficiency of c-Si-based and TF-based commercial modules will increase to 23 and 16 % by 2020. Performance of commercial PV technologies is tabulated in Table 1 [9].

Since multimegawatt PV power plants require large areas of land, they are usually installed in remote areas, far from cities. For example, the 10 MW grid-connected solar PV power plant in Ramagundam, India, occupied over 50 acres of land [11]. Ramagundam's plant installed about 44,448 PV modules with a total of 1852 strings. For power transmission, a medium voltage network is commonly used. A 33 kV transmission grid is used to transfer power from Ramagundam plant to utility grid. Figure 5 shows the architectural layout of 10 MW solar PV power plant in Ramagundam, India [11]. However, the intermittent nature of solar energy source, in terms of the output voltage and power, is a major challenging issue for grid integration.

On the other hand, when PV arrays are used to harvest solar energy, high cost and low energy conversion efficiency are two important factors that could limit the implementation of PV power plants. In PV systems, the PV array represents about 30–50 % of the total cost of the system, and the remaining costs include the installation, the energy storage, balance of system, control circuit, and the power electronic components. The battery storage corresponds to about 20–30 % of the system cost. The inverters and maximum power point tracker (MPPT) contribute to only 7 % of the total system cost. Due to the low conversion efficiency and high cost of solar array, it is very desirable to operate the PV panel at the maximum

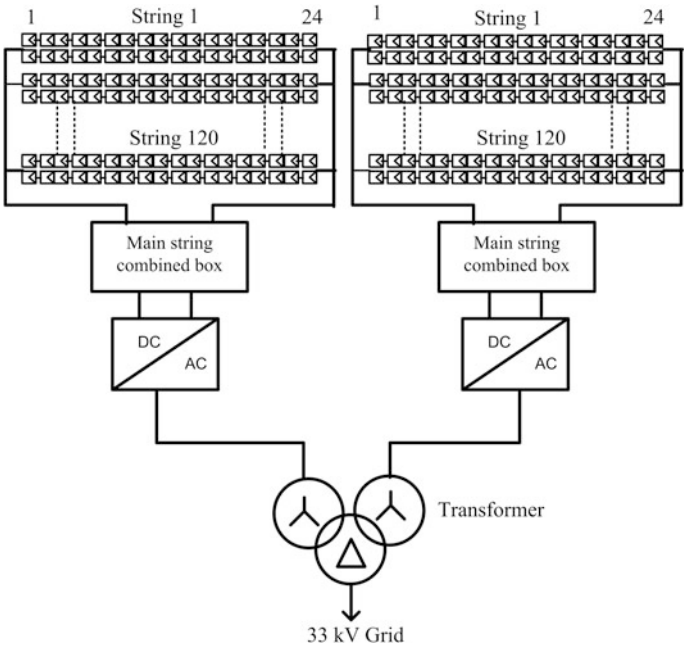

Fig. 5 Layout of 10 MW solar PV power plant in Ramagundam, India

power point (MPP). ASEA Brown Boveri (ABB) and Siemens are the leading manufacturers of PV inverters. Most of the inverters convert the DC power generated by PV arrays into single or 3-phase AC power with a voltage rating of 300–400 V [12]. The power converter topology, system stability, and control of grid-connected PV power plants have attracted considerable interest in recent years, as the existing technologies are not suitable for large-scale PV power plants yet. In the last two decades, extensive research has been carried out in proposing new inverter topologies, e.g., inverters with or without high-frequency transformers, with common DC or magnetic links, and with multilevel concepts [7, 13–15]. Beside the development of inverter topologies, considerable research efforts have also been directed toward the progress of MPPT algorithms, e.g., particle swarm optimisation, line search, chaos search, and simulated annealing. Recently, pumped hydro and compressed air energy storages other than traditional batteries have been developed specially for utility-scale energy storage systems. At the end of lifetime, the recycling of PV modules is necessary for environmental and economic purposes. It is estimated that about 800 metric tons of waste will be produced from 10 MW PV modules. A solar module is full of numerous encapsulating plastic materials, such as ethylene vinyl acetate and polyvinyl fluoride. Research is needed to push these technologies to solve two enormous challenges, i.e., energy and environment by replacing conventional power plants with solar PV power plants.

2 Major Objectives of the Book

The main objective of the book is to present the design and implementation process of large-scale solar PV power plants. The chapters are prepared and arranged in such a way that the book provides a consistent compilation of fundamental theories, a compendium of current research and development activities as well as new directions to overcome some critical limitations of the existing grid integration technologies. It is expected that the contents of this book will have great useful for future renewable power plants and smart grid applications.

3 Organization of the Book

For grid integration of PV system, either compact high-frequency transformer or bulky low frequency transformer is employed in the dc- or ac-side of the PV inverter, respectively, to step up the low output voltage of the PV modules to the grid voltage. Galvanic isolation is provided and the safety is assured with the use of transformer. Because of the high cost and significant loss of the transformer, the PV inverter becomes expensive and poor efficient. To mitigate these problems, the transformer is removed from the PV inverter. The transformerless PV inverter is smaller, cheaper, and higher in efficiency. Various transformerless PV inverter topologies, with different circuit configuration and modulation techniques, have been developed recently. The operating principle and the converter structure are evaluated in Chap. 2. It is expected that the transformerless PV inverter would have great potential for future renewable generation and smart micro grid applications.

Tracking the maximum power of the PV arrays at real time is very important to increase the whole system performance. In the past decades, there are a large number of maximum power point tracking (MPPT) methods have been proposed for PV system, such as constant-voltage tracing method (CVT), perturbation, and observation method (P&O), incremental conductance method (INC), curve fitting method, look-up table method, and so on. Actually, these conventional methods can track the MPP. But these methods have some drawbacks, like oscillation, miscalculation, poor accuracy, unimodal *P–U* curves only. To overcome the limitation of these methods, some advanced MPPT methods are introduced in Chap. 3. In Chap. 4, the criteria for assessing the performance of MPPT methods are defined followed by a complete description and discussion of both techniques designed for uniform environmental conditions and those designed for nonuniform environmental conditions.

Most of the conventional MPPT algorithms are incapable to detect global peak power point with the presence of several local peaks. A hybrid particle swarm optimization and artificial neural network (PSO-ANN) algorithm is proposed in Chap. 5 to detect the global peak power. The performance of the proposed algorithm is compared with that of the standard PSO algorithm. The proposed algorithm

is tested and verified by hardware experiment. The simulation and the experimental results are compared and discussed in the Chapter.

Accuracy in prediction of global horizontal irradiance is vitally important for photovoltaic energy prediction, its installation and pre-sizing studies. A change in the solar radiation directly impacts the electricity production and in turn, the plant economics. Hence employing a model possessing improved prediction accuracy significantly affects the photovoltaic energy prediction. Furthermore, monthly mean data is required for prediction of long term performance of solar photovoltaic systems making the same to be concentrated for the present contribution. The available models for prediction of irradiance and energy unlike physical and statistical models depend on input parameters whose availability, assumption, and determination is difficult. This finally creates complexity in predicting the desired response. Hence empirical models are chosen preferable over physical and statistical based models. Empirical models correlate only the available input atmospheric parameters affecting solar irradiance and energy, thereby reducing the complexity experienced by physical and statistical model. Yet, the reliability or accuracy of model varies with location. The reliability of an empirical model depends on the incorporation of input's and data set (training set) for its formulation. Thus, the consideration of significant input factors lies to be a persistently prevailing challenge driving the need for an improved prediction model delivering irradiance and energy. In Chap. 6, an empirical model is proposed for prediction of irradiance and energy. The incorporated input factors for the formulation of energy prediction model is emphasized by performance and energy analysis of solar photovoltaic systems. The proposed model hence combines the thermal and electrical aspects of photovoltaic systems gaining reliability and limiting the dependence toward real time measured input factors.

Chapter 7 reviews the recent trend and development of control techniques for islanding mode particularly for PV grid-connected systems. The fundamental concept and theory of operation of popularity used anti-islanding detection methods are described. In addition, the advantages and disadvantages of each control method have been highlighted. The operation characteristics and system parameters of each detection techniques are analyzed and discussed. Moreover, the comparison of islanding detection method based on various characteristics has been detailed. It can be concluded that anti-islanding detection methods are greatly governed by the nature of system application as well as the scale of the system. Finally, this chapter also explains construction of the simulation of the PV grid-connected anti-islanding detection method in MATLAB/Simulink simulation software.

Unlike conventional generating units, PV plants do not have inertias. Therefore, the increasing penetration of PV may impact a system's oscillations negatively as PV units add additional dynamics to power system. Therefore, it is essential to analyze a system's behavior before replacing conventional generators by large-scale solar PV units. Chapter 8 analyzes the impacts of increasing penetration of PV units on power systems. The effect of control mode of PV generator on the system's stability is investigated. Both static and dynamic stability analysis methods are conducted to find out the critical issues. The simulation results effectively identify

the impact of high PV penetration on the stability of the studied system which show that voltage control mode of PV generator can improve the performance of a system. However, high penetration of PV can interact negatively with the system in certain cases.

The major disadvantage for use of solar technology is its intermittent and unpredictable nature. This influence the power quality and consistency of the power grid, particularly at large-scale solar energy systems. The variation of sun light may lead to overproduction of electricity at one time and lack of production at another time. The variable nature of solar power causes significant challenges for the electric grid operators. To smooth out the intermittency of solar energy production, electrical energy storage technology will become necessary. In order to increase the solar energy penetration with appropriate reliability, Chap. 9 presents a range of energy storage systems that could technically and economically be used in association with solar photovoltaic energy.

Superconducting magnetic energy storage (SMES) technology has been progressed actively recently. To represent the state of art SMES research for applications, Chap. 10 presents the system modeling, performance evaluation, and application prospect of emerging SMES techniques in modern power system and future smart grid integrated with photovoltaic power plants. A novel circuit-field-superconductor coupled SMES energy exchange model is built and verified to bridge the applied superconductivity field to the electrical engineering and power system fields. As an emerging SMES application case to suit photovoltaic power plants, a novel low voltage rated DC power system integrated with superconducting cable and SMES techniques is introduced and verified to implement both the high-performance fault current limitation and transient power buffering functions. Four principal SMES application schemes of a sole SMES system, a hybrid energy storage system (HESS) consisting of small-scale SMES and other commercial energy storage systems, a distributed SMES (DSMES) system, and a distributed HESS (DHESS) are proposed and compared for achieving efficient and economical power management applications in future photovoltaic power plants.

Although solar energy is a green energy, it can produce a significant amount of waste. Some types of solar cells use rare elements or precious metals as the component material. Therefore, the recycling of PV modules is necessary for environmental and economic purposes. The recycling process for PV modules includes chemical and physical treatment methods, which have been successfully used in other recycling industries, such as electronics or hardware recycling. The use of these mature technologies can decompose and recycle PV module materials. There are still some differences between PV module recycling and electronic recycling. A solar cell module contains several encapsulating plastic materials, such as ethylene vinyl acetate and polyvinyl fluoride. In recycling programs, removing the plastic materials is the first step. In Chap. 11, several types of recycling processes are introduced, which correspond to different types of PV modules. These methods have been validated and successfully implemented in PV module recycling plants.

4 Summary

According to International Energy Agency about 17 % of the global population did not have access to electricity in 2013. Every government has a vision to provide electricity to all of their citizens. Due to the geographical conditions, e.g., remote areas which are far away from existing grid line and sometime isolated from main land, it is very difficult to fulfill the vision in near future by grid power only. In this regard, renewable energy resource-based off grid electrification program could be a possible solution for remote areas. Solar energy is richly available in almost every country and now it is proven and well accepted all over the world. Solar energy technology is environment friendly and price of the solar module is decreasing day by day. Scientists worldwide are now trying to enhance the solar PV technology to mitigate the growing energy demands through solar PV power plants instated of conventional power plants. The book provides a consistent compilation of fundamental theories, a compendium of current research and development activities as well as new directions to overcome some critical limitations of the solar PV technologies for future solar PV power plants.

References

1. Islam MR, Islam MR, Beg MRA (2008) Renewable energy resources and technologies practice in Bangladesh. Renew Sustain Energy Rev 12(2):299–343
2. Islam MR, Guo YG, Zhu JG, Dorrell (2011) Design and comparison of 11 kV multilevel voltage source converters for local grid based renewable energy systems. In: Proceedings of the 37th annual conference on IEEE Industrial Electronics Society, Melbourne, Australia, 7–10 Nov 2011, pp 3596–3601
3. Islam MR, Guo YG, Zhu JG (2011) H-bridge multilevel voltage source converter for direct grid connection of renewable energy systems. In: 2011 IEEE PES Innovative Smart Grid Technologies Asia (ISGT), Perth, Australia, 13–16 Nov 2011, pp 1–7
4. Earth Policy Institute (2015) Climate, energy and transportation, world cumulative wind turbine installations. (Online) Available at: http://www.earth-policy.org. Accessed on 20 Nov 2015)
5. Islam MR, Guo YG, Zhu JG (2014) Introduction. Power converters for medium voltage networks. Springer-Verlag, Berlin, Heidelberg, pp 1–15
6. Islam MR, Guo YG, Zhu JG (2012) 11-kV series-connected H-bridge multilevel converter for direct grid connection of renewable energy systems. J Int Conf Elec Mach Syst 1(2):211–219
7. Islam MR, Guo YG, Zhu JG (2014) Power converters for small- to large-scale photovoltaic power plants. Power converters for medium voltage networks. Springer-Verlag, Berlin, Heidelberg, pp 17–49
8. Islam MR, Guo YG, Zhu JG (2011) Transformer-less local grid based 11 kV SCHB multilevel converter for renewable energy systems. In: 2011 international conference on electrical machines and systems, Beijing, China, 20–23 Aug 2011, pp 1–6
9. International Renewable Energy Agency (IRENA). Solar photovoltaics technology brief. (Online) Available at: http://www.irena.org. Accessed on 10 Dec 2015
10. Power Division, Ministry of Power, Energy and Mineral Resources, Government of the Peoples Republic of Bangladesh. 500 MW solar programme. (Online) Available at: http://www.powerdivision.gov.bd. Accessed on 5 Jan 2016

11. Kumar BS, Sudhakar K (2015) Performance evaluation of 10 MW grid connected solar photovoltaic power plant in India. Energy Rep 1(1):184–192
12. Islam MR, Guo YG, Zhu JG (2014) A multilevel medium-voltage inverter for step-up-transformer-less grid connection of photovoltaic power plants. IEEE J Photovoltaics 4(3):881–889
13. Islam MR, Guo YG, Zhu JG (2014) A high-frequency link multilevel cascaded medium-voltage converter for direct grid integration of renewable energy systems. IEEE Trans Power Electron 29(8):4167–4182
14. Islam MR, Lei G, Guo YG, Zhu JG (2014) Optimal design of high-frequency magnetic-links for power converters used in grid connected renewable energy systems. IEEE Trans Magn 50 (11), art 2006204
15. Islam MR, Guo YG, Lin ZW, Zhu JG (2014) An amorphous alloy core medium frequency magnetic-link for medium voltage photovoltaic inverters. J Appl Phys 115(17):17E710-1–17E710-3

Photovoltaic Inverter Topologies for Grid Integration Applications

Tan Kheng Suan Freddy and Nasrudin Abd Rahim

Abstract For grid integration photovoltaic (PV) system, either compact high-frequency transformer or bulky low-frequency transformer is employed in the DC- or AC side of the PV inverter, respectively, to step up the low output voltage of the PV modules to the grid voltage. Galvanic isolation is provided and the safety is assured with the use of transformer. Because of the high cost and high loss of the transformer, the PV inverter becomes expensive and low efficient. To mitigate these problems, the transformer is removed from the PV inverter. The transformerless PV inverter is smaller, cheaper, and higher in efficiency. Various transformerless PV inverter topologies, with different circuit configuration and modulation techniques, have been developed recently. The operating principle and the converter structure are evaluated in this chapter. It is expected that the transformerless PV inverter would have great potential for future renewable generation and smart microgrid applications.

Keywords Photovoltaic (PV) inverters · Transformerless · Common-mode voltage (CMV) · Leakage current

1 Introduction

Photovoltaic (PV) energy has experienced remarkable growth in recent decades owing to the renewable energy policy, feed-in-tariff and cost reduction of the PV installation. According to the IEA-PVPS report, the cumulative capacity of installed

T.K.S. Freddy (✉) · N.A. Rahim
UM Power Energy Dedicated Advanced Centre (UMPEDAC),
University of Malaya, 59990, Kuala Lumpur, Malaysia
e-mail: freddytan.86@gmail.com

N.A. Rahim
Renewable Energy Research Group, King Abdulaziz University,
21589, Jeddah, Saudi Arabia
e-mail: nasrudin@um.edu.my

M.R. Islam et al. (eds.), *Advances in Solar Photovoltaic Power Plants*,
Green Energy and Technology, DOI 10.1007/978-3-662-50521-2_2

PV reaches 177 GW by 2014, out of which the majority (∼90 %) is grid-connected system [1]. The increase demand of the PV installation, especially grid-connected PV system, indicates that there is a need for in-depth research and development.

Cost-effectiveness and efficiency are the most considered criteria for PV inverter design. Therefore, the PV inverters must be designed with high efficiency at minimum cost. Various types of PV inverters can be found in the market. For grid integration application, there are generally two types of PV inverters, i.e., with transformer and without transformer. The transformer used can be high-frequency transformer on the DC side or low-frequency transformer on the AC side of the inverter. In order to reduce the cost and to increase the efficiency, the recent technology is to remove the transformer from the PV inverter. The transformerless PV inverter becomes smaller, lighter, cheaper, and highly efficient [2–4].

Nevertheless, safety issue is the main concern of the transformerless PV inverter due to high leakage current. Without galvanic isolation, a direct path can be formed for the leakage current to flow from the PV arrays to the grid. When the PV arrays are grounded, stray capacitance is created. The fluctuating potential, also known as common-mode voltage (CMV), charges and discharges the stray capacitance which generates high leakage current. In order to assure the safety operation of the inverter, VDE 0126-1-1 [5] and IEC 60755 [6] standards recommend the use of a residual current monitor unit (RCMU) to monitor the leakage current of the transformerless PV inverter. According to the standards, the inverter must be disconnected within 0.3 s if the leakage current exceeds 300 mA. In addition to safety concern, the leakage current will degrade the performance of the PV inverter owing to the increased grid current ripples, losses, and electromagnetic interference (EMI).

In order to comply with the standards requirements, various transformerless PV inverter topologies have been introduced, with leakage current minimized by the means of galvanic isolation and CMV clamping methods. The galvanic isolation can be achieved via DC-decoupling or AC-decoupling, for isolation on the DC- or AC side of the PV inverter, respectively. Nonetheless, leakage current cannot be simply eliminated by galvanic isolation and modulation techniques, due to the presence of switches' junction capacitances and resonant circuit effects. Hence, CMV clamping method is employed in some topologies to completely eliminate the leakage current [7].

The aim of this chapter is to provide an overview of the recent PV inverter topologies. Several relevant transformerless PV inverters, with different converter structures and modulation techniques, are evaluated. The operation principle of the inverter topologies and leakage current reduction method are briefly investigated. The chapter is organized as follows: Sect. 2 provides an overview of PV configuration for grid integration. Common-mode behavior of the PV inverter is analyzed in Sect. 3. Section 4 describes the leakage current reduction method for transformerless application. The transformerless PV inverter topologies, with the circuit configuration and operating principle, are presented in Sect. 5. Finally, the chapter is concluded in Sect. 6.

2 Overview of PV Configuration for Grid Integration

Based on the state-of-the-art technology, the PV configuration can be classified into four categories: module, string, multi-string and central, as indicated in Fig. 1 [8]. Each configuration comprises a combination of series or/and paralleled PV modules, converters (DC–DC converters or/and DC–AC inverters), depending on the requirement of the system application.

2.1 Centralized Configuration

When a large number of PV modules are interfaced with a single three-phase inverter as shown in Fig. 1d, this configuration is termed as central inverter. The PV modules are connected into series (called strings) to achieve sufficiently high voltage. These PV strings are then made parallel (called arrays) to reach high power level. A blocking diode is connected in series with each PV string branch to avoid reverse current. Central inverter is widely installed in large-scale PV plant. Because of the centralized configuration (with single set of sensors, control platform, and monitoring unit), the central inverter becomes cost-effective for large-scale application. However, the simple configuration comes at a cost of high-level mismatch loss between the PV modules owing to the utilization of a common maximum power point tracking (MPPT) for the entire PV arrays. The power generation loss becomes apparent during the inverter outages. The expansion of the power plant is also difficult to be realized at centralized level.

The conventional central inverter topology is a two-level three-phase full-bridge converter, as indicated in Fig. 2. It is called two-level because it can apply only two voltage levels: the DC supply voltage and the reverse of that voltage. The two-level inverter consists of DC-link capacitors, full-bridge inverter (6 IGBTs) and filters. The central inverter is connected to medium voltage network via a transformer to step up the voltage from LV (e.g., 400 V) to MV level (e.g., 11 kV). To meet higher power requirement, the PV inverter industry, such as ABB PVS800 central inverter [9], introduces a parallel connection directly to the AC side, enabling power to be fed to the medium voltage network via a single transformer as illustrated in Fig. 3. This avoids the need of individual transformer for each central inverter, reducing the cost and space. Nevertheless, in systems where the DC side needs to be grounded, a separate transformer must be employed for galvanic isolation.

The demand of higher power central inverter (MW range) has been continuously increasing with the emerging large-scale PV plant. Although advanced semiconductors with higher nominal voltage and current capability are available, they are very relatively more expensive with high loss. On the other hand, the high-power central inverter is made possible with multilevel configuration. Because of its reduced voltage derivatives (dv/dt) and higher voltage operating capability, the

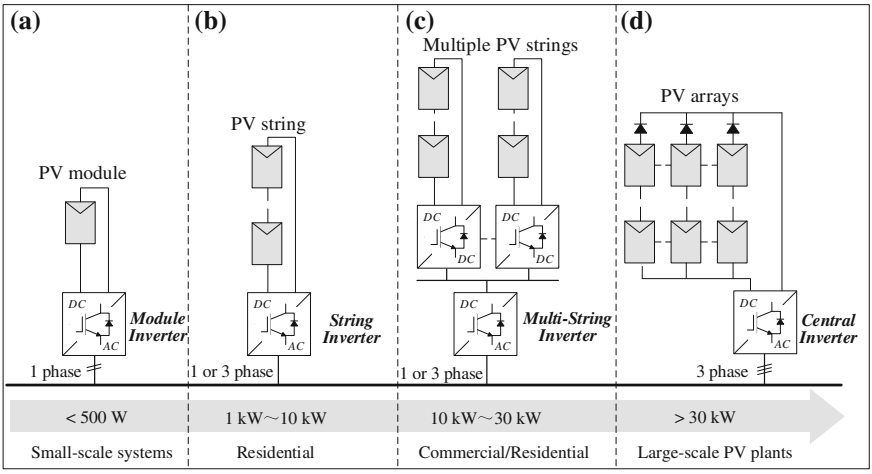

Fig. 1 Configuration of PV systems: **a** module inverter, **b** string inverter, **c** multi-string inverter, **d** central inverter [8]

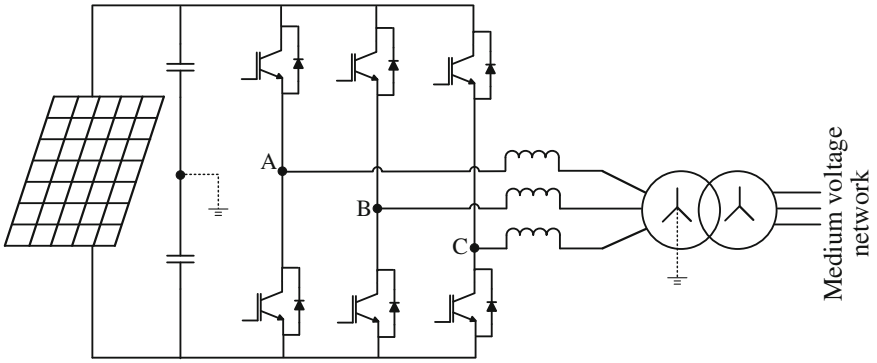

Fig. 2 Three-phase two-level centralized inverter configuration

Fig. 3 The parallel connection of two central inverter to MV network via a single transformer

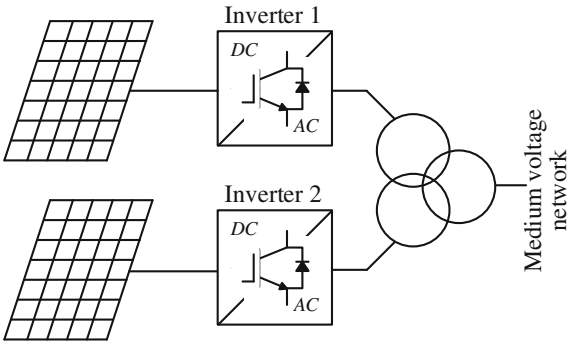

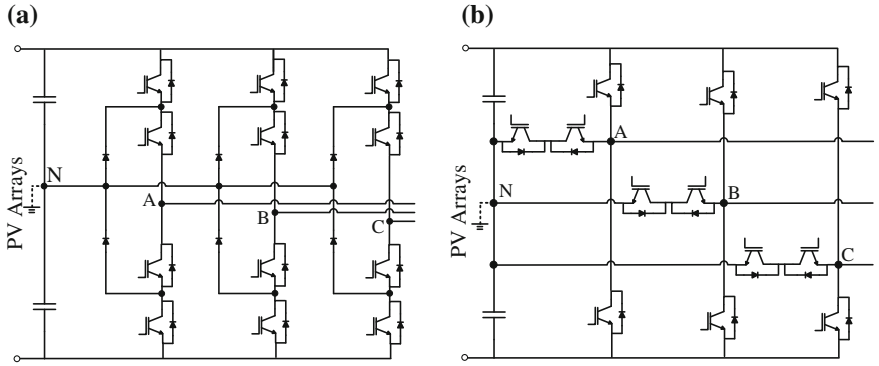

Fig. 4 Three-level central inverter: **a** NPC, **b** T-Type

multilevel converter becomes attractive for high power application. The multilevel converter generates increased level at output phase voltage, which leads to higher power quality and reduced switching loss. Nonetheless, the high power quality requires higher complexity of circuit configuration and the corresponding control, which leads to higher initial cost. The three-phase three-level neutral point clamped (3L-NPC) converter and the T-type (3L-T) converter are two widely used converter as shown in Fig. 4 [10]. The NPC and T-type converter modules have been commercialized by several manufacturers such as Semikron, Infineon and Fuji [11].

2.2 Module Configuration

Module inverter is also known as micro-inverter. In contrast to centralized configuration, each micro-inverter is attached to a single PV module, as shown in Fig. 1a. Because of the "one PV module one inverter concept," the mismatch loss between the PV modules is completely eliminated, leading to higher energy yields. With module configuration, expansion and installation become an easy task. Micro-inverter certainly allows for a very high degree of flexibility, but it comes at an expense of higher upfront costs and greater service requirements. A large number of inverters are required for large-scale application. DC–DC converter is usually included in micro-inverter to boost the low voltage of the PV module to meet the grid requirement. High voltage amplification may shrink overall efficiency and increase price per watt. Although micro-inverters are typically used in low-power application, large-scale PV plant with micro-inverters is emerging. As shown in Fig. 5, Enphase (ENPH) installed a 2 MW solar project at Ontario, Canada's Vine Fresh Produce, with 9000 Enphase® M215 micro-inverters [12].

Micro-inverters usually come with longer warranty up to 25 years, thanks to their effort to extend the lifespan of the capacitors. The first approach is to eliminate the use of electrolytic capacitors by Enecsys [13]. Enecsys 240 W micro-inverters

Fig. 5 A photo of 2.3 MW micro-inverter solar project at Ontario, Canada's Vine Fresh Produce

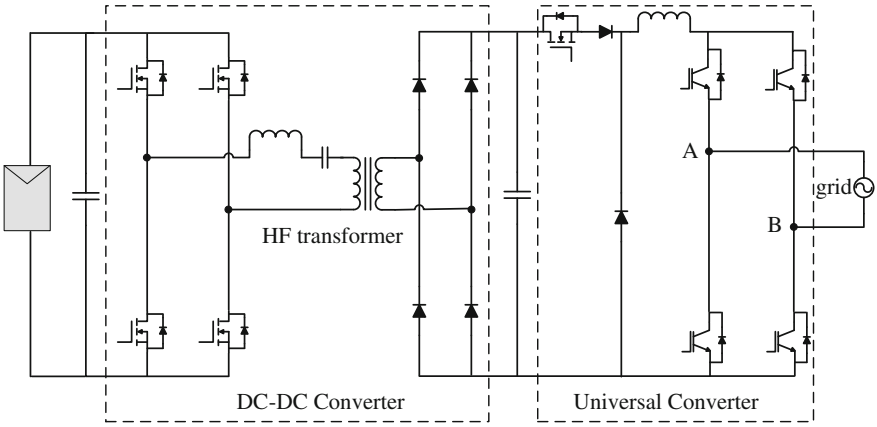

Fig. 6 Commercial Enecsys micro-inverter

are the first micro-inverters without electrolytic capacitors to achieve higher reliability. The micro-inverter configuration is shown in Fig. 6, which includes a DC–DC boost converter and a DC–AC inverter (universal converter). The DC–DC converter is made up of a resonant H-bridge, a high-frequency (HF) transformer, and a bridge rectifier. With buck, boost and buck–boost capability, the universal converter can operate with a wide range of input voltage, improving the power quality and the efficiency [10]. Without the use of electrolytic capacitors, the inverter has an operating life expectancy of greater than 25 years, matching that of solar PV modules. The second approach is the use of interleaved flyback converter. The Enphase micro-inverter configuration is shown in Fig. 7 [14]. The flyback

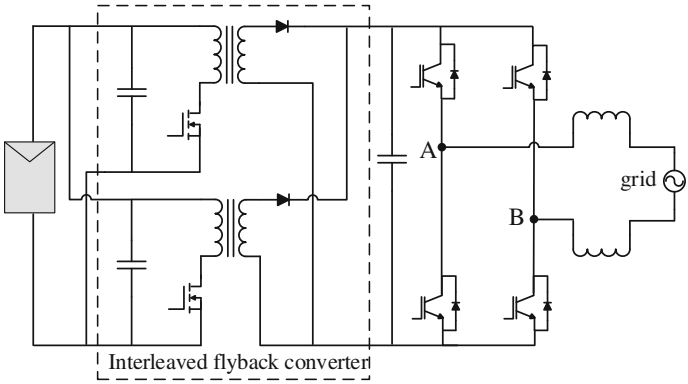

Fig. 7 Commercial Enphase micro-inverter

converter is connected in parallel, and modulated with interleaved PWM. Compared with the conventional flyback converter, interleaved topology requires smaller filter capacitors and smaller HF transformer, which offers higher power capability with greater life expectancy.

2.3 *String Configuration*

In string configuration, each inverter is attached to only one PV string, avoiding the use of blocking diode as shown in Fig. 1b. String inverter combines the advantages of simple structure central inverter and high-energy-yield micro-inverter. Higher energy yield is achieved with MPPT operating at string level, thereby reducing the mismatch loss between the PV modules as compared to centralized configuration. Since the configuration is made up of one PV string per inverter, the string inverter is usually designed for low power application, typically for residential rooftop application.

In the past, U.S. regulations dictated that all electrical systems must be grounded. For grounded PV system, galvanic isolation must be provided in order to avoid the leakage current. Galvanic isolation can be provided via HF transformer on the DC side or via LF transformer on the AC side as shown in Fig. 8 [15]. Besides isolation, transformer steps up the input voltage, which provides a wide range of input voltage. However, the transformer is bulky, heavy, and expensive. Even though significant size and weight reduction can be achieved with HF transformer, the use of transformer still reduces the efficiency of the entire PV system.

Since 2005, the National Electric Code update for allowing ungrounded system opens a huge market for transformerless technology. There are numerous types of string inverters available in the market, and only several will be covered here as shown in Fig. 9. The simplest transformerless string inverter is the full-bridge

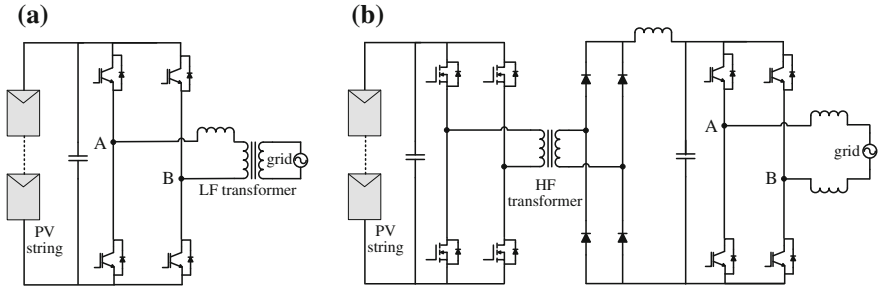

Fig. 8 String inverters with galvanic isolation: **a** with LF transformer, **b** with HF transformer

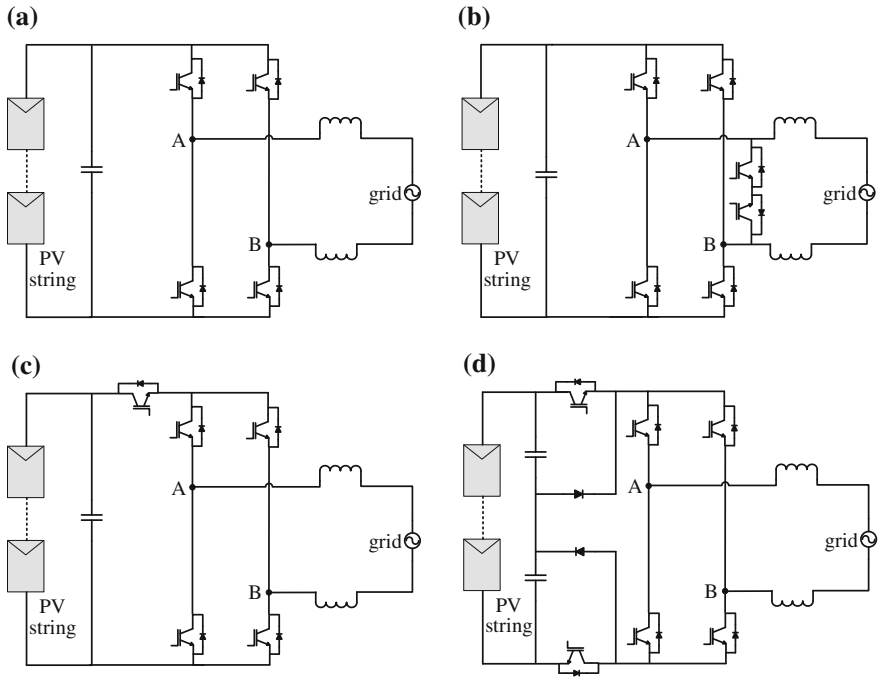

Fig. 9 Two-level string inverters: **a** full-bridge, **b** HERIC, **c** H5, **d** H6

topology as shown in Fig. 9a. The full-bridge topology is modulated by bipolar PWM in order to generate constant CMV, to eliminate the leakage current. Nonetheless, the two-level bipolar PWM doubles the voltage stress and current ripples across the filter inductors, reducing the efficiency of the PV system.

To achieve high efficiency, various inverter manufacturers have developed different circuit configuration with three-level unipolar PWM. The Sunway HERIC topology (Fig. 9b) [16] and the SMA H5 topology (Fig. 9c) [17] introduce DC decoupling and AC decoupling methods, respectively, to disconnect the PV string

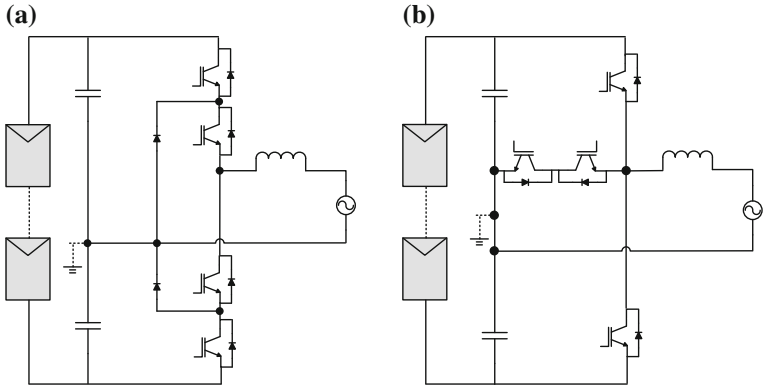

Fig. 10 Three-level string inverters: **a** NPC, **b** T-type

from the grid. The former provides lower conduction loss due to reduced semiconductors in the conduction path. However, galvanic isolation alone cannot completely eliminate the leakage current due to the influence of switches' junction capacitances and parasitic parameters. Therefore, CMV clamping method is proposed in the H6 topology by Ingeteam [18] to completely eliminate the leakage current as shown in Fig. 9c. Two clamping diodes are added in additional to the DC decoupling switches to completely clamp the freewheeling path to half of the input voltage, $V_{DC}/2$.

The high-efficiency three-level inverter is also very suitable for transformerless application. With the neutral of the grid connected to the midpoint of the DC link capacitors as shown in Fig. 10, the high-frequency component of the CMV is eliminated in Danfoss T-type and Conergy NPC converters [19]. Without high-frequency CMV, leakage current is thoroughly eliminated. The low loss and high power quality characteristics make the three-level converter very attractive for large-scale applications. Despite the outstanding performances, the three-level configuration requires double input voltage as compared to that of the two-level inverter. As a result, DC–DC converter with high boost capability is required. Structure and control of the converter become complex with additional cost.

2.4 Multi-string Configuration

The multi-string inverter is the combination of central and string configurations as shown in Fig. 1d. Several PV strings with individual DC–DC converter (MPPT) are connected to a common inverter. It is the mainstream inverter today. While

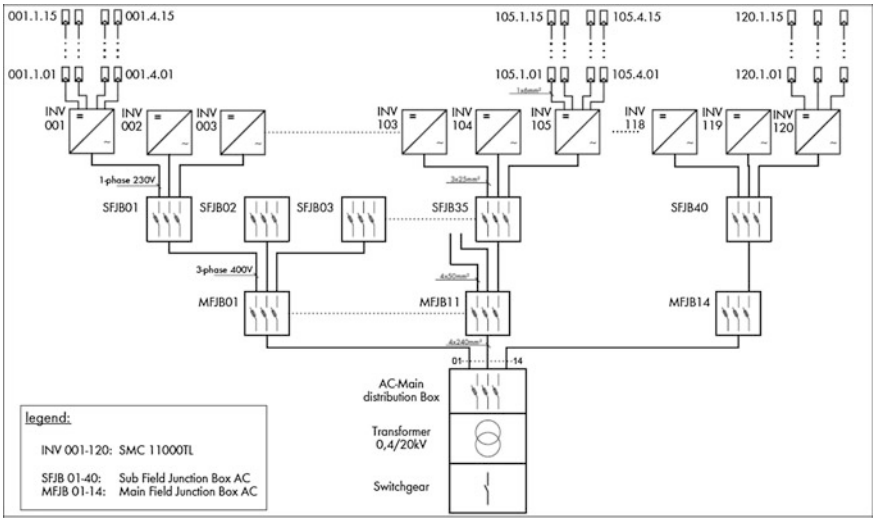

Fig. 11 Block diagram of a 1.2 MW PV plant with SMC 11000TL multi-string inverters

retaining the simple structure and cost-effective characteristic of the centralized configuration, the multi-string inverter minimizes the mismatch loss between the PV modules with each MPPT per PV string. Figure 11 shows a block diagram of 1.2 MW PV plant with single-phase transformerless multi-string SMA inverters [20]. Although multi-string configuration requires larger amount of inverters with higher investment cost, the ease of installation, commissioning, and maintenance are pushing the market toward the use of multi-string inverters in large-scale PV plants. Installing large central inverters requires advanced infrastructure for shipping and installation. Multi-string inverters come on standard palettes, simplifying and expediting shipping and other on-site logistics. With multi-string configuration, the PV plant can be easily expanded, with additional PV strings and inverters added to it without affecting the existing system structure.

Figure 12 presents the basic DC-DC converter structures for multi-string inverter. HF-based converter as indicated in Fig. 12a, provides a wide range of input voltage. It is suitable for applications in the countries where galvanic isolation is priority. This type of converter suffers from complexity of control and relative higher loss compared to boost converter shown in Fig. 12b. The boost converter is simple in structure and in control. Besides boosting the input voltage, it operates the MPPT. Multi-string inverter covers a wide range of topologies. All the discussed topologies, ranging from two-level to multilevel configurations, have the potential to be multi-string inverter. Both single- and three-phase inverters are available in the market.

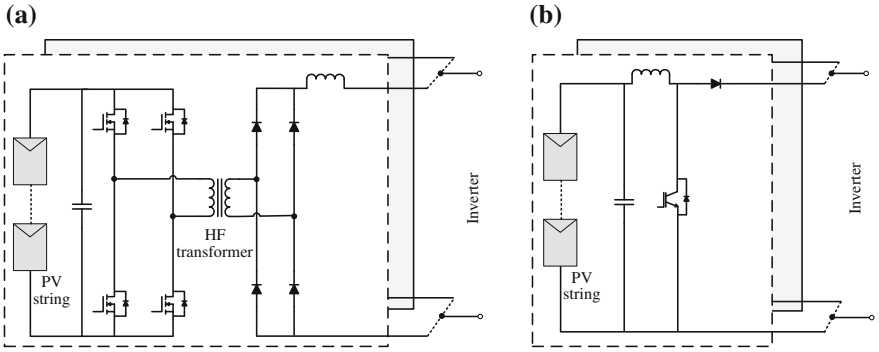

Fig. 12 DC–DC converters for multi-string inverter: **a** HF transformer-based converter, **b** boost converter

3 Common-Mode Behavior

The transformerless technology offers high-efficiency PV inverter at reduced cost. This explained why the PV inverter trend is moving toward transformerless topology. In order to understand the fundamental principle of the transformerless topology, the common-mode behavior will be analyzed here based on single-phase system. The similar common-mode behavior analysis can be extended to three-phase system, and thus the three-phase analysis will not be covered here.

When the transformer is removed from PV inverter, galvanic connection is formed between the PV arrays and the grid. This galvanic connection creates a leakage current path as shown in Fig. 12. When the CMV is produced by the inverter topology with corresponding pulse width modulation (PWM), the CMV charges and discharges the stray capacitance. As a result, leakage current is generated, flowing through the leakage current path between the PV arrays and the grid. In order to design a suitable transformerless PV inverter topology with reduced leakage current, the common-mode behavior must first be understood. A common-mode model circuit is derived here and simplified stage by stage to study the common-mode behavior of the transformerless PV inverter.

For transformerless inverter, a resonant circuit is formed as shown in Fig. 13. This resonant circuit includes the parasitic capacitance (C_{PV}), the filter inductors (L_1 and L_2), leakage current (I_L). Here, the power converter is represented by a block with four terminals to allow a general representation of various converter topologies. On the DC side, P and N are connected to the positive and negative terminal of the DC link respectively; while on the AC side, terminals A and B are connected to the single-phase grid via filter inductors [15].

From the view of point of grid, the power converter block as shown in Fig. 14 can be considered as voltage sources, generating into equivalent circuit which consists of V_{AN} and V_{BN}. Obviously, the leakage current is a function of V_{AN}, V_{BN}, grid voltage, L and C_{PV}. Since the grid is a low-frequency voltage source (50 or

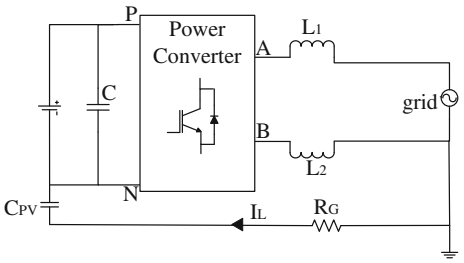

Fig. 13 Resonant circuit for single-phase transformerless PV inverter

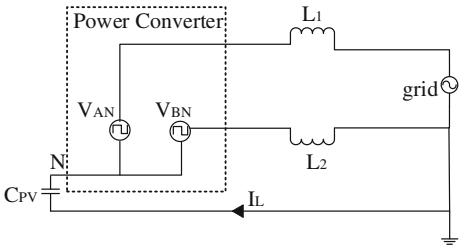

Fig. 14 Simplified resonant circuit for single-phase transformerless topology

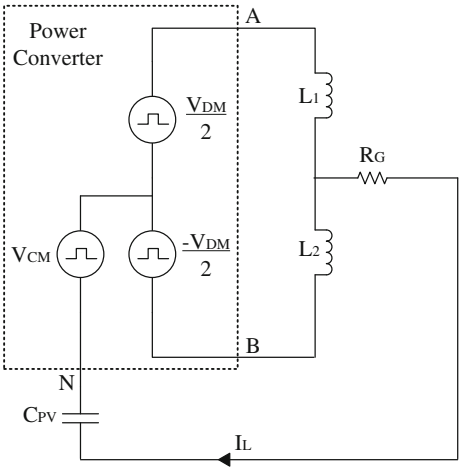

Fig. 15 Simplified resonant circuit for single-phase transformerless topology

60 Hz), the impact on the common-mode model will be ignored here. Therefore, a simplified common-mode is obtained as shown in Fig. 15 by expressing voltages V_{AN} and V_{BN} as the functions of V_{CM} and V_{DM}.

The CMV (V_{CM}) and differential-mode voltage (V_{DM}) can be defined as

$$V_{CM} = \frac{V_{AN} + V_{BN}}{2} \tag{1}$$

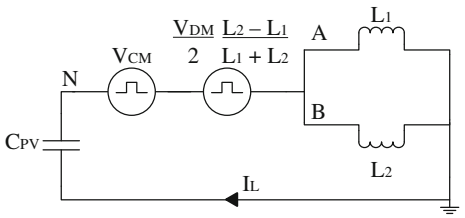

Fig. 16 The simplest resonant circuit for single-phase transformerless topology

$$V_{DM} = V_{AN} - V_{BN} \tag{2}$$

Rearranging (1) and (2), the output voltages can be expressed in terms of V_{CM} and V_{DM} as

$$V_{AN} = V_{CM} + \frac{V_{DM}}{2} \tag{3}$$

$$V_{BN} = V_{CM} - \frac{V_{DM}}{2} \tag{4}$$

Using (3) and (4) and considering only the common-mode components of the circuit, a simplified common-mode model can be obtained as in Fig. 15. The equivalent CMV (V_{ECM}) is defined as (5). Based on the derivation, the simplest common-mode model circuit can be obtained as indicated as Fig. 16.

$$V_{ECM} = V_{CM} + \frac{V_{DM}}{2}\frac{L_2 - L_1}{L_1 + L_2} \tag{5}$$

In order to avoid the influence of V_{DM}, two identical ($L_1 = L_2$) must be used. This also explains why the two filter inductors, i.e., one in line and the other in neutral, are always used in transformerless PV inverter instead of one inductor. Assuming identical inductors ($L_1 = L_2$) are used, the V_{ECM} is equal to V_{CM}

$$V_{ECM} = V_{CM} = \frac{V_{AN} + V_{BN}}{2} \tag{6}$$

According to the common-mode model analysis, it can be concluded that the leakage current is very much dependent of the CMV. If the CMV is varying at high frequency, the C_{PV} will be charged and discharged which leads to high leakage current flowing in the current path. On the other hand, the leakage current will be eliminated when the CMV is kept constant. Therefore, the converter structure and the modulation technique must be designed to generate constant CMV in order to eliminate the leakage current.

4 Leakage Current Reduction Methods

4.1 Galvanic Isolation

In transformerless PV inverter, the galvanic connection between the PV arrays and the grid allows leakage current to flow. The galvanic isolation can basically be categorized into DC decoupling and AC decoupling methods. For DC decoupling method, DC bypass switches are added on the DC side of the inverter to disconnect the PV arrays from the grid during the freewheeling period. However, the DC bypass branch, which consists of switches or diodes, is included in the conduction path as shown in Fig. 16. The output current flows through two switches and the two DC bypass branches during the conduction period. Hence, the conduction losses increase due to the increased number of semiconductors in the conduction path.

On the other hand, bypass branch can also be provided on the AC side of the inverter (i.e., AC decoupling method). This AC bypass branch functions as a freewheeling path which is completely isolated from the conduction path, as shown in Fig. 17. As a result, the output current flows through only two switches during the conduction period. In other words, topologies employing AC decoupling techniques are found to be higher in efficiency as compared to DC decoupling topologies.

One setback of galvanic isolation is that there is no way of controlling the CMV by PWM during the freewheeling period. Figures 18 and 19 show the operation modes of galvanic isolation topology which employs DC decoupling method (one DC bypass branch) during the positive half-cycle. As indicated in Fig. 18, during the conduction period, S_1 and S_4 conduct to generate the desired output voltage. At the same time, V_A is directly connected to V_{DC} and V_B is connected to the negative terminal (N) of the DC link. Hence, the CMV becomes

$$V_{CM} = \frac{V_{AN} + V_{BN}}{2} = \frac{1}{2}(V_{DC} + 0) = \frac{V_{DC}}{2} \tag{7}$$

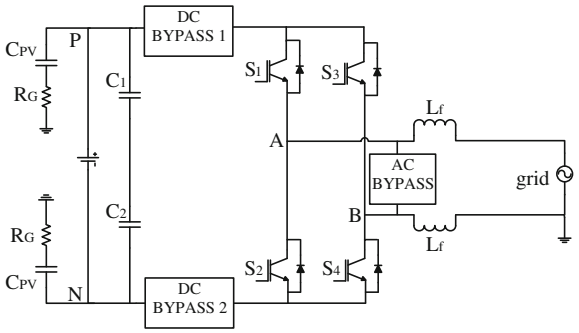

Fig. 17 Galvanic isolation topology via DC- or AC decoupling method

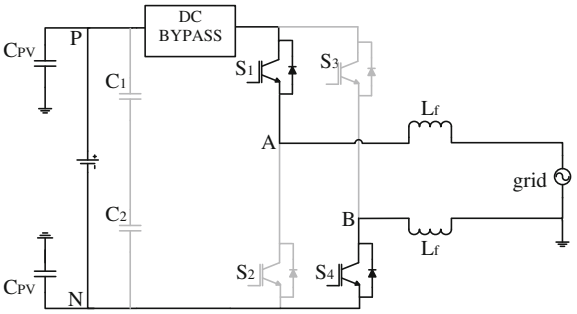

Fig. 18 Operation of DC decoupling topology in conduction mode

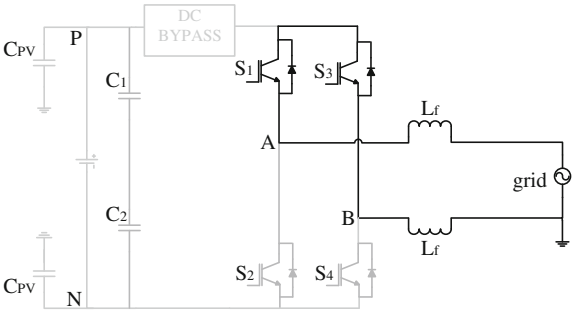

Fig. 19 Operation of DC-decoupling topology in freewheeling mode

Nevertheless, during the freewheeling period, the DC bypass switch disconnects the DC link from the grid. Point A and point B are isolated from the DC link, and V_A and V_B are floating with respect to the DC link as shown in Fig. 19. The CMV during this period of time is not determined by the switching state, but instead, is oscillating with amplitude depending on the parasitic parameters and the switches' junction capacitances of the corresponding topology. As a result, leakage current can still flow during freewheeling period. The same is the case for converters using AC decoupling method. The analysis shows that the leakage current cannot be completely eliminated with the galvanic isolation topology alone.

4.2 CMV Clamping

With galvanic isolation method alone, the leakage current is not completely eliminated as explained in the previous section. The CMV in these topologies cannot be manipulated via PWM due to the parasitic parameters of the resonant circuit. In order to generate constant CMV, clamping branch is introduced [15], as shown in Fig. 20. Generally, the clamping branch consists of diodes or switches and a capacitor divider which ensures the freewheeling path is clamped to the half of the input voltage ($V_{DC}/2$). With the combined effect of galvanic isolation and CMV clamping, leakage current is completely eliminated.

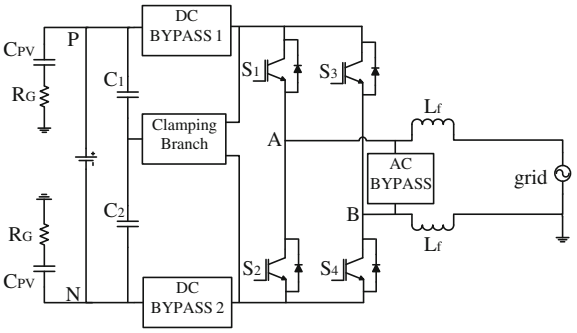

Fig. 20 CMV clamping topology

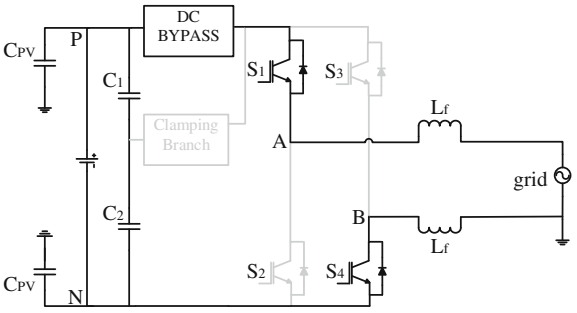

Fig. 21 Operation of DC decoupling topology with CMV clamping branch in conduction mode

Figure 21 illustrates the conduction mode of CMV clamping topology which employs DC decoupling method during the positive half-cycle. S_1 and S_4 conduct to generate the desired output voltage. At the same time, V_A is directly connected to V_{DC} and V_B is connected to the negative terminal (N) of the dc-link. Thus, the CMV becomes

$$V_{CM} = \frac{V_{AN} + V_{BN}}{2} = \frac{1}{2}(V_{DC} + 0) = \frac{V_{DC}}{2} \tag{8}$$

In the freewheeling mode, the DC bypass switch disconnects the DC link from the grid. At this moment, the clamping branch operates, as shown in Fig. 22, so that point A and point B are clamped to $V_{DC}/2$. The CMV reads

$$V_{CM} = \frac{V_{AN} + V_{BN}}{2} = \frac{1}{2}\left(\frac{V_{DC}}{2} + \frac{V_{DC}}{2}\right) = \frac{V_{DC}}{2} \tag{9}$$

The CMV clamping branch ensures the complete clamping of the freewheeling path to constant. As a result, the leakage current is completely eliminated. It is worth noting that the CMV branch is employed with DC- or AC decoupling branch for leakage current reduction. The latter provides lower losses due to the reduced switch count in conduction path as explained earlier.

5 Transformerless PV Inverter Topologies

5.1 Full-Bridge Topology

Full-bridge topology is widely used for various applications due to the simplicity of design and low cost. The full-bridge structure consists of four switches, S_1–S_4, as shown in Fig. 23. Conventionally, the full-bridge topology is modulated by bipolar modulation for transformerless application.

Each pair of the diagonal switches, i.e., S_1, S_4 and S_2, S_3, is operated simultaneously at switching frequency during the positive and negative half-cycle respectively. Current flows through the corresponding pair of diagonal switches to generate the desired output voltage. Bipolar modulation is also known as two-level modulation. As shown in Fig. 24, it generates two-level output voltage, i.e., $+V_{DC}$ and $-V_{DC}$. In every switching transition, the voltage changes across the inductor by twice of input voltage, $2V_{DC}$. This doubles the voltage stress, current ripple and loss across the filter inductors. Thus, the overall efficiency is reduced. Larger filter inductors are required to compensate the high PWM ripple which leads to higher cost.

With bipolar modulation technique, the CMV is constant as illustrated in Fig. 25. The leakage current is completely eliminated. The results show that bipolar modulation is suitable for transformerless PV inverter applications at the expense of reduced system efficiency.

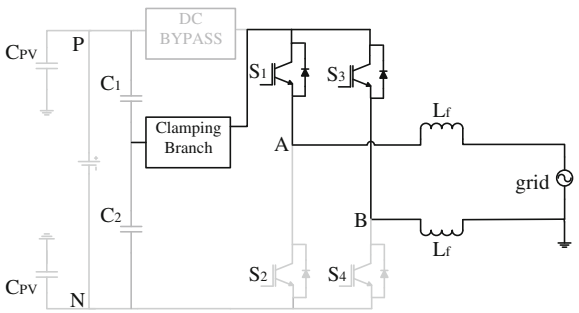

Fig. 22 Operation of DC decoupling topology with CMV clamping branch in freewheeling mode

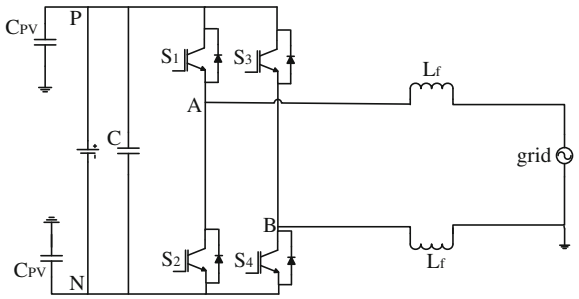

Fig. 23 Full-bridge topology

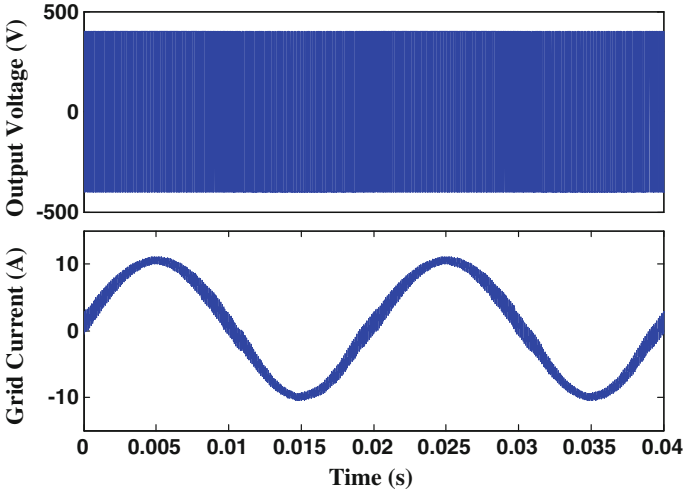

Fig. 24 Output voltage (*top*) and grid current (*bottom*) for bipolar modulation

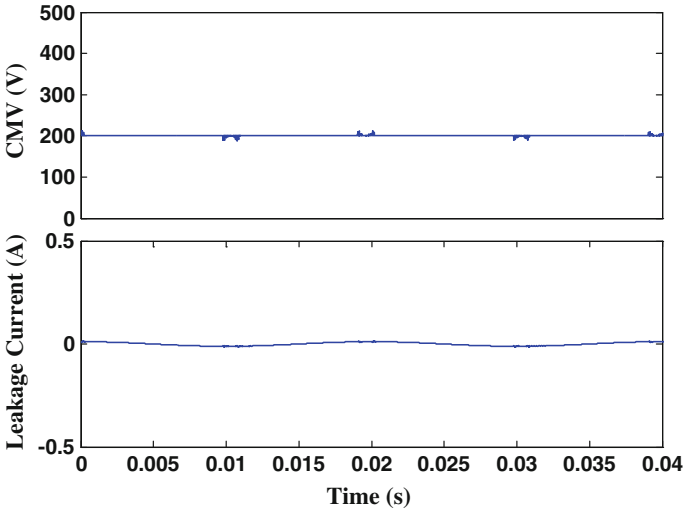

Fig. 25 CMV (*top*) and leakage current (*bottom*) for bipolar modulation

5.2 H5 Topology

H5 inverter [17] is patented by SMA. Given that a total of five switches are utilized, this topology is referred to as H5 inverter. A DC bypass switch, S_5, is added in the input DC side of the conventional full-bridge inverter structure as shown in Fig. 26.

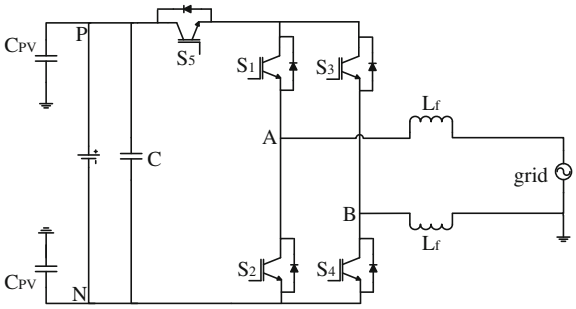

Fig. 26 H5 topology

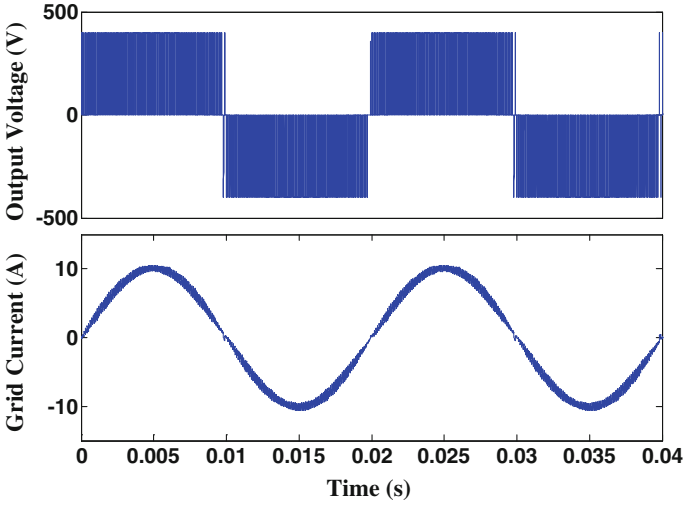

Fig. 27 Output voltage (*top*) and grid current (*bottom*) for H5 topology

The introduction of the Dc bypass switch is to provide galvanic isolation to disconnect the leakage current path during the freewheeling period.

The upper pair of switches S_1 and S_3 is operated at grid frequency while the lower pair of switches S_2 and S_4 is operated at switching frequency. During the conduction period of positive half-cycle, S_1, S_4 and S_5 are ON to generate the desired output voltage. As compared to bipolar modulation, the grid current ripples are smaller due to unipolar output voltage as presented in Fig. 27. Current flows through S_5, S_1, grid, and S_4. During the freewheeling period of positive half-cycle, S_4 and S_5 are OFF, disconnecting the PV from the grid. Current freewheels through S_1 and the anti-parallel diode of S_3.

On the other hand, S_2, S_3, and S_5 are ON to generate the desired output voltage during the conduction period of negative half-cycle. Current flows through S_5, S_3, grid, and S_2. During the freewheeling period of negative half-cycle, S_2 and S_5 are

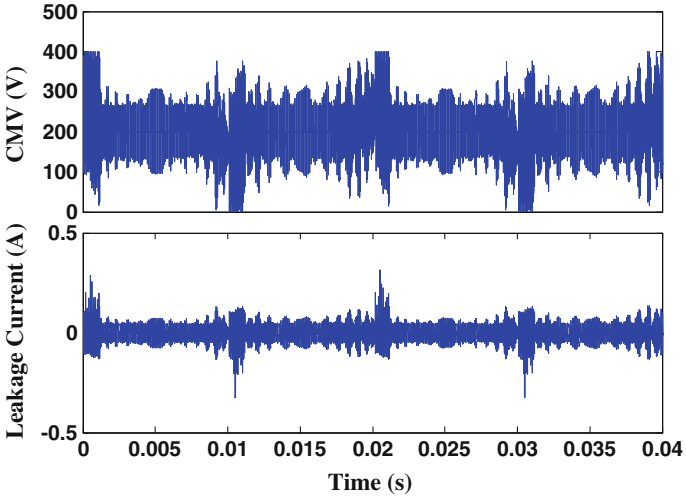

Fig. 28 CMV (*top*) and leakage current (*bottom*) for H5 topology

OFF, disconnecting the PV from the grid. Current freewheels through S_3 and the anti-parallel diode of S_1.

With the galvanic isolation of H5 inverter, leakage current path is disconnected. Nonetheless, the CMV is not constant. Large oscillation with magnitude up to 400 V is observed in Fig. 28. As explained in Sect. 4.1, V_A and V_B are isolated from the dc-link during the freewheeling period when S_5 is OFF. V_A and V_B are floating with respect to the dc-link during the freewheeling period. The CMV is oscillating with amplitude depending on the parasitic parameters. The leakage current can still flow due to the charging and discharging of the stray capacitances by the CMV.

5.3 HERIC Topology

The patented Highly Efficient and Reliable Inverter Concept (HERIC) inverter by Sunway, [16] is well known with its high-efficiency performance. A freewheeling path (S_5 and S_6) is added to the output AC side of conventional full-bridge inverter structure as shown in Fig. 29. Despite the low-loss AC-decoupling topology, the freewheeling switches are operated only at grid frequency. This reduces the switching loss significantly.

Each pair of the diagonal switches, i.e., S_1, S_4 and S_2, S_3, is operated simultaneously at switching frequency during the positive and negative half-cycle respectively. Current flows through the corresponding pair of diagonal switches to generate the unipolar output voltage and sinusoidal grid current as shown in Fig. 30. On the other hand, the freewheeling switches, S_5 and S_6, are ON

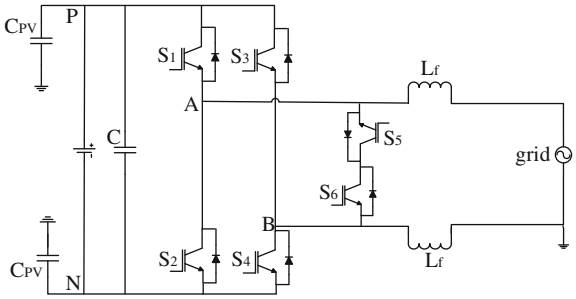

Fig. 29 HERIC topology

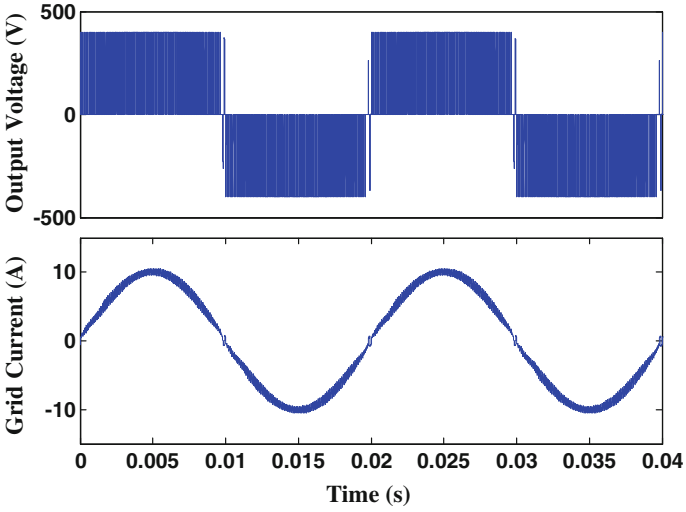

Fig. 30 Output voltage (*top*) and grid current (*bottom*) for HERIC topology

throughout the negative and positive half-cycle respectively. During the freewheeling period of positive half-cycle, current freewheels through S_5, the anti-parallel diode of S_6 and the grid; and through S_6, the anti-parallel diode of S_5 and the grid during the freewheeling period of negative half-cycle.

Galvanic isolation is provided via the freewheeling path. Similar to H5 topology, the CMV is not constant and large oscillation is observed in Fig. 31. The CMV is oscillating with amplitude depending on the parasitic parameters of the resonant circuit. As illustrated in Fig. 31, the leakage current is generated owing to the charging and discharging of the stray capacitances by the CMV.

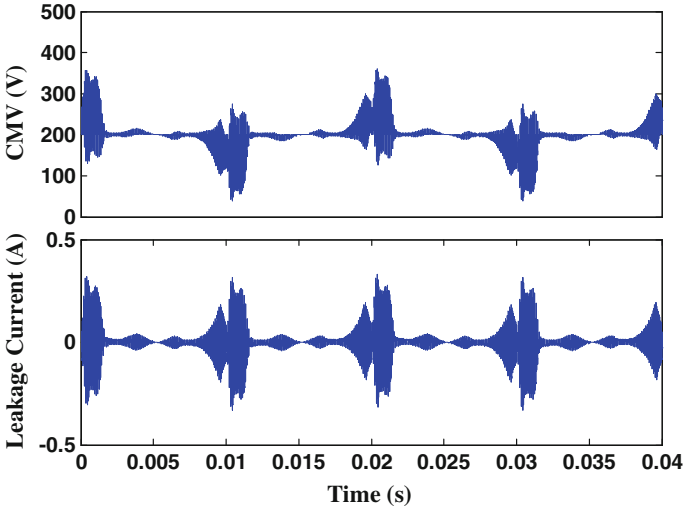

Fig. 31 CMV (*top*) and leakage current (*bottom*) for HERIC topology

Fig. 32 H6 topology

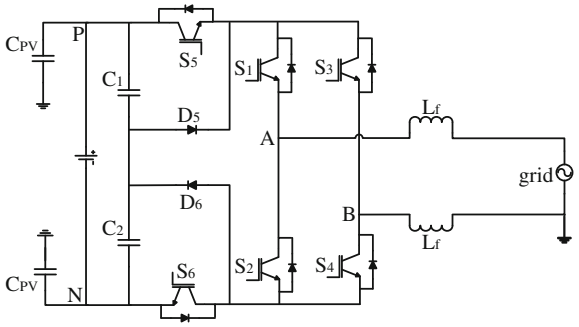

5.4 H6 Topology

H5 and HERIC focus only on providing galvanic isolation while neglecting the effect of the CMV. As a matter of fact, the CMV of these topologies is still floating due to the influence of switches' junction capacitances and parasitic parameters. This issue is mitigated by the clamping branch of H6 topology [18]. Two DC bypass switches, S_5 and S_6 and two clamping diodes, D_5 and D_6, are added to the conventional full-bridge inverter as presented in Fig. 32.

Throughout the positive half-cycle, S_1 and S_4 are ON. S_5 and S_6 commutate simultaneously at switching frequency while S_2 and S_3 commutate together but complementarily to S_5 and S_6. Current flows through S_5, S_1, S_4, and S_6 to generate

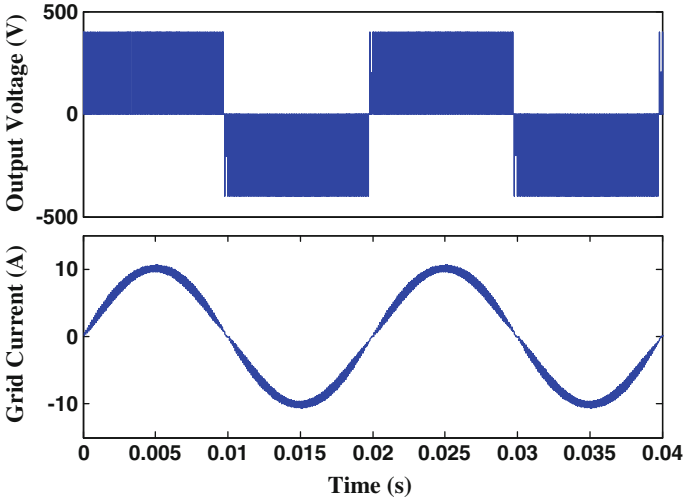

Fig. 33 Output voltage (*top*) and grid current (*bottom*) for H6 topology

the desired output voltage as shown in Fig. 33. Similarly, S_2 and S_3 are ON throughout the negative half-cycle. S_5 and S_6 commutate simultaneously at switching frequency while S_1 and S_4 commutate together but complementarily to S_5 and S_6. During the freewheeling period of negative half-cycle, S_5 and S_6 are OFF and S_1 and S_4 are ON.

During the freewheeling period of positive half-cycle, S_5 and S_6 are OFF and S_2 and S_3 are ON. Therefore, freewheeling current finds its path in two ways, i.e., S_1 and the anti-parallel diode of S_3; S_4 and the anti-parallel diode of S_2. At this moment, the clamping diodes clamp the freewheeling path completely to constant, $V_{DC}/2$. Freewheeling current finds its path in two ways, i.e., S_3 and the anti-parallel diode of S_1, and S_2 and the anti-parallel diode of S_4. The PV is disconnected from grid by the use dc-bypass switches, S_5 and S_6. At this moment, the clamping diodes (D_5 and D_6) clamp the freewheeling path completely to constant at $V_{DC}/2$.

With implementation of the clamping diodes, the CMV is clamped to the constant, and thus the leakage current is eliminated as indicated in Fig. 34. Nevertheless, H6 topology suffers from high conduction losses as the bypass switches have been added into the conduction path.

5.5 oH5 Topology

Similar to H6, oH5 topology [21] is designed with CMV clamping branch. A DC bypass switch S_5 and a clamping switch S_6 are added into the conventional

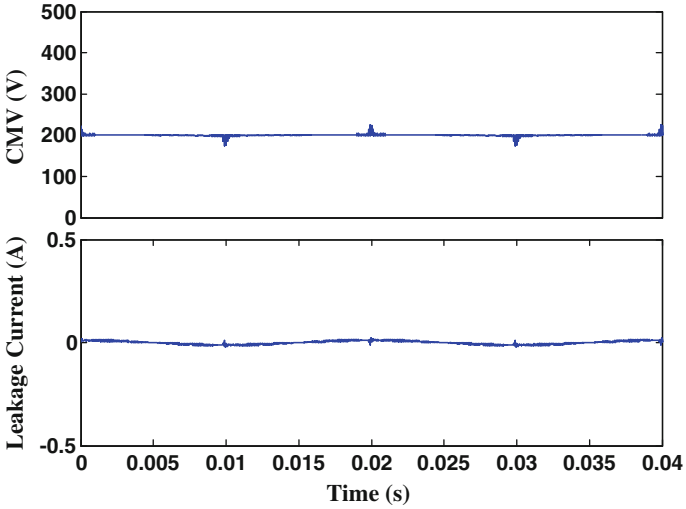

Fig. 34 CMV (*top*) and leakage current (*bottom*) for H6 topology

Fig. 35 oH5 topology

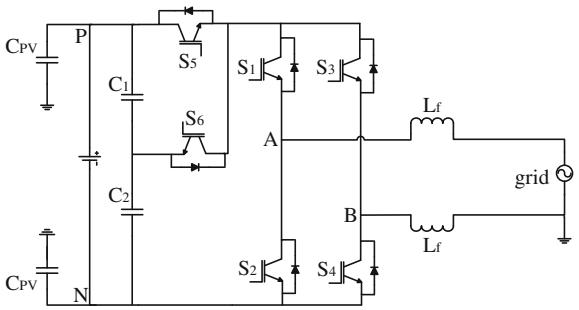

full-bridge inverter structure as shown in Fig. 35. The voltage divider is made up of two capacitors.

Throughout the positive half-cycle, S_1 is ON. S_4 and S_5 commutate simultaneously at switching frequency but complementarily to S_3 and S_6. During the conduction period of positive half-cycle, current flows through S_1, S_4 and S_5 to generate the desired output voltage as shown in Fig. 36. On the other hand, S_3 is ON throughout the negative half-cycle. S_2 and S_5 commutate simultaneously at switching frequency but complementarily to S_1 and S_6. During the conduction period of negative half-cycle, current flows through S_2, S_3 and S_5 to generate the desired output voltage.

The current freewheels through S_1 and anti-parallel diode of S_3 during the freewheeling period of positive half-cycle. At this moment, the clamping switch, S_6, is ON to clamp the freewheeling path completely to constant at $V_{DC}/2$. The current freewheels through S_3 and anti-parallel diode of S_1 during the freewheeling period.

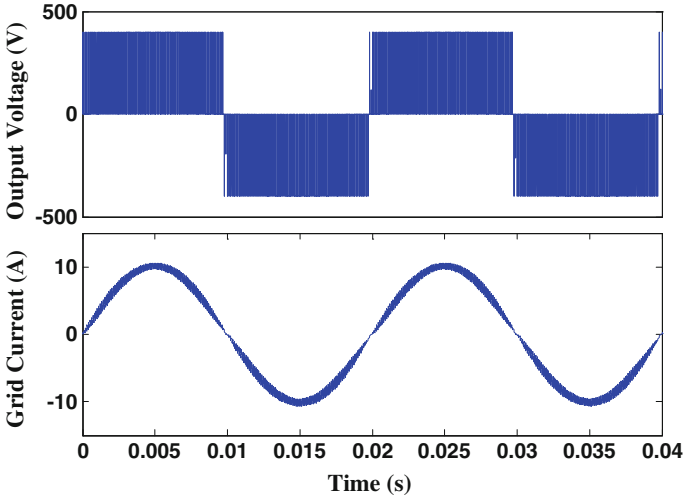

Fig. 36 Output voltage (*top*) and grid current (*bottom*) for oH5 topology

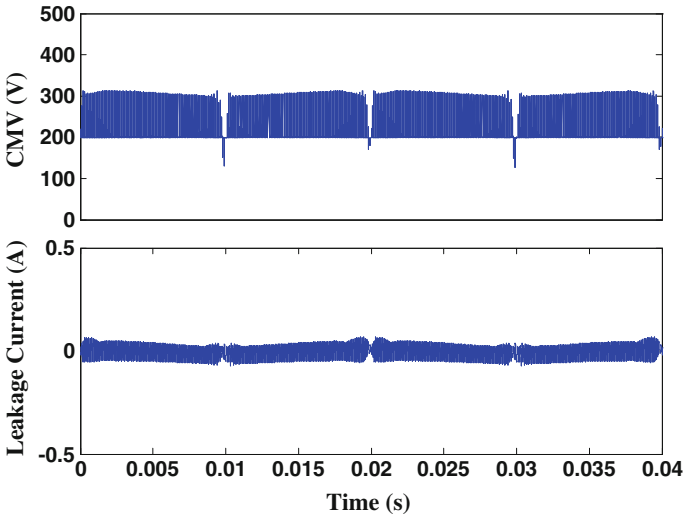

Fig. 37 CMV (*top*) and leakage current (*bottom*) for oH5 topology

Similarly, the freewheeling path is not floating but is being clamped to constant at $V_{DC}/2$ via S_6.

With the clamping switch, the CMV is clamped completely to the constant and the leakage current is eliminated. Despite constant CMV, spikes are still observed as shown in Fig. 37. The occurrence of these spikes is the result of dead time

between S_5 and S_6. Similar to H6 topology, oH5 topology suffers from high conduction losses as the bypass switches have been added into the conduction path.

5.6 HBZVR-D Topology

HBZVR-D inverter [15] is designed with an ac bidirectional freewheeling path and a CMV clamping branch as shown in Fig. 38. The bidirectional freewheeling path consists of a switch, S_5, and a full-bridge rectifier (D_1–D_4). Diodes D_5 and D_6 form the clamping branch of the freewheeling path. The voltage divider is made up of two capacitors.

Each pair of the diagonal switches, i.e., S_1, S_4 and S_2, S_3, is operated simultaneously at switching frequency during the positive and negative half-cycle respectively. Current flows through the corresponding pair of diagonal switches to generate the desired unipolar voltage as shown in Fig. 39. On the other hand, S_5, is ON during the freewheeling period. Current freewheels through D_2 and D_3, and, D_1 and D_4 during the positive and negative half-cycle respectively. At the same time, D_5 or D_6 conducts and clamps the CMV to constant, $V_{DC}/2$, as presented in Fig. 40. The leakage current is completely eliminated.

The clamping branch of HBZVR-D ensures the complete clamping of CMV to $V_{DC}/2$ during the freewheeling period. It is well noted that the output current flows through only two switches in every conduction period. This explains why HBZVR-D has relatively higher efficiency than those of DC decoupling topologies. HBZVR-D combines the advantages of the low-loss AC decoupling method and the complete leakage current elimination of the CMV clamping method.

6 Loss Analysis

Figure 41 presents the loss distribution for various topologies. Conventional bipolar modulation yields the highest total loss due to its two-level modulation technique. H5 and oH5 add one DC bypass switch, whereas H6 adds two DC bypass switches

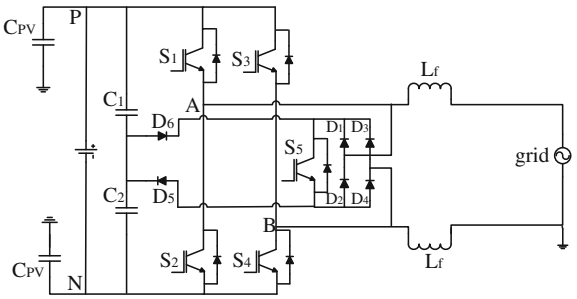

Fig. 38 HBZVR-D topology

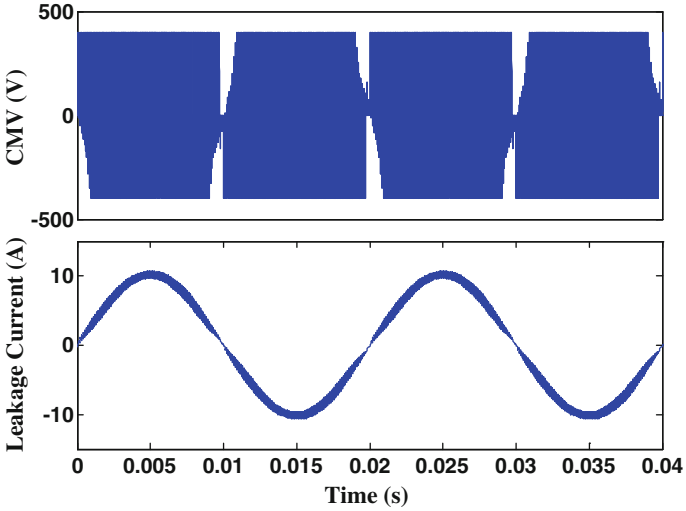

Fig. 39 Output voltage (*top*) and grid current (*bottom*) for HBZVR-D topology

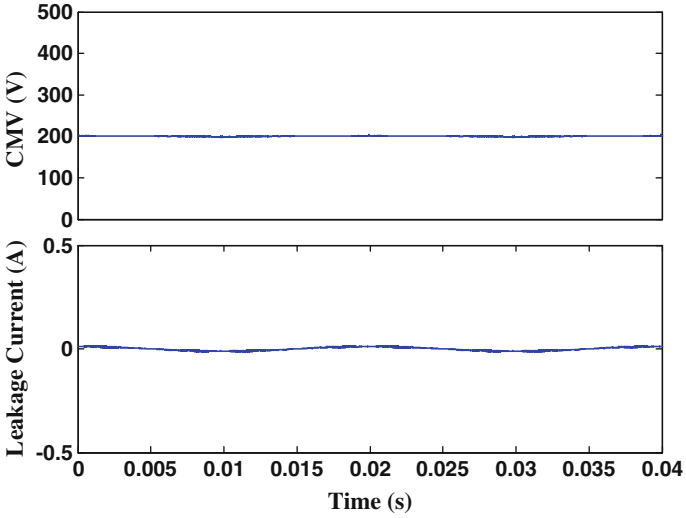

Fig. 40 CMV (*top*) and leakage current (*bottom*) for HBZVR-D topology

and diodes into the conduction path. This explains why all the DC decoupling topologies (H5, oH5, and H6) have higher (conduction) loss as compared to the AC-decoupling topologies (HERIC, and HBZVR-D). H6 topology yields the highest device losses due to excessive components that are added into the conduction path. As expected, HERIC topology has the lowest device losses.

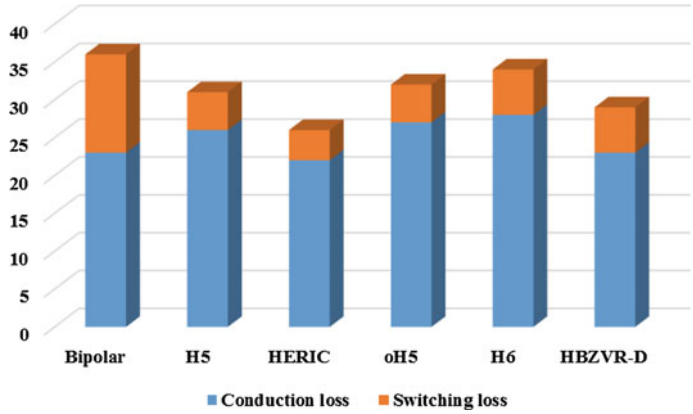

Fig. 41 Loss distribution of various topologies at 1 kW

HBZVR-D has slightly higher losses than HERIC but they are still much lower than those of the DC decoupling family. Obviously, the conduction losses are the main contributor as shown in Fig. 41. The results show that ac-decoupling family outperforms DC-decoupling family in terms of loss.

7 Summary

This chapter provides a comprehensive overview of the PV inverter topologies for grid integration applications. The state-of-the-art PV configurations with several commercial PV inverter topologies are presented. The common-mode behavior are discussed in detail to provide the principle operation of the transformerless PV inverter technologies. The performance of the transformerless PV inverters is investigated.

Today, the PV market is driven by the cost and the efficiency. To meet these requirements, the researchers and manufacturers are continuously looking for new power converters and new semiconductor technology. The high-power-quality and high-efficiency multilevel converter has gained attention from the industries. For semiconductor technology, the wide bandgap materials such as silicon carbide (SiC) and gallium nitride (GaN) outperforms the conventional silicon (Si) material. The SiC MOSFET can operate at high frequency at very low loss, which is very suitable for high-efficiency applications. Although the production cost of the wide bandgap materials are still high, it is expected these materials with the multilevel converters will be widely used in the future.

References

1. International Energy Agency Photovoltaic Power System Program (2014) Trends 2014 in photovoltaic applications: survey report of selected IEA countries between 1992 and 2013, report
2. Suan FTK, Rahim NA, Hew WP (2011) Modeling, analysis and control of various types of transformerless grid connected PV inverters. In: Proceedings of 2011 IEEE first international conference on clean energy and technology (CET), 27–29 June 2011, Kuala Lumpur, Malaysia, pp 51–56
3. Suan FTK, Rahim NA, Hew WP (2013) Three-phase transformerless grid-connected photovoltaic inverter to reduce leakage currents. In: Proceedings of 2013 IEEE international conference on clean energy and technology (CEAT), 18–20 Nov 2013, Langkawi, Malaysia, pp 277–280
4. Islam MR, Guo YG, Zhu JG (2014) Multilevel converters for step-up transformer-less direct grid integration of renewable generation units with medium voltage smart microgrids. In: Large scale renewable power generation: advances in technologies for generation, transmission and storage. Springer, Berlin, pp 127–149
5. VDE, Automatic Disconnection Device between a Generator and the Public Low-Voltage Grid (2005) DIN Electrotechnical Standard DIN VDE 0126-1-1, Standard
6. International Electrotechnical Commission (2011) Safety of power converters for use in photovoltaic power systems—Part 2: particular requirements for inverters, IEC 62109-2 Ed. 1, Standard
7. Freddy TKS, Rahim NA, Hew WP, Che HS (2015) Modulation techniques to reduce leakage current in three-phase transformerless H7 photovoltaic inverter. IEEE Trans Ind Electron 62 (1):322–331
8. Yang YH (2013) Advanced control strategies to enable a more wide-scale adoption of single-phase photovoltaic systems. Dissertation, Aalborg University
9. ASEA Brown Boveri (ABB) Solar photovoltaic central inverter (online). Available at: http://www.abb.com. Accessed on 1 Nov 2015
10. Islam MR, Guo YG, Zhu JG (2014) Power converters for small- to large-scale photovoltaic power plants. In: Power converters for medium voltage networks. Springer, Berlin, pp 17–49
11. Samir K, Bin W, Haitham AR, Frede B (2014) Photovoltaic energy conversion systems. In: Power electronics for renewable energy systems, transportation and industrial applications. Wiley, Chichester, pp 160–198
12. Bennett (2013) Enphase system deployed in 2.3 MW agricultural installation in Canada. Enphase Energy, Inc. http://newsroom.enphase.com/releasedetail.cfm?releaseid=784444. Accessed 1 Nov 2005
13. Garrity P (2013) Solar photovoltaic power conditioning units. US Patent 8391031 B2
14. Fornage M (2010) Method and apparatus for converting direct current to alternating current. US Patent 7796412 B2
15. Freddy TKS, Rahim NA, Hew WP, Che HS (2014) Comparison and analysis of single-phase transformerless grid-connected PV inverters. IEEE Trans Power Electron 29(10):5358–5369
16. Schmidt H, Siedle C, Ketterer J (2005) DC/AC converter to convert direct electric voltage into alternating voltage or into alternating current. US Patent 2005/0174817 A1
17. Victor M, Greizer F, Bremicker S, Hubier U (2005) Method of converting a direct current voltage from a source of direct current voltage, more specifically from a photovoltaic source of direct current voltage, into a alternating current voltage. US Patent 2005/0286281 A1
18. Senosiain RG, Calahorra JC, Palomo LM, Taberna JL, Gurpide PS (2009) Single-phase inverter circuit to condition and transform direct current electric power into alternating current electric power. US Patent 2009/0316458 A1
19. Teodorescu R, Liserre M, Rodriguez P (2011) Photovoltaic inverter structures. In: Grid converters for photovoltaic and wind power systems. Wiley, Chichester, pp 5–29

20. SMA (2009) Decentralized inverter technology in large-scale PV plants, technical information, BL-DezWT-UEN103511
21. Xiao H, Xie S, Chen Y, Huang R (2011) An optimized tranasformerless photovoltaic grid-connected inverter. IEEE Trans Ind Electron 58(5):1887–1895

Advanced Control Techniques for PV Maximum Power Point Tracking

Wei Xu, Chaoxu Mu and Lei Tang

Abstract The Photovoltaic (PV) power has rapid growth due to it is clean, no noise and little maintenance. However, all PV systems have two major drawbacks, i.e. the efficiency of PV power generation is very low and the output power of a PV system is nonlinear, which depends closely on weather conditions, such as ambient temperature and the solar irradiance. Hence, tracking the maximum power of the PV arrays at real time is very important to increase the whole system performance. In the past decades, there are a large number of maximum power point tracking (MPPT) methods have been proposed for PV system, such as constant voltage tracking (CVT) method, perturbation and observation (P&O) method, incremental conductance (INC) method, curve-fitting method, look-up table method, and so on. Actually, these conventional methods can track the maximum power point (MPP). But these methods have some drawbacks, like oscillation, miscalculation, poor accuracy, unimodal *P–U* curves only. To overcome the limitation of these methods, some advanced MPPT methods are introduced in this chapter. The experiment and simulation investigation demonstrate the excellent performance of the new method.

Keywords Photovoltaic · MPPT method · MPPT converter · Nonlinear approach · Fuzzy control · Neural network · Variable step size · Iteration

W. Xu (✉)
School of Electrical and Electronic Engineering, Huazhong University of Science and Technology, Wuhan 430074, China
e-mail: weixu@hust.edu.cn

C. Mu
School of Electrical and Automation Engineering, Tianjin University, Tianjin 300072, China
e-mail: cxmu@tju.edu.cn

L. Tang
School of Electrical Engineering, Xi'an Jiaotong University, Xi'an 710049, China
e-mail: leitangsai@foxmail.com

M.R. Islam et al. (eds.), *Advances in Solar Photovoltaic Power Plants*, Green Energy and Technology, DOI 10.1007/978-3-662-50521-2_3

1 Introduction

As the PV power generation performs a nonlinear current–voltage (*I–U*) curve and the output power of a PV system largely depends on the array temperature and the solar irradiance level, so it is necessary to constantly track the maximum power point (MPP) of the solar array [1]. For years, several methods have been proposed to draw the maximum power of the PV array. All these tracking method have their own advantages and disadvantages but the main technical characters of those methods can be summarized in three points: tracking velocity, tracking accuracy, and stability [2, 3]. The constant voltage tracking (CVT) method transmission algorithm based on the mathematical model of PV cells, find out the maximum output voltage of PV cell point, this method is simple, operation is convenient, but there are some errors, unable to achieve maximum power tracking in the true sense [4]. The perturbation and observation (P&O) method is characterized by simple and clear, hardware and software are conducive to implement, and easy to form the control system of modular, affected by the outside adverse conditions such as the weather changes, easy to the normal operation of the system, and the system of step length and the initial value of the set have bigger influence on the system [5, 6]. Incremental conductance (INC) method of control precision, the speed is faster, adapt to the larger changes in the external environment, the demand for sensor is higher, the cost is relatively high, there will be some loss in the process of actual work [7]. To overcome the limitations of the conventional maximum power point tracking (MPPT) method, some advanced schemes are proposed in recently years. With the development of intelligent control theory, fuzzy logic control, biological swarm algorithm and artificial neural network theory have been applied into every field of electrical engineering, and MPPT of PV power generation technology [8–10]. The fuzzy and neural network method show many advantages like a high accuracy and a better stability. For most of the algorithms, the step size of MPPT methods determines how fast the MPP is tracked. Fast tracking can be achieved with bigger increments, but the system might not run exactly at the MPP and oscillates around it. This situation will turn to the contrary when the MPPT is operating with a smaller increment [11]. To increase the tracking robustness and get better drive performance, iteration and variable step-size algorithms have been proposed. As some of conventional methods are based on the “hill-climbing” principle which moves the operating point (OP) to the direction of power increases. So it can be only applied in the unimodal *P–U* curves, which will absent when the PV arrays operating under partially shaded conditions (PSCs) [12, 13]. According to the fuzzy mathematics and information diffusion theory, a probability algorithm is proposed and the mathematical relationship between global peak (GP) and sampling points of PV curve can be described by a distribution function. In other words, there is a fuzzy probability for GP located into the vicinity of sampling points. And this probability obeys the exponential rising law approximately. At last, the experiment and simulation results demonstrate the excellent performance of these new methods [14, 15].

2 The Physical Basis and Mathematical Model of PV

2.1 The Mathematical Model

The PV cell is made up of semiconductor materials which can convert solar irradiance into electrical energy. Based on the electronics theory of semiconductor p-n junction, it can be described by a current source. The equivalent circuit model of PV cell is shown in Fig. 1. It consists of an ideal current source I_{ph} in parallel, reverse diode, series resistance R_s and parallel resistance every R_{sh} [1].

I_{ph} is the PV generated current which is relative to the solar radiation and temperature. The stronger the irradiance is, the greater the I_{ph} will be. The output character of a single PV cell is described as

$$i = I_{ph} - I_0\left[\exp\left(\frac{q(u+iR_s)}{AkT}\right) - 1\right] - \frac{(u+iR_s)}{R_{sh}} \tag{1}$$

where I_0 is the PV cell reverse saturation current that mainly depends on the temperature (its magnitude is 10^{-4} A), q is the electronic charge of an electron (1.6×10^{-19} C), T is the temperature of the PV cell, k is Boltzmann's constant (1.38×10^{-23} J/K), A is the ideality factor (1.2 for Si-mono), i the PV cell output current, u the PV cell output voltage, R_s and R_{sh} the equalized resistors that related to the temperature.

Although (1) has been widely used in the analysis of PV cell theory, but the expression of five parameters, including I_{ph}, I_0, R_{sh}, R_s and A appeared in the equation, are not only related to the temperature and the irradiance levels, but also it is difficult to determine, and inconvenience in the engineering application, so we do the following simplification.

- Due to R_{sh} is very big and I_{sh} have little impact on the photocurrent, so we can ignore the value of $V + IR_s/R_{sh}$.
- Set I_{ph} is equal to I_{sc}, because R is very small.
- Define the open-circuit conditions $u = U_{oc}$, $U = U_m$ and $I = I_m$ at the MPP.

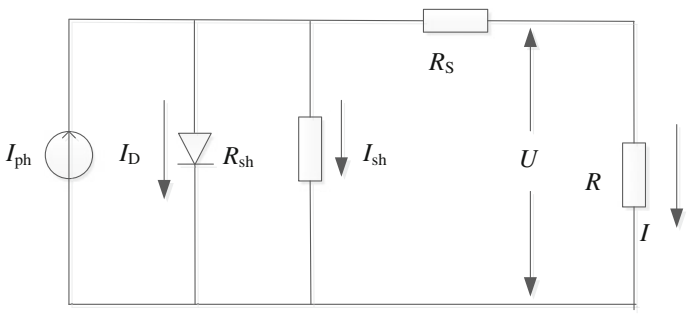

Fig. 1 Equivalent circuit model of PV cell

So the PV cell output characteristic equation can be expressed as

$$i = I_{SC}\left\{1 - C_1\left[\exp\left(\frac{u}{C_2 U_{OC}}\right) - 1\right]\right\} \tag{2}$$

where the C_1 and C_2 can be described as

$$\begin{aligned} C_1 &= \left(1 - \frac{I_m}{I_{SC}}\right)\exp\left(-\frac{U_m}{C_2 U_{OC}}\right) \\ C_2 &= \left(\frac{U_m}{U_{OC}} - 1\right)\Big/\ln\left(1 - \frac{I_m}{I_{SC}}\right) \end{aligned} \tag{3}$$

where U_m is the MPP's voltage for PV model and U_{OC} is the open-circuit voltage. Since $u \in [0, U_{OC}]$, the PV array output power is

$$P(u) = uI_{SC}\left\{1 - C_1\left[\exp\left(\frac{u}{C_2 U_{OC}}\right) - 1\right]\right\} \tag{4}$$

The efficiency of PV cell depends on not only internal shunt resistance but also irradiance, array temperature and load. Here set I_{SCref}, U_{OCref}, U_{mref}, and I_{mref} as the PV parameters under standard conditions, i.e. irradiance S_{ref} = 1000 W/m^2 and circumstance temperature T_{ref} = 25 °C, then I_{SC}, U_{OC}, U_m and I_m could be calculated by

$$I_{SC} = I_{SCref} \cdot \frac{S}{S_{ref}}(1 + a \cdot \Delta T) \tag{5}$$

$$U_{OC} = U_{OCref} \cdot \ln(e + b \cdot \Delta S)(1 - c \cdot \Delta T) \tag{6}$$

$$I_m = I_{mref} \cdot \frac{S}{S_{ref}}(1 + a \cdot \Delta T) \tag{7}$$

$$U_m = U_{mref} \cdot \ln(e + b \cdot \Delta S)(1 - c \cdot \Delta T) \tag{8}$$

where $\Delta S = (S/S_{ref} - 1)$, $\Delta T = (T - T_{ref})$, and typical values of a, b, c can be taken as 0.025/°C, 0.5/(W/m^2), and 0.00288/°C respectively. As shown in Fig. 2, with the circumstance condition changing, the output characteristic of PV cell will change too.

2.2 The Output Characteristic of the PV Cell

PV output characteristic curve it refers to the PV cell output current, output voltage and output power in certain irradiance and environment temperature. Fantasy of PV cell voltage, current, power output characteristic in each part of graph, respectively.

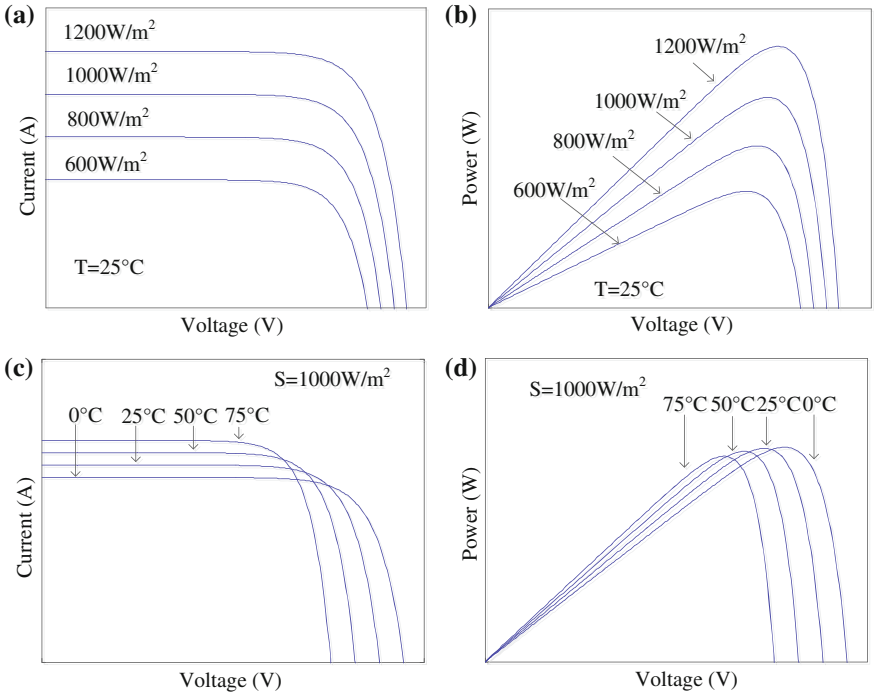

Fig. 2 The output characteristics of PV module under different irradiance and temperature: **a** and **c** are the *I–U* curves, **b** and **d** are the *P–U* curves

The nonlinear is one of the characteristics of PV cells. Within a certain range of output voltage, PV cells are similar to a constant current source. When voltage is more than a certain range continues and continue rising, the PV cell is similar to a constant voltage source [2].

The efficiency of the PV cell depends on not only the internal shunt resistance but also on the irradiance level, array temperature and load. With changing conditions the output characteristic of the PV cell will change. As shown in Fig. 2, the PV array is highly nonlinear, but there is one unique operating point on the curve which gives the maximum efficiency under those conditions. With the circumstance condition changing, the output characteristic of PV cell will change too [12].

Therefore, we should seek the optimal working state of the PV cells for PV power generation systems, to convert solar energy into electrical. By using the method of control to realize the operation of the maximum power output of PV cell technology is known as the MPPT technology. Generally speaking, it is difficult to get a very precise mathematical model of PV cells, so it is too hard to use the mathematical model for accurate MPPT control.

3 The Basic Theory of MPPT

The MPPT method for PV system aims to find the operation point where the product of output voltage and output current are the largest. Theoretically, according to the circuit theory, the PV cells output the maximum power when the output impedance of PV cell is equal to the load. Therefore, the MPPT process of PV cells actually makes PV cells output impedance and load impedance match gradually each other. Since environmental factors have influences on the output impedance of PV cells, it is possible to achieve MPPT control if load impedance is adjusted in real-time tracking output impedance of PV cells. For better discussion, the equivalent impedance of the PV cells R_{opt} is defined as the ratio of the MPP voltage U_{MPP} and the MPP current I_{MPP}, namely $R_{opt} = U_{MPP}/I_{MPP}$. Obviously, the environment condition changes, the R_{opt} will change too. However, there is a load matching problem since they're powered to the particular load in the practical application process.

The curves I and II show the characteristic curve of PV devices under different situations. The point A and B are the maximum output power points of PV devices under different irradiance conditions. Load 1 and load 2 are two load curves. As shown in Fig. 3, the PV devices operating at point A. It will be transferred to the point A′ if the irradiance is suddenly strengthened due to the constant load. In order to get the maximum power of PV devices, it is necessary to make the PV device work at the point B on characteristic curve I. That is to say, the external circuit of the PV devices must be controlled so that the load characteristics become the load curve 2 to implement the power match of the PV devices. In this case, the maximum power of PV devices is outputted.

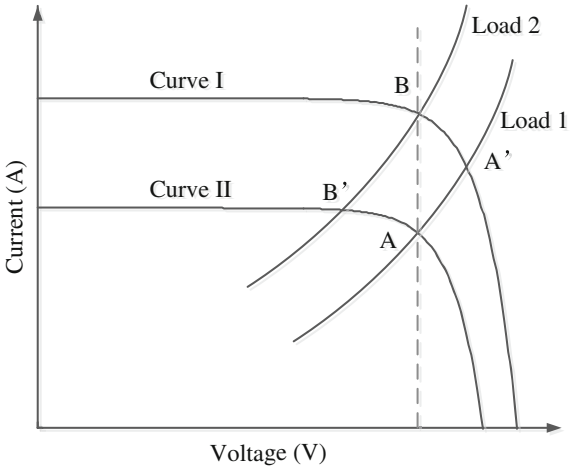

Fig. 3 Schematic diagram of MPPT

4 The Basic Topologies of PV System for MPPT

According to different topologies and positions of MPPT control, PV grid-connected inverter is divided into two categories: two-stage grid-connected PV and single-stage grid-connected PV. In the following, the two basic topologies about MPPT control are discussed.

4.1 The Two-Stage Grid-Connected Structure

Conventional two-stage grid-connected PV inverter consists of the front DC/DC converter (commonly boost converter) and an inverter. Under normal circumstances, it is necessary to use the boost converter to power up the DC output voltage of PV cells, since the output voltage of the PV cells is usually lower than the peak voltage of the grid. Then, the inverter is used to transform DC to AC current. Finally, it is injected into the grid. Because there are two power conversion units in the two-stage grid-connected PV inverter, the MPPT control of PV cells can be achieved by the boost converter or the inverter, which is analyzed as follows [16].

4.1.1 The MPPT Control Based on the Inverter

Figure 4 shows the diagram with the inverter for the MPPT control [17].

In the MPPT control process based on the inverter, first, the MPPT controller is used to calculate the current error ΔI_0 of inverter output. Then, the current amplitude adjustment I_0 of inverter output is got by the proportional integral (PI). The instantaneous current reference I_{ref} of inverter output is obtained by the product

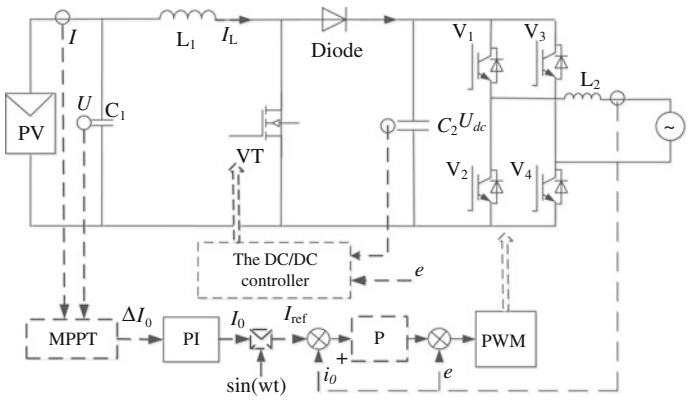

Fig. 4 The MPPT control based on the DC/AC inverter

of I_0 and the sinusoidal value which keep synchronous with grid. The modulation signal is sum of grid voltage feedforward signal and PI regulator value for the error of I_{ref} and instantaneous value i_g of grid current. Finally, the PWM control signal is obtained by the comparison of above modulation signal and of triangular wave in order to achieve the control goal MPPT and unity power factor sinusoidal current. In whole control process, dynamic balance of energy transmission is guaranteed by coordinating the response speed of boost converter and inverter control, in order to stabilize the DC bus voltage. Therefore, in the control system design, response speed of front DC/DC converter control is faster than inverter.

4.1.2 The MPPT Control Based on DC/DC Converter

Compared with the previous discussion of the MPPT control based on the inverter, the MPPT control based on the front inverter shown in Fig. 5 is more common, which completes the MPPT control and sinusoidal current control of inverter simultaneously, where the backward inverter achieves the voltage control of the DC-triangular wave in order to achieve the control goal-bus, and the front boost converter achieves the MPPT control. Since the output voltage of the boost converter is controlled by the inverter, the input current of the boost converter can be controlled by adjusting the duty ratio in order to regulate the output voltage of the PV cells [18].

The voltage reference U_{ref} of PV operating point is obtained by MPPT control algorithm, based on output voltage and current detection of PV cells. Then, in boost converter, MPPT control of PV cells is achieved by closed-loop control of PI regulator value for the error of U_{ref} and output voltage sample value U_{PV} of PV cells.

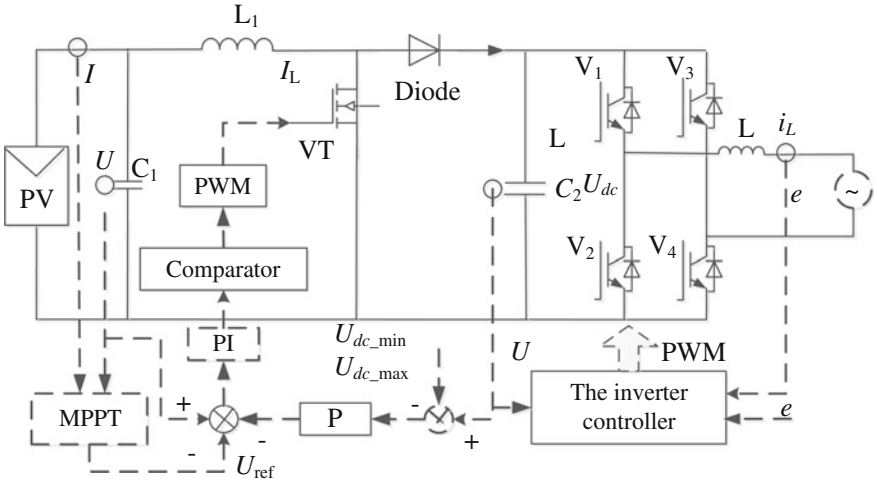

Fig. 5 The MPPT control based on the front DC/AC inverter

Then, the dual control strategy of voltage loop and current loop in the inverter is adopted, where the voltage outer loop is based on the power balance principle to achieve voltage control of the DC bus. While current inner loop achieve the goal of power factor sinusoidal current control by tracking the grid current. In this control strategy, output power of front boost converter is dynamic because of environment changes. In the control system design, response speed of DC voltage control of backward inverter is faster than MPPT control of front boost converter, in order to ensure real-time power delivery without the power accumulation in the DC bus. Actually, DC bus overvoltage problem is solved by increasing the capacitance of the DC bus, or cut-off negative feedback control of DC bus voltage limit shown in Fig. 5.

4.2 Single-Stage Grid-Connected Structure

In the two-stage grid-connected PV, each converter has its independent goal. And the control scheme is simple, independent, and wide for illumination, temperature, and other environmental changes. However, due to the complex structure of the two-stage converter, the cost and the loss energy of this structure are high compared with the other single-stage grid-connected PV system. Therefore, a simple structure, low cost, high efficiency single-stage grid-connected PV inverter system has been paid wide attention. However, in the single-stage grid-connected PV inverter system, there is only one DC/AC, in order to achieve the energy conversion. Then grid voltage synchronous and the sinusoidal current output are controlled by the DC/AC link. And the control strategy of this structure is relatively complicated [19].

The single-stage grid-connected PV inverter system consists of PV cells, a DC-link capacitor *C*, the inverter bridge, the filter inductor *L,* and other components. However, in some cases, it is necessary to add the extra boost converter when the voltage of PV cells is lower than allowable value. Therefore, this single-stage PV inverter system is adopted only when the voltage of PV cells is high enough [19, 20] (Fig. 6).

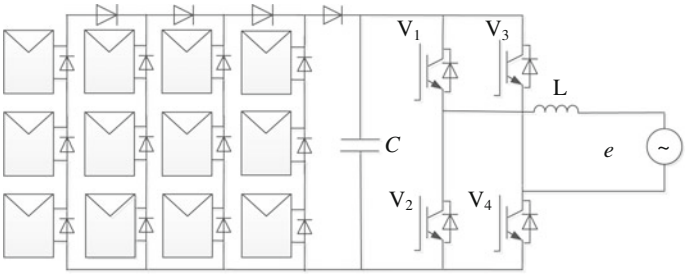

Fig. 6 Single-stage grid-connected structure

4.2.1 The Three-Loop Control Structure

In the single-stage grid-connected PV structure, a three-loop control strategy is used: the current loop, the DC voltage loop and the power loop of MPPT. As shown in Fig. 7, the current loop is mainly constituted by the grid voltage and current sampling module, the voltage synchronous, the current regulator, the PWM modulation and drive. These modules achieve the conversion from DC to AC and the sinusoidal current control. The DC voltage loop is mainly made by the bus voltage and the voltage regulator to regulate the DC bus voltage. The MPPT power loop is mainly constituted by the input power sampling module and the control link of the power point. The output of the MPPT power is taken as the DC voltage reference of the loop of the DC voltage. The voltage in the DC voltage loop is regulated to search the MPP of PV cells, such that the grid-connected PV system achieves MPPT operation [21].

4.2.2 Dual-Loop Control Structure

In three-loop control structure, the MPPT control is performed by regulating the DC bus voltage of grid-connected inverter. When the PV operating voltage is greater than the PV MPP voltage, the voltage loop and the current loop are both used to increase the output power of the inverter circuit, so that the PV cell operating voltage is reduced. When the PV voltage works less than the MPP, it is also regulated by the double loops of the voltage and the current, which reduces the output power of the inverter circuit, such that the PV cell operating voltage increases. Actually, in the grid-connected PV inverter MPPT tracking process, it can be used the simplified double-loop control, which includes MPPT power loop and the current loop. As shown in Fig. 8, in this control, when the PV cell voltage is greater than the voltage at the MPP, it will increase the current amplitude to

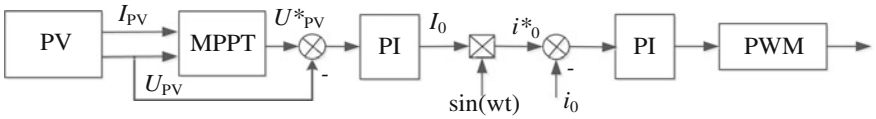

Fig. 7 The three-loop control structure for the single-stage grid-connected inverter MPPT control

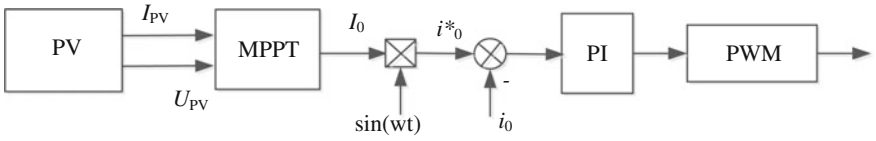

Fig. 8 The double-loop control structure for MPPT control of the single-stage grid-connected inverter

increase the power output of the inverter circuit. With this mechanism, the PV cell operating voltage is reduced. Similarly, when the PV cell voltage is less than the voltage at the MPP, it will reduce the current amplitude to reduce the power output of the inverter circuit. As the result, the PV cell operating voltage is reduced. That is to say, the double-loop control does not regulate the DC bus voltage in the three-loop control structure, but directly adjusts the current in the double-loop control structure to operate the inverter power output.

5 The Advanced MPPT Method

5.1 The Fuzzy Algorithm

Fuzzy control is a new control method based on fuzzy set theory. It is suitable for the mathematical model of the unknown and complex nonlinear system. PV system is a strongly nonlinear system, the performance of the PV cells is difficult to describe with accurate mathematical model, and therefore, fuzzy control method for MPPT is very appropriate, the fuzzy control has been introduced to the MPPT control of PV system, which will produce rapid response to the external environment, and be able to weaken the power oscillation near the MPP [22].

To realize the MPPT control method, the fuzzy control system samples the data to determine the positional relationship between the operation point and MPP, and automatic correct the value of voltage at operation point, to obtain the MPP. So define the output variables of the fuzzy logic controller for the operation point voltage correction of dU. Input variables are the slope value of the continuous sampling points of attachment e and the change in unit time slope Δe on the PV cells P–U curve, respectively.

$$e(k) = \frac{\mathrm{d}P(k)}{\mathrm{d}U(k)} = \frac{P(k) - P(k-1)}{U(k) - U(k-1)} \tag{9}$$

$$\Delta e(k) = e(k) - e(k-1) \tag{10}$$

where $P(k)$ and $I(k)$ are the output power and the output current of PV cells of the sampling value of k times. Obviously, if $e(k) = 0$, suggests that PV cells have been working in the maximum power output state.

By analyzing P–U characteristic curve of PV cells as shown in Fig. 9, we can conclude following the logic of the MPPT control rules

1. When $e(k) < 0$ and $\Delta e(k) < 0$, P from the left side close to the P_{MPP}. dU should be positive, to continue to close to the MPP;
2. When $e(k) < 0$ and $\Delta e(k) > 0$, P from the left side far away from the P_{MPP}. dU should be positive, to close to the MPP;

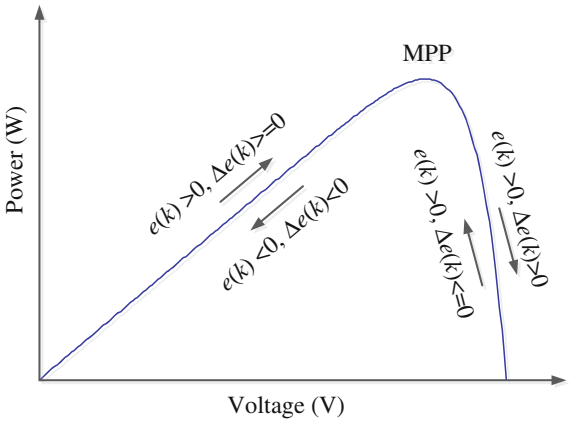

Fig. 9 The PV *P–U* characteristic curve

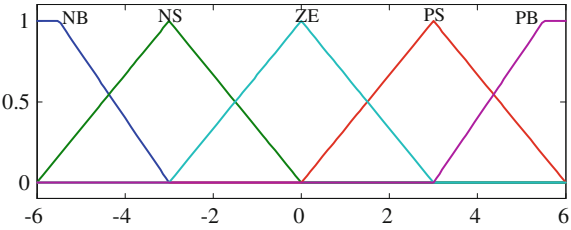

Fig. 10 The membership functions

3. When $e(k) > 0$ and $\Delta e(k) < 0$, P from the right side close to the P_{MPP}. dU should be negative, to continue to close to the MPP;
4. When $e(k) > 0$ and $\Delta e(k) > 0$, P from the right side far away from the P_{MPP}. dU should be negative, to close to the MPP.

5.1.1 Fuzzification

The process that transforms digital value from sampling to fuzzy quantity which controller can identify and use is known as fuzzification. Input variables are usually referred to as language in the fuzzy logic control, and the linguistic terms to describe the variable characteristics are often with positive big (PB), positive medium (PM), positive small (PS), zero (ZE), negative small (NS), negative medium (NM), negative big (NB), these seven descriptive phrases to represent. In this case, we use positive big (PB), positive small (PS), zero (ZE), negative small (NS), negative big (NS) these five phrases to describe the input and output variables.

As shown in Fig. 10 the membership function is given, it uses the uniform distribution of triangular membership functions to determine the input variables e and Δe and output (dU) between the different values with corresponding linguistic variables of membership (u). Each linguistic variable corresponds to a specific

value range. For example, when the value of e is equal to 6, the membership relations with PB (positive big) is 1, which e completely belongs to the fuzzy subset of PB (positive big). e associated with PB (positive big) at this time better than e value of 4.5. Membership function maps the input variables from the continuous scale to one or more of the fuzzy quantity. As shown in Fig. 10, e, Δe, $\mathrm{d}U$ any variables in the membership functions of the same, for the simplicity on the horizontal axis and marked the e, Δe, $\mathrm{d}U$.

5.1.2 Fuzzy Reasoning Arithmetic

After fuzzy quantity, we develop an operational rule based on the rules of expert knowledge. As discussed above, it is concluded that the fuzzy control output process in fact is the process of fuzzy reasoning algorithm, and it is concluded that the output is still in the form of fuzzy quantity. According to the above analysis of the different combination of e and Δe, in order to follow to the MPP, to make corresponding changes to cope with the change of output voltage value, i.e., the change of $\mathrm{d}U$ should make the operation point to the direction search close to the MPP.

We can obtain the fuzzy rules reasoning table which is shown in Table 1 through the logic of MPPT control rules, the table reflect the fact that when the input variables e and Δe change, the corresponding output variable rules of $\mathrm{d}U$ change. Thus the corresponding linguistic variables are obtained. For example, it shows the slope of two sample points of attachment is negative when e is NB (negative big), and the absolute value is larger, to show that the operation point on the left side of the MPP and is far away from the MPP. At this point if Δe also is NB (negative big) that was followed by the voltage change and further away from the MPP. This can make the output variable $\mathrm{d}U$ for PB (positive big), thus the operation point voltage is sharp increase and close to the MPP quickly.

5.1.3 Defuzzification

Defuzzification refers to fuzzy variables of the linguistic variables return to the precise numerical value, which is calculated according to the output of fuzzy subset membership to determine the value of the output variable. There are many methods in the defuzzification, which usually using maximum membership degree method

Table 1 Rules of fuzzy controller

$\Delta e(k)$	$e(k)$				
	NB	NS	ZE	PS	PB
NB	PB	PS	PS	ZE	ZE
NS	PB	PS	PS	ZE	ZE
ZE	PB	PS	ZE	NS	NB
PS	ZE	ZE	NS	NS	NB
PB	ZE	ZE	NB	NB	NB

and the area of the center of gravity method. Area of the center of gravity method computation formula is as follows

$$dU = \frac{\sum_{i=1}^{n} \mu(U_i) \cdot U_i}{\sum_{i=1}^{n} \mu(U_i)} \tag{11}$$

where dU is the output voltage correction for fuzzy logic controller. According to membership function is given, e and Δe according to the value corresponding to the corresponding linguistic variables, according to Table 1 can determine output variables corresponding to the language, the language variable in the center of the membership functions of the corresponding numerical interval value is the U_i.

5.2 MPPT Control Based on Neural Networks

The neural network-based control is considered as a mode-free control method, which is suitable for nonlinear systems. Recently, intelligent control methods based on neural networks are also used for the MPPT control of grid-connected PV inverter. This section describes the basic neural network-based control algorithm and its application in the grid-connected PV inverter MPPT control [23].

5.2.1 Preliminaries

In grid-connected PV power generation system, the neural network-based MPPT controller can combine a three-layer feedforward neural network with proportion integration differentiation (PID) controller to control the inverter such that PV cells are operated at the point of MPP. As shown in Fig. 11, the system requires that the

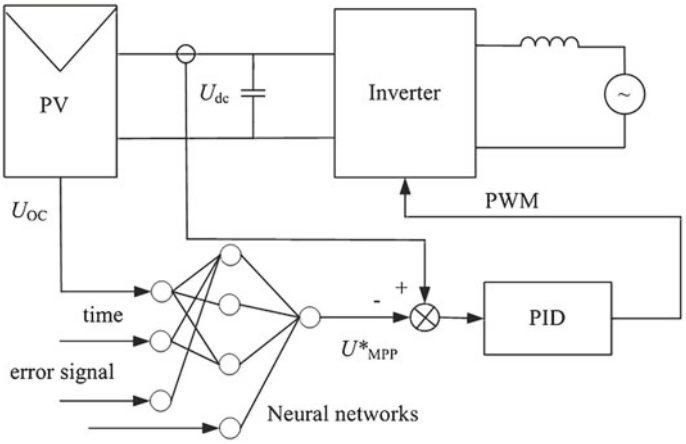

Fig. 11 The MPPT control system based on neural network

controller can real-time estimate of the MPP of PV cells, while the neural network algorithm is able to meet this requirement. Before the neural network algorithm is used, it is necessary to train the neural networks based on a large number of sample data. When a MPP is searched by the neural networks, the algorithm outputs the MPP.

In this example, the open-circuit voltage of the PV cells U_{OC} and the time constant T_p are used as the inputs of the three-layer neural networks. During the estimation operation, the neural network algorithm uses the open-circuit voltage U_{OC} and the time instance T_p to estimate the real-time MPP voltage value U_{MPP}. U^*_{MPP} is compared with the output voltage comparator U_{dc} with the same sampling frequency. The PID regulator takes the difference with U^*_{MPP} and U_{dc} as its input, and then the output of the PID regulator is the control signal of the inverter, which adjusts the operating voltage U_{dc} to track the MPP voltage U^*_{MPP}.

5.2.2 Neural Network-Based Control

The typical three-layer feedforward neural network structure is shown in Fig. 12, which is used to identify the MPP voltage U^*_{MPP} of PV cells. The neural network comprises three layers: the input layer, the hidden layer and the output layer, where the numbers of neurons in the three layers are 3, 5, 1, respectively. The input signal of the input layer neurons is the open-circuit voltage U_{OC} obtained from the detection unit and time constant T_p from the controller. The output of the input layer directly transmits to the neurons in the hidden layer, and the output of the output layer is the estimated voltage U^*_{MPP} at the MPP. For each neuron in the hidden layer and output layer, the used activation function is

$$O_i(k) = \frac{1}{1 + e^{-\lambda_i(k)}} \tag{12}$$

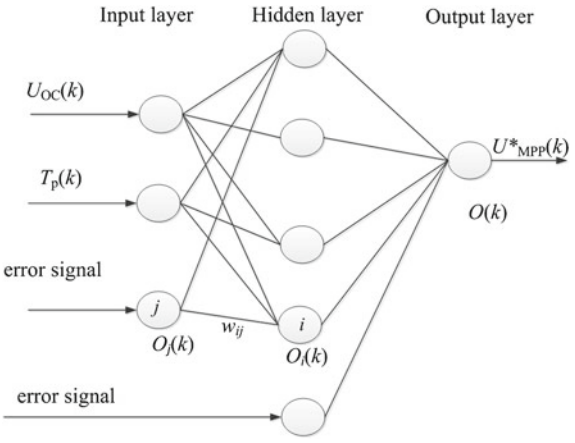

Fig. 12 The three-layer feedforward neural network

where the function $O_i(k)$ is used to define the input–output characteristics of neurons, and $\lambda_i(k)$ is the input signal of neuron i when using the kth sample data. The input signal $\lambda_i(k)$ is the weighted summation of the output of the previous layer, namely

$$I_i(k) = \sum_j \omega_{ij}(k) O_j(k) \tag{13}$$

where w_{ij} is the connection weights between neurons i and j, and $O_j(k)$ is the output signal of the neuron j.

In order to accurately determine the MPP, the weights must be determined according to the training of typical sample data. The training of the neural network needs a set of input–output sample data. All calculations in the training process are done offline. The weights are adaptively updated until they satisfy the input–output mode based on the sample data. When the mean square error reaches its minimum value, the training is finished.

$$E = \sum_{k=1}^{N} [t(k) - O(k)]^2 \tag{14}$$

where N is the total number of training samples, $t(k)$ is the desired output, and $O(k)$ is the actual output. In order to verify the feasibility of the control scheme, the neural network-based control can be applied to track the MPP in the PV system, and the following formula can be used to evaluate the estimation error

$$P_{\text{day}} = \sum_k P_{\text{MPP}}(k) \Delta T \tag{15}$$

$$I_{\text{day}} = \sum_k I_{\text{MPP}}(k) \Delta T \tag{16}$$

$$U_{\text{ave}} = \sum_k U_{\text{MPP}}(k) / M \tag{17}$$

$$E_p = \sum_k \left| P_{\text{MPP}}(k) - P^*_{\text{MPP}}(k) \right| \Delta T \tag{18}$$

$$E_i = \sum_k \left| I_{\text{MPP}}(k) - I^*_{\text{MPP}}(k) \right| \Delta T \tag{19}$$

$$E_u = \sum_k \left| U_{\text{MPP}}(k) - U^*_{\text{MPP}}(k) \right| / M \tag{20}$$

where M is the total number of samples within a day, $P_{\text{MPP}}(k)$, $I_{\text{MPP}}(k)$, and $U_{\text{MPP}}(k)$ are the measured maximum power and the corresponding optimal current and voltage respectively. $P^*_{\text{MPP}}(k)$, $I^*_{\text{MPP}}(k)$, and $U^*_{\text{MPP}}(k)$ are the corresponding desired value. E_p, E_i, and E_u are the total average error of maximum power within a

day, the optimal current, and the optimal voltage respectively. P_{day}, I_{day}, and U_{day} are the total maximum power, the total optimal current and the total average optimal voltage, respectively.

5.3 The Variable Step-Size MPPT Method

The fixed step algorithms, like perturbation observation method, INC, step size determines the tracking speed of the step length, the greater step length, the faster response, and vice versa. In order to obtain both speed and accuracy, the variable step-size algorithm arises at the historic moment. In PV MPPT schemes, the fixed step algorithm cannot meet both speed and accuracy, there are oscillation and miscalculation in fixed step P&O method, the system cannot track the MPP accurately, which will cause the energy loss, so need to improve the fixed step-size method, and the variable step tracking algorithm is proposed. The basic principle of variable step disturbance observation method as: when the operation voltage in the area far away from the MPP, in order to improve the tracking speed and reduce the PV cell in low power output in time, the larger step size is adopted. When near the MPP area, using the small step to guarantee the tracking accuracy. Variable step-size algorithm usually includes two important parameters: the speed factor and the maximum step [11].

According to the PV traits, the slope of the PV P–U curve is zero at the MPP, positive at the left side of the MPP, and negative at the right side. The slope of power versus voltage curves is asymmetric at MPP. As shown in Fig. 13, when $u \in [0,\ U_m]$, $P'(u)$ will change slowly. While when $u \in [U_m,\ U_{OC}]$, $P'(u)$ will change rapidly. And the $P'(u)$ can be expressed by

$$P'(u) = I_{SC}\left(1 + C_1 - C_1 \exp\left(\frac{u}{C_2 U_{OC}}\right)\right) - \frac{C_1 I_{SC} u}{C_2 U_{OC}} \exp\left(\frac{u}{C_2 U_{OC}}\right) \tag{21}$$

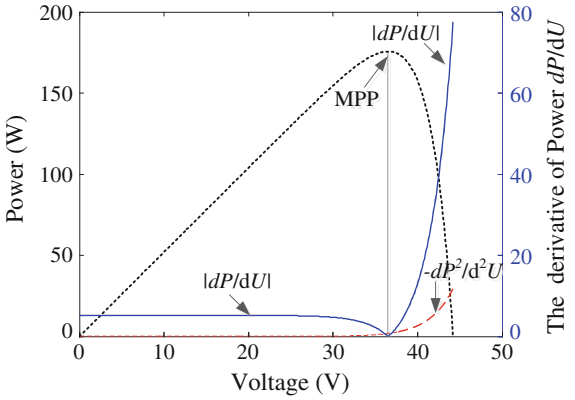

Fig. 13 Variation of the power and slope of power versus voltage

A good variable step-size algorithm requires both reasonable step size and acceptable step change rate $P''(u)$. A smaller step change rate could make contribution to faster dynamics when it is far away from the MPP, while a lager step change rate could do well to steady-state accuracy when it is around the MPP. $P''(u)$ is a monotonically decreasing curve and the value of $P''(u)$ is always less than 0.

$$P''(u) = -\frac{2C_1 I_{SC}}{C_2 U_{OC}} e^{\frac{u}{C_2 U_{OC}}} - \frac{C_1 I_{SC} u}{(C_2 U_{OC})^2} e^{\frac{u}{C_2 U_{OC}}} \tag{22}$$

Based on (22), some estimations have been done to indicate that, the value of $P''(u)$ is almost zero when $u < U_m$ and it will be larger when $u > U_m$. This is why it is difficult to balance the tracking speed on both side of MPP. So it has become very important to determine a suitable maximum step size, or there will be some serious defects for PV system such as poor response characteristic.

Generally, some conventional algorithms have introduced scaling factors to dissolve this problem. The performance of the MPPT system will essentially be decided. Here, one typical equation of variable step-size algorithm is given by

$$U_{(k)} = U_{(k-1)} + \alpha \frac{dP}{dU} \tag{23}$$

where k is the number of cycle and coefficient α is the scaling factor. As (23) shows that the update rule for duty cycle is related to coefficient α and dP/dU, so it is important to acquire optimal values of α that would be employed to ensure the convergence of the variable step-size MPPT methods. However, most of the variable step-size algorithms either lack of the derivation of scaling factor or just suitable for one operating condition.

5.3.1 The Improved Variable Step-Size Algorithm

In this improved method, the arctangent value of $P'(u)$ is introduced to unify the mathematical properties on both side of the MPP. According to the P–U output characteristic, $P'(u)$ (curve (1) in Fig. 14) is varied between two sides of MPP, but $\arctan[P'(u)]$ (curve (2) in Fig. 14) is a constant. As shown in Fig. 14, the tangent line through point $(u_x, P(u_x))$ is set as $L(u_x)$. The slope of $L(u_x)$ is $P'(u_x) = dP(u_x)/du_x$, and the contingence angle is θ [11, 24]. The expression of θ is

$$\theta = \arctan\frac{dP}{du} = \arctan\left[i - \frac{C_1 I_{SC} u}{C_2 U_{OC}} \exp\left(\frac{u}{C_2 U_{OC}}\right)\right] \tag{24}$$

The curve (2) in Fig. 14 is a variation of θ with voltage, and the curve (4) is the derivation of the $\arctan[P'(u)]$ which can be expressed as $1/[1 + P'(u)^2]$. As can be

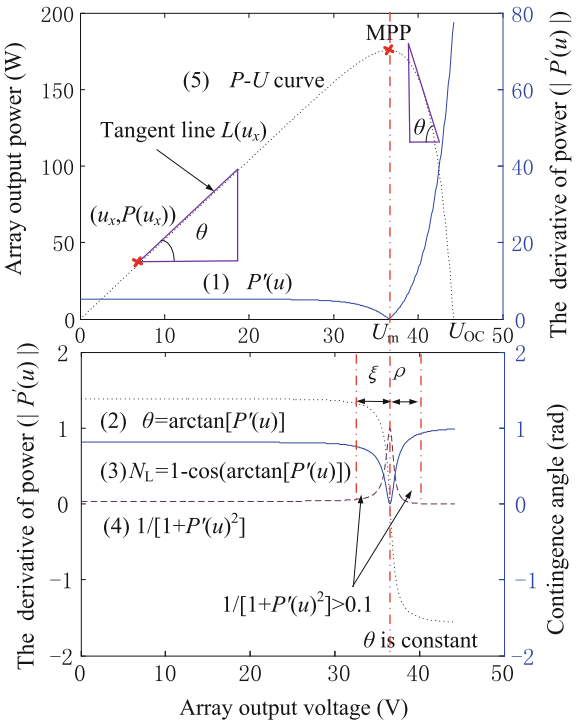

Fig. 14 The diagram of the speed factor N_L

seen from this picture, when $1/[1 + P'(u)^2]$ is less than 0.1 (or another small number), for all $u \in [0, U_m - \xi]$ (defined as the "Constant Current Region") or $u \in [U_m + \rho, U_{OC}]$ (defined as the "Constant Voltage Region"), the change rate θ of voltage versus current or current versus voltage is approximately equal to a constant. On the contrary, the change rate of θ would vary tremendously when $u \in [U_m - \xi, U_m - \rho]$. Therefore, θ is an ideal parameter for the scaling factor, which may overcome the two disadvantages of traditional methods aforementioned. In order to simplify the calculation of maximal step size, the normalization of θ is needed. Then the scaling factor of new method $N_L(u)$ could be expressed as

$$N_L(u) = 1 - \cos\left[\arctan\left(\frac{dP(u)}{du}\right)\right] \tag{25}$$

The curve (3) in Fig. 14 is a variation of the $N_L(u)$ with voltage. Then the expression of step-size $D(u)$ is

$$D(u) = D_{max} - D_{max} \cdot \cos\left[\arctan\left(\frac{dP(u)}{du}\right)\right] \tag{26}$$

The derivation of (26) is the change rate of $D(u)$, as expressed as

$$D'(u) = D_{\max} \sin[\arctan(P'(u))] \cdot \frac{1}{\left(1 + P'(u)^2\right)} \cdot P''(u) \tag{27}$$

In order to simplify the theoretical analysis, (26) can be modified by trigonometric transformation, and du can be replaced by Δu, as expressed by

$$\begin{aligned} D(u) &= D_{\max} - D_{\max} \cdot \sqrt{1 \Big/ \left[1 + (P'(u))^2\right]} \\ &\approx D_{\max} - D_{\max} \cdot \sqrt{\Delta u^2 \Big/ \left(\Delta u^2 + \Delta P(u)^2\right)} \end{aligned} \tag{28}$$

With regarding to (28), it can get reference voltage from formula $U_{\text{ref}}(k + 1) = U_{\text{ref}}(k) \pm D(u)$ conveniently. And the difference between U_{ref} and u will be adjusted by PI regulator.

As seen from Fig. 15a, the rising process of P&O method with a constant voltage slope lasts too long, e.g. 10 s. The steady-state performance with obvious ripples seems very poor, and the average power is about 21.59 W. In Fig. 15b, because the system controlled by PI model must reach the steady state before the next MPPT cycle, so the experimental waveforms based on the new method performs a significant deceleration process. The new method based on contingence angle can get a big change rate of the step size α at point A, and then the step size will changed greatly to guarantee the astringency of new method. It can be seen that the new method uses shorter time (5 s) to track the MPP successfully, and the average power of whole process is 24.78 W. However, in practice the accuracy of one method is often limited by detection and control modules, the experimental operation voltage in this paper cannot approach to MPP infinitely. Typically, when $D(u)$ is less than threshold δ, the system will stop automatically. So the steady-state waveforms in Fig. 15b are linear traits.

5.3.2 One Novel Variable Step-Size Algorithm

In order to avoid calculating the scaling factor, a novel variable step-size algorithm is proposed to get the MPP. The primary difference between the new algorithm and others is that it does not need to calculate the maximum step size and scaling factor α. As the design of the two parameters is difficult, this method is devoted to obtain an effective way to ameliorate the traits of both dynamics and stable state performance. The principle of new method is described in Fig. 16 [25].

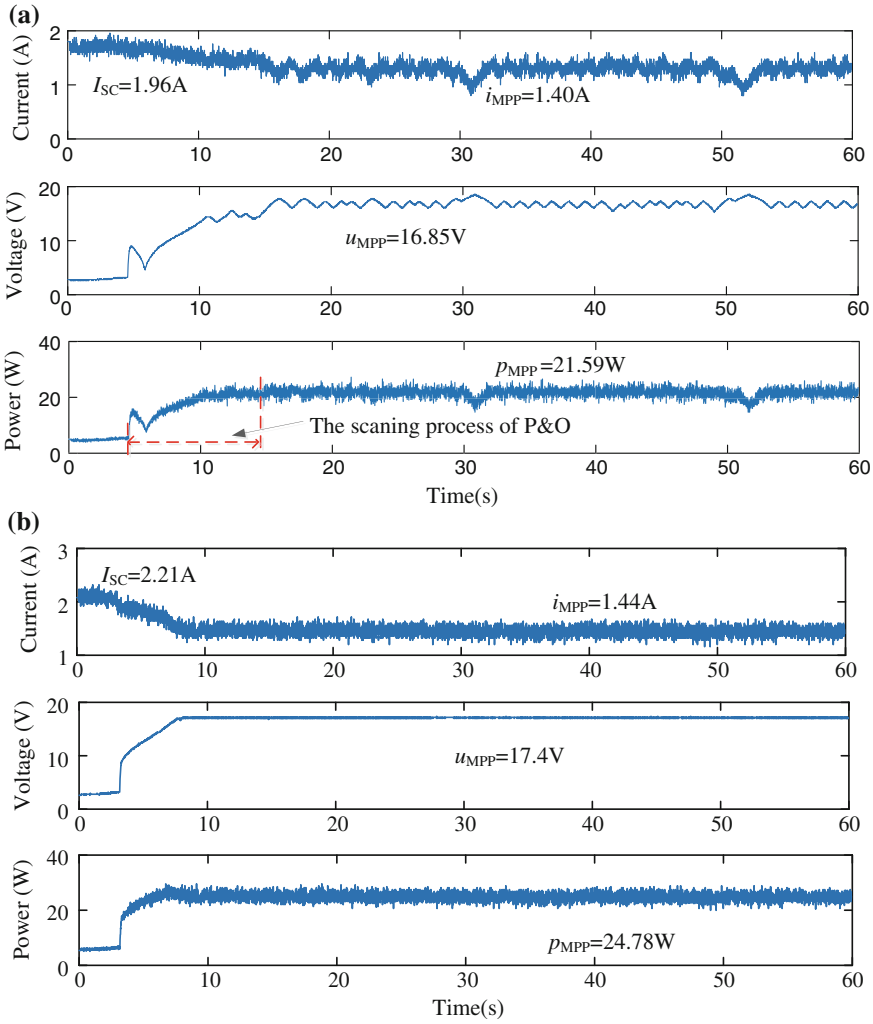

Fig. 15 The experimental results: **a** P&O method, **b** new method

The working process of the new method can be summarized as below:

Step 1: Take two points u_L and u_R from the PV curve ($u_L = 0.02 * U_{OC}$ and $u_R = 0.98 * U_{OC}$). And the slope of power versus voltage u_L and u_R is $P'(u_L)$ and $P'(u_R)$.

Step 2: The straight line that connect point (u_L, $P'(u_L)$) and (u_R, $P'(u_R)$) is named $L_i(u)$, the slope of $L_i(u)$ is $K_i(K_i < 0)$. Then, the $L_i(u)$ and $P'(u) = 0$ will intersect at point O_i.

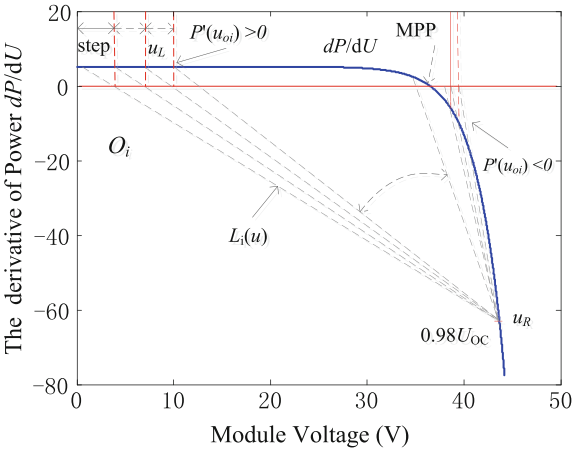

Fig. 16 The principle of the new algorithm

Step 3: As $P'(u_{oi})$ is always above zero, it could set $u_L = u_{oi}$. When $P'(u_{oi})$ is less than 0, it always indicates that the weather condition such as temperature and the solar irradiance has changed. Then u_R needs to be reset.

Step 4: By repeating Steps 1–3, there will be a series of points $\{(u_{oi}, P'(u_{oi})\}$, which will converge to the MPP.

In addition, the $|O_{i+1} - O_i|$ is the step size of the proposed method, which is depicted as

$$P'(u_O) = \frac{P'(u_L) - P'(u_R)}{u_L - u_R}(u_O - u_L) + P'(u_L) \tag{29}$$

The intersection of $L_i(u)$ and $P'(u) = 0$ can be expressed as

$$u_O = u_L - \frac{u_L - u_R}{P'(u_L) - P'(u_R)}P'(u_L) \tag{30}$$

In order to prevent misjudgment, one two-way perturbation method with hysteresis characteristics is adopted to calculate the slope. The flowchart of the new variable step-size MPPT algorithm is shown in Fig. 17. When $|P'(u_{oi}) - 0| < \varepsilon$, the step size is automatically adjusted to 0.

Compared with the P&O method in Fig. 18b, the proposed method in Fig. 18a can search MPP more rapidly. The P&O method is closely related to its step size, and its large step size makes contribution to faster dynamics but excessive steady-state oscillations, which finally results in a low efficiency for PV generation. Furthermore, it will be reversed while the MPPT is running with a smaller step size. In this process, the voltage of proposed method could converge finally to 36.52 V at 0.01 s. Nevertheless, it will take the P&O method 0.72 s to finish the same process. Generally, a PV module is comprised of a number of PV cells that are connected in either series or parallel, and the voltage of MPP is relatively high. In this way, it

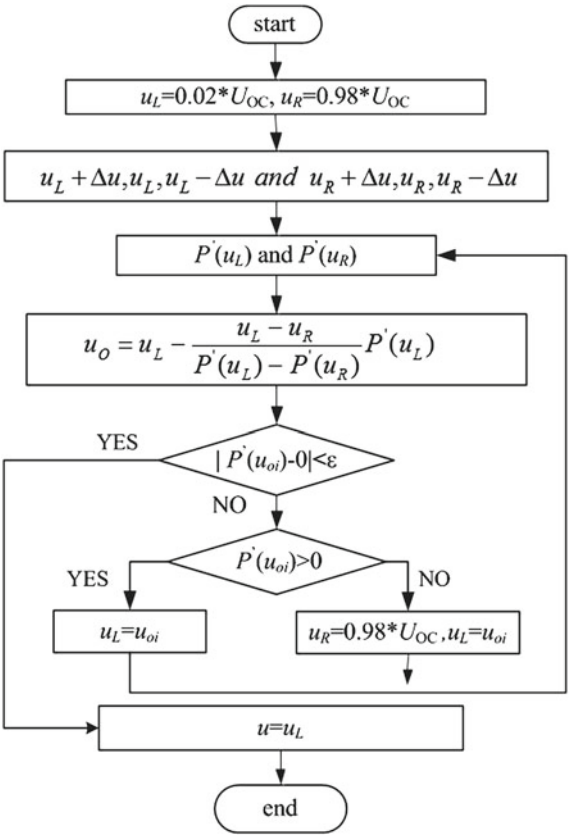

Fig. 17 The flowchart of the improved variable step algorithm

will take more time for the P&O method to track MPP, which could waste a lot of energy. In contrast, the new method always has a lager step size when far away from MPP to obtain a fast response speed and it can reduce the step size near the MPP rapidly to get better steady-state traits than those of traditional MPPT strategies with fixed step sizes [26–29].

5.4 The Iterative Algorithm

5.4.1 Novel Linear Iteration Method

A PV power generator is neither a constant voltage source nor a constant current source and cannot supply stable power to a load. But from the principle of PV, as discussed above, the *I–U* curve of PV includes two regions, i.e., the constant current

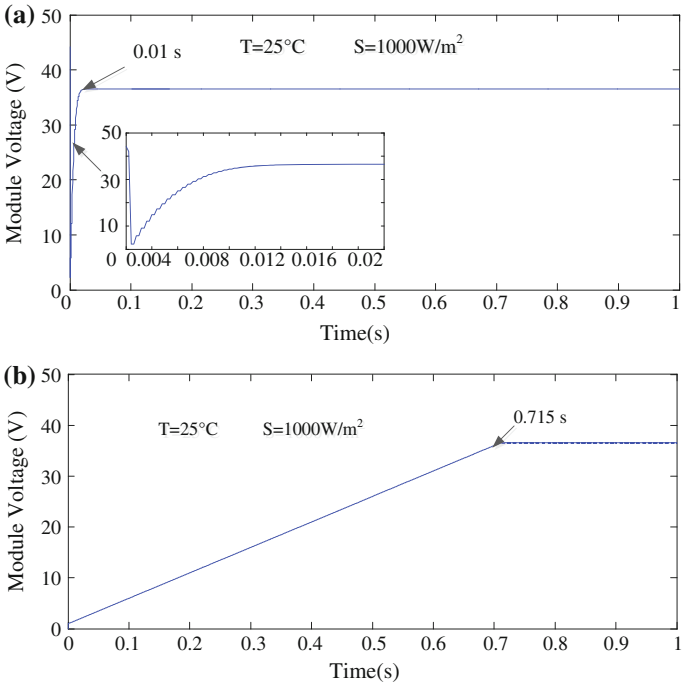

Fig. 18 The starting waveforms of the PV output voltages: **a** improved method, **b** P&O method

region when $u \in [0, U_m - \xi]$ and the constant voltage region when $u \in [U_m + \rho, U_{OC}]$, ξ, $\rho > 0$, as shown in Fig. 19. The derivative of the power to voltage (dP/dU) depicted by curve (1) in Fig. 19, can be described by

$$P'(u) = I_{SC}\left(1 + C_1 - C_1 \exp\left(\frac{u}{C_2 U_{OC}}\right)\right) - \frac{C_1 I_{SC} u}{C_2 U_{OC}} \exp\left(\frac{u}{C_2 U_{OC}}\right) \tag{31}$$

$H(u_x)$ is set as the tangent line through point $(u_x, P(u_x))$ of the P–U curve, which can be calculated by

$$H(u_x) = P'(u_x) \times (u - u_x) + P(u_x) \tag{32}$$

θ is supposed as an angle between the tangent line $H(u_x)$ and x-axis which are depicted by curve (2) in Fig. 19. Its expression is

$$\theta = \arctan\frac{dP}{du} = \arctan\left[i - \frac{C_1 I_{SC} u}{C_2 U_{OC}} \exp\left(\frac{u}{C_2 U_{OC}}\right)\right] \tag{33}$$

The derivative of $\arctan(P'(u))$ can be estimated by

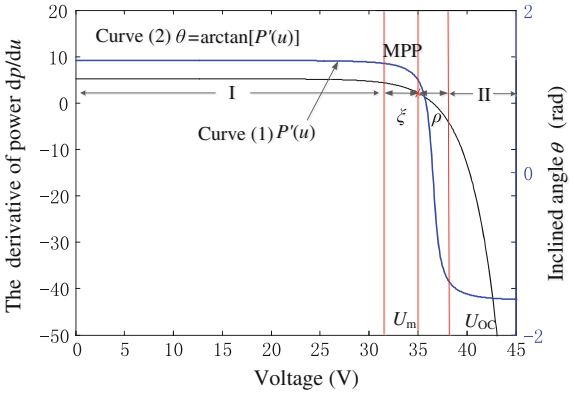

Fig. 19 The curves of $P'(u)$ and angle θ

$$\frac{d\arctan(P'(u))}{\mathrm{d}u} = \frac{1}{(1+P'(u)^2)} \tag{34}$$

when $u \in [0, U_m - \xi]$ or $u \in [U_m + \rho, U_{OC}]$, $1/[1+P'(u)^2]$ shown in Fig. 19 is less than 0.1. It illustrates that i and u nearly keep constants in the constant current region and the constant voltage region, respectively. Hence, the estimation of MPP saves time consumption and achieves high accuracy by using two first-order Taylor series expansions. From the view of geometry, θ is the most intuitive representation of $P'(u)$, and it changes very slowly when PV system works on the regions of constant current or constant voltage.

The new algorithm includes linear prediction and error correction. Linear prediction approximately estimates the MPP and brings some errors to the estimation process. Then, the error correction increases the prediction accuracy by iteration [30]. The procedures are summarized as follows:

Step 1: Take any two points u_L and u_R from the PV curve. Let $u_L \in [0, U_m - \xi]$ and $u_R \in [U_m + \rho, U_{OC}]$).

Step 2: Define $H_L(u)$ is the left tangent line through point $(u_L, P(u_L))$, $H_R(u)$ is the right tangent line through point $(u_R, P(u_R))$. The corresponding slopes are $P'(u_L)$ and $P'(u_R)$, where $P'(u_L) > 0$ and $P'(u_R) < 0$. $H_L(u)$ and $H_R(u)$ can be expressed by

$$\begin{cases} H_L(u) = P'(u_L) \times (u - u_L) + P(u_L) \\ H_R(u) = P'(u_R) \times (u - u_R) + P(u_R) \end{cases} \tag{35}$$

Step 3: As $P'(u_L) > 0$and $P'(u_R) < 0$ are always true, the two tangent lines will intersect at O_1, and set the corresponding point on the PV curve as P_1. Then it considers point P_1 as the prediction MPP of the PV curve, so the segment O_1P_1 is the truncation error referring to Fig. 20a. And the abscissa of point P_1 is

$$u_{P_1} = \frac{P(u_R) - P(u_L) + P'(u_L) \times u_L - P'(u_R) \times u_R}{P'(u_L) - P'(u_R)} \tag{36}$$

Step 4: The tangent line through point P_1 is $H(u_{P1})$ and its slope is $P'(u_{P1})$. If $P'(u_{P_1} > 0)$, set $u_L = u_{P_1}$; otherwise, set $u_R = u_{P_1}$. Referring to (35) and (36), update $P(u_L)$, $P(u_R)$, $P'(u_L)$, $P'(u_R)$, $H_L(u)$ and $H_R(u)$.

Step 5: Update the intersection point O_i *of* $H_L(u)$ and $H_R(u)$ and the corresponding P_i. Calculate u_{P_i} referring to (36). If $|H(u_{O_i}) - P(u_{P_i})| \geq \varepsilon$, return step 3 until the terminal condition is satisfied. If the truncation error $|H(u_{O_i}) - P(u_{P_i})| < \varepsilon, \varepsilon > 0$, the iteration stops, and maintain the operating voltage u_{P_i} until the system restarts or the irradiance changes.

Figure 20a, b describes the processes of linear prediction and error correction. Figure 20c is the algorithm flowchart. When $|H(u_{O_i}) - P(u_{P_i})| < \varepsilon$, the algorithm stops and the operating voltage is maintained until the next duty cycle.

Due to $P''(u) < 0$, the $P(u)$ can be regarded as one continuous convex function. According to the PV curve, $u_O \in [u_L, u_R]$, the interval $[u_L, u_R]$ will become $[u_L^i, u_R^i]$ after i times error correction, and the equations are obtained as follows

$$\left|u_O^i - u_R^i\right| = L_i \cdot \left|u_L^i - u_R^i\right| \tag{37}$$

$$L_i \cdot \left|u_L^i - u_R^i\right| = \left|u_L^{i+1} - u_R^{i+1}\right| \tag{38}$$

where L_i is a scale factor less than 1. Thus, it can get

$$L_{i+k-1} \cdot \left|u_L^{i+k-1} - u_R^{i+k-1}\right| = \left|u_L^i - u_R^i\right| \cdot \prod_{n=i}^{i+k-1} (L_n) \tag{39}$$

As $L_i < 1$, when $k \to \infty$, $\left|u_L^{i+k} - u_R^{i+k}\right|$ will get close to 0. Due to $u_{max} \in \left[u_L^{i+k}, u_R^{i+k}\right]$, the result will finally converge to the MPP ($u_P^{i+k} \to u_{max}$), as shown in Fig. 21. Due to the constant area of PV, it can be seen that the first step (linear prediction) can drive the operation point to the vicinity of MPP rapidly, and then others will improve the tracking accuracy though repeated iterations. This tracking style makes a great contribution to working efficiency and energy saving. The point u_L and u_R in Fig. 21 are the simulation tracking trajectory of linear iteration.

Figure 22 is the tracking speed comparison between Newton iteration and the proposed methods. The formula of Newton's iterative algorithm is

$$u_{k+1} = \frac{P(u_{k-1}) - P(u_k) - [P'(u_{k-1}) \times u_k - P'(u_k) \times u_{k-1}]}{P'(u_k) - P'(u_{k-1})} \tag{40}$$

In Fig. 22a, Newton iteration method has a character of quadratic convergence, and it just takes eight calculation cycles to obtain the optimal solution under standard conditions. But it is less stable for great dependence on its initial iteration value,

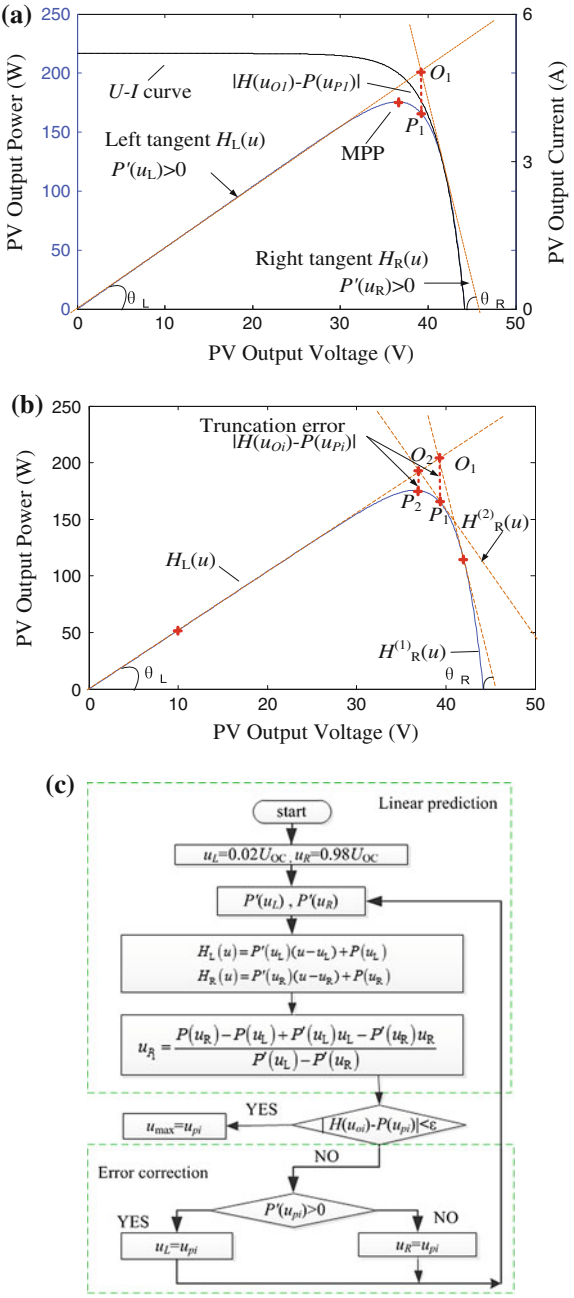

Fig. 20 The procedure of linear prediction algorithm: **a** linear prediction, **b** error correction, **c** algorithm flowchart

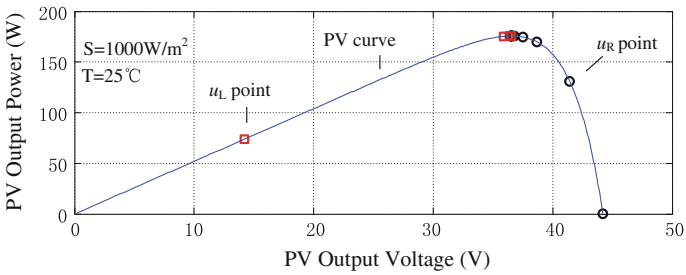

Fig. 21 Tracking trajectory in mathematical theory

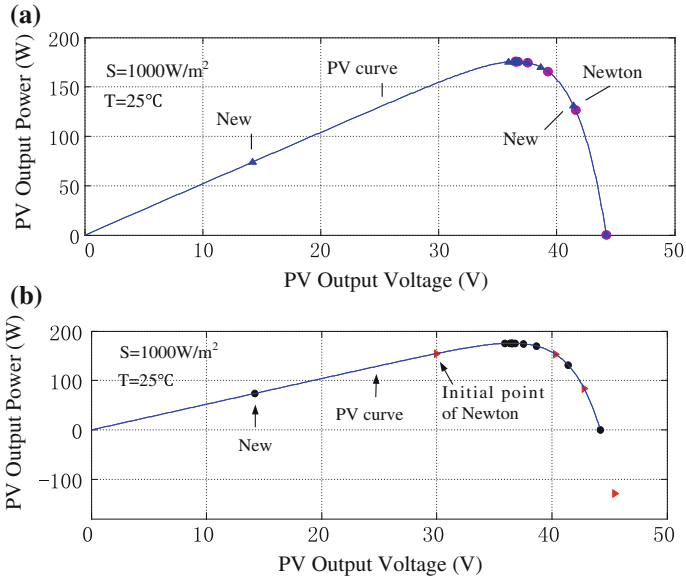

Fig. 22 The simulation of Newton iteration and proposed methods: **a** newton iteration method, **b** the proposed method

which can be solved effectively by the new method in this paper. As shown in Fig. 22b, when the initial point $u_0 \in [0, U_m]$, the iteration result of Newton method will diverge. However, the proposed method has little requirement of the initial value, and it has almost similar tracking response speed (13 calculation cycles) for MPP.

Figure 23 gives the simulation result. It sets the increment of new algorithm $\Delta u = 1$ V which use to calculate the derivative of $P'(u)$, and the $P'(u)$ can be express by $\Delta P/\Delta u$ approximately. Set $\Delta u_S = 1$ V in P&O method. From Fig. 23, the voltage can converge to 36.59 by the proposed method, which is very close to the theoretical $u_{MPP} = 36.52$ even with a big increment, while the voltage oscillates between 36 and 38 by P&O method. It is obvious that the proposed method is more

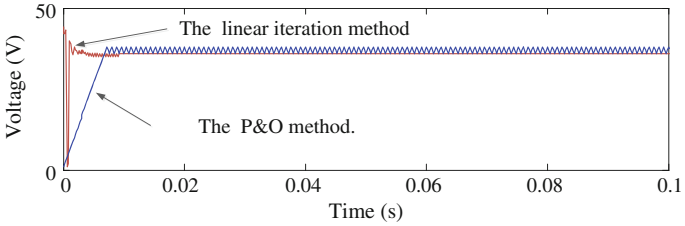

Fig. 23 The simulation results of linear iteration method and P&O method

accurate than the P&O method even with a big perturbation step. Δu is much smaller than Δu_S in practice, and hence, the new method could have much higher accuracy in this condition.

The experimental results of tracking voltage, current, and power by the constant voltage method, P&O method and the linear prediction method are given in Fig. 24 [31, 32]. Figure 24a shows the 0 voltage starting-wave of P&O method with step size of 1 V. The scanning process is so obvious that it could be easily caught from this figure. This method must measure the voltage and current step by step, which needs up to 10 s to finish the scanning process. The proposed method with $\Delta u = 0.05$ V is demonstrated in Fig. 24b where the point A and point B is u_L and u_R, respectively. The process between u_L and u_R is made by linear prediction, and after three times error corrections as shown clearly in Fig. 24b, the new method will converge to MPP finally. Theoretically, the convergence speed of the new method is faster than P&O method. But it takes 15 s to finish the whole tracking process, 6 s for linear perdition and 9 s for error correction, which do not exhibits a very good dynamic performance like simulation results. It just because the system should reach the steady state in each MPPT cycle that is always controlled by the PI model before another MPPT cycle begins, when there are lots of outside interferences. This method will have a good performance under the high voltage and high power situation.

5.5 The Probability Algorithm

5.5.1 The Constant Voltage Tracking

Constant voltage tracking (CVT) method is one of the open-loop MPPT methods on basis of the output characteristic curve, which is the simplest one of all MPPT methods. As shown in the Fig. 25, under the condition of a certain temperature and the value of temperature change is not big, when the irradiance changing, both MPPs distributed in a vertical straight line on both sides, the output voltage of PV cells generally does not change. Therefore, the output voltage of the PV power supply control near the MPP of a constant voltage, the PV cells will work under

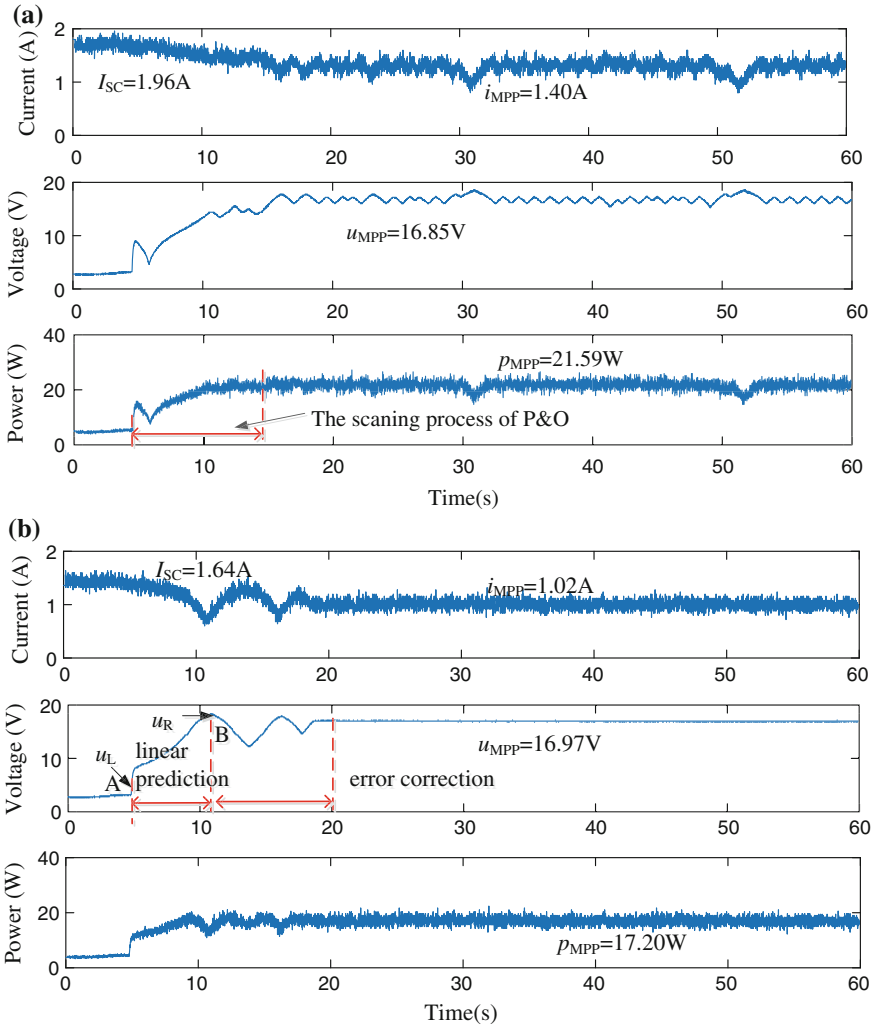

Fig. 24 Experiment comparisons among different methods: **a** P&O method, **b** proposed method

approximate maximum power. Convert MPPT control to constant voltage control actually, which is the theory basis of constant voltage control.

The CVT transmission algorithm based on the mathematical model of PV cells, and find out the maximum output voltage of PV cell point, this method is simple, and the operation is convenient. But due to ignoring the influence of temperature on the PV cell output voltage, therefore, the larger temperature difference, the CVT method of MPPT error become greater. It cannot achieve the true sense of maximum power tracking. Although CVT method is difficult to realize MPPT accurately, but it has advantages as simple and quick close to the MPP, so the CVT

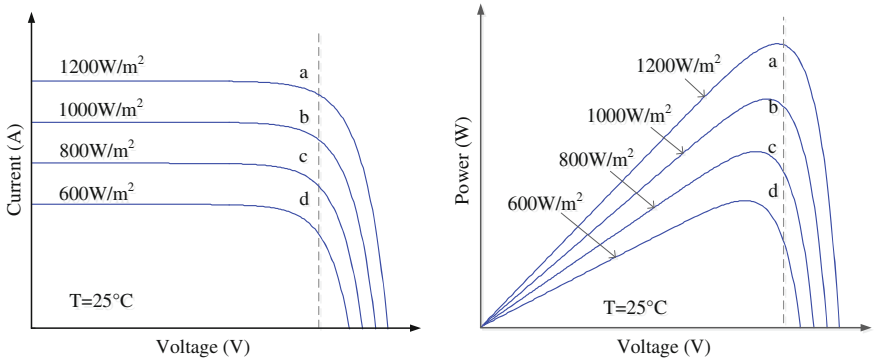

Fig. 25 The principle of constant voltage tracking method

method is often combined with other methods of closed-loop MPPT, which can adopt the CVT method in PV systems at the process of start to close the MPP voltage quickly, and then use the other closed-loop MPPT algorithm of MPP for further search. This combination of MPPT method can effectively reduce the power loss in the process of start, which is caused by the far away from the area of MPP to search. Voltage tracking method can be used in low price and simple system in which control requirements is not high in general.

5.5.2 The Probability Algorithm

According to the viewpoint of probability, the two-stage method and CVT actually belong to probability algorithms. For an input/output system, X and Y are the input and output sets, respectively. Set the input variable $x \in X$, output variable $y \in Y$ and $\Omega = \{(x, y)|x \in \mathrm{X}, y \in \mathrm{Y}\}$, where $X = \{x|x = f_{\mathrm{R}}\}$, $Y = \{u_{\mathrm{MPP}}, \bar{u}_{\mathrm{MPP}}\}$. The function Prob could be defined as the probability function for output y is equal to u_{MPP} if the input x is equal to f_{R} [32–36].

$$\mathrm{Prob}(f_{\mathrm{R}}, u_{\mathrm{MPP}}) = f_{Y|X}(u_{\mathrm{MPP}}|f_{\mathrm{R}}) = \frac{f(f_{\mathrm{R}}, u_{\mathrm{MPP}})}{\int_{\alpha \in Y} f(f_{\mathrm{R}}, \alpha)\mathrm{d}\alpha} \tag{41}$$

where f is the distribution function of Ω. As discussed above, there are three different types of probability functions about u_{MPP}, i.e., $\mathrm{Prob}(f_{\mathrm{R}}(u), u_{\mathrm{MPP}})$, $\mathrm{Prob}(f_{\mathrm{R}}(p), u_{\mathrm{MPP}})$, $\mathrm{Prob}(f_{\mathrm{R}}(u, p), u_{\mathrm{MPP}})$, can be proposed based on the statistical regularities in P–U coordinate system. From the previous studying, the two functions, $\mathrm{Prob}(f_{\mathrm{R}}(u), u_{\mathrm{MPP}})$, and $\mathrm{Prob}(f_{\mathrm{R}}(u, p), u_{\mathrm{MPP}})$ in this probability theory, can be illustrated with the example of CVT method and two-stage tracing method. The CVT method is derived from the observation that, usually, the MPP voltage is located at a fraction of open-circuit voltage (U_{OC}). Then, the probability function of this method can be expressed by $\mathrm{Prob}(f_{\mathrm{R}}(u), u_{\mathrm{MPP}})$, where $f_{\mathrm{R}}(u) = kU_{\mathrm{OC}}$, $k = 0.8$.

$$\text{Prob}(kU_{\text{OC}}, u_{\text{MPP}}) = \begin{cases} 1, & u = kU_{\text{OC}} \\ 0, & u \neq kU_{\text{OC}} \end{cases} \tag{42}$$

The CVT method voltage is always used to track the MPP under uniform insolation. With the regulation of MPP, CVT method can be used under PSCs also. The two-stage tracing method is always adopted to track the MPP under PSCs [33]. In the first stage, the control process moves the operating point into the vicinity of MPP on the load line $R_{\text{pm}} = U_{\text{pm}}/I_{\text{pm}}$, where U_{pm} and I_{pm} are approximately equal to 80 and 90 % of the open-circuit voltage U_{OC} and short-circuit current I_{SC} of the PV array [34, 35]. Set the intersectional of load line and curve *I–U* is (u_0, i_0), where i_0 is equal to $I_{\text{PV}}(u_0)$ and $I_{\text{PV}}(u_0)U_{\text{pm}} - I_{\text{pm}}u_0 = 0$. As discussed above, the probability function $\text{Prob}(f_{\text{R}}(u, p), u_{\text{MPP}})$ can be safely conducted.

$$\text{Prob}(f_{\text{R}}(u_0, P(u_0)), u_{\text{MPP}}) = \begin{cases} 1, & f_{\text{R}}(u_0, P(u_0)) > 0 \\ 0, & f_{\text{R}}(u_0, P(u_0)) < 0 \end{cases} \tag{43}$$

The function f_{R} $(u_0, P(u_0))$ can be expressed as

$$f_{\text{R}}(u) = \left(\frac{u}{P(u)/u} + \frac{\text{d}u}{\text{d}P(u)/u}\right)\left(I_{\text{MPP}} - \frac{P(u)}{u}\right) \tag{44}$$

where $P(u)$ is the output power function of PV arrays.

However, if the global power peak lies on the left side of the load line (*R*pm), the operating point is temporarily shifted to 90 % of *U*OC, thereby missing the MPP [36]. According to this theory, the key of the probability method is to find the relationship between MPP and sampling points. i.e., u_1, $u_2 \ldots u_N$. The simplest probability function of proposed method can be expressed as

$$\text{prob}(\hat{u}_{\max}, u_{\text{MPP}}) = \begin{cases} 1, & \hat{u}_{\max} - \Delta u \leq u_{\max} \leq \hat{u}_{\max} + \Delta u \\ 0, & u_{\max} \leq \hat{u}_{\max} - \Delta u, u_{\max} \geq \hat{u}_{\max} + \Delta u \end{cases} \tag{45}$$

where $\hat{u}_{\max}$ is the maximum sampling point and $N_{\text{B}}(\hat{u}_{\max}, \Delta u) = \{u | \hat{u}_{\max} - \Delta u < u < \hat{u}_{\max} + \Delta u\}$ is the neighborhood of $\hat{u}_{\max}$. But the study of this method is still at the beginning.

Figure 26 illustrates the experimental results of the tracking current, voltage, and power for three schemes. Figure 26a is the two-stage MPPT method. In this method, firstly, the short-circuit current I_{SC} and open-circuit voltage U_{OC} should be sampled. Then, the equivalent load line $R_{\text{pm}} = U_{\text{pm}}/I_{\text{pm}}$ and reference voltage could be obtained. However, this two-stage MPPT method failed to track the MPP, as the global peak (GP) lies on the left side of the equivalent load line 0. The proposed method under partial shade is demonstrated in Fig. 26b. It takes 5 s to finish the sampling process and 5 s to decrease the operating voltage to the neighborhood of most likely sampling point which records in the memory card. As the number of sampling points is equal to 7, the step size of sampling process is 2 V. As

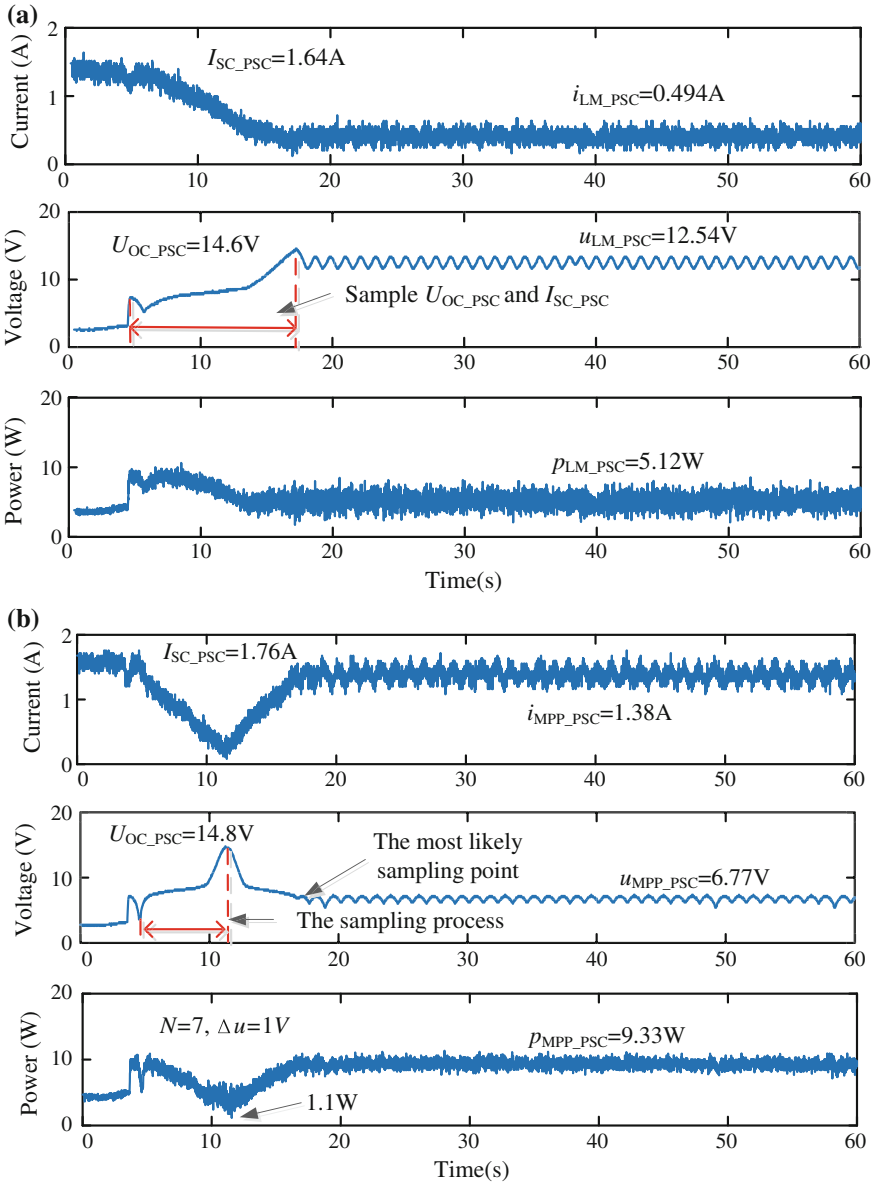

Fig. 26 Experimental results of tracking voltage, current, and power of probability method under partially shaded conditions: **a** two-stage MPPT algorithms, **b** probability method under partial shade

previously mentioned, this algorithm can estimate a most likely interval for MPP and assure a larger power output state relatively, no matter what PV output characters are.

6 Conclusion

In order to improve the efficiency, MPPT methods are always used in PV generation system. As the performance of conventional methods is not very good, some improved MPPT methods are introduced in this section. The fuzzy controller samples the data through fuzzy logic to determine the positional relationship between the operation point and MPP. The neural network algorithm can estimate the MPP of PV arrays real-time when the train process which based on a large number has finished. These intelligent methods show many advantages like a high accuracy and a better stability. For most of the fix-step algorithms, the step size of MPPT methods determines how fast the MPP is tracked. The fixed step algorithm cannot meet both speed and accuracy. So the variable step tracking algorithm is proposed. As the mathematical properties of $P'(u)$ has a great difference in both sides of the MPP and the maximal step-size and scaling factor always make influences with each other. It is difficult to determine these two parameters. This section provides two improved variable step-size MPPT algorithms and one linear iteration method that are based on numerical calculation and trigonometric function to solve this problem. Comprehensive simulation and experiment results verify the feasibility of the proposed method. Comparing with P&O method, the advanced MPPT methods have a better dynamic and steady performance. This section also makes fully analysis of PV MPPT process from the constant current region and constant voltage region separately.

References

1. Zhang X, Cao RX (2010) Solar photovoltaic grid connected power generation and solar photovoltaic grid-connected power generation and inverter control. Proceedings of China Machine Press, Beijing, 2012, pp 181–258
2. Brito MAG, Galotto L Jr, Sampaio LP, Melo GA, Canesin CA (2013) Evaluation of the main MPPT techniques for photovoltaic applications. IEEE Trans Industr Electron 60(3):1156–1167
3. Esram T, Chapman PL (2007) Comparison of PV array maximum power point tracking techniques. IEEE Trans Energy Convers 22(2):439–449
4. Hussein KH, Muta I, Hshino T, Osakada M (1995) Maximum photovoltaic power tracking: An algorithm for rapidly changing atmospheric conditions. IEE Proc Gener Transm Distrib 142(1):59–64
5. Femia N, Petrone G, Spagnuolo G, Vitelli M (2005) Optimization of perturb and observe maximum power point tracking method. IEEE Trans Power Electron 20(4):963–973
6. Femia N, Granozio D, Petrone G, Spagnuolo G, Vitelli M (2007) Predictive and adaptive MPPT perturb and observe method. IEEE Trans Aerosp Electron Syst 43(3):934–950

7. Mei Q, Shan MW, Liu LY, Josep MG (2011) A novel improved variable step size incremental-resistance MPPT method for PV systems. IEEE Trans Industr Electron 58 (6):2427–2434
8. Hiyama T, Kouzuma S, Imakubo T (1995) Identification of optimal operating point of PV modules using neural network for real time maximum power tracking control. IEEE Trans Energy Convers 10(2):360–367
9. Chen LR, Tsai CH, Lin YL, Lai YS (2010) A biological swarm chasing algorithm for tracking the PV maximum power point. IEEE Trans Energy Convers 25(2):484–493
10. Zhou L, Chen Y, Guo K, Jia FC (2011) New approach for MPPT control of PV system with mutative-scale dual-carrier chaotic Search. IEEE Trans Power Electron 26(4):1038–1048
11. Liu AF, Duan SX, Liu F, Liu BY, Kang Y (2008) A variable step size INC MPPT method for PV systems. IEEE Trans Industr Electron 55(7):2622–2628
12. Scarpa VVR, Buzo S, Spiazzi G (2009) Low complexity MPPT technique exploiting the effect of the PV Module MPP Locus characterization. IEEE Trans Industr Electron 56(5):1531–1538
13. Patel H, Agarwal V (2008) Maximum power point tracking scheme for PV systems operating under partially shaded conditions. IEEE Trans Industr Electron 55(4):1689–1698
14. Masoum MAS, Dehbonei H, Fuchs EF (2002) Theoretical and experimental analyses of PV systems with voltage and current based maximum power-point tracking. IEEE Trans Energy Convers 17(4):514–522
15. Yu GJ, Jung YS, Choi JY, Kim GS (2003) A novel two-mode MPPT control algorithm based on comparative study of existing algorithms. Sol Energy 76:455–463
16. Yang B, Li WH, Zhao Y, He XN (2010) Design and analysis of a grid-connected PV power system. IEEE Trans Power Electron 25(4):992–1000
17. Chen Y, Smedley K (2008) Three-phase boost-type grid-connected inverter. IEEE Trans Power Electron 23(5):2301–2309
18. Chen YM, Liu YC, Wu FY (2004) Multi input converter with power factor correction, maximum power point tracking, and ripple-free input currents. IEEE Trans Power Electron 19 (3):631–639
19. Sahan B, Vergara AN, Henze N, Engler A, Zacharias P (2008) A single-stage PV module integrated converter based on a low-power current-source inverter. IEEE Trans Industr Electron 55(7):2602–2609
20. Mastromauro RA, Liserre M, Kerekes T, Dell'aquila A (2009) A single phase voltage-controlled grid-connected PV system with power quality conditioner functionality. IEEE Trans Industr Electron 56(11):4436–4444
21. Lopez-Lapena O, Penella MT, Gasulla M (2012) A closed-loop maximum power point tracker for subwatt PV panels. IEEE Trans Industr Electron 59(3):1588–1596
22. Chiu CS (2010) T-S fuzzy maximum power point tracking control of solar power generation systems. IEEE Trans Energy Convers 25(4):1123–1132
23. Veerachary M, Senjyu T, Uezato K (2003) Neural-network-based maximum power point tracking of coupled inductor interleaved boost converter supplied PV system using fuzzy controller. IEEE Trans Industr Electron 50(4):749–758
24. Tang L, Xu W, Zhang Y, Zeng C (2013) Novel variable step-size maximum power point tracking control strategy for PV systems based on contingence angles. In: Proceedings of energy conversion congress and exposition (ECCE), Denver, America, 14–17 Sept 2013, pp 3904–3911
25. Tang L, Xu W, Zeng C, Lv J (2012) One novel variable step-size MPPT algorithm for photovoltaic power generation. In Proceedings of IEEE Industrial Electronics Society (IECON), Montreal, QC, Canada, 25–28 Oct 2012, pp 5750–5755
26. Ropp M, Gonzalez S (2009) Development of a MATLAB/Simulink model of a single-phase grid-connected PV system. IEEE Trans Energy Convers 21(1):195–202
27. Patel H, Agarwal V (2008) MATLAB-based modeling to study the effects of partial shading on PV array characteristics. IEEE Trans Energy Convers 23(1):203–310
28. Kwon JM, Nam KH, Kwon BH (2006) PV power conditioning system with line connection. IEEE Trans Industr Electron 53(4):1048–1054

29. Lee TY (2007) Operating schedule of battery energy storage system in a time-of-use rate industrial user with wind turbine generators: a multi pass iteration particle swarm optimization approach. IEEE Trans Energy Convers 22(3):774–782
30. Xu W, Mu C, Jin J (2014) Novel linear iteration maximum power point tracking algorithm for photovoltaic power generation. IEEE Trans Appl Supercond 24(5):1–6
31. Koutroulis E, Kalaitzakis K, Voulgaris NC (2001) Development of a microcontroller-based PV maximum power point tracking control system. IEEE Trans Power Electron 16(1):46–54
32. Alonso-Gracia MC, Ruiz JM, Chenlo F (2006) Experimental study of mismatch and shading effects in the. Solar Energy Mater Solar Cells 90(3):329–340
33. Sera D, Teodorescu R, Hantschel J, Knoll M (2008) Optimized maximum power point tracker for fast-changing environmental conditions. IEEE Trans Industr Electron 55(7):2629–2637
34. Ji YH, Jung DY, Kim JG, Kim JH, Lee TW, Won CY (2011) A real maximum power point tracking method for mismatching compensation in PV array under partially shaded conditions. IEEE Trans Power Electron 26(4):1001–1009
35. Kobayashi K, Takano I, Sawada Y (2006) A study of a two stage maximum power point tracking control of a PV system under partially shaded insolation conditions. Solar Energy Mater Solar Cells 90(18/19):2975–2988
36. Nguyen TL, Low KS (2010) A global maximum power point tracking scheme employing direct search algorithm for PV systems. IEEE Trans Industr Electron 57(10):3456–3467

Maximum Power Point Tracking Methods for PV Systems

Sarah Lyden, M. Enamul Haque and M. Apel Mahmud

Abstract Maximum power point tracking (MPPT) is an important consideration in photovoltaic (PV) systems. These systems exhibit variable nonlinear current–voltage (I–V) and power–voltage (P–V) characteristics which vary with environmental conditions. The optimum operation of a PV system occurs when the system operates at the unique maximum power point (MPP) for the given environmental conditions. Key environmental conditions include the irradiance on the cell, temperature of the cell and any shading phenomenon. Shading can occur due to objects, dust or dirt and module mismatch arising from damage or manufacturing tolerances. These shading effects introduce further nonlinearity into the I–V and P–V characteristics of the system. An extensive variety of MPPT techniques has been proposed which vary from simple estimation techniques to advanced tracking techniques. In this chapter, the criteria for assessing the performance of MPPT methods are defined followed by a complete description and discussion of both techniques designed for uniform environmental conditions and those designed for non-uniform environmental conditions.

Keywords Maximum power point tracking · Photovoltaic systems · Partial shading conditions

1 Introduction

Maximum power point tracking (MPPT) techniques can be classified as those that are designed for uniform environmental conditions and those that are designed for non-uniform environmental conditions. Each of these categories contains many

S. Lyden
School of Engineering and ICT, University of Tasmania, Hobart, TAS 7005, Australia
e-mail: Sarah.Lyden@utas.edu.au

M.E. Haque (✉) · M.A. Mahmud
School of Engineering, Deakin University, Geelong, VIC 3220, Australia
e-mail: enamul.haque@deakin.edu.au

M.A. Mahmud
e-mail: apel.mahmud@deakin.edu.au

M.R. Islam et al. (eds.), *Advances in Solar Photovoltaic Power Plants*,
Green Energy and Technology, DOI 10.1007/978-3-662-50521-2_4

different approaches for ensuring the efficient operation of a PV system. A PV system is limited by the environmental conditions to which it is exposed. In the real outdoor environment, PV systems will experience rapidly varying irradiance due to cloud cover, damage and cell mismatch, and shading from objects in the environment. The operation of PV systems under these real environmental conditions has sparked the development of techniques designed for non-uniform environmental conditions.

PV systems have a high cost of energy [1] and must be operated effectively to utilise this investment. PV systems have nonlinear current–voltage (*I–V*) and power–voltage (*P–V*) characteristics which lead to a unique point corresponding to the maximum available power. This maximum power point (MPP) will vary with both irradiance and temperature. When PV systems operate in the real outdoor environment, it is possible that the modules will experience different levels of irradiance and cell temperature based on orientation, shading from objects in the environment or due to cell mismatch and damage. These non-uniform conditions increase the nonlinearity of the *I–V* and *P–V* characteristics leading to multiple MPPs due to the presence of bypass diodes internal to each module. Under non-uniform environmental conditions *I–V* and *P–V* characteristics such as those shown in Fig. 1a, b, respectively, are produced.

In this chapter, the criteria for assessing the performance of a MPPT method are defined based on the performance in both uniform and non-uniform environmental conditions. The main MPPT methods are described and discussed with respect to their performance against these criteria. Two key factors influence the performance of PV systems substantially. These factors are rapidly changing irradiance, and non-uniform irradiance. Each factor has a different effect on the system and can be accommodated by different MPPT approaches.

This chapter first introduces the importance of MPPT in PV systems and then defines appropriate criteria for assessing the performance of such methods. MPPT techniques are then described and assessed based on the following grouping of techniques:

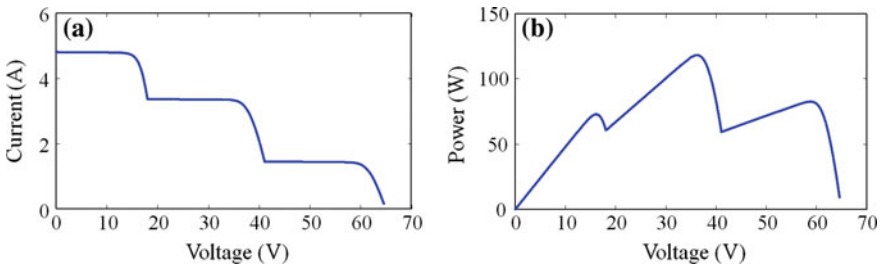

Fig. 1 Characteristics for three modules under non-uniform environmental conditions. **a** *I–V*, **b** *P–V*

- Techniques intended for uniform environmental conditions
- Techniques designed or modified to accommodate non-uniform environmental conditions

The chapter concludes with some remarks regarding the future of MPPT development and an assessment of the usefulness of existing techniques.

2 Criteria for Assessing MPPT Methods

In assessing the performance of MPPT methods, it is important to consider the environment within which PV systems operate. The outdoor environment presents rapidly changing irradiance due to the passage of clouds across the sky, and may involve non-uniform irradiance occurring across the modules in a system due to shading. Shading could arise as a result of structures or trees in the nearby environment, or due to cell degradation, mismatch or damage [2]. In assessing MPPT methods, the following list of criteria has been established to identify which techniques are effective MPPT methods for both uniform and non-uniform conditions [3].

- Able to differentiate between a global and local maxima
- Ability to locate the global maxima
- Quickly track to the maxima
- Quickly track under a change in environmental conditions
- Minimal oscillations in steady state
- Minimal dependence on the key electrical parameters of the PV panel or on system-specific parameters
- Minimal cost and complexity

These criteria will be considered with respect to each MPPT method identified in this chapter.

3 Conventional MPPT Methods

A variety of MPPT methods proposed in the literature can be considered as conventional MPPT techniques. A conventional MPPT method is a method which has been traditionally designed to work for uniform environmental conditions. The conventional techniques considered in this section include, maximum power point estimation (MPPE) techniques, hill climbing methods, artificial intelligence methods and other categories of conventional techniques.

3.1 Maximum Power Point Estimation

Maximum power point estimation (MPPE) techniques represent the simplest form of conventional technique for controlling the power captured from a PV system. These techniques utilise a measured value and predefined relationships to identify a likely MPP location. The predefined relationship is usually defined between known quantities for uniform environmental conditions.

The simplest MPPE methods rely on relating either the short-circuit current or the open-circuit voltage to the MPP current and voltage, respectively via a linear relationship. These techniques are called the fractional short-circuit current and fractional open-circuit voltage methods. A constant of proportionality is used in each case to relate the measured quantity to the desired quantity as shown in (1) and (2). Here the constant k_1 typically takes a value between 0.71 and 0.78, and k_2 between 0.78 and 0.92 [4].

$$V_{\text{mpp}} = k_1 V_{\text{oc}} \tag{1}$$

$$I_{\text{mpp}} = k_2 I_{\text{sc}} \tag{2}$$

These techniques provide a very simple approximation of the MPP location based on a linear relationship that will degrade with time. Under non-uniform environmental conditions, these techniques will also have poor performance as the linear relationship will be unable to capture the complexities of shading [5].

The next class of MPPE methods utilise more than one measurement to improve the estimation of the MPP location. Six current–voltage (I, V) pairs can be sampled to provide an approximation of the *I–V* curve and therefore predict a likely MPP location [6].

Other MPPE approaches take a model-based approach by utilising either empirical relationships [7] or analytical relationships [8, 9] to provide an estimation of the MPP location under particular environmental conditions. These techniques provide a good estimation of the MPP location under uniform environmental conditions; however, the analytical and empirical relationships cannot capture information relating to non-uniform shading of the system.

The MPP locus is also defined as a MPPE technique. This technique provides a relationship linking the locations of the MPPs under different irradiance levels along the *I–V* characteristic [10–13]. An example MPP locus is shown in Fig. 2. From the inspection of Fig. 2, it can be seen that the MPP locus follows a curved path. Usually in MPP locus implementations, this curve is approximated as either linear or piece-wise linear [12]. To use the MPP locus technique, just like with the simple fractional techniques, some system parameters must be measured to provide an estimation of the MPP location. While this measurement is taken, although only for short fraction of time, the system power output will be zero if the short-circuit or open-circuit condition is used [10]. The MPP locus as shown in Fig. 2, is defined based on uniform operating conditions. The complexity of non-uniform environmental conditions cannot be expressed with the MPP locus method.

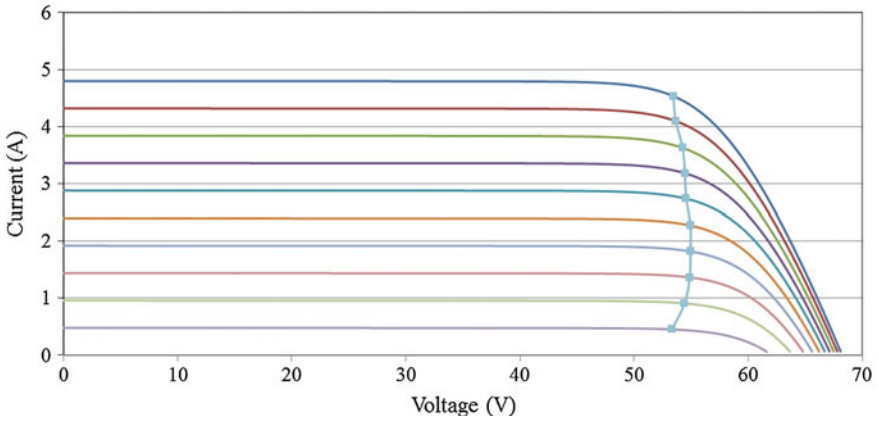

Fig. 2 MPP Locus

Another MPPE method with increased complexity involves utilising an iterated unscented Kalman filter with six measured (I, V) points and information of the *I–V* and *P–V* curves from the manufacturer datasheet to first approximate the parameters of a simple model (the single diode model) and then estimate the MPP location from the characteristic [14]. Again this model fitting approach will only be applicable to uniform operating conditions.

In general, all MPPE estimation techniques rely on some predefined relationships and some real-time measurements to provide an estimation of the likely location of the MPP. Each technique contains an approximation which is primarily based on the key characteristics under uniform environmental conditions and this is why these techniques perform poorly under non-uniform environmental conditions or when partial shading arises in the environment.

MPPE can be executed very quickly as it typically only relies on taking one or a limited number of samples of operating points for the system. The techniques, however, cannot guarantee that exact MPPT will occur and power losses occur when sampling the open-circuit voltage and short-circuit current. As the cells degrade over time the performance of the estimation methods will also degrade. Each MPPE method exhibits no oscillations in steady state and can be easily implemented with both low cost and low complexity.

3.2 Hill Climbing Methods

Hill climbing methods are based on a key property of the *P–V* characteristic of PV systems, i.e., the MPP is a maxima around which the power decreases on either side. Hill climbing methods include Perturb and Observe (P&O), Hill Climbing (HC) and Incremental Conductance (IncCond). All of these methods are based on

the same premise, that a perturbation in some control variable, be it the current, voltage or duty cycle [15], can lead to determining a suitable tracking direction to locate the MPP.

Typically HC uses a perturbation in the duty ratio of the converter [4, 16], and P&O and IncCond may use a perturbation in the voltage [4, 17]. Current perturbation is rarely used because it has a slow transient response under a change in irradiance and the signal is more prone to noise [15].

Each hill climbing method essentially compares the change in power that occurs with a perturbation in the operating point to determine a suitable direction to track the MPP. For instance, on the left of the MPP a positive step in voltage will result in a positive step in power so the technique will continue to take a positive step in the voltage. However, on the right hand side of the MPP, a positive step in voltage will result in a negative step in power so the technique will reverse the direction of the perturbation in the control variable. When operating at the MPP, the derivative of the power with respect to the voltage should be zero. These relationships, applicable particularly to the P&O method, are given in (3).

$$\begin{aligned} \frac{\mathrm{d}P}{\mathrm{d}V} &> 0 \rightarrow \text{left of MPP} \\ \frac{\mathrm{d}P}{\mathrm{d}V} &= 0 \rightarrow \text{at MPP} \\ \frac{\mathrm{d}P}{\mathrm{d}V} &< 0 \rightarrow \text{right of MPP} \end{aligned} \tag{3}$$

The flowchart of the P&O method is shown in Fig. 3.

The IncCond approach is built on the same idea and involves comparing the instantaneous and incremental conductance under each perturbation to determine the next direction to sample in. Equations (4) and (5) describe the operation of the IncCond technique. The flowchart of the IncCond method is shown in Fig. 4.

$$\frac{\mathrm{d}P}{\mathrm{d}V} = \frac{\mathrm{d}(IV)}{\mathrm{d}V} = I + V.\frac{\mathrm{d}I}{\mathrm{d}V} \approx I + V.\frac{\Delta I}{\Delta V} \tag{4}$$

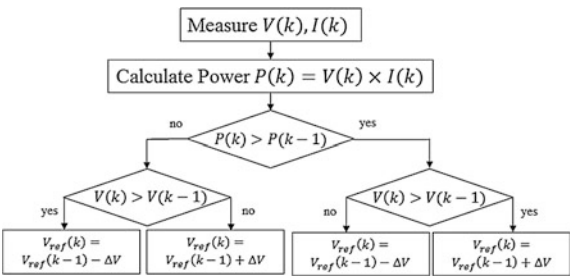

Fig. 3 Flowchart of the P&O method

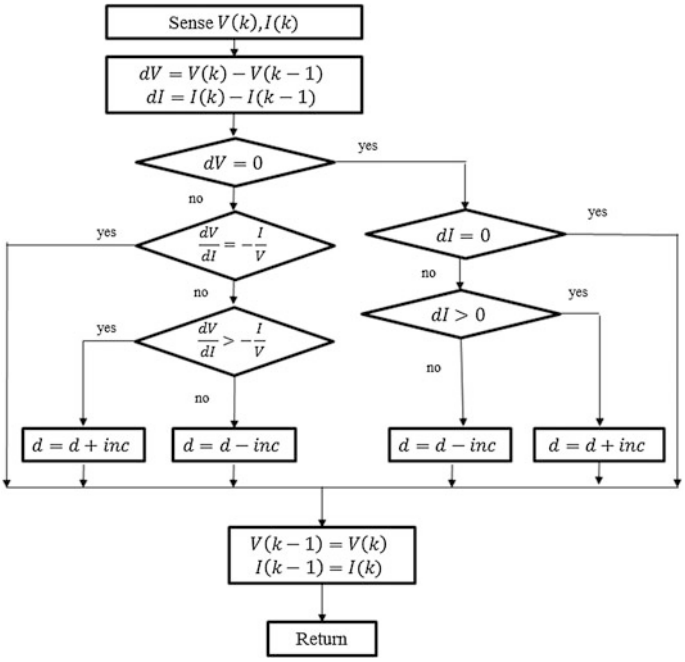

Fig. 4 Flowchart of the IncCond method

$$\begin{aligned} \frac{\Delta I}{\Delta V} &> -\frac{I}{V} \rightarrow \text{left of MPP} \\ \frac{\Delta I}{\Delta V} &= -\frac{I}{V} \rightarrow \text{at MPP} \\ \frac{\Delta I}{\Delta V} &< -\frac{I}{V} \rightarrow \text{right of MPP} \end{aligned} \tag{5}$$

The P&O and HC approaches are shown to have good steady-state performance under consistent environmental conditions [18, 19]. However, when rapid changes in irradiance occur, these methods have a tendency to lose the MPP and initially track in the wrong direction [20–22]. The IncCond technique experiences the same limitations as the P&O and HC implementations. The authors of [23] suggest that the IncCond technique should be considered as a particular implementation of P&O rather than as a technique in its own right, due to the similar performance and the fact that both techniques are formulated on the same premise. However, results in [24] suggest that the IncCond technique has advantages when compared with P&O, including having a more rapid response to changes in irradiance and fewer oscillations under steady-state conditions. The IncCond technique can also be considered to have improved robustness to measurement noise due to the fact that the control decision is dependent on the values of two distinct variables [25].

All HC approaches to MPPT are commonly used in commercial inverters due to their simplicity and low cost of implementation [16, 18, 19, 22]. The operation of these techniques does not rely on knowledge of the PV module characteristics and is only limited by the appropriate choice of step size [22, 26]. A large step size ensures a quick convergence, however, leads to a large oscillation and subsequent power loss occurring around the MPP. A small step size leads to a slow tracking speed with minimal oscillations around the MPP [18, 19]. In designing a HC-based MPPT implementation this tracking speed and steady-state performance trade-off is a significant issue. Another key limitation of HC approaches is that these are unable to distinguish between local and global maxima, as the method will simply track until it first locates a MPP regardless of if this is the global MPP (GMPP). In the event that a change in the environmental conditions occurs simultaneously with an applied perturbation, these techniques do not have the intelligence to distinguish which of these factors has resulted in the change in power [20]. For instance, if a positive step in voltage is applied at the same time that the irradiance increases, the power at the operating point may increase regardless of if continuing to step in this direction will lead to the MPP.

A multitude of enhanced HC approaches is developed in the literature with the goal of addressing the key limitations of the basic implementation outlined above. In particular, these enhanced HC approaches work to address the trade-off between tracking speed and steady-state dynamics, the tendency to track in the wrong direction when an irradiance change occurs, and improve the performance of the technique under non-uniform environmental conditions. A small subset of the enhanced techniques and their performance are described below.

To address the trade-off between tracking speed and steady-state dynamics, a variable step size implementation is a logical choice [16, 21, 27–29]. A variable step size implementation will apply a large step when the operating point is far from the MPP and this step size will reduce as the MPP is approached. Many of these variable step size implementations rely upon the definition of a scaling factor which must be developed and tuned for the particular system and conditions [21]. This dependency on a system defined parameter impacts on the universal application of the variable step size implementation to other PV systems.

Specific to the IncCond implementation, based on the *I–V* characteristics, when operating on the left hand side of the MPP location there may be a potential tracking delay due to the sensitivity of the incremental conductance. This arises due to the fact that $\Delta I \approx 0$ when operating in the current source region. To avoid this tracking delay a PI-INC method is proposed which utilises power-increment coarse tracking along the *P–V* curve until a certain zone, termed the Threshold Tracking Zone (TTZ) is entered [30]. Inside the TTZ the IncCond technique is applied in the standard form.

Some approaches have attempted to move away from system-specific parameters in developing a variable step size implementation of HC. Such attempts include developing an adaptive perturbation based on the change in PV power controlled with PI control [18], optimising the perturbation period utilising an online procedure based on a cross correlation method [31], and basing the step size on $M.dP/dV$

in the delta P&O implementation where M is a scaling parameter which is automatically tuned [21].

To avoid tracking in the wrong direction under an irradiance change, approaches such as dP-P&O have been proposed [19, 32]. This technique takes an additional power measurement in the middle of the sample period to enable the change due to perturbation and the change due to environmental conditions to be isolated. The change due to the MPP perturbation and the irradiance change is encapsulated in $dP_{0.5}$ and the change just due to the irradiance is given in dP_1. The change in power due to the perturbation can be found by considering (6) to (8).

$$\mathrm{d}P_{0.5} = P(k-0.5) - P(k-1) \tag{6}$$

$$\mathrm{d}P_1 = P(k) - P(k-0.5) \tag{7}$$

$$\mathrm{d}P = \mathrm{d}P_{0.5} - \mathrm{d}P_1 \tag{8}$$

Another approach to minimise the time spent tracking in the wrong direction when a change in irradiance occurs, integrates the full curve estimation (FulCurvE) method with a HC approach [21]. This method utilises the trend of the power-duty cycle curve (P-D) and obtains three sampled points at a speed faster than atmospheric changes to decide the direction of the next step. By integrating the FulCurvE method with the delta P&O method an implementation can be developed that has both good steady-state and dynamic performance with minimal drift under changes in environmental conditions [21].

Other strategies to address both the limitations of HC techniques include using an adaptive step size with the dP-P&O technique [33], combining P&O with model predictive control [34], utilising direct control methods with P&O [15] and fuzzy approaches to HC [16].

Generalised P&O (GPO) is a method designed to address the tendency of the P&O method to become trapped in local power curve traps that arise due to measurement noise [35]. In the GPO method, the measured power at the current step is compared with a previously measured power, not necessarily the most recent, based on some scaling factor $\alpha_1 < 1$. The value of α_1 is selected to avoid becoming trapped in any small power curve traps that arise on the P–V characteristic due to measurement noise and can be calculated using (9).

$$\alpha_1 = \frac{P_{t,\min}}{P_{t,\max}} \tag{9}$$

Another approach to improve the performance of HC methods includes the 3-points incremental P&O (3PI-P&O) method which uses sampling at three points to determine the next tracking direction [36]. As this method relies on the sampling of three points, it can detect more states than conventional P&O approaches and has improved ability to track in the correct direction when a change in the environmental conditions occurs.

Standard HC approaches such as HC, P&O and IncCond are limited by trade-offs between the tracking speed and oscillations in steady state due to the choice of step size. The techniques are also incapable of distinguishing between local and global maxima and of locating more than one maxima under given environmental conditions. These techniques, however, do have minimal complexity and cost of implementation which makes them popular options in commercial PV inverters. As described in this section, several enhanced HC approaches have been identified to minimise the key limitations identified for these techniques, however, each of these implementations adds to the complexity of the control or introduces system-specific parameters.

3.3 Artificial Intelligence Methods

MPPT techniques based on artificial intelligence methods for uniform environmental conditions include techniques based on fuzzy logic and artificial neural networks (ANN).

Fuzzy logic enables inputs and possible outputs or outcomes to be represented on a scale rather than as true or false values. The fuzzy inference process is used when solving a particular problem using a fuzzy system, and involves fuzzifying the inputs, evaluating the rules, combining the rule outputs and then defuzzifying the output [37].

With respect to fuzzy logic-based MPPT implementations, there are two distinct categories. These involve using fuzzy model-based approaches [38–43], or using fuzzy logic to decide variable step sizes to use with other conventional techniques [16, 27, 44–46]. The Takagi-Sugeno fuzzy system requires few rules and coefficients and therefore can be implemented with lower complexity and computational time than the Mamdani method [39–41, 47]. For this reason, Takagi-Sugeno is frequently used in MPPT implementations. One key limitation of fuzzy logic-based approaches to MPPT is that the technique must be designed for a specific system and is not generalizable.

ANNs are modelled based on the structure and interactions of the human brain. Neurons with links comprise the ANN and model the reasoning processes used in the human brain by adjusting the weighting assigned to the links between neurons. During training, the weights of the links are adjusted allowing the network to *learn* [37]. ANNs are composed of an input layer, one or more hidden layers and an output layer.

Typically MPPT approaches utilising ANN develop a nonlinear mapping between the environmental conditions and a MPP location [42, 48, 49]. However, over time the cells will degrade and this nonlinear mapping may no longer represent the location of the MPP under particular environmental conditions [48]. Frequently, ANN-based MPPT approaches rely on weather data inputs; these, however, can be difficult to measure and may not always be available in the same location as the PV installation [42, 49].

ANN approaches can be effectively utilised in two stage approaches with other conventional techniques such as P&O. In a two stage approach, the ANN will approximate the MPP location and then the P&O method with a small step size can track to the MPP exactly [42]. This minimises the need for periodic retraining of the ANN as the cells degrade and minimises the oscillations in steady state as P&O can be applied with a relatively small step size. Other two stage approaches incorporate ANN with IncCond [48].

Fuzzy logic and ANN-based techniques for PV MPPT generally rely on mapping or modelling the nonlinear *I–V* and *P–V* characteristics. Extensive calculations, however, may be required in their execution [50]. As the cells degrade, the initial mapping developed under uniform conditions will no longer match with the actual characteristics and the techniques have no capability to model non-uniform environmental conditions. Retraining of the ANN algorithm as the cells degrade has the potential to improve the performance, however, adds to the cost of implementation and highlights that these techniques are system specific. When combined in a two stage approach with a technique such as P&O or IncCond, small oscillations may be exhibited in steady-state operation.

3.4 Other Methods

A variety of other techniques are also proposed in the literature for performing MPPT under uniform environmental conditions. A subset of these will be considered in this section to highlight the breadth of the field of MPPT for PV systems. The techniques considered in this section include beta method, parabolic curve prediction, ripple correlation control (RCC), extremum seeking control (ESC), bisection search theorem, sliding mode control and MPPT through optimisation of output parameters.

3.4.1 Beta Method

The beta method for MPPT relies on an intermediate variable β defined in (10). When at the optimum point, the variable β should be constant. The technique acts to drive this parameter to a constant value through a control loop [51, 52]. Once the parameter β is calculated, it is compared with the reference value range given by $\beta_{\min}$ to $\beta_{\max}$ to determine if the system has reached steady state. Inside this range, a conventional MPPT method such as HC can be applied to track the MPP directly [51, 52]. When outside of the range, the error is calculated and a new duty cycle for testing is established. The parameter β is quite insensitive to changes in the environmental conditions and the β method can be an effective approach for MPPT as it provides quick tracking to the MPP under normal and changing environmental conditions. The definition of the range $\beta_{\min}$ to $\beta_{\max}$ will not make it possible for the technique to distinguish between local and global maxima.

$$\beta = \ln\left(\frac{I_{\text{pv}}}{V_{\text{pv}}}\right) - cV_{\text{pv}} \tag{10}$$

where $c = \frac{q}{AkTN_s}$, q is the electron charge (1.6×10^{-19} C), A is the diode ideality factor, k is the Boltzmann constant (1.38×10^{-23} J/K), T is the temperature on absolute scale (K), and N_s is the number of series connected cells.

3.4.2 Parabolic Curve Prediction

Parabolic curve prediction relies on defining a parabolic curve based on three duty cycle working points and their corresponding powers to predict the next suitable duty cycle to sample [53]. Tracking along the curve defined by the three working points will allow the method to converge to the MPP and the performance under rapidly changing environmental conditions has been experimentally verified. By sampling three points rather than comparing two points as is done with other conventional MPPT techniques, this method is more robust and has a reduced chance of tracking in the wrong direction when a change in conditions occurs. This technique promotes quick convergence with no oscillations in steady-state operation.

The parabolic curve is defined by the three powers P_1, P_2 and P_3 and their corresponding duty cycles δ_1, δ_2 and δ_3. Shifting of the duty cycles occurs to ensure that the power measurement for P_2 is centrally located and the largest of the three powers. An example of parabolic curve shifting process is shown in Fig. 5. When a change in irradiance occurs, the technique may need to shift and rearrange the duty cycles to ensure that the central measurement is the largest. This shifting and

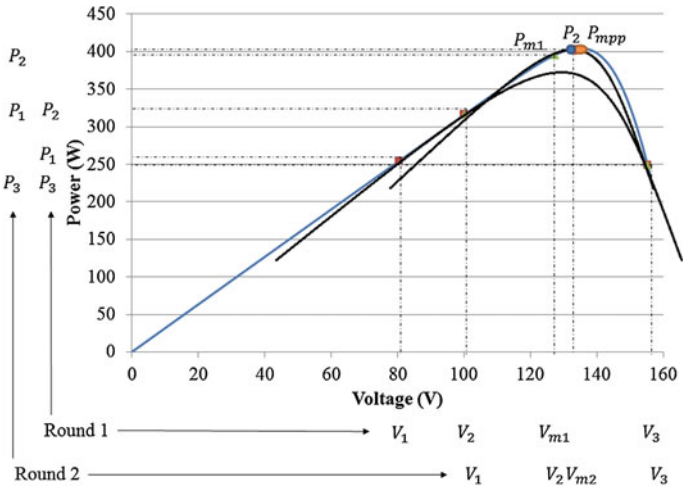

Fig. 5 Sample parabolic *curve* prediction

rearranging may affect the efficiency of the technique under a change in environmental conditions.

3.4.3 Ripple Correlation Control

Ripple correlation control (RCC) makes use of the switching ripple from switching converters to enable MPPT [54–56]. The switching ripple creates a kind of perturbation in the system and by utilising an integrator to drive the signal error to zero observation can be realised similar to the P&O method. RCC enables MPPT to be achieved in a similar way to P&O, but without the need for an external perturbation. This means that the technique will not exhibit oscillations around the MPP and will converge asymptotically to the MPP without requiring knowledge of the system parameters. Discrete implementations of the RCC approach are less expensive and can be more flexible as well as robust [54].

RCC is enhanced by utilising a PWM dithering signal which can improve the average PWM resolution and lead to fast tracking speed and accuracy [57].

3.4.4 Extremum Seeking Control

Extremum seeking control (ESC) approaches are quite similar to RCC, but require an external dither signal to be used. ESC can be enhanced by knowledge of the system model, such as in the Adaptive ESC (AESC) approach [58]. Reducing the perturbation size when in the neighbourhood of the MPP enables the ESC approach to converge directly to the MPP rather than to a limit cycle surrounding the MPP [59]. This can be achieved by utilising a Lyapunov-based switching scheme.

3.4.5 Bisection Search Theorem

Bisection search theorem (BST) is a bracketing approach for locating the roots of equations. For MPPT, BST can be applied on a function defined to link the change in power to the voltage [60]. The roots of this function are found by regulating the voltage of the system and by progressively reducing the size of the interval the MPP can be identified. Under non-uniform operating conditions, the technique cannot distinguish between local and global maxima.

BST is also sometimes referred to as binary search. Binary search and RCC have been combined to provide a fast and efficient searching for the MPP under uniform operating conditions and when a change in the irradiance occurs [61].

A linear prediction method which extends the Newton iterative method utilises a left and right tangent to enable searching [62]. The MPP can be tracked rapidly using this approach without needing a step size reference. The steepest descent and centred differentiation can be combined to perform MPPT [63]. In this particular implementation, the perturbations are ceased when the MPP is located to avoid

oscillations occurring in steady state. When a change in the environmental conditions occurs, the tracking is reinitialised by detecting a change in the resistance or conductance of the panel.

3.4.6 Sliding Mode Control

Sliding mode control (SMC) has good performance and insensitivity to parameter variations which makes it a good optimisation and control method [64]. A switching surface must be defined in a SMC implementation that represents the dynamics required by the particular system. A variable structure control is also needed that allows any state far from the switching surface to be driven to the switching surface [65].

SMC-based approaches have been proposed for PV MPPT including hybrid methods that combine SMC with fuzzy-based MPPT [41], current-based P&O [66], IncCond [67] or with a dynamic optimal voltage estimator [68]. SMC approaches require an appropriate sliding surface to be defined; however, it is not possible to define a surface that will be applicable for all uniform and non-uniform conditions [69].

3.4.7 Optimisation of Output Parameters

In some cases MPPT is achieved by optimising the output of the DC–DC converter to which the PV module is connected rather than locating the MPP on the PV panel side. These implementations often rely on a single sensor and achieve MPPT by optimising the output parameters of the converter such as optimising the load current or the voltage [24, 70, 71]. Due to losses occurring in the DC–DC converter, the optimised converter output will not match directly with the MPP of the PV panel itself [70]. A common assumption in single sensor and output parameter maximisation approaches is that the converter is lossless, such that maximising the load power achieves MPPT [4]. As loads can typically be classified as voltage source type, current source type, resistive type or as a combination, each type of load has an inherent parameter which could be optimised. For instance, for a current source type load, to obtain maximum power it would be necessary to maximise the load voltage, however, a costly current sensor would be required in the process [71]. By maximising some output parameters based on knowledge of the load type, single sensor implementations become possible which reduces the overall cost of the PV system.

A variety of different single sensor approaches are possible including measuring the reference inductor current and correlating this with PV output current for MPPT [72], P&O with a single current sensor [73], gradient ascent algorithm with a single voltage sensor [7], and a single sensor to measure the voltage across a capacitive load to correlate with the tracking direction towards the MPP [74]. Mutli-channel systems (systems comprised of multiple PV modules which can be controlled

independently), can also be developed as single sensor approaches [75]. A single voltage sensor is utilised with an adaptive neuro-fuzzy (ANFIS) solar cell model to improve the MPPT response time while minimising the hardware requirements [76]. Single voltage sensor applications can also be used with advanced power electronics interface such as a double capacitor interface (DCI) converter to follow the MPP through charging the DC link of the inverter [77]. Model predictive control (MPC) can be utilised with a single voltage sensor to approximate the current and apply the P&O method in an implementation that has a faster response when rapid changes in the environmental conditions occur [78].

When compared with other MPPT techniques, single sensor and output maximisation techniques present a lower cost and complexity due to the use of a single sensor. However, these methods are not true MPPT techniques of the PV module, as they optimise the output from a unit comprised of both the PV module and the associated power electronics. Depending on the actual implementation of the single sensor approach, the reduction in sensors does not improve the performance in distinguishing between local and global maxima and may exhibit oscillations in steady state. The techniques can be operated free from system dependent parameters or knowledge of the PV module characteristics and represent an ideal approach for PV systems employed in applications where a low cost is a key driving factor.

4 Methods Designed for MPPT Under Non-uniform Environmental Conditions

In this section, methods designed to operate more successfully under non-uniform environmental conditions are outlined. A basic classification is used where techniques either involve modification of a conventional technique to improve its performance under non-uniform conditions, techniques built on observations of the key characteristics of the *P–V* and *I–V* characteristics under partial shading, or those techniques designed specifically for non-uniform environmental conditions.

4.1 Modification of Conventional Techniques for MPPT Under Non-uniform Environmental Conditions

As has been described in previous sections, conventional MPPT techniques frequently fail to track a global maxima when non-uniform environmental conditions are experienced. A few simple strategies have been applied to conventional techniques to improve their performance under such conditions, however, these strategies do not necessarily guarantee global MPPT (GMPPT). The strategies used involve periodic reset and periodic curve scanning, widening the search range and two stage methods.

4.1.1 Periodic Reset and Periodic Curve Scanning

By incorporating a periodic reset or a periodic curve scan, the performance of conventional MPPT techniques in locating the global maxima can be improved slightly. Often periodic reset is utilised as a means to reduce the likelihood that the method will become trapped in a local maxima, such as the use of the periodic reset with the 3PI-P&O method [36]. By moving the system operating point to a random point every 5–10 min, the probability of finding the global maxima is increased, but not guaranteed.

Periodic searches can be used to define the *P–V* and *I–V* characteristics under certain environmental conditions to then facilitate more accurate MPPT. These scans typically occur every 15 min [79] and then a conventional technique is applied to track the MPP exactly. By utilising a fast sweep of the characteristics, the power losses can be minimised [80]. A sweep of the characteristics could be achieved by disconnecting the load for a short-period of time and connecting the system to an external capacitor [81]. However, when sweeping the entire *P–V* curve there is a considerable disadvantage which arises due to the fact that there are regions of the characteristic where the MPP is unlikely to be located. Additionally, extra circuit components such as switches, resistors, and capacitors are often needed to perform a periodic curve trace which will add to the cost and complexity of implementation.

Periodic scanning has also been used to enhance the performance of MPPE techniques by updating the constant of proportionality, defining the fractional short-circuit current and open-circuit voltage techniques [4]. This minimises the impact that a change in environmental conditions has on these simple techniques but also adds to the cost and complexity. Additionally, if a change in environmental conditions occurs before a new constant of proportionality is determined; the method may operate at a point far from the MPP.

A periodic reset or curve scan can enhance the performance of a conventional MPPT technique but is unable to guarantee that the system operates at the global optimum point under all conditions. The implementation of these strategies will result in a minimal increase in the cost and complexity of each of the conventional MPPT techniques.

4.1.2 Widening Search Range

Increasing the searching range of conventional MPPT techniques has also been utilised to improve the use of such techniques under non-uniform environmental conditions [16, 80, 82, 83]. Increasing the search range adds to the time required for searching and may also lead to considerable power losses during the tracking process. Rather than searching the entire solution space, some approaches recommend searching in optimal regions [1, 84]. These optimal regions can have local optimisation performed within them to enable effective determination of the GMPP [1]. Other approaches include searching first on the left and then the right of a

located optimum in the process of finding the global optimum [85]. However, under certain environmental conditions this may require that most of the *P–V* curve be considered.

4.1.3 Two-Stage Method

Two-stage methods, where typically a conventional technique such as P&O operates in the second stage, are a viable option to improve the performance of MPPT under non-uniform environmental conditions [28, 85–87]. In the first stage some process is applied that will move the operating point near to the neighbourhood of the expected GMPP. The local search is then applied in this neighbourhood in the second stage to track to the MPP. Often a load line or linear relationship is defined to move the operating point during the first stage [28, 85–88]. The load line is based on an equivalent resistance which is proportional to the ratio of the open-circuit voltage to the short-circuit current. This load line, however, does not exclusively move the operating point to the neighbourhood of the global maxima so global searching around the operating point may still be necessary [85]. Performing a two stage method utilising a load line calculation in the first stage, requires that the open-circuit voltage and short-circuit current be periodically measured. During this measurement time, no power will be supplied to the load.

Other two-stage approaches include combining variable step size P&O with the fractional open-circuit voltage technique [89]. The operating point in this implementation is adjusted automatically when a large change in current is measured. The P&O method is combined with PSO in a two-stage approach where first a local MPP is found using P&O followed by global searching with PSO [90]. This process reduces the global searching time that is required by the PSO method and also improves the tracking speed when operating under varying environmental conditions.

The use of two-stage methods enables conventional MPPT techniques to perform better under non-uniform environmental conditions. However, a small increase in implementation cost and complexity is typically required, the time required for searching may increase and under some conditions, the two stage methods will be unable to locate the global maxima.

4.2 Techniques Based on Observations of the I–V *and* P–V *Characteristics for MPPT Under Non-uniform Environmental Conditions*

Studies of the key properties of the *I–V* and *P–V* characteristics for PV modules have led to some key realisations that can guide MPP searching under non-uniform environmental conditions. In particular, the separation of the MPPs is approximately 80 % of the open-circuit voltage of the module and on either side of the

GMPP, the MPPs will decrease in magnitude [91]. These observations can be used to guide a global search to find all MPPs on the *P–V* curve, followed by utilising a conventional technique for local search in the neighbourhood of the GMPP. By focussing on the regions of interest, the entire curve does not need to be considered which will reduce the time required in searching for the MPP. The observations have also been applied with IncCond used as the local search method [92].

Auxiliary curves can be defined based on the fact that the change in voltage or current along the defined curve is quicker than the change occurring along the *I–V* curves, and this can guide MPPT techniques [93].

By considering the spacing between successive MPPs under non-uniform environmental conditions, a voltage window search (VWS) can be conducted [94]. This technique utilises a global voltage step which has an optimum value approximately equal to the voltage difference between two adjacent peaks. The voltage window is defined based on the power operating triangle (POT) which is defined by constant current and constant voltage lines. A conventional technique will be applied for local searching and the VWS is applied periodically unless a large change in power is sensed, triggering an earlier global search.

By basing techniques on key properties of the *I–V* and *P–V* characteristics that have been measured experimentally or simulated under non-uniform environmental conditions, it becomes possible to offer improved tracking performance under non-uniform environmental conditions. The techniques described in this section may, however, add to the cost and complexity of the implementation and in some cases will lead to temporary tracking of a local MPP.

4.3 Techniques Designed Specifically MPPT Under Non-uniform Environmental Conditions

While conventional techniques have been modified to perform more effectively for MPPT under non-uniform environmental conditions, techniques designed specifically for tracking under these conditions have also been developed. These approaches include line search methods such as DIRECT and Fibonacci search, partial swarm optimisation (PSO), simulated annealing (SA) and chaos search.

4.3.1 Line Search

Line searches work by the restriction and shifting of an interval to ensure that it always contains the optimum value [82]. Dividing Rectangles (DIRECT) and Fibonacci search are line search methods which have been commonly used for MPPT.

The DIRECT method involves making the searching interval progressively smaller based on the value of samples within the interval and some conditions to determine which interval is the most likely to hold the global optimum [95].

DIRECT works effectively for functions that can be classified as Lipschitz, and the *P–V* characteristic meets this criterion, leading to reliable identification of the global optimum.

In the Fibonacci search, the length of the interval is defined based on the numbers in the Fibonacci sequence [82, 96]. To utilise Fibonacci search with non-uniform environmental conditions, a condition must be defined to identify when the non-uniform conditions arise and to re-initialise the global search [82].

These line search methods enable GMPPT to occur while relying on relatively simple test conditions. In some cases, the methods may converge to local MPPs and the effectiveness of special conditions to detect when non-uniform conditions arise is a key limitation of these techniques. Additionally, these techniques are sensitive to the initial values of parameters, and if the parameter values are not selected appropriately the method may not converge.

4.3.2 Particle Swarm Optimisation

Particle swarm optimisation (PSO) is based on the optimisation process and behaviour of birds flocking and fish schooling. The optimisation process uses a collection of particles that share information to collectively solve a particular problem. Each particle has its own position, and acceleration, and these will be updated to take into account the particle's own best position and the global best position. PSO requires the definition of a number of key parameters including the momentum factor, speed determining constants and the number of particles [97]. Fewer parameters are needed, and the performance is seen to improve when a deterministic approach is taken and the random parameters are removed [98].

The particle position at the next step is given by (11), where x_i^k is the previous particle position, x_i^{k+1} is the new particle position and Φ_i^{k+1} is the particle's new velocity.

$$x_i^{k+1} = x_i^k + \Phi_i^{k+1} \tag{11}$$

The velocity of the particle is calculated based on its previous velocity, the differences between its current position and best position and the difference between the global best position and the current particle position. The particle velocity is given in (12) where ω_i is the inertia weight, c_1, c_2 are the acceleration coefficients, $r_1, r_2 \in U(0,1)$ are random numbers, $P_{\text{best},i}$ is the best position of particle i and G_{best} is the best position of all particles in the population.

$$\Phi_i^{k+1} = \omega_i^k \Phi_i^k + c_1 r_1 (P_{\text{best},i} - x_i^k) + c_2 r_2 (G_{\text{best}} - x_i^k) \tag{12}$$

Examples of PSO-based MPPT approaches include combining PSO with a gravitational search algorithm to lead to minimised oscillations in steady state when

a change in the irradiance occurs [99], or utilising a colony of flashing fireflies to exhibit better performance than standard PSO [100].

PSO-based MPPT approaches typically have a good performance in identifying the global optimum under non-uniform environmental conditions. However, if the initial particle positions are not selected appropriately, it is entirely possible that the algorithm will converge to a local MPP [97]. Additionally, the PSO-based approaches rely on several system dependent constants which must be appropriately selected for optimal operation. PSO is a time-invariant technique so it requires an appropriately defined re-initialisation condition to restart the tracking when a change in the conditions occurs. Such conditions are still under development.

4.3.3 Simulated Annealing

Simulated annealing (SA) is an optimisation approach based on the annealing process used with metals. While traditionally used for global minimisation, a small change to the key criteria of the method enables it to be used for global maximisation. The SA-based MPPT method has been applied to uniform [101] and non-uniform operating conditions [102, 103] and exhibits good performance under both with limited optimisation of the parameters. To find the MPP with the SA-based method, an initial temperature, final temperature and cooling rate must be defined. A variety of different cooling schedules could be utilised to guide the search ranging from the geometric cooling schedule [104, 105] to the Lundy cooling schedule [106]. If a new candidate operating point has a power larger than the reference operating point, it will be accepted as the new reference operating point. However, if the candidate operating point has a power less than the reference point, it may still be accepted depending on the acceptance probability. At a high temperature, the method is more likely to accept a solution that reduces the power of the reference point enabling the method to escape from local minima [105]. The acceptance probability is given by (13) where P_k is the power at the candidate voltage, P_i is the power at the reference voltage and T_k is the current temperature of the search.

$$\Pr = \exp\left(\frac{P_k - P_i}{T_k}\right) \tag{13}$$

The global searching nature of the SA optimisation process makes it well-suited to performing MPPT. However, this technique will frequently track to a neighbourhood around the MPP and may require a local search to improve the accuracy of the tracking [107]. Additionally, like other time-invariant techniques, including PSO, the SA algorithm relies on an appropriate re-initialisation condition to reset the global search when a change in the conditions occurs.

4.3.4 Chaos Search

Chaos search can be employed to lead to good performance of MPPT under non-uniform environmental conditions. Dual carriers where a logistic mapping is selected and an additional function is used to map the chaos generators can lead to improved performance [108]. Chaotic behaviour can be shown to be deterministic despite its random appearance which leads chaos search-based approaches to have a better performance than a purely random search. While no additional circuit components are required in the realisation of the dual carrier chaotic search, the complexity of the technique far exceeds that of conventional MPPT techniques.

Other approaches that utilise chaos search combine this searching mechanism with techniques such as PSO [109]. The merging of these two techniques for flexible PV modules is termed as the hybrid chaotic PSO (HCPSO) method. Flexible PV modules experience multiple maxima due to the non-uniform irradiance that arises due to being applied to a curved surface. The chaotic search mechanism in this implementation acts to re-initialise the positions of the particles in the case that they become trapped at local maxima. The HCPSO can be applied periodically and conventional MPPT can be applied to remain at the MPP before the next global tracking cycle is initiated.

Chaos search techniques can improve the performance of MPPT under non-uniform environmental conditions, however, lead to an implementation with increased complexity. Depending on how the chaos search is utilised, oscillations may be observed in steady state such as when chaos search is used in a two-stage implementation. Another limitation is that a re-initialisation condition must be defined to restart the chaos search when a change in conditions occurs.

5 Conclusion

This chapter has explored the main MPPT methods designed to work with uniform and with non-uniform environmental conditions. These techniques have been assessed against several criteria to define how effective these methods are at achieving MPPT accurately, quickly and with minimal cost and complexity. The discussion presented in this chapter highlights that no single existing MPPT method is able to meet all criteria defined for an effective MPPT method. Rather, some techniques perform very well for certain criteria and not so well against other criteria. This suggests that the choice of MPPT technique is quite dependent on the constraints of the application. Future work in the field of MPPT for PV systems may include combining the advantages of individual techniques to develop more hybrid methods, development of effective re-initialisation conditions to enable the wider use of time-invariant optimisation methods and further development through understanding of non-uniform environmental conditions.

References

1. Lei P, Li Y, Seem J (2011) Sequential ESC based global MPPT control for photovoltaic array with variable shading. IEEE Trans Sustain Energy 2(3):348–358
2. Patel H, Agarwal V (2008) MATLAB-based modeling to study the effects of partial shading on PV array characteristics. IEEE Trans Energy Convers 23(1):302–310
3. Lyden S, Haque ME (2015) Maximum Power Point Tracking techniques for photovoltaic systems: a comprehensive review and comparative analysis. Renew Sustain Energy Rev 52:1504–1518
4. Esram T, Chapman PL (2007) Comparison of photovoltaic array maximum power point tracking techniques. IEEE Trans Energy Convers 22(2):439–449
5. Bekker B, Beukes HJ (2004) Finding an optimal PV panel maximum power point tracking method. In: Proceedings of AFRICON Conference in Africa (AFRICON), pp 1125–1129
6. Blanes JM, Toledo FJ, Montero S, Garrigós A (2013) In-site real-time photovoltaic I-V curves and maximum power point estimator. IEEE Trans Power Electron 28(3):1234–1240
7. Pandey A, Dasgupta N, Mukerjee AK (2007) A Simple single-sensor MPPT solution. IEEE Trans Power Electron 22(2):698–700
8. Farivar G, Asaei B, Mehrnami S (2013) An analytical solution for tracking photovoltaic module MPP. IEEE J Photovolt 3(3):1053–1061
9. Kuperman A (2014) Comments on 'an analytical solution for tracking photovoltaic module MPP'. IEEE J Photovoltaics 4(2):734–735
10. Patel S, Shireen W (2011) Fast converging digital MPPT control for photovoltaic (PV) applications. In: 2011 IEEE Power and Energy Society General Meeting, pp 1–6
11. Scarpa V, Buso S, Spiazzi G (2009) Low-complexity MPPT technique exploiting the PV module MPP locus characterization. IEEE Trans Ind Electron 56(5):1531–1538
12. Liu YH, Yang ZZ, Wang SC, Huang JW (2011) A novel analog MPPT technique for low power photovoltaic systems. In: IEEE Region 10 conference, pp 833–837
13. Hartmann LV, Vitorino MA, Correa MBR, Lima AMN (2013) Combining model-based and heuristic techniques for fast tracking the maximum-power point of photovoltaic systems. IEEE Trans Power Electron 28(6):2875–2885
14. Abdelsalam AK, Goh S, Abdelkhalik O, Ahmed S, Massoud A (2013) Iterated unscented Kalman filter-based maximum power point tracking for photovoltaic applications. In: IECON 2013—39th annual conference of the IEEE Industrial Electronics Society, pp 1685–1693
15. Elgendy MA, Zahawi B, Atkinson DJ (2012) Assessment of perturb and observe MPPT algorithm implementation techniques for PV pumping applications. IEEE Trans Sustain Energy 3(1):21–33
16. Alajmi B, Ahmed K, Finney S, Williams B (2011) Fuzzy logic controlled approach of a modified hill climbing method for maximum power point in microgrid stand-alone photovoltaic system. IEEE Trans Power Electron 26(4):1022–1030
17. Carannante G, Fraddanno C, Pagano M, Piegari L (2009) Experimental performance of MPPT algorithm for photovoltaic sources subject to inhomogeneous insolation. IEEE Trans Ind Electron 56(11):4374–4380
18. Abdelsalam AK, Massoud AM, Ahmed S, Enjeti PN (2011) High-performance adaptive perturb and observe MPPT technique for photovoltaic-based microgrids. IEEE Trans Power Electron 26(4):1010–1021
19. Sera D, Teodorescu R, Hantschel J, Knoll M (2008) Optimized maximum power point tracker for fast-changing environmental conditions. IEEE Trans Ind Electron 55(7):2629–2637
20. Chikh A, Chandra A (2011) An optimum method for maximum power point tracking in photovoltaic systems. In: IEEE Power and Energy Society General Meeting, pp 1–6
21. Pandey A, Dasgupta N, Mukerjee AK (2008) High-performance algorithms for drift avoidance and fast tracking in solar MPPT system. IEEE Trans Energy Convers 23(2):681–689

22. Mastromauro RA, Liserre M, Dell'Aquila A (2012) Control issues in single-stage photovoltaic systems: MPPT, current and voltage control. IEEE Trans Ind Inf 8(2):241–254
23. Sera D, Mathe L, Kerekes T, Spataru SV, Teodorescu R (2013) On the Perturb-and-observe and incremental conductance MPPT methods for PV systems. IEEE J Photovolt 3(3):1070–1078
24. Dzung PQ, Vu NTD, Anh NB, Phuong LM, Hiep LC, Lee HH (2012) The low-cost single-stage grid connected photovoltaic system with a modified MPPT method. In: IEEE International conference on Power System Technology (POWERCON), pp 1–6
25. Elgendy MA, Zahawi B, Atkinson DJ (2013) Assessment of the incremental conductance maximum power point tracking algorithm. IEEE Trans Sustain Energy 4(1):108–117
26. Al-Atrash H, Batarseh I, Rustom K (2010) Effect of measurement noise and bias on hill-climbing MPPT algorithms. IEEE Trans Aerosp Electron Syst 46(2):745–760
27. Huang JW, Liu CL, Leou RC, Liu YH (2011) Design and implementation of a FLC-based MPPT technique for photovoltaic systems. In: IEEE Region 10 conference, pp 903–907
28. Ji YH, Jung DY, Kim JG, Kim JH, Lee T, Won CY (2011) A real maximum power point tracking method for mismatching compensation in PV array under partially shaded conditions. IEEE Trans Power Electron 26(4):1001–1009
29. Liu F, Duan S, Liu F, Liu B, Kang Y (2008) A variable step size INC MPPT method for PV systems. IEEE Trans Ind Electron 55(7):2622–2628
30. Hsieh GC, Hsieh HI, Tsai CY, Wang CH (2013) Photovoltaic power-increment-aided incremental-conductance MPPT With two-phased tracking. IEEE Trans Power Electron 28 (6):2895–2911
31. Manganiello P, Ricco M, Petrone G, Monmasson E, Spagnuolo G (2014) Optimization of perturbative PV MPPT methods through on line system identification. IEEE Trans Ind Electron 61(12):6812–6821
32. Yu B, Yu G, Kim Y (2011) Design and experimental results of improved dynamic MPPT performance by EN50530. In: IEEE 33rd International Telecommunications Energy Conference (INTELEC), pp 1–4
33. Scarpetta F, Liserre M, Mastromauro RA (2012) Adaptive distributed MPPT algorithm for photovoltaic systems. In: 38th annual conference on IEEE Industrial Electronics Society, pp 5708–5713
34. Mosa M, Abu Rub H, Ahmed ME, Rodriguez J (2012) Modified MPPT with using model predictive control for multilevel boost converter. In 38th annual conference on IEEE Industrial Electronics Society, pp 5080–5085
35. Jones DC, Erickson RW (2013) Probabilistic analysis of a generalized perturb and observe algorithm featuring robust operation in the presence of power curve traps. IEEE Trans Power Electron 28(6):2912–2926
36. Ingegnoli A, Iannopollo A (2010) A maximum power point tracking algorithm for stand-alone photovoltaic systems controlled by low computational power devices. In: IEEE Mediterranean Electrotechnical Conference (MELECON), pp 1522–1527
37. Negnevitsky M (2002) Artificial intelligence: a guide to intelligent systems, 2nd edn. Pearson Education Limited
38. Purnama I, Lo YK, Chiu HJ (2011) A fuzzy control maximum power point tracking photovoltaic system. In: IEEE international conference on Fuzzy Systems (FUZZ-IEEE), pp 2432–2439
39. Chiu CS (2010) T-S Fuzzy maximum power point tracking control of solar power generation systems. IEEE Trans Energy Convers 25(4):1123–1132
40. Chiu CS, Ouyang YL (2011) Robust maximum power tracking control of uncertain photovoltaic systems: a unified T-S Fuzzy model-based approach. IEEE Trans Control Syst Technol 19(6):1516–1526
41. Mishra S, Sekhar PC (2012) Ts fuzzy based adaptive perturb algorithm for MPPT of a grid connected single stage three phase VSC interfaced PV generating system. In: IEEE Power and Energy Society General Meeting, pp 1–7

42. Alabedin AMZ, El-Saadany EF, Salama MMA (2011) Maximum power point tracking for Photovoltaic systems using fuzzy logic and artificial neural networks. In: IEEE Power and Energy Society General Meeting, pp 1–9
43. Noman AM, Addoweesh KE, Mashaly HM (2012) A fuzzy logic control method for MPPT of PV systems. In: 38th annual conference on IEEE Industrial Electronics Society, pp 874–880
44. Al Nabulsi A, Dhaouadi R (2012) Efficiency optimization of a DSP-based standalone PV system using fuzzy logic and dual-MPPT control. IEEE Trans Ind Inf 8(3):573–584
45. Garraoui R, Sbita L, Ben Hamed M (2013) MPPT controller for a photovoltaic power system based on fuzzy logic. In 10th international multi-conferences on systems, signals & devices 2013 (SSD13), pp 1–6
46. Rahim NA, Che Soh A, Radzi MAM, Zainuri MAAM (2014) Development of adaptive perturb and observe-fuzzy control maximum power point tracking for photovoltaic boost dc–dc converter. IET Renew Power Gener 8(2):183–194
47. Mishra S, Sekhar PC (2014) Takagi-Sugeno fuzzy-based incremental conductance algorithm for maximum power point tracking of a photovoltaic generating system. IET Renew Power Gener 8(8):900–914
48. Lee HH, Phuong LM, Dzung PQ, Vu NTD, Khoa LD (2010) The new maximum power point tracking algorithm using ANN-based solar PV systems. In: IEEE Region 10 conference, pp 2179–2184
49. Islam MA, Kabir MA (2011) Neural network based maximum power point tracking of photovoltaic arrays. In: IEEE Region 10 Conference, pp 79–82
50. Ishaque K, Salam Z, Amjad M, Mekhilef S (2012) An improved particle swarm optimization (PSO)–based MPPT for PV with reduced steady state oscillation. IEEE Trans Power Electron 27(8):3627–3638
51. Jain S, Agarwal V (2007) Comparison of the performance of maximum power point tracking schemes applied to single-stage grid-connected photovoltaic systems. IET Electr Power Appl 1(5):753–762
52. Dineshkumar T, Subramani M (2013) Design and implementation maximum power point Tracking in photovoltaic cells. In: International conference on energy efficient technologies for sustainability, pp 792–795
53. Pai FS, Chao RM, Ko SH, Lee TS (2010) Performance evaluation of parabolic prediction to maximum power point tracking for PV array. IEEE Trans Sustain Energy 2(1):60–68
54. Kimball JW, Krein PT (2008) Discrete-time ripple correlation control for maximum power point tracking. IEEE Trans Power Electron 23(5):2353–2362
55. Bazzi AM, Krein PT (2011) Concerning 'maximum power point tracking for photovoltaic optimization using ripple-based extremum seeking control'. IEEE Trans Power Electron 26 (6):1611–1612
56. Esram T, Kimball JW, Krein PT, Chapman PL, Midya P (2006) Dynamic maximum power point tracking of photovoltaic arrays using ripple correlation control. IEEE Trans Power Electron 21(5):1282–1291
57. Barth C, Pilawa-Podgurski RCN (2015) Dithering digital ripple correlation control for photovoltaic maximum power point tracking. IEEE Trans Power Electron 30(8):4548–4559
58. Li X, Li Y, Seem JE, Lei P (2011) Maximum power point tracking for photovoltaic systems using adaptive extremum seeking control. In: IEEE conference on decision and control and European Control Conference, pp 1503–1508
59. Moura SJ, Chang YA (2010) Asymptotic convergence through Lyapunov-based switching in extremum seeking with application to photovoltaic systems. In: American Control Conference, pp 3542–3548
60. Wang P, Zhu H, Shen W, Choo FH, Loh PC, Tan KK (2010) A novel approach of maximizing energy harvesting in photovoltaic systems based on bisection search theorem. In: IEEE Applied Power Electronics Conference and Exposition (APEC), pp 2143–2148

61. Shiota N, Phimmasone V, Abe T, Miyatake M (2013) A MPPT algorithm based on the binary-search technique with ripples from a converter. In: International conference on Electrical Machines and Systems (ICEMS), pp 1718–1721
62. Tang L, Xu W, Zeng C, Dorrell D, Yu X (2012) A linear-prediction maximum power point tracking algorithm for photovoltaic power generation. In: 38th annual conference on IEEE Industrial Electronics Society, pp 3334–3339
63. Dunford WG, Palmer PR, Capel A (2007) Application of centered differentiation and steepest descent to maximum power point tracking. IEEE Trans Ind Electron 54(5):2539–2549
64. Young KD, Utkin VI, Ozguner U (1999) A control engineer's guide to sliding mode control. IEEE Trans Control Syst Tech 7(3):328–342
65. Hung JY, Gao W, Hung JC (1993) Variable structure control: a survey. IEEE Trans Ind Electron 40(1):2–22
66. Bianconi E, Calvente J, Giral R, Mamarelis E, Petrone G, Ramos-Paja CA, Spagnuolo G, Vitelli M (2013) A fast current-based MPPT technique employing sliding mode control. IEEE Trans Ind Electron 60(3):1168–1178
67. Hussain A, Kumar A, Behera L (2013) Sliding mode control of a buck converter for maximum power point tracking of a solar panel. In: IEEE International conference on Control Applications (CCA), pp 661–666
68. Jimenez-Brea E, Salazar-Llinas A, Ortiz-Rivera E, Gonzalez-Llorente J (2010) A maximum power point tracker implementation for photovoltaic cells using dynamic optimal voltage tracking. In: 25th annual IEEE Applied Power Electronics Conference and Exposition (APEC), pp 2161–2165
69. Levron Y, Shmilovitz D (2013) Maximum power point tracking employing sliding mode control. IEEE Trans Circ Syst I, Reg Pap 60(3):724–732
70. Shmilovitz D (2005) On the control of photovoltaic maximum power point tracker via output parameters. IEE Proc—Electr Power Appl 152(2):239–248
71. Amaratunga GAJ, Urayai C (2013) Single-sensor maximum power point tracking algorithms. IET Renew Power Gener 7(1):82–88
72. Patel H, Agarwal V (2009) MPPT Scheme for a PV-Fed Single-Phase Single-Stage Grid-Connected Inverter Operating in CCM With Only One Current Sensor. IEEE Trans Energy Convers 24(1):256–263
73. Abu Qahouq JA (2011) Multiple solar panels maximum power point tracking using the output current. In: IEEE 33rd International Telecommunications Energy Conference (INTELEC), pp 1–5
74. Dallago E, Finarelli DG, Gianazza UP, Barnabei AL, Liberale A (2013) Theoretical and experimental analysis of an MPP detection algorithm employing a single-voltage sensor only and a noisy signal. IEEE Trans Power Electron 28(11):5088–5097
75. Jiang Y, Abu Qahouq JA (2012) Single-sensor multi-channel maximum power point tracking controller for photovoltaic solar systems. IET Power Electron 5(8):1581–1592
76. Chikh A, Chandra A (2015) An optimal maximum power point tracking algorithm for PV systems with climatic parameters estimated. IEEE Trans Sustain Energy 6(2):644–652
77. Dallago E, Liberale A, Miotti D, Venchi G (2015) Direct MPPT algorithm for PV sources with only voltage measurements. IEEE Trans Power Electron 30(12):6742–6750
78. Metry M, Shadmand MB, Liu Y, Balog RS, Abu Rub H (2015) Maximum power point tracking of photovoltaic systems using sensorless current-based model predictive control. In: IEEE Energy Conversion Congress and Exposition (ECCE), pp 6635–6641
79. Koutroulis E, Blaabjerg F (2012) A new technique for tracking the global maximum power point of PV arrays operating under partial-shading conditions. IEEE J Photovolt 2(2):184–190
80. Wang D (2010) A method for instantaneous measurement of PV VI characteristics and its application for MPPT control. In: IEEE Photovoltaic Specialists Conference, pp 2904–2907

81. Spertino F, Ahmad J, Ciocia A, Di Leo P (2015) A technique for tracking the global maximum power point of photovoltaic arrays under partial shading conditions. In: IEEE Power Electronics for Distributed Generation Systems (PEDG), pp 1–5
82. Miyatake M, Inada T, Hiratsuka I, Hongyan Z, Otsuka H, Nakano M (2004) Control characteristics of a fibonacci-search-based maximum power point tracker when a photovoltaic array is partially shaded. In: International Power Electronics and Motion Control Conference (IPEMC), vol 2, pp 816–821
83. Yang CY, Hsieh CY, Feng FK, Chen KH (2012) Highly efficient analog maximum power point tracking (AMPPT) in a photovoltaic system. IEEE Trans Circ Syst I Reg Pap 59 (7):1546–1556
84. Lei P, Li Y, Chen Q, Seem JE (2010) Extremum seeking control based integration of MPPT and degradation detection for photovoltaic arrays. In: American Control Conference (ACC), pp 3536–3541
85. Kazmi S, Goto H, Ichinokura O, Hai-Jiao G (2009) An improved and very efficient MPPT controller for PV systems subjected to rapidly varying atmospheric conditions and partial shading. In: Australasian Universities Power Engineering Conference (AUPEC), pp 1–6
86. Bifaretti S, Iacovone V, Cina L, Buffone E (2012) Global MPPT method for partially shaded photovoltaic modules. In: IEEE Energy Conversion Congress and Exposition (ECCE), pp 4768–4775
87. Kobayashi K, Takano I, Sawada Y (2003) A study on a two stage maximum power point tracking control of a photovoltaic system under partially shaded insolation conditions. IEEE Power Eng Soc Gen Meet 4:2617
88. Sokolov M, Shmilovitz D (2008) A modified MPPT scheme for accelerated convergence. IEEE Trans Energy Convers 23(4):1105–1107
89. Kabir S, Bansal R, Nadarajah M (2012) Effects of partial shading on photovoltaic with advanced MPPT scheme. In: IEEE International Conference on Power and Energy (PECon), pp 354–359
90. Lian KL, Jhang JH, Tian IS (2014) A Maximum power point tracking method based on perturb-and-observe combined with particle swarm optimization. IEEE J Photovolt 4(2):626–633
91. Patel H, Agarwal V (2008) Maximum power point tracking scheme for PV systems operating under partially shaded conditions. IEEE Trans Ind Electron 55(4):1689–1698
92. Tey KS, Mekhilef S (2014) Modified incremental conductance algorithm for photovoltaic system under partial shading conditions and load variation. IEEE Trans Ind Electron 61 (10):5384–5392
93. Escobar G, Ho CNM, Pettersson S (2012) Maximum power point searching method for partial shaded PV strings. In: IEEE Industrial Electronics Society Conference (IECON), pp 5726–5731
94. Boztepe M, Guinjoan F, Velasco-Quesada G, Silvestre S, Chouder A, Karatepe E (2014) Global MPPT scheme for photovoltaic string inverters based on restricted voltage window search algorithm. IEEE Trans Ind Electron 61(7):3302–3312
95. Nguyen TL, Low KS (2010) A global maximum power point tracking scheme employing DIRECT search algorithm for photovoltaic systems. IEEE Trans Ind Electron 57(10):3456–3467
96. Ramaprabha R, Mathur B, Ravi A, Aventhika S (2010) Modified fibonacci search based MPPT scheme for SPVA under partial shaded conditions. In: International Conference on Emerging Trends in Engineering and Technology (ICETET), pp 379–384
97. Miyatake M, Veerachary M, Toriumi F, Fujii N, Ko H (2011) Maximum power point tracking of multiple photovoltaic arrays: a PSO approach. IEEE Trans Aerosp Electron Syst 47(1):367–380
98. Ishaque K, Salam Z (2013) A deterministic particle swarm optimization maximum power point tracker for photovoltaic system under partial shading condition. IEEE Trans Ind Electron 60(8):3195–3206

99. Dhas BGS, Deepa SN (2013) A hybrid PSO and GSA-based maximum power point tracking algorithm for PV systems. In: IEEE international conference on computational intelligence and computing research, pp 1–4
100. Sundareswaran K, Peddapati S, Palani S (2014) MPPT of PV systems under partial shaded conditions through a colony of flashing fireflies. IEEE Trans Energy Convers 29(2):463–472
101. Azam MA, Abdullah-Al-Nahid S, Kabir MA, Chowdhury SMH (2012) Microcontroller based maximum power tracking of PV using stimulated annealing algorithm. In: International Conference on Informatics, Electronics & Vision (ICIEV), pp 298–303
102. Lyden S, Haque ME (2015) A simulated annealing global maximum power point tracking approach for PV modules under partial shading conditions. IEEE Trans Power Electron, vol (in press)
103. Lyden S, Haque ME (2014) Comparison of the Perturb and Observe and simulated annealing approaches for maximum power point tracking in a photovoltaic system under partial shading conditions. In IEEE Energy Conversion Congress and Exposition (ECCE), pp 2517–2523
104. Yang Y, Pei W, Qi Z (2012) Optimal sizing of renewable energy and CHP hybrid energy microgrid system. In: IEEE PES Innovative Smart Grid Technol 1–5
105. Poole DL, Mackworth AK (2010) Artificial intelligence: foundations of computational agents. Cambridge University Press, Cambridge
106. Cohn H, Fielding MJ (1999) Simulated annealing: searching for an optimal temperature schedule. SIAM J Optim 9(3):779–802
107. Lyden S, Haque ME (2015) A hybrid simulated annealing and perturb and observe method for maximum power point tracking in PV systems under partial shading conditions. In: Australasian Universities Power Engineering Conference (AUPEC), pp 1–6
108. Zhou L, Chen Y, Guo K, Jia F (2011) New approach for MPPT control of photovoltaic system with mutative scale dual carrier chaotic search. IEEE Trans Power Electron 26 (4):1038–1048
109. Konstantopoulos C, Koutroulis E (2014) Global maximum power point tracking of flexible photovoltaic modules. IEEE Trans Power Electron 29(6):2817–2828

Photovoltaic Multiple Peaks Power Tracking Using Particle Swarm Optimization with Artificial Neural Network Algorithm

Mei Shan Ngan and Chee Wei Tan

Abstract Photovoltaic (PV) array may receive different level of solar irradiance, such as partially shaded by clouds or nearby building. Multiple peak power points occur when PV module is under partially shaded conditions, which would significantly reduce the energy produced by PV without proper control. Therefore, a Maximum Power Point Tracking (MPPT) algorithm is used to extract maximum available PV power from the PV array. However, most of the conventional MPPT algorithms are incapable to detect global peak (GP) power point with the presence of several local peaks (LP). A hybrid Particle Swarm Optimization and Artificial Neural Network (PSO-ANN) algorithm is proposed in this article to detect the GP power. The PV system which consists of PV array, DC–DC boost converter, and a resistive load, were simulated using MATLAB/Simulink. The performance of the proposed algorithm is compared with that of the standard PSO algorithm. The proposed algorithm is tested and verified by hardware experiment. The simulation results and the experimental results are compared and discussed. It shows that the proposed algorithm performs well to detect the GP of the PV array under partial shaded conditions. In this work, the tracking efficiency of the proposed algorithm is in the range of 92.7–99.7 %.

Keywords Photovoltaic (PV) · Partial shading · Maximum power point tracking (MPPT) · Particle swarm optimization (PSO) · Artificial neural network (ANN)

M.S. Ngan
Department of Electrical and Electronic Engineering, Faculty of Engineering and Information Technology, Southern University College, Johor Bahru, Malaysia
e-mail: msngan@sc.edu.my

C.W. Tan (✉)
Department of Electrical Power Engineering, Faculty of Electrical Engineering, Universiti Teknologi Malaysia (UTM), Skudai, Johor Bahru, Malaysia
e-mail: cheewei@utm.my

M.R. Islam et al. (eds.), *Advances in Solar Photovoltaic Power Plants*, Green Energy and Technology, DOI 10.1007/978-3-662-50521-2_5

1 Introduction

Photovoltaic (PV) is one of the most promising renewable sources due to its environmental friendliness and low maintenance cost [1, 2]. However, there are two major challenges that need to be tackled for large-scale PV systems to be implemented: (1) high installation cost, and (2) low efficiency in PV conversion [3, 4]. Moreover, the PV output characteristics are nonlinear as it varies with solar irradiance and module temperature. Due to these characteristics, a maximum power point tracking (MPPT) controller is utilized to extract the maximum available power from PV array. The MPPT algorithm is used to control the duty cycle of the DC–DC or DC–AC converter which is inserted in between the PV modules and the load [2, 5].

Over the years, numerous MPPT algorithms for PV array under uniform irradiance have been proposed [6]. The widely used techniques include Perturb and Observe (P&O) [7–10], Incremental Conductance (IC) [11, 12], Hill Climbing (HC) [8, 13], open-circuit voltage [13, 14], and short-circuit current algorithm [13, 15]. Recently, several artificial intelligent methods, i.e., Fuzzy Logic Controller (FLC) [16–21], Artificial Neural Network (ANN) [16, 22, 23] are explored. The above-mentioned conventional MPPT algorithms are not capable of tracking the true maximum power point (MPP) if the PV array is partially shaded, such as covered by heavy clouds, falling tree leaves, birds' litters on the array or shaded by buildings [24]. PV cells under low illumination (shaded condition) could be damaged by overheating problem (known as hot spot) attributed to a larger current that flows from other fully illuminated PV cells. This problem can be overcome by inserting bypass diode across the PV cells [25]. However, the insertion of bypass diodes creates multiple peaks, namely global peak (GP) and local peaks (LP), in which only the GP is the true MPP on P–V characteristic curve. The conventional algorithms are not intelligent enough to differentiate among the global and the LP, where the control of operating point tends to linger around the LP [26]. For instance, the P&O is perturbed by comparing the present detected power to the value of the previous power periodically until the MPP is achieved. Similarly, in IC technique, the incremental conductance ($\Delta I/\Delta V$) is compared to the instantaneous conductance (I/V). The open-circuit voltage algorithm (offline MPPT) which only depends on the linear relationship between the PV maximum point voltages with the PV array's open-circuit voltage will stop tracking once the nearby peak point is located regardless of GP or LP.

Several studies have been carried in tracking multiple peaks condition [27–32]. Agarwal et al. had proposed a new MPPT method to track GP under partial shaded condition [29]. The authors claimed that the proposed method is simple and effective. Nevertheless, they only tested for series–parallel PV configuration but no verification was done on series-connected (string) PV configuration. Reference [28] proposed DIRECT search algorithm, which is an area dividing strategy and potentially optimal interval technique (POI) to detect GP. The proposed algorithm can track the GP quickly with increased tracking efficiency than existing methods

but it is rather complicated since it involves decision-making in the control process that burdens the computational time. The authors in reference [27] had implemented the voltage square-based MPPT method to quantify the location of the MPP using a set of mathematical equations. It was tested using SEPIC topology which is costly compared with other converters.

Particle Swarm Optimization (PSO) is a global gradientless stochastic search method. It is used to search for continuous variable for optimization problems [33–35]. Artificial Neural Network (ANN) is an information processing paradigm, which is based on the functional concepts of biological nervous systems. It works best to deal with nonlinear dependence between the inputs and outputs [36–38]. In this work, a hybrid PSO and ANN method is proposed to extract the GP under partial shaded condition. The ANN algorithm initializes the optimal current initial value at the prevailing solar irradiance levels. This initial current is then fed into the PSO to reach the GP location. ANN acts as a platform to aid the PSO algorithm to locate GP in a smaller range. Therefore, PSO can reach the true GP without having to sweep over the wide range of PV voltage which ultimately cut short the computational time. This avoids the operating point from lingering at LP and guarantees the reach of GP.

This chapter commences with the description of PV characteristics under partial shaded condition. If follows by the explanation of the hybrid Particle Swarm Optimization and Artificial Neural Network (PSO-ANN) algorithm. The simulations of the proposed method and the standard PSO algorithm are presented. The proposed method is then tested with the hardware setup. The results of the simulations and hardware testing are compared and discussed. The conclusion is drawn in the last section.

2 PV Arrays Under Partial Shaded Conditions

PV modules are typically connected in series and parallel to obtain the expected voltage and current level [25, 39, 40]. For PV array, every PV module may receive different amount of sunlight as some modules may be partially shaded. In this scenario, the performance of PV array will be severely affected by shaded PV cells. Therefore, the generated PV power significantly drops which in turn reduces the efficiency of the PV system [26]. In a series-connected PV cells, all cells carry the same PV current even though some of the cells are shaded. Hence, the shaded cells are forced to absorb the electric power generated by other fully illuminated PV cells, which will be dissipated as heat [41]. This phenomenon is known as the hot spot problem, whereby the shaded PV cells are damaged without appropriate protection. For that, a bypass diode is typically connected in parallel and in opposite polarity to a group of PV cells to minimize the impact of shadow on PV module [42, 43]. Ideally, one bypass diode per PV cell is the best solution but would definitely increase the PV cost. Under partially shaded condition, the values of short-circuit current for each cell would be different among the series-connected PV

cells. This scenario causes the bypass diode to be forward biased, where the particular shaded PV cell is bypassed by which the current flows through the external circuit to prevent hot spot. An illustration of this phenomenon for two series-connected PV modules under partial shaded condition is shown in Fig. 1.

The insertion of bypass diodes in PV modules causes multiple peaks on the *P–V* characteristics curves under partial shaded conditions [44, 45]. Figure 2 shows a comparison of *P–V* characteristics for two series-connected PV modules, simulated under condition of fully illuminated and partially shaded conditions for PV modules with and without bypass diode. Only one maximum point appears under uniform illumination and also PV without bypass diode, but two peaks are generated for PV with bypass diode under partial shaded condition.

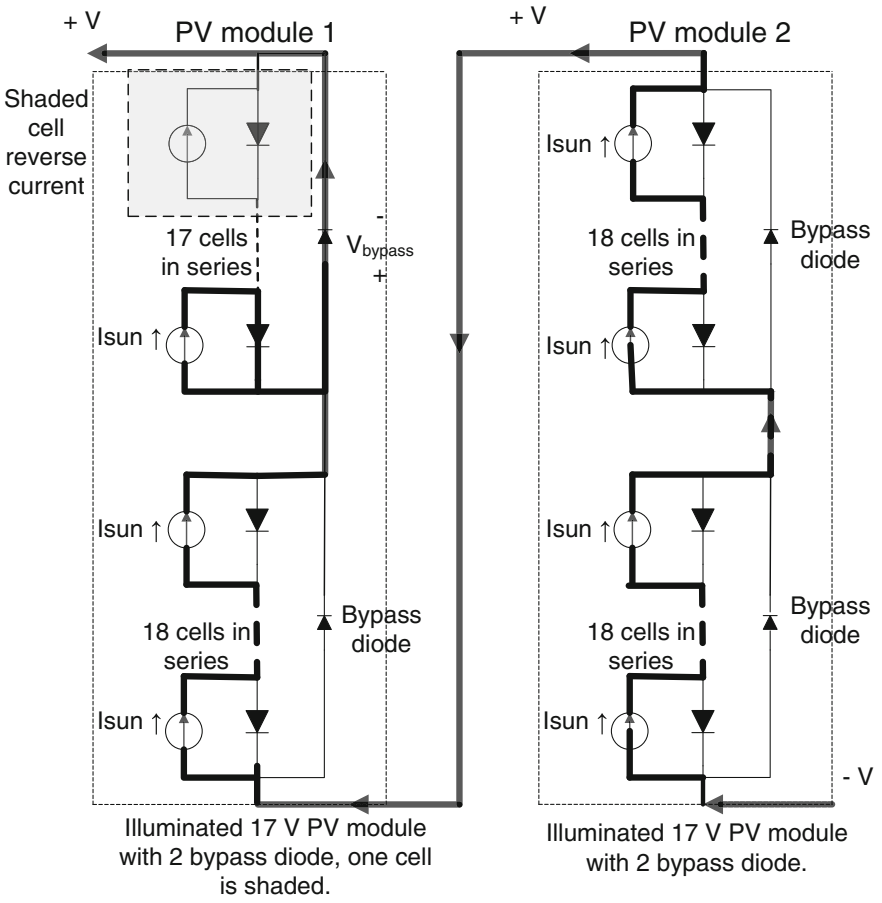

Fig. 1 Two PV modules connected in series with one PV module partially shaded

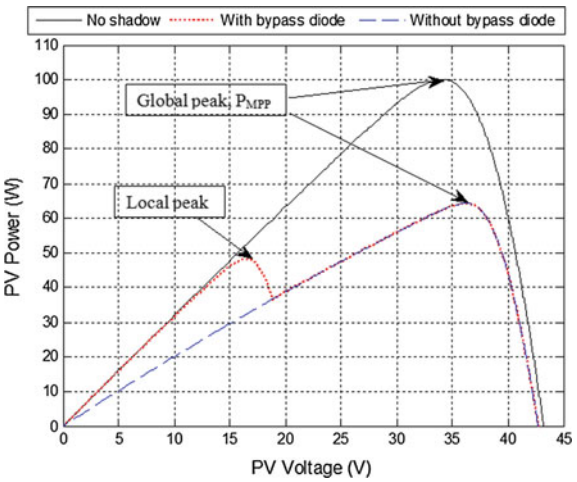

Fig. 2 The *P–V* characteristic curves: a comparison of partially shaded (series-connected) PV modules with and without bypass diode

3 Particle Swarm Optimization (PSO) Algorithm

Particle Swarm Optimization (PSO) was inspired by the dynamic movement of organisms such as insects, birds, and fish. This optimization technique works by having a population (swarm of several particles), where these particles are distributed randomly in a given search space based on a set of designated equations [46–48]. In general, optimization method requires a clear objective function (fitness function) of a specific problem, either it should be maximized or minimized. In the PSO designated equation, there are two important operators, namely the velocity update and the position update as expressed in Eqs. (1) and (2) [46, 49, 50]. One should define the number of particles, M, to be injected into the equations. The more particles improve the accuracy of search but the trade-off is the increase burden of computational times. These particles are used to determine the optimized values of the objective function, associated with a velocity vector, $\left(v_i^k\right)$ for each particle. A new velocity vector $\left(v_i^{k+1}\right)$ is generated based on the current velocity $\left(v_i^k\right)$, current position $\left(S_i^k\right)$, previous best position $(p_{\text{best}i})$, global best position (g_{best}), and the initial coefficients as shown in Eq. (1). The best position, $p_{\text{best}i}$ is the best value in associated vector found within the particles, while the global best position, g_{best} is the best value found among the swarm within the loops generation. The updated velocity vector $\left(v_i^{k+1}\right)$ is then used to update the position vector $\left(S_i^{k+1}\right)$ based on the changes of the previous position $\left(S_i^k\right)$ vector, as expressed in Eq. (2) [49, 51]. The process is repeated until the objective function achieves the optimized value.

$$v_i^{k+1} = wv_i^k + c_1 r_1 \left(p_{\text{best}i} - S_i^k\right) + c_2 r_2 \left(g_{\text{best}} - S_i^k\right) \tag{1}$$

$$S_i^{k+1} = S_i^k + v_i^{k+1} \tag{2}$$

4 Artificial Neural Network (ANN) Algorithm

Artificial Neural Network (ANN) is a type of computational model based on the functional aspects of biological neural networks, which is the method deduced from how the human brain performs computations [36, 52]. This method is suitable for fitting nonlinear functions and recognizing patterns. This is why ANN is popularly applied in the field of physics, automotive, banking, image processing, transportation industries, etc. [53].

Typically, ANN algorithm consists of three significant parameters [54]:

i. The interconnection pattern between the neurons of different layers,
ii. The learning process for updating the weights of different layers, and
iii. The activation functions that convert the input to its expected output.

In general, there are three layers in ANN, explicitly the input layer, hidden layer, and output layer. Transfer functions include *tansig* function (inverse tangent sigmoidal function), *logsig* function (logarithm sigmoidal function), and *purelin* function (linear function), which are used as mathematical functions for the hidden and the output layers [32, 55]. The process of adjusting the weights of neurons is known as learning or training process. There are two types of learning process—supervised learning and unsupervised learning. The former learning requires a set of example pairs (inputs and outputs). The correct output is generated with the new input given according to the example sets trained [36, 55]. This means that the data contains the prior knowledge on the problem domain. In the latter learning process, the output data is produced by a determined function when an input is given.

Table 1 shows two samples of trained data in ANN algorithm. For instance, when the solar irradiance of three PV modules are varied in 900, 900, and 800 W/m^2, respectively, the corresponding PV current for the maximum PV power to be reached is 2.448 A (I_{PV}). In order to move the operating point near the maximum power at I_{mpp}, the initial PV currents are set as 0.76, 0.75, and 0.77 of short-circuit current, I_{SC} (3.25 A in this work). This means that the PSO algorithm will search the correct peak power in the range of 2.4375–2.5025 A. Typically, the commonly used PSO algorithm keeps on searching until the stopping criteria is met. The above-mentioned scenario is only for one shaded condition; if the shaded pattern of the PV array is changed, the range of PV current varies accordingly as the solar irradiance levels change. For that reason, if the initial values of the PV current are preset at a wrong region, PSO algorithm will need longer computational time to search the true peak. For this reason, in this chapter, a confined range of the PV current is trained and generated by the help of ANN algorithm. It is then sent to the PSO algorithm as the second input.

The objective function of the PSO algorithm changes due to the sudden change of the environmental conditions when the PV system is in a real-time operation. This is because of the PV voltage and PV current generated by the PV arrays which are governed by both the solar irradiance level and the ambient temperature. Therefore, the particles should be reinitialized to search the new location of MPP

Table 1 Two samples of I_c and ΔP trained in ANN algorithm

Solar irradiance, G (W/m^2)			PV current, I_{PV} (A)	Maximum PV power, P_{PV} (W)	Initial PV current set, I_c (A)			Change of PV power, ΔP
900	900	800	2.448	262.3	0.76 * I_{SC}	0.75 * I_{SC}	0.77 * I_{SC}	0.116
600	400	300	2.962	144.5	0.92 * I_{SC}	0.91 * I_{SC}	0.93 * I_{SC}	0.309

for the prevailing environmental conditions. This is subjected to the quantity test as expressed in Eq. (3) is triggered, where ΔP is a change of PV power (the difference of present power as compared to the power of previous iteration). The values of ΔP are trained and generated by the ANN algorithm, and then it will be sent into the PSO algorithm as the third input. It can be noticed that the searching process of PSO algorithm will carry on as long as Eq. (3) is fulfilled. The output of PSO algorithm is the reference PV current generated when the simulation time is stopped or stopping criteria is met whichever is completed in prior. Sample data for the values of ΔP and I_c correspond to different combinations of solar irradiance levels which were learned and trained by the supervised learning process of ANN simulation block. The switch selection block, which is connected in between the PSO block and the ANN algorithm block will send the generated ΔP and I_c from ANN block to PSO block, if only if, there is a change of solar irradiance detected.

$$\frac{\left|P_{(S_i+1)} - P_{(S_i)}\right|}{P_{(S_i)}} > \Delta P \tag{3}$$

5 The Proposed Multiple Peaks MPPT

As mentioned above, the conventional MPPT algorithms do not have the capability to locate the GP. Therefore, for multiple peaks tracking, a stochastic search method should be used. This chapter details the hybrid MPPT algorithm that integrate PSO algorithm with ANN. The flowchart of the hybrid PSO-ANN algorithm is shown in Fig. 3. This tracking method is proposed to control the duty ratio of the power converter to locate the global MPP under partial shaded condition.

The design specification of the ANN algorithm in MATLAB/Simulink is illustrated in the block diagram in Fig. 4. A three layer feedforward neural network with the most widely used, backpropagation method is implemented for the estimation of I_c and ΔP (inputs to PSO algorithm). The *sigmoid* function and *purelin* function are the transfer functions for the hidden layer and output layer, respectively. There are 50 epochs, which are the total number of operations needed to train the data. Figure 5 shows the graphs of mean squared error (MSE) against number of epochs for the performance of Neural Network algorithm. It can be noticed that train set error, test set error, and validation set error have same characteristics as all the blue,

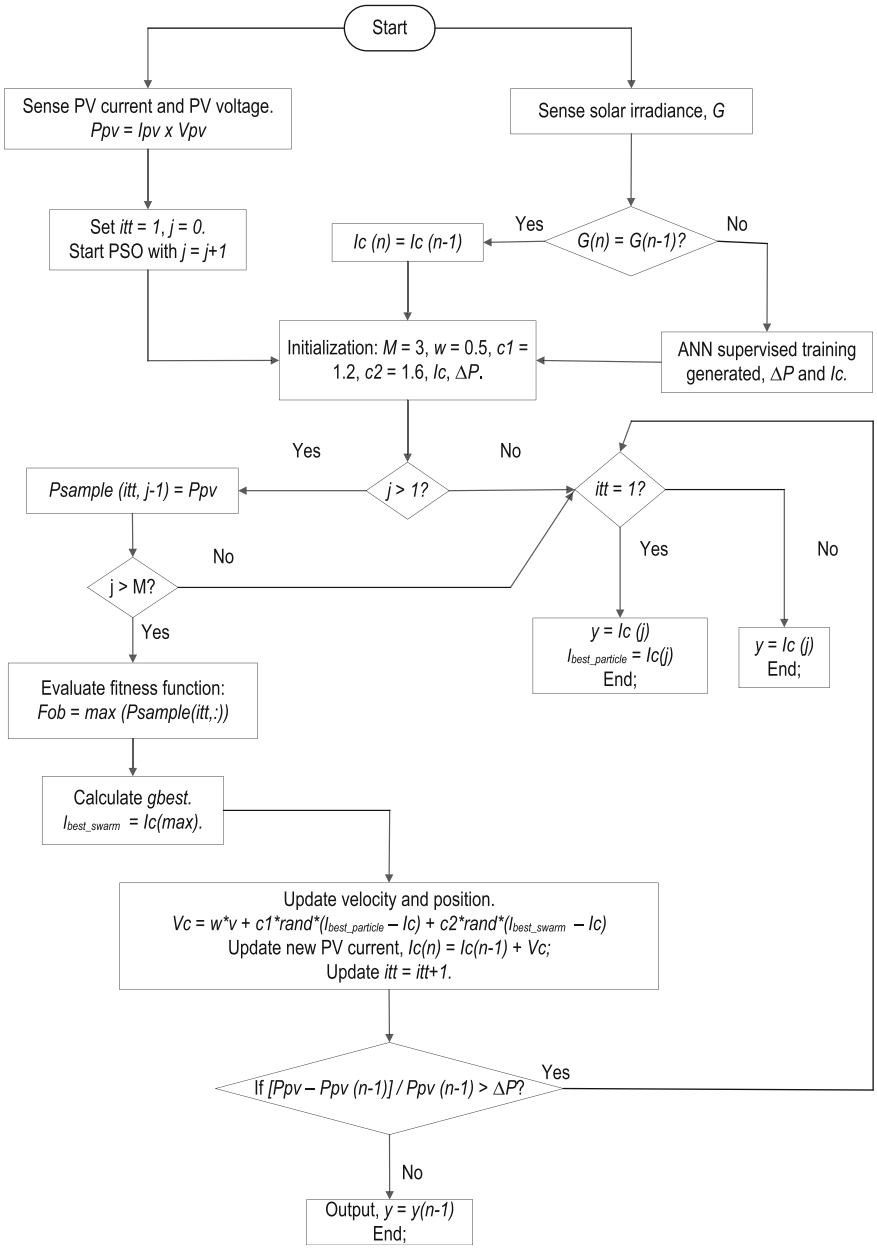

Fig. 3 The flowchart of the proposed hybrid PSO-ANN MPPT algorithm

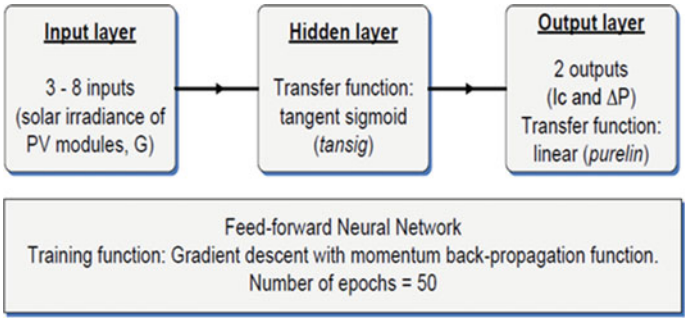

Fig. 4 The block diagram of the specification of ANN algorithm in the simulation

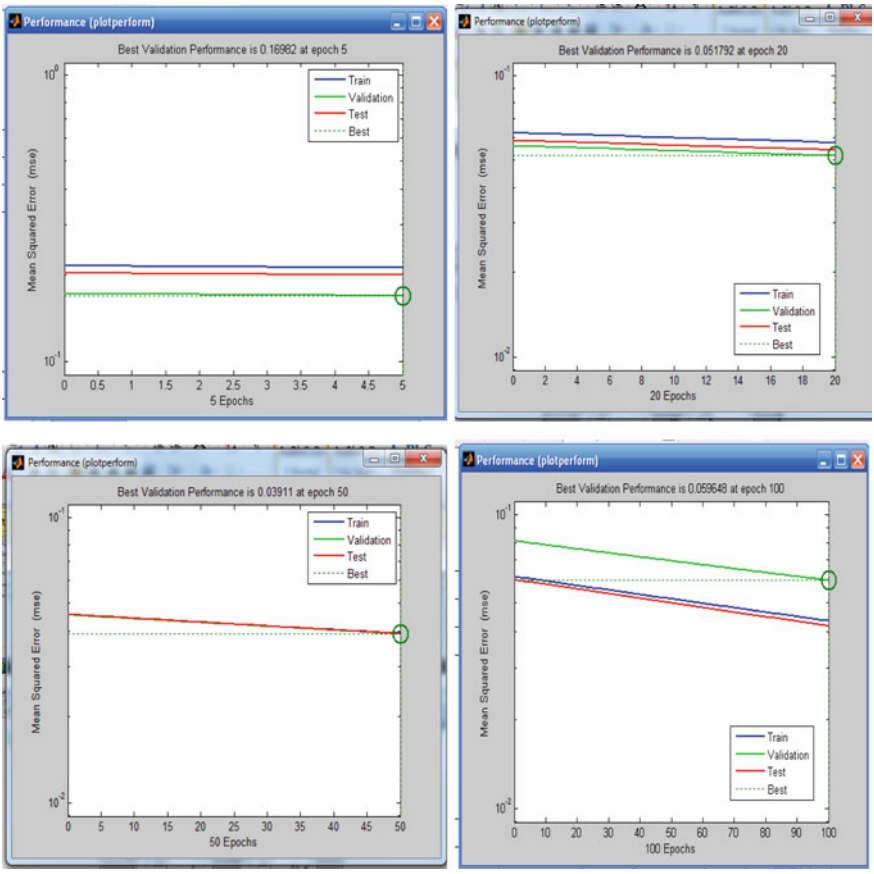

Fig. 5 Graphs of mean squared error (MSE) against different number of epochs for ANN algorithm

red, and green lines converge in one line for the 50 epochs graph. Its best validation performance is 0.03911. Therefore, 50 epochs are chosen for the ANN algorithm.

In the PSO algorithm block, the number of particles (M) and the other three parameters of PSO algorithm include the weight inertia (w), the cognitive coefficient (c_1), and the social coefficient (c_2) were initialized in the beginning of the process. The initialization values were set 3, 0.5, 1.6, and 1.2, respectively. These initial values were determined by simulations as referred to literature [46, 49].

Based on the proposed MPPT algorithm (refer to Fig. 3), when the PV array is illuminated, the generated PV current/voltage (I_{PV}/V_{PV}) as well as the solar irradiance (G) are measured by current/voltage transducers and PV reference cell, respectively. PV power (P_{PV}) is calculated by multiplication of the measured PV voltage and PV current. In this case, the PV power is the objective function of the PSO algorithm as shown in Eq. (3), which is the first input of the algorithm. The initial PV current, I_c is a vector of three particles, it is a fraction of the short-circuit current based on the solar irradiance received by the PV module. This parameter is the main feature in the proposed method. It is used to narrow down the range of searching in the PSO algorithm so that the objective function is maximized.

6 Simulation Setup

Figure 6 shows the simulation blocks that were built in the MATLAB/Simulink. It consists of a PV array, a DC–DC boost converter, a resistive load, a hybrid PSO-ANN algorithm, a switch selection block, a PID controller, and a PWM generator [56]. In the simulation, six PV modules are connected in series to form the PV

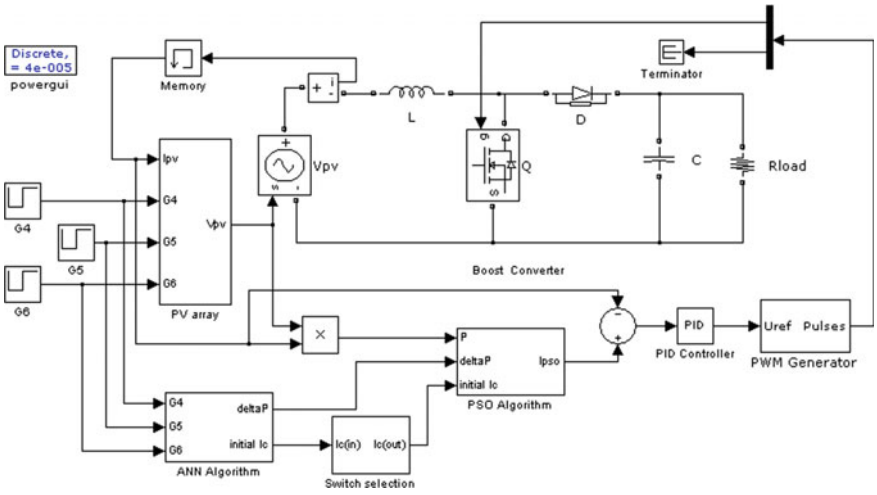

Fig. 6 The simulation blocks of the PSO-ANN MPPT PV system made in MATLAB/Simulink

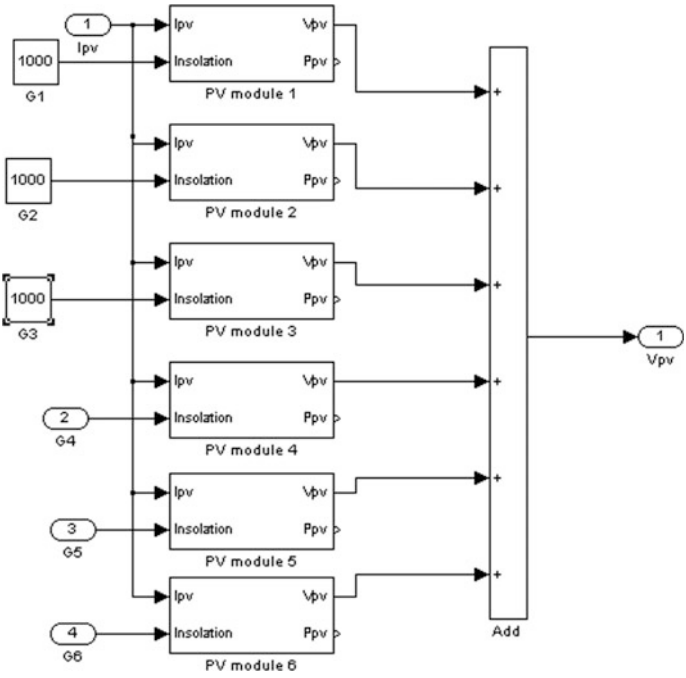

Fig. 7 The PV array simulation block that consists of six series-connected PV modules

array as shown in Fig. 7. The *I–V* data used to model the PV module are shown in Fig. 8. Each PV module is modeled using the single diode equations with bypass diodes connected across a group of PV cells based on the specifications of 8U-50P Polycrystalline solar panel [57]. The specifications of the described PV module are tabulated in Table 2. The input of the PV array is the value of solar irradiance. Therefore, the inputs of the first three PV modules were set as 1000 W/m^2, while the inputs of the rest of the PV modules were varied for partial shaded conditions testing.

The input of the DC–DC boost converter is the controlled voltage source, or PV voltage which is generated by the PV array. The boost converter consists of an inductor, L of 5 mH, a MOSFET switch, Q, a Schottky diode, D, and an output capacitor, C of 3 μF. The output of the DC–DC converter is a resistive load, R_{load} of 33 Ω. The MOSFET switch was controlled by a discrete pulse-width modulation (PWM) generator block with a switching frequency, f_s of 50 kHz and sample time of 10 μs. The proposed hybrid PSO-ANN algorithm worked with PID controller to control the PWM block. The switch selection block is used to switch on the ANN algorithm to send the initial current, I_c values to the PSO algorithm once the solar irradiances of the three PV modules are changed.

The ANN algorithm consists of three inputs (varied solar irradiance for three PV modules) and two outputs (ΔP and I_c). The PSO algorithm also consists of three inputs: PV power generated, ΔP, and I_c. The output of the PSO algorithm is the PV

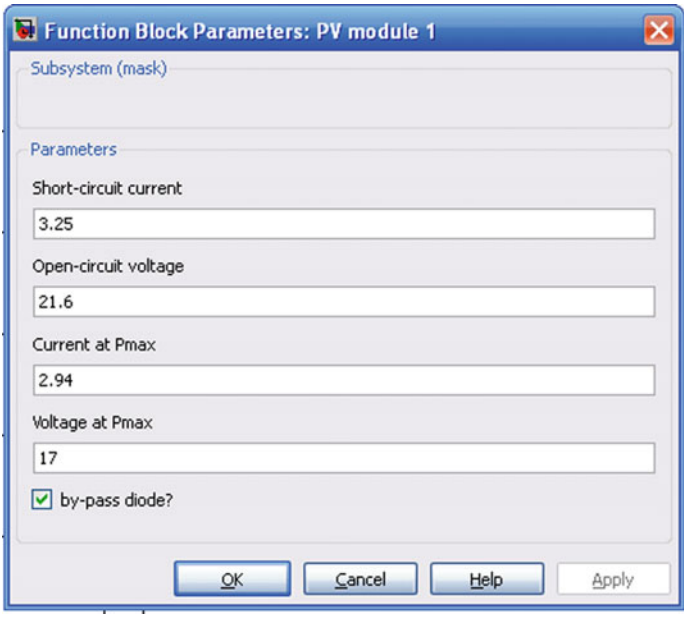

Fig. 8 The input parameters for the series-connected PV modules

Table 2 The specifications of 8U-50P polycrystalline solar module

At temperature	25 °C
Open-circuit voltage, V_{OC}	21.6 V
Short-circuit current, I_{SC}	3.25 A
Voltage at maximum power, V_{MPP}	17 V
Current at maximum power, I_{MPP}	2.94 A
Maximum power, P_{max}	50 W

current generated, I_{PSO} which acts as the reference current and is compared to the PV current generated by the PV array, I_{PV}. An error signal, *e,* which is generated by the difference of reference current (I_{PSO}) and PV current generated (I_{PV}), is further enhanced by the PID controller. The PID controller used in the integration of MPPT algorithm with boost converter include k_p of 5.518, k_i of 0.118, and k_d of 0.036, where these coefficients are designed using Ziegler Nichols Tuning Algorithm from the Control and Estimation Tools Manager and the SISO Design Tool in MATLAB/Simulink software. The output of the PID controller is used to govern the PWM generator and then to control the switching of the MOSFET switch. The discrete sample time of the simulation was 40 μs.

There are two sets of simulation that had been performed to assess the tracking performance of the proposed MPPT algorithm. The simulations include the six series-connected PV modules (small-scale PV array) and the twelve series-connected PV modules (large-scale PV array). In the first simulation, the

P–V characteristic curves were simulated and plotted under full illumination and partial shaded conditions before it is connected to power converter as shown in Fig. 7.

For the small-scale PV array, six combinations of varied solar irradiance with the corresponding maximum PV powers for six PV modules are tabulated in Table 3. To emulate the shading condition, the solar irradiance values are fixed at 1000 W/m^2 for the first three PV modules in the PV array (*G*1–*G*3), while the solar irradiance values for the other three PV modules (*G*4–*G*6) are varied.

In the large-scale PV array, a few combinations of varied solar irradiance representing different shading patterns are shown in Fig. 9. The combinations of solar irradiance with their corresponding maximum PV powers for testing of the 12 PV modules that are tabulated in Table 4. The number of shaded PV modules is represented by the indication of different solar irradiance level. There are eight PV modules (*G*5–*G*12) with varied solar irradiances in Cases 1 and 2; six PV modules

Table 3 Combinations of solar irradiance level with the corresponding maximum power for six series-connected PV modules (small-scale)

Case	*G*1–*G*3 (W/m^2)	*G*4 (W/m^2)	*G*5 (W/m^2)	*G*6 (W/m^2)	Maximum power, P_{max} (W)
1	1000	1000	1000	1000	299.8
2	1000	1000	1000	700	248.1
3	1000	900	600	400	187.3
4	1000	800	600	300	171.1
5	1000	700	500	400	152.8
6	1000	600	300	200	144.6

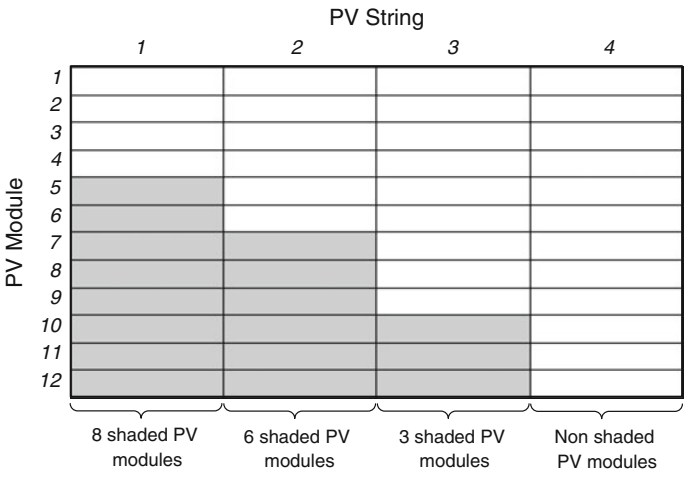

Fig. 9 Different shaded patterns of the twelve series-connected PV modules

Table 4 Combinations of solar irradiance level with the corresponding maximum power for twelve series-connected PV modules (large-scale)

Case	*G*1–*G*4 (W/m^2)	*G*5–*G*6 (W/m^2)	*G*7–*G*8 (W/m^2)	*G*9–*G*10 (W/m^2)	*G*11–*G*12 (W/m^2)	Maximum power, P_{max} (W)
1	1000	[800, 1000]	[700, 1000]	[500, 1000]	[400, 1000]	[301.6, 599.6]
2	1000	[1000, 900]	[1000, 900]	[1000, 800]	[1000, 500]	[599.6, 431.0]
Case	*G*1–*G*6 (W/m^2)	*G*7–*G*8 (W/m^2)	*G*9–*G*10 (W/m^2)	*G*11–*G*12 (W/m^2)	–	Maximum power, P_{max} (W)
3	1000	[1000, 800]	[1000, 500]	[1000, 300]		[599.6, 343.2]
4	1000	[900, 1000]	[800, 1000]	[400, 1000]		[434.0, 599.6]
Case	*G*1–*G*9 (W/m^2)	*G*10 (W/m^2)	*G*11 (W/m^2)	*G*12 (W/m^2)	–	Maximum power, P_{max} (W)
5	1000	[900, 1000]	[600, 1000]	[500, 1000]		[479.8, 599.6]
6	1000	[1000, 500]	[1000, 400]	[1000, 300]		[599.6, 444.6]

(*G*7–*G*12) with varied solar irradiance in Cases 3 and 4; and three PV modules (*G*10–*G*12) with varied solar irradiance in Cases 5 and 6. The other PV modules are set under full illumination of 1000 W/m^2. The solar irradiance in square bracket is to represent step change of irradiance level. For instance, *G*4 = [1000, 400], *G*5 = [1000, 400], *G*6 = [1000, 800]. This means that, at the beginning point the solar irradiance of PV modules 4, 5, and 6 are at the irradiance level of 1000 W/m^2 (the first value in the bracket), and it is followed by a step change of irradiance at irradiance levels of 400, 400, and 800 W/m^2, respectively (represented by the second value in the bracket).

In this simulation, when the number of shaded PV modules increases, the number of inputs of the ANN algorithm also increases. Hence, the numbers of training data for the supervised learning ANN algorithm increases too. This is because the combination of different solar irradiance in large PV array is greater than the small PV array. Consequently, the computational time for ANN algorithm in the large PV array simulation is longer than the small-scale PV array.

In the second simulation, the small-scale PV array is connected to the DC–DC boost converter controlled by the proposed ANN-PSO algorithm and a resistive load. The simulation was conducted with three varied step change of solar irradiances. The simulations were carried out with four combinations of solar irradiance in step change as shown in Table 5. In order to benchmark the tracking performance of the proposed algorithm, the same PV array was connected to the standard PSO algorithm for further testing. The performance and effectiveness of both algorithms (ANN-PSO and PSO) are compared and studied.

In the third simulation, the large-scale PV array is connected to the DC–DC boost converter controlled by the proposed ANN-PSO algorithm and a resistive load. The simulation was conducted with different shaded patterns as shown in

Table 5 Combinations of solar irradiance step change

Case	$G4$ (W/m^2)	$G5$ (W/m^2)	$G6$ (W/m^2)
1	[1000, 400]	[1000, 400]	[1000, 800]
2	[700, 900]	[500, 600]	[400, 400]
3	[1000, 800]	[1000, 600]	[700, 300]
4	[600, 400]	[300, 400]	[200, 800]

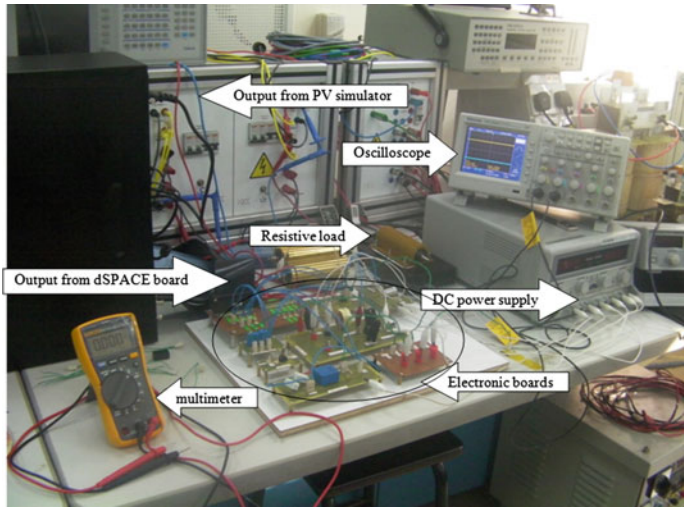

Fig. 10 The overview of the experimental verification setup

Fig. 9. The inputs of PV array are the step changes of solar irradiance as presented in Table 4. Similarly to small-scale PV array, the large-scale PV array is also benchmarked with the standard PSO algorithm. The performance and effectiveness of both algorithms are then compared and studied as well.

7 Hardware Experimental Setup

Figure 10 shows the experimental setup for a stand-alone PV system. The output of the PV array simulator is connected to the PV output board which consists of a switch breaker. The PV output board is the interface between the PV simulator and the test equipment. When the power supply of the PV simulator is adjusted, the current will flow from the PV simulator to the PV output board connected to the input of the DC–DC boost converter. The output of the dSPACE DS1104 R&D Controller Board is connected by a 50-pin connector to the input of the gate driver board. The electronic boards include the gate driver circuit, DC–DC converter circuit, and sensors circuits. The DC power supply provides voltage supply to all

Table 6 The specification of electronic components used for hardware setup

Electronic component	Model	Rating
Gate drive optocoupler	HCPL 3120	±20 V
Current transducer	HY5P	±4 V
Voltage transducer	LV25P	±25 V
MOSFET for boost converter	IRF1640G	V_{DS} 200 V
Inductor for boost converter	7122-RC	25.5 mH
Capacitor for boost converter	ECA2DHG3R3	3.3 μF
Resistor for boost converter	HS300 33RJ	33 Ω

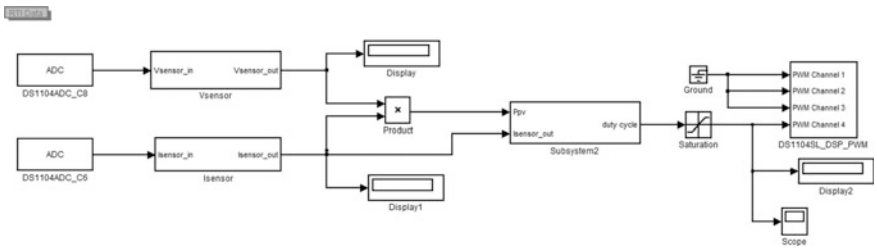

Fig. 11 The integration of the proposed PSO-ANN algorithm for experiment in RTI model in Simulink

the electronic boards except the DC–DC converter. The oscilloscope is connected to the gate driver in order to observe the pulse-width signal provided by the dSPACE DS1104 R&D Controller Board and the pulse-width signal driven by the gate driver. The resistive load is connected to the output of the DC–DC converter. The multimeter is used to measure the input voltage from the PV array simulator and the output voltage at the resistive load. Table 6 shows the specifications of the electronic components used for hardware setup.

Figure 11 shows the integration of the Simulink blocks with the dSPACE RTI lib blocks for the experiment of the proposed MPPT algorithm in PV system. It consists of ADC blocks (*DS1104ADC_C8*and *DS1104ADC_C6*), voltage sensing subsystem (V_{sensor}), current sensing subsystem (I_{sensor}), the proposed PSO-ANN algorithm (*subsystem2*), *saturation* block and pulse-width modulator (*DS1104SL_DSP_PWM*). The ADC blocks are the analog-to-digital converter pins that convert the voltage and current signals into digital values for the simulation of the MPPT algorithm. *DS1104ADC_C8* is the ADC block at channel 8, which is connected to the output of the voltage transducer. Meanwhile *DS1104ADC_C6* is the ADC block at channel 6, which is connected to the output of the current transducer. The *Saturation* block sets the duty cycle value in the range of 0.01–0.99. *DS1104SL_DSP_PWM* is the built-in pulse-width modulator in the

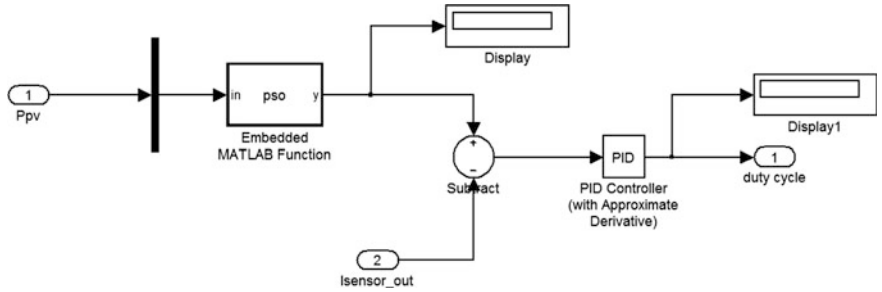

Fig. 12 Subsystem of the proposed PSO-ANN algorithm block as in *Subsystem2*

dSPACE DS1104 R&D Controller Board. The PWM has four channels, but only channel 4 is utilized for the simulation, the rest of the channels are grounded. The switching frequency for the PWM is set as 20 kHz, where the PV system is first tested with the switching frequency which is lower than that in the simulation.

Figure 12 shows the subsystem of the proposed PSO-ANN algorithm block. The input of this subsystem is the value of the PV power. It is a multiplication of the output values of the voltage and current sensing blocks. The proposed PSO-ANN algorithm is written in the Embedded MATLAB Function block, where the coding of the PSO algorithm is converted from the initial coding written in m-file of the MATLAB Function block. The ANN algorithm is not connected to the PSO algorithm because the ANN functions are the ready-built-in functions in MATLAB/Simulink. These ready-built-in functions are not recognized by the Embedded MATLAB Function block. Therefore, the initial PV current of the PSO algorithm is not initialized by the ANN algorithm in the experiment. Instead it is initialized manually by substituting new initial values when the solar irradiance curves are changed for testing in the PV simulator software.

The output of the Embedded MATLAB Function is the predicted PV current corresponding to the maximum PV power by the PSO algorithm. Then, this value is subtracted by the current value from the current sensing block ($I_{\text{sense\_out}}$). The difference of these values is fetched to the *PID controller* for further enhancement. Lastly, the output of the *PID controller* is the duty cycle value that is fetched to the *Saturation* block.

Figure 13 shows the PV curve which is generated in RAM 3 of PVAS1. It consists of four peaks, where there is only one global power peak and three LP. Figure 14 shows the *P–V* and *I–V* curves on the same diagram with the online global searching point. The green marker on the *I–V* curve is global power peak, while the red marker is the searching operating point. The orange bar in Fig. 14 is the MPP match which is shown in percentage. Table 7 shows the specifications of the PV array in PVAS1.

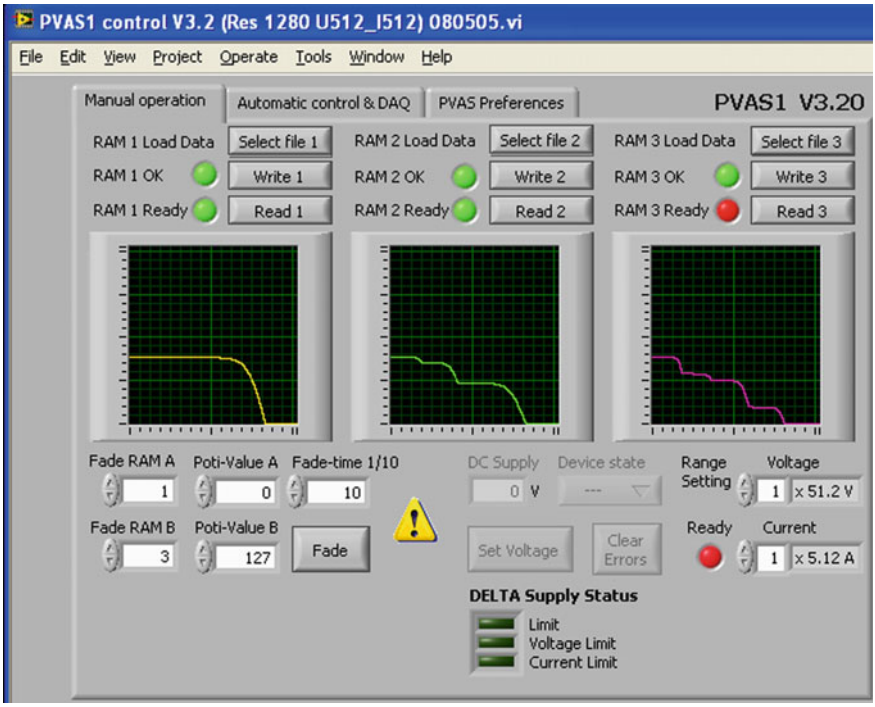

Fig. 13 The insertion of PV models under partial shaded condition in PVAS1 control screen, the *P–V* curve shown in RAM 3 is read and written into the PVAS1

When the voltage supply of the PVAS1 is adjusted to 42 V, the red marker operating point is moved along the *I–V* curve from 0 to 40 V. The proposed MPPT algorithm in MATLAB/Simulink blocks is turned on by sending the command coding into the MOSFET through the dSPACE DS1104 R&D Controller Board. Then, the red marker operating point searched the global power peak along the *I–V* curve. It can be noticed that the operating point almost overlapped the expected global power peak (green marker) as shown in Fig. 14. The measurements of the global power peak searched includes maximum PV current of 1.22 A, maximum PV voltage of 25.7 V, and maximum PV power of 31 W. The MPP match shown is about 99.7 %. It is the percentage matched between the green marker and red marker.

In order to match the results obtained from the experiment, the results are compared to simulation results made in MATLAB/Simulink. Four series-connected PV modules are used in the PV array model for simulation. The solar irradiance values are adjusted manually by trial and error. The *P–V* and *I–V* characteristics

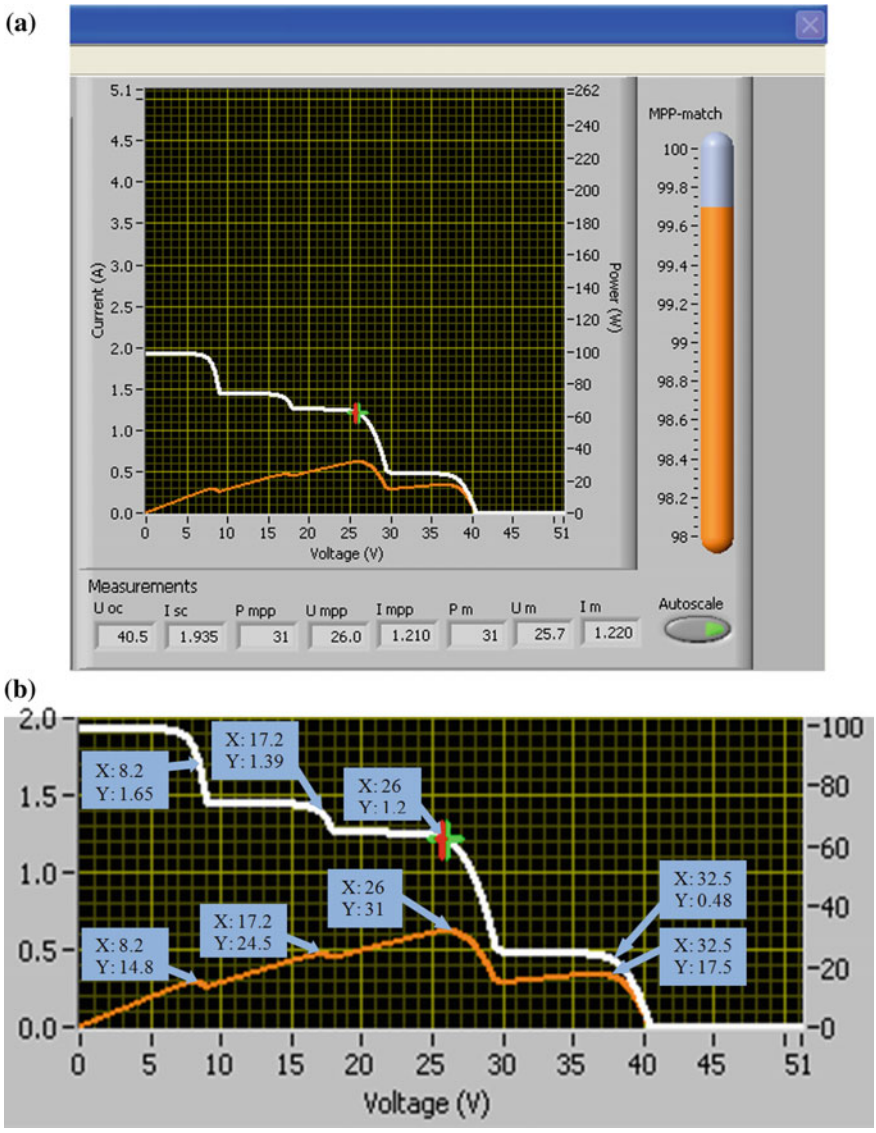

Fig. 14 **a** The online searching of global peak for PV string under partial shaded condition in PVAS1 GUI control screen; **b** a zoomed in view of the characteristic curves

graphs are generated by the PV array model as shown in Fig. 15, which are similar to experimental curves generated by PVAS1. Both characteristics graphs have four multiple peaks, they have almost the same shape and the multiple peaks as in the hardware experiment as shown in Fig. 14. The maximum power peak is at the PV voltage of 26.2 V, the PV current of 1.178 A, and the PV power of 30.88 W.

Table 7 The specifications of PV string in PVAS1

Open-circuit voltage, V_{OC}	40.5 V
Short-circuit current, I_{SC}	1.935 A
Maximum power, P_{max}	31 W
Voltage at maximum power, V_{MPP}	26 V
Current at maximum power, I_{MPP}	1.21 A

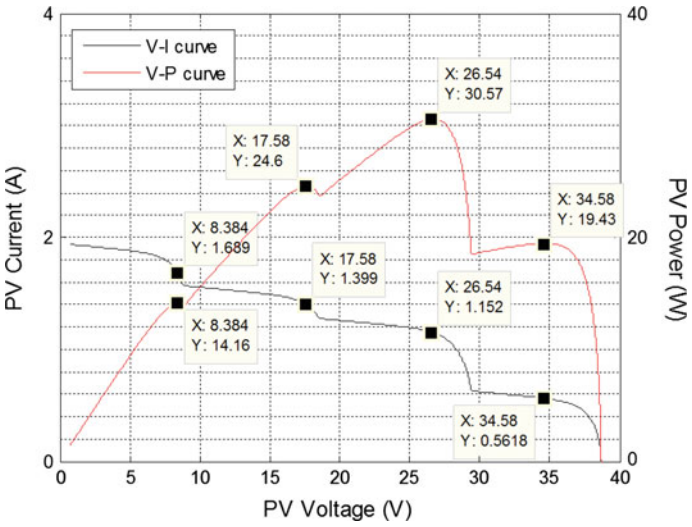

Fig. 15 The *P–V* characteristics graph and the *I–V* characteristics graph, which are simulated using MATLAB/Simulink to resemble the hardware experimental result

8 Results and Discussion

8.1 Simulation Results

The *P–V* characteristic curves of the six series-connected PV array generated in the first simulation are shown in Fig. 16. The corresponding maximum PV powers for each case are recorded in Table 3. In Case 1, the PV array was fully illuminated, hence there was only one GP generated at 299.8 W. When there was only one PV module partially illuminated at 700 W/m^2 in Case 2, hence there were two peaks in the *P–V* characteristic curve. In Cases 3, 4, 5, and 6, all three PV modules are partially shaded, therefore four peaks are established in the characteristic curves for each case. The green dots shown in Fig. 16 are the global MPP peaks for each case, while the purple dots shown in Fig. 16 are the multiple LP for each case.

Figure 17a–c shows the tracking performance of the proposed algorithm with respect to the *P–V* characteristic curves, for the large-scale PV array case with the

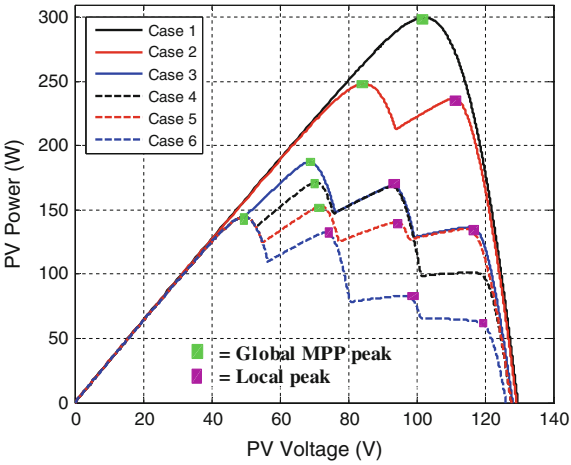

Fig. 16 The *P–V* characteristic curves for six series-connected PV array at a series of solar irradiance combination as tabulated in Table 3

solar irradiance combinations as tabulated in Table 4. The black color curves are the *P–V* characteristic curves simulated under the full illumination and also two cases of partially shaded conditions. The arrows show the direction of the operating point in tracking the step change of solar irradiance, while the bolded colors (plotted with markers) of blue and purple curves show the traces of the operating points in searching the GPs under each step change of irradiances.

Figure 18a–d shows the PV power waveforms that were plotted against the simulation time of 0.01 s where the step change of solar irradiance occurs at 0.005 s according to the solar irradiance variations in Table 5 for second simulation. It can be noticed that the PV power curves generated with the implementation of hybrid PSO-ANN algorithm, are quite smooth and constant at steady state for all cases. The PV power curves generated by PSO algorithm in Cases 3 and 4 create obvious ripples at steady state for lower solar irradiance.

Table 8 analyzes the PV power curve in more detail by comparing the expected maximum PV power with the MPPT power generated for each different cases of both MPPT algorithms. The values of P_{max} generated were obtained by plotting the *P–V* characteristic curves of the PV array as if in the first simulation. It can be noticed that the P_{max} generated are recorded in Table 3. The solar irradiance variations in Table 5 are the step change combinations of solar irradiance in Table 3. The MPPT powers, $P_{PSO\text{-}ANN}$, and P_{PSO} are the PV power generated with the implementation of the proposed MPPT algorithm and PSO algorithm when there is a step change of solar irradiance in the input of PV array. The comparison of both PV power were further analyzed by the tracking efficiency of the MPPT algorithm according to (4) as below.

$$\text{Tracking efficiency, } E = \frac{P_{MPPT}}{P_{max}} \times 100\,\% \tag{4}$$

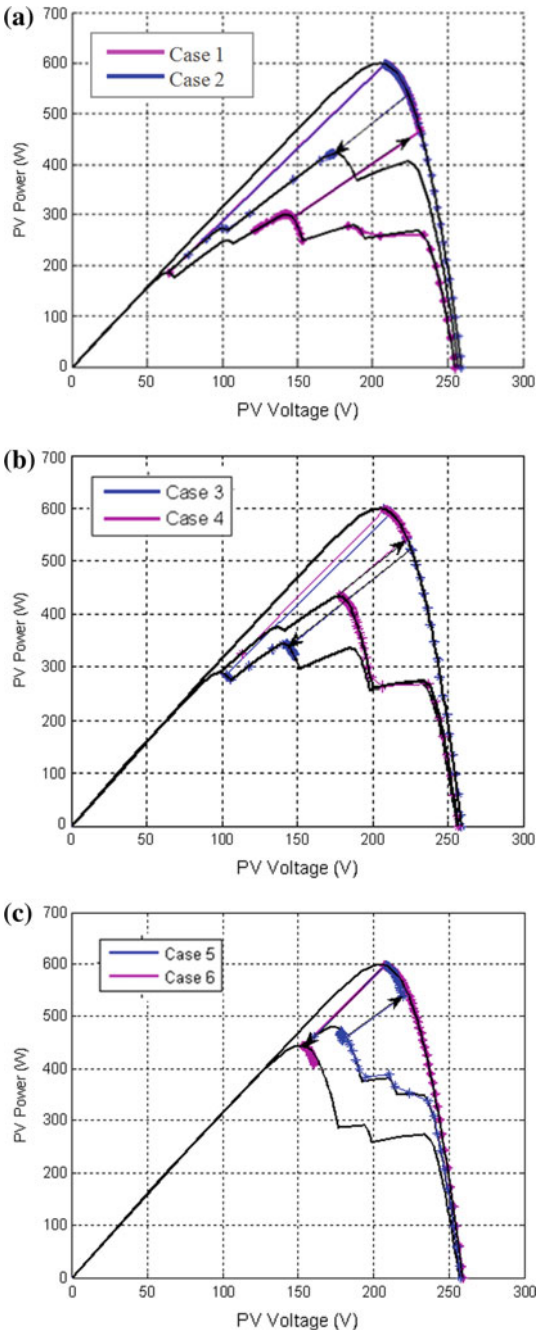

Fig. 17 The trace of operating point under the *P–V* characteristic curves for large-scale PV array: **a** PV array with eight shaded PV modules in Cases 1 and 2, **b** PV array with six shaded PV modules in Cases 3 and 4, **c** PV array with three shaded PV modules in Cases 5 and 6

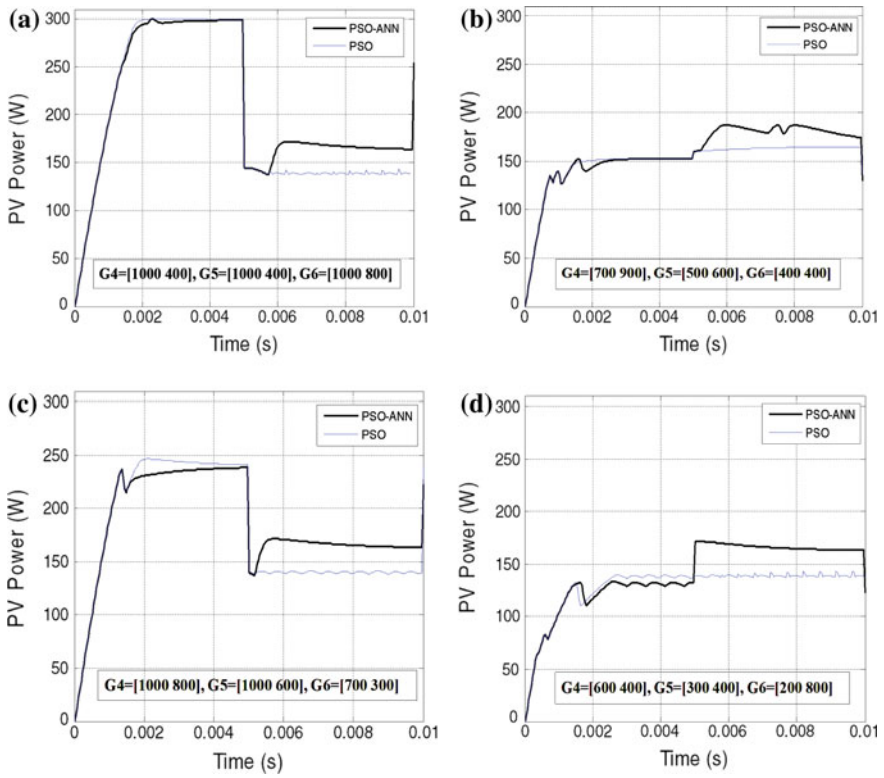

Fig. 18 The PV waveforms correspond to solar irradiance step change of **a** case 1, **b** case 2, **c** case 3 and **d** case 4 as stated in Table 5 for the second simulation

Table 8 The comparison of the maximum PV power and the generated tracked power for the small-scale PV array

Case	Maximum power, P_{max} (W)	MPPT power, $P_{PSO\text{-}ANN}$ (W)	MPPT power, P_{PSO} (W)	Efficiency for PSO-ANN, $E_{PSO\text{-}ANN}$ (%)	Efficiency for PSO, E_{PSO} (%)
1	[299.8, 171.1]	[299, 167]	[299, 137]	[99.7, 97.6]	[99.7, 80.1]
2	[152.8, 187.3]	[152, 182]	[152, 164]	[99.5, 97.2]	[99.5, 87.6]
3	[248.1, 171.1]	[236, 167]	[243, 140]	[95.1, 97.6]	[97.9, 81.8]
4	[144.6, 171.1]	[134, 166]	[138, 138]	[92.7, 97.0]	[95.4, 80.7]

According to Fig. 18 and Table 8, the proposed algorithm can always detect the maximum power when the smaller scale PV array is partially shaded. Even though the values of MPPT power generated, $P_{PSO\text{-}ANN}$ are slightly different with the real

maximum power, P_{max}, yet the results show that the tracking efficiency of the PSO-ANN algorithm for each case is in the range of 92.7–99.7 %. When the PV array is partially shaded, the ANN algorithm will generate initial values of current for the PSO algorithm, where it will search the global power peak in the confined smaller range of PV current. Hence, the proposed algorithm can always reach to MPP if there is a change of solar irradiance.

Figure 19a–c show the PV power waveforms for large-scale PV array in the third simulation. The circled regions as shown in Fig. 19 are the indications of change of solar irradiance, where the PV array is partially shaded by clouds, trees, buildings, etc. The searching of maximum PV power will stop when the GP is reached, therefore the PV power remains constant as shown in each different cases in Fig. 16. There are four curves in each diagram in Fig. 19, where the bolded blue and purple curves are the PV power waveforms tested with the proposed PSO-ANN algorithm, while the dotted blue and purple curves are the PV power waveforms tested with standardized PSO algorithm. The initial PV currents for the standard PSO algorithm were fixed for all simulated cases. Table 9 shows the comparison of the expected PV power from the *P–V* characteristic curves and the PV power values generated by the proposed PSO-ANN algorithm and the standardized PSO algorithm for each case. The tracking efficiencies of both algorithms are also calculated for the testing of larger scale of PV array.

It should be highlighted that in Fig. 19, the standard PSO algorithm was incapable to detect the global power peak when there is a change of solar irradiance, especially for lower solar irradiance. The algorithm will always get stuck in the local peak and oscillates around that point. It can be noticed that at the first part, the efficiency of PSO algorithm is almost the same or even better than the PSO-ANN algorithm, however, the efficiency of PSO algorithm is decreased greatly when there is a change of solar irradiance. This situation due to the initial values of current is not reinitialized when there is a change of solar irradiance, hence the PSO algorithm searches the power peak in a wide range of PV current.

Figure 19 and Table 9 show that the proposed PSO-ANN algorithm also can detect the GP when large-scale PV array is under partial shaded conditions. The tracking efficiency of the MPPT algorithm for twelve series-connected PV array is in the range of 95.0–99.7 %. It indicates that the confined smaller range of PV current generated by the ANN algorithm with the corresponding of different combinations of solar irradiance is very useful for the PSO algorithm to search among the multiple peaks, until it reached the GP.

Similar to the case of small-scale PV array, it can be noticed that the PSO algorithm was incapable to detect the global power peak when there is a change of solar irradiance as shown in Fig. 19a, b for Cases 1, 2, 3, and 4. The standard PSO algorithm always linger in the LP and oscillates around that point because the initial PV currents are fixed at one common range in all cases (it is fixed at 0.9 * I_{SC} 0.91 * I_{SC} and 0.92 * I_{SC} in this testing). Meanwhile the tracking efficiency of the

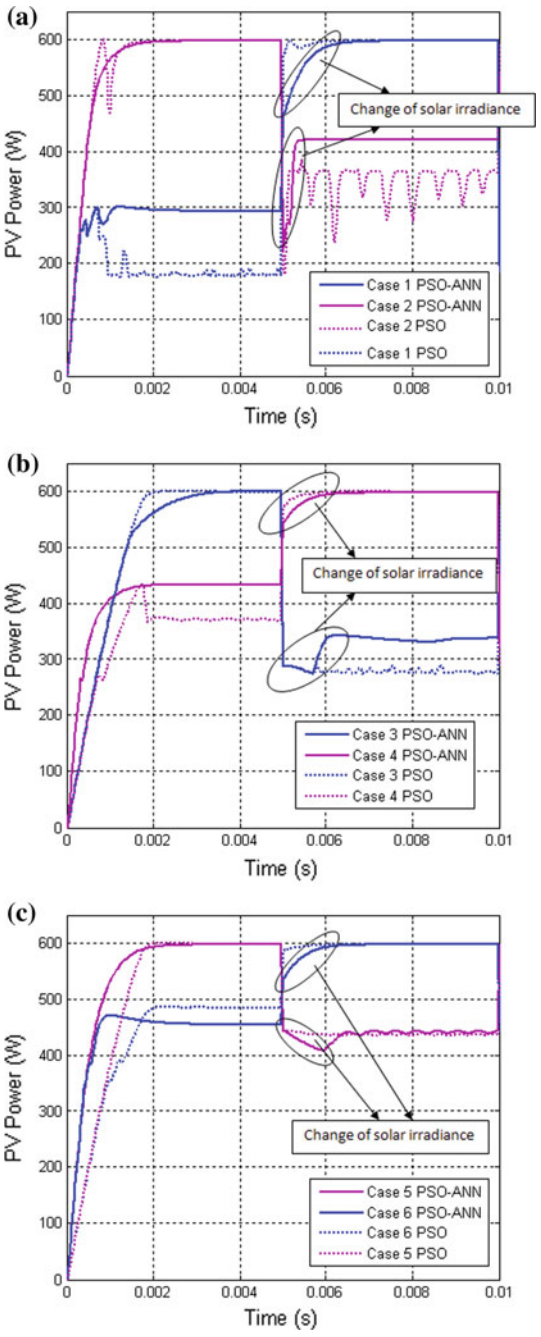

Fig. 19 The PV power waveforms correspond to solar irradiance variations in Table 4 for the third simulation. **a** PV array with eight shaded PV modules in Cases 1 and 2, **b** PV array with six shaded PV modules in Cases 3 and 4, **c** PV array with three shaded PV modules in Cases 5 and 6

Table 9 The comparisons of maximum PV power and the generated MPPT power of the large-scale PV array

Case	Maximum PV power, P_{PV} (W)	MPPT power, $P_{PSO\text{-}ANN}$ (W)	MPPT power, P_{PSO} (W)	Efficiency for PSO-ANN, $E_{PSO\text{-}ANN}$ (%)	Efficiency for PSO, E_{PSO} (%)
1	[301.6, 599.6]	[296, 597]	[188, 597]	[98.1, 99.6]	[62.3, 99.6]
2	[599.6, 431.0]	[597, 421]	[597, 365]	[99.6, 97.7]	[99.6, 84.7]
3	[599.6, 343.2]	[597, 334]	[597, 280]	[99.6, 97.3]	[99.6, 81.6]
4	[434.0, 599.6]	[433, 597]	[369, 597]	[99.7, 99.6]	[85.0, 99.6]
5	[599.6, 444.6]	[597, 443]	[597, 436]	[99.6, 99.6]	[99.6, 98.1]
6	[479.0, 599.6]	[455, 596]	[477, 597]	[95.0, 99.4]	[99.6, 99.6]

PSO algorithm in Cases 5 and 6 is high and better as compared to those of PSO-ANN algorithm because the fixed initial PV currents range is perfect match with that of the corresponding MPP for these combinations of solar irradiance.

In brief, the *P–V* characteristic curves show multiple peaks when the PV array is partially shaded. Even though the ANN algorithm might be time-consuming during the simulation, yet the proposed hybrid algorithm performs well to detect the global MPP when there is a step change of solar irradiance as compared to the PSO algorithm. However, the design of the PV system in this chapter should be further improved to increase the tracking efficiency of the MPPT algorithm in low solar irradiance.

8.2 Experimental Results

Figure 20 shows the waveforms of the PV voltage, PV current, and PV power, which are plotted by the LeCroy Oscilloscope. The first graph shows the PV voltage which is scaled at 10.0 V per division. Initially, the PV voltage is at about 40 V, which is the open-circuit voltage of the PV string. The PV voltage is then dropped at about 25 V when the proposed MPPT algorithm is applied. It is the approximated PV voltage at maximum power condition. The second graph shows the PV current which is scaled at 500 mA per division. Initially, the PV current is at 0 A, which is the corresponding PV current point when the operating point is at about 40 V. The PV current is then increased to about 1.2 A when the proposed MPPT algorithm is applied. This value is also the approximated PV current at maximum power condition. The third graph is the graph of multiplication of the first graph and the second graph, it is the product of the PV voltage and the PV current. Thus, it is the PV power graph. The power axis is scaled at 10.0 W per division. Initially, the PV power is at 0 W as the PV current is 0 A. The PV power is increased to about 30 W, when the proposed MPPT algorithm is applied. It is the maximum PV power for the PV string under partial shaded condition.

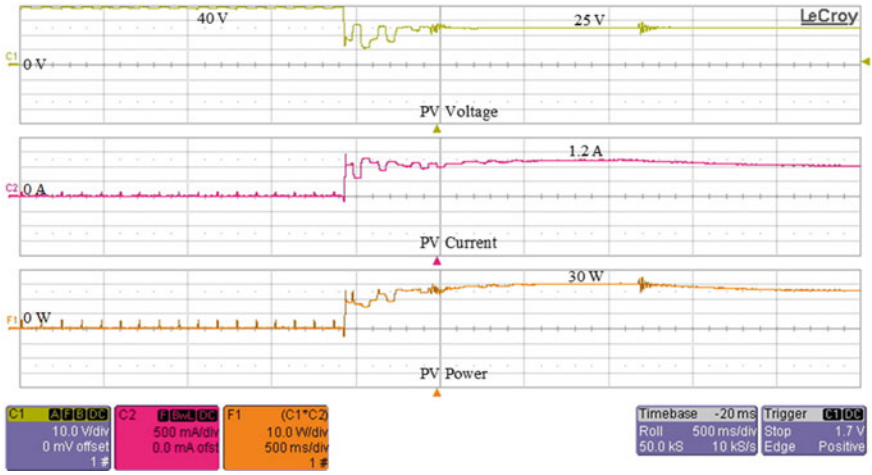

Fig. 20 The voltage, current, and power waveforms of PV system for the first experiment, which is captured in the LeCroy Oscilloscope

Figure 21 shows the waveforms of the PV voltage, PV current, and PV power, which are simulated by the PV array in MATLAB/Simulink under partial shaded condition in order to benchmark the first experiment. The first graph is the PV voltage versus time graph. The PV array is at 25.05 V during the steady state. The second graph is the PV current versus time graph. Initially, the PV current is at about 1.9 A, which is the short-circuit current of the PV string. The PV array is at 1.213 A during the steady state. The third graph is the PV power versus time graph. The PV array is at 30.39 W during the steady state.

Table 10 shows the comparison of the theoretical and the experimental PV powers of both hardware and simulation. It can be noticed that the expected PV powers only differ slightly for both experimental and simulation values. It is to ensure that the testing of PV system is comparable in hardware and simulation. The measured PV power for hardware is about 30 W, which is 1 W less than the expected PV power. Therefore, the proposed MPPT tracking efficiency is about 96.8 %. Meanwhile, the measured PV power for simulation is about 30.39 W, which is slightly less than the expected value of 30.88 W. It indicates that the tracking efficiency of the proposed MPPT algorithm is about 98.4 %.

The simulation results show that the PSO-ANN algorithm can perform very well to search for the global maximum power peak when the PV array is under partial shaded conditions. Its tracking efficiency can reach to as high as 99.7 %. However, the experimental results show that the tracking efficiency of the proposed MPPT algorithm is slightly less than that of simulation results. Its tracking efficiency is at about 96.9 %. This might be due to the power loss in the electronic components when the whole PV system is functioning.

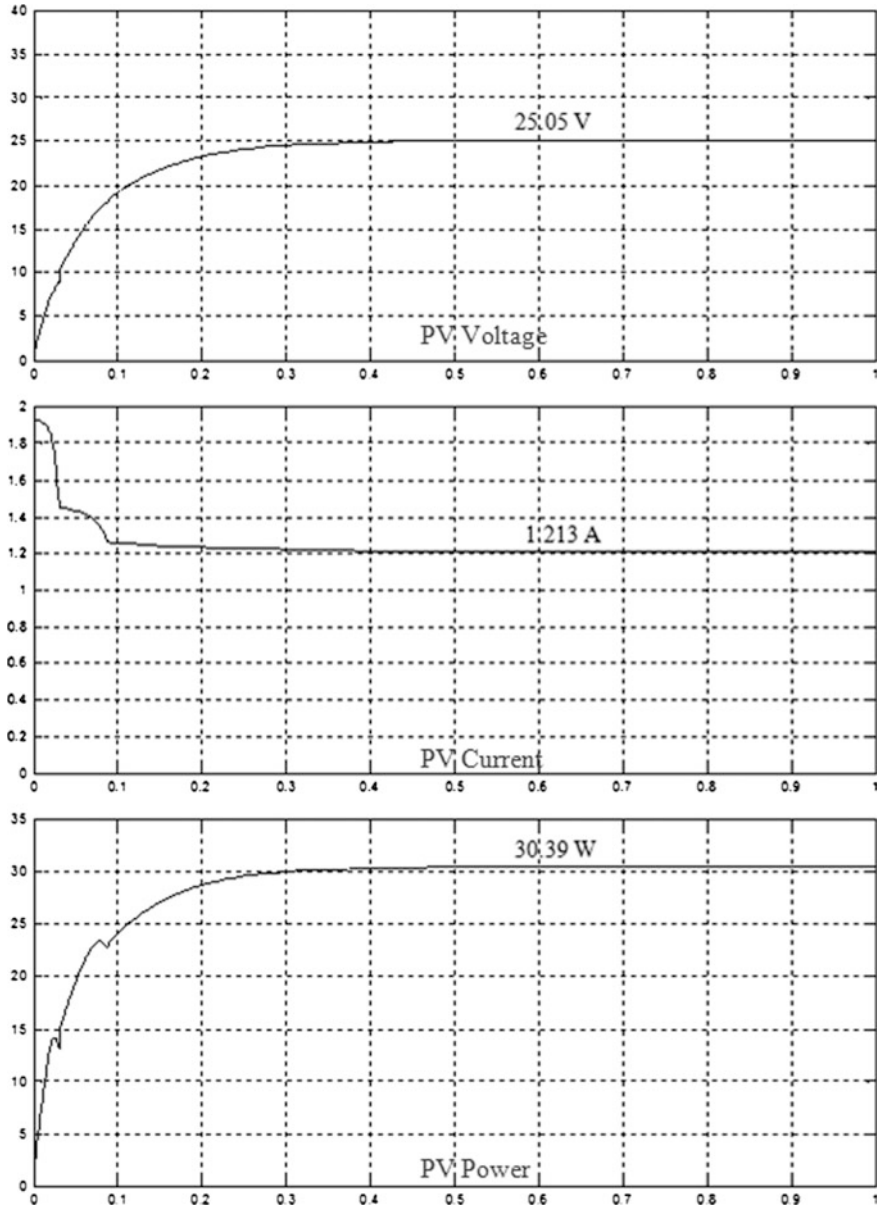

Fig. 21 The voltage, current, and power waveforms of PV system for the first experiment, which is simulated in MATLAB/Simulink

Table 10 The comparison of the experimental result and its compatible simulation result

Test	Theoretical maximum PV power (W)	Experimental PV power (W)	MPPT tracking efficiency (%)
Simulation	30.88	30.39	98.4
Experimental	31	30	96.8

9 Conclusion

When the PV array is partially shaded, hot spot will occur in the shaded PV cells. This problem can be solved by inserting bypass diode across the PV cells; however this will create multiple peaks in the *P–V* characteristic curve. The conventional MPPT algorithms are incapable to detect the GP, hence the PV system are unable to extract the maximum PV power. The performance and efficiency of the hybrid PSO-ANN algorithm are compared with those of PSO algorithm. The simulation results show that the proposed hybrid method can always detect the GP of PV array that is under partial shaded conditions. The simulation results also indicated that the tracking efficiency of the MPPT algorithm is in the range of 92.7–99.7 %. Therefore, when there is a change of solar irradiance, PSO algorithm performs well with the help of ANN algorithm to reinitialize the initial values of PV current. ANN algorithm helps to refine the search region to a smaller range which avoids the operating point from lingering around the LP under partially shaded conditions. When there is a change of solar irradiance, the initial values of PV current should be reinitialized by the ANN algorithm. The proposed algorithm is tested with hardware setup. The PV simulator is used to generate PV current to the boost converter. A PV curve with four peaks is tested with the hardware electronic boards. The results show that the tracking efficiency of the proposed MPPT algorithm is about 96.9 %. The same PV curve is simulated in MATLAB/Simulink. The results show that the tracking efficiency of the proposed MPPT algorithm is about 99.7 %. Both of the experimental results and the simulation results show that the PSO-ANN algorithm can perform well to detect the global power peak when the PV array is under partial shaded conditions. However, their tracking efficiencies are slightly different.

References

1. Yu GJ, Jung YS, Choi JY, Kim GS (2006) A novel two-mode MPPT control algorithm based on comparative study of existing algorithms. Sol Energy 76(4):455–463
2. Abo-Khalil AG, Lee DC, Choi JW, Kim HG (2006) Maximum power point tracking controller connecting PV system to grid. J Power Electron 6(3):226–234
3. Gules R, De Pellegrin Pacheco J, Hey HL, Imhoff J (2008) A maximum power point tracking system with parallel connection for PV stand-alone applications. IEEE Trans Ind Electron 55 (7):2674–2683

4. Ishaque K, Salam Z, Taheri H, Syafaruddin (2011) Modeling and simulation of photovoltaic (PV) system during partial shading based on a two-diode model. Simul Model Pract Theory 19:1613–1626
5. Hohm DP, Ropp ME (2003) Comparative study of maximum power point tracking algorithms. Prog Photovoltaics Res Appl 11(1):47–62
6. Ngan MS, Tan CW (2011) A study of maximum power point tracking algorithms for stand-alone photovoltaic systems. In: Applied power electronics colloquium (IAPEC), Johor Bahru, pp 22–27
7. Petrone G, Spagnuolo G, Vitelli M (2011) A multivariable perturb-and-observe maximum power point tracking technique applied to a single-stage photovoltaic inverter. IEEE Trans Ind Electron 58(1):76–84
8. Piegari L, Rizzo R (2010) Adaptive perturb and observe algorithm for photovoltaic maximum power point tracking. IET Renew Power Gener 4(4):317–328
9. D'Souza NS, Lopes LAC, Liu XJ (2010) Comparative study of variable size perturbation and observation maximum power point trackers for PV systems. Electr Power Syst Res 80:296–305
10. Femia N, Petrone G, Spagnuolo G, Vitelli M (2005) Optimization of perturb and observe maximum power point tracking method. IEEE Trans Power Electron 20(4):963–973
11. Liu F, Duan S, Liu F, Liu B, Kang Y (2008) A variable step size INC MPPT method for PV systems. IEEE Trans Ind Electron 55(7):2622–2628
12. Mei Q, Shan M, Liu L, Guerrero JM (2011) A novel improved variable step-size incremental-resistance MPPT method for PV Systems. IEEE Trans Ind Electron 58 (6):2427–2434
13. Faranda R, Leva S (2008) Energy comparison of MPPT techniques for PV systems. WSEAS Trans Power Syst 3(6):446–455
14. Salas V, Olias E, Barrado A, Lazaro A (2006) Review of the maximum power point tracking algorithms for stand-alone photovoltaic systems. Sol Energy Mater Sol Cells 90:1555–1578
15. Esram T, Chapman PL (2007) Comparison of photovoltaic array maximum power point tracking techniques. IEEE Trans Energy Convers 22(2):439–449
16. Kottas TL, Boutalis YS, Karlis AD (2006) New maximum power point tracker for PV arrays using fuzzy controller in close cooperation with fuzzy cognitive networks. IEEE Trans Energy Convers 21(3):793–803
17. Chaabene M, Ammar MB, Elhajjaji A (2007) Fuzzy approach for optimal energy-management of a domestic photovoltaic panel. Appl Energy 84:992–1001
18. Larbes C, Aït Cheikh SM, Obeidi T, Zerguerras A (2009) Genetic algorithms optimized fuzzy logic control for the maximum power point tracking in photovoltaic system. Renew Energy 34 (10):2093–2100
19. Algazar MM, Hamdi Al-monier, EL-halim HA, Salem MEEK (2012) Maximum power point tracking using fuzzy logic control. Electr Power Energy Syst 39:21–28
20. Ramaprabha R, Balaji M, Mathur BL (2012) Maximum power point tracking of partially shaded solar PV system using modified Fibonacci search method with fuzzy controller. Electr Power Energy Syst 43:754–765
21. Oh SK, Jang HJ, Pedrycz W (2011) Optimized fuzzy PD cascade controller: a comparative analysis and design. Simul Model Pract Theory 19:181–195
22. Liao CC (2010) Genetic k-means algorithm based RBF network for photovoltaic MPP prediction. Energy 35(2):529–536
23. Bahgat ABG, Helwa NH, Ahmad GE, El Shenawy ET (2005) Maximum power point traking controller for PV systems using neural networks. Renew Energy 30(8):1257–1268
24. Silvestre S, Chouder A (2008) Effects of shadowing on photovoltaic module performance. Prog Photovolt Res Appl 16:141–149
25. Wang YJ, Hsu PC (2010) Analytical modelling of partial shading and different orientation of photovoltaic modules. IET Renew Power Gener 4(3):272–282

26. Carannante G, Fraddanno C, Pagano M, Piegari L (2009) Experimental performance of MPPT algorithm for photovoltaic sources subject to inhomogeneous insolation. IEEE Trans Ind Electron 56(11):4374–4380
27. Veerachary M, Shinoy KS (2005) V^2-based power tracking for nonlinear PV sources. IEE Proc Electric Power Appl 152(5):1263–1270
28. Nguyen TL, Low KS (2010) A global maximum power point tracking scheme employing DIRECT search algorithm for photovoltaic systems. IEEE Trans Ind Electron 57(10):3456–3467
29. Patel H, Agarwal V (2008) Maximum power point tracking scheme for PV systems operating under partially shaded conditions. IEEE Trans Ind Electron 55(4):1689–1698
30. Veerachary M, Senjyu T, Uezato K (2002) Feedforward maximum power point tracking of PV systems using fuzzy controller. IEEE Trans Aerosp Electron Syst 38(2):969–981
31. Syafaruddin EK, Hiyama T (2009) Artificial neural network-polar coordinated fuzzy controller based maximum power point tracking control under partially shaded conditions. IET Renew Power Gener 3(2):239–253
32. Karlis AD, Kottas TL, Boutalis YS (2007) A novel maximum power point tracking method for PV systems using fuzzy cognitive networks (FCN). Electr Power Syst Res 77:315–327
33. Bai Q (2010) Analysis of particle swarm optimization algorithm. Comput Inf Sci 3(1):180–184
34. Mostafa HE, El-Sharkawy MA, Emary AA, Yassin K (2012) Design and allocation of power system stabilizers using the particle swarm optimization technique for an interconnected power system. Electr Power Energy Syst 34:57–65
35. Ishaque K, Salam Z, Taheri H, Shamsudin A (2011) Maximum power point tracking for PV system under partial shading condition via particle swarm optimization. In: IEEE applied power electronics colloquium (IAPEC), pp 5–9
36. Krose B, van der Smagt P (1996) An introduction to neural network, pp 1–135
37. Eslami M, Shareef H, Mohamed A, Khajehzadeh M (2012) An efficient particle swarm optimization technique with chaotic sequence for optimal tuning and placement of PSS in power systems. Electr Power Energy Syst 43:1467–1478
38. Chiou JS, Tsai SH, Liu MT (2012) A PSO-based adaptive fuzzy PID-controllers. Simul Model Pract Theory 26:49–59
39. Alonso-García MC, Ruiz JM, Herrmann W (2006) Computer simulation of shading effects in photovoltaic arrays. Renew Energy 31:1986–1993
40. Hengsritawat V, Tayjasanant T, Nimpitiwan N (2012) Optimal sizing of photovoltaic distributed generators in a distribution system with consideration of solar radiation and harmonic distortion. Electr Power Energy Syst 39:36–47
41. Ramabadran R, Mathur B (2009) MATLAB based modelling and performance study of series connected SPVA under partial shaded conditions. J Sustain Dev 2(3):85–94
42. Patel H, Agarwal V (2008) MATLAB-based modeling to study the effects of partial shading on PV array characteristics. IEEE Trans Energy Convers 23(1):302–310
43. Ishaque K, Salam Z, Shamsudin A, Amjad M (2012) A direct control based maximum power point tracking method for photovoltaic system under partial shading conditions using particle swarm optimization algorithm. Appl Energy 99:414–422
44. Di Piazza MC, Vitale G (2010) Photovoltaic field emulation including dynamic and partial shadow conditions. Appl Energy 87:814–823
45. Wang Y, Lin X, Kim Y, Chang N, Pedram M (2012) Enhancing efficiency and robustness of a photovoltaic power system under partial shading. In: 13th international symposium on quality electronic design, pp 592–600
46. Miyatake M, Veerachary M, Toriumi F, Fuji N, Ko HY (2011) Maximum power point tracking of multiple photovoltaic arrays: a PSO approach. IEEE Trans Aerosp Electron Syst 47 (1):367–380
47. Chowdhury SR, Saha H (2010) Maximum power point tracking of partially shaded solar photovoltaic arrays. Solar Energy Mater Solar Cells 94:1441–1447

48. Ngan MS, Tan CW (2011) Multiple peaks tracking algorithm using particle swarm optimization incorporated with artificial neural network. In: World Academy of Science, Engineering and Technology (WASET), Bali Indonesia, pp 379–385
49. Sedighizadeh D, Masehian E (2009) Particle swarm optimization methods, taxonomy and applications. Int J Comput Theory Eng 1(5):1793–8201
50. Kornelakis A, Marinakis Y (2010) Contribution for optimal sizing of grid-connected PV-systems using PSO. Renew Energy 35(6):1333–1341
51. Ishaque K, Salam Z, Amjad M, Mekhilef S (2012) An improved particle swarm optimization (PSO)—based MPPT for PV with reduced steady-state oscillation. IEEE Trans Power Electron 27(8):3627–3638
52. Kalogirou SA (2001) Artificial neural networks in renewable energy systems applications: a review. Renew Sustain Energy Rev 5:373–401
53. Matallanas E, Castillo-Cagigal M, Gutiérrez A, Monasterio-Huelin F, Caamaño-Martín E, Masa D, Jiménez-Leube J (2012) Neural network controller for active demand-side management with PV energy in the residential sector. Appl Energy 91:90–97
54. Wijnings P (2011) Training neural networks with particle swarm optimization, pp 1–60
55. Haykin S Feedforward neural network: an introduction, pp 1–16
56. Chouder A, Silvestre S, Sadaoui N, Rahmani L (2012) Modeling and simulation of grid connected PV system based on the evaluation of main PV module parameters. Simul Model Practice Theory 20:46–58
57. Papaioannou IT, Purvins A (2012) Mathematical and graphical approach for maximum power point modelling. Appl Energy 91:59–66

Empirical-Based Approach for Prediction of Global Irradiance and Energy for Solar Photovoltaic Systems

Sivasankari Sundaram and J.S.C. Babu

Abstract Accuracy in prediction of global horizontal irradiance is vitally important for photovoltaic energy prediction, its installation and pre-sizing studies. A change in the solar radiation directly impacts the electricity production and in turn, the plant economics. Hence employing a model possessing improved prediction accuracy significantly affects the photovoltaic energy prediction. Furthermore, monthly mean data is required for prediction of long-term performance of solar photovoltaic systems, making the same to be concentrated for the present contribution. The available models for prediction of irradiance and energy unlike physical and statistical models depend on input parameters whose availability, assumption and determination is difficult. This finally creates complexity in predicting the desired response. Hence empirical models are chosen preferable over physical and statistical-based models. Empirical models correlate only the available input atmospheric parameters affecting solar irradiance and energy, thereby reducing the complexity experienced by physical and statistical models. Yet, the reliability or accuracy of model varies with location. The reliability of an empirical model depends on the incorporation of input's and data set (training set) for its formulation. Thus the consideration of significant input factors lies to be a persistently prevailing challenge, driving the need for an improved prediction model delivering irradiance and energy. In this chapter, an empirical model is proposed for prediction of irradiance and energy. The incorporated input factors for the formulation of energy prediction model is emphasized by performance and exergy analysis of solar photovoltaic systems. The proposed model hence combines the thermal and electrical aspects of photovoltaic systems gaining reliability and limiting the dependence towards real-time measured input factors.

Keywords Global solar irradiance · Empirical model · Energy prediction model · Performance analysis · Exergy analysis · Percentage error

S. Sundaram (✉) · J.S.C. Babu
Department of Chemical Engineering, National Institute of Technology Tiruchirappalli, Tiruchirappalli 620015, Tamil Nadu, India
e-mail: sivasankari66@gmail.com

M.R. Islam et al. (eds.), *Advances in Solar Photovoltaic Power Plants*,
Green Energy and Technology, DOI 10.1007/978-3-662-50521-2_6

1 Introduction

The advantages of solar with respect to its availability and environmental friendly nature cause increasing penetration of the same into electrical grid. But despite the advantages, the inherent nature of solar irradiation causes intermittency in the production of energy generated by a solar photovoltaic system posing potential challenges for power system operation or grid operators. Moreover, the main task of the power system is to ensure a reliable state-of-the-art supply-on-demand system. Thus reliability can be achieved only if the deliverable amount of energy from a photovoltaic system to the grid is known. This can be reinforced through predictive technologies or models employed for the prediction of energy generated by a solar power plant over a time-based horizon. The performance ratio or plant capacity factor of a solar photovoltaic power plant is always evaluated over a long-term horizon. Also, a performance comparison among solar PV plants is always made based on the annual long term (monthly average daily) monitored or evaluated response. Hence long-term prediction over an annual horizon is practically required for moving towards smarter grid or making reliability a reality.

The necessity of solar resource assessment for prediction of energy generated by a typical solar photovoltaic distribution system is made clear. This necessity creates a dependence on theoretical modelling of global solar irradiance and energy generation. There currently occur three modelling aspects for prediction of global irradiance and energy. These include physical or mathematical models, statistical models and empirical models. Physical or parameterized models of kind included for prediction of irradiance and energy were reported by researchers as seen in [1–8]. The physics-based models for irradiance rely on the physics of interaction between the extraterrestrial irradiance and constituents of atmosphere. The disadvantage of physics-based models for irradiance and energy include complex structure and dependence of it towards more number of input parameters such as station pressure, temperature, Rayleigh scattering, ozone reduced path, perceptible water, aerosol scattering albedo, aerosol optical thickness, temperature coefficient of modules, solar irradiance at plane of array and PV characteristic parameters. Hence models based on statistical approach were also reported to exist for prediction of irradiance. Statistical-based models employing time series based modelling strategies such as moving average, support vector regression and auto regression integrated moving average (ARIMA) [9, 10] are commonly employed for minutely or hourly based forecasting. These techniques are too complex to be employed for monthly average-based prediction. This further resulted in empirical-based approach for prediction of solar potential in a desired location of interest. Empirical models correlate the desired response (global horizontal irradiance and energy) to the available and accessible inputs. This reduces the dependence of the model towards more number of input parameters (as in case of physical models). Furthermore, the empirical constants are derived employing simple regression-based methodology limiting the complexity experienced with statistical models.

Though empirical models possess advantages as compared to physical and statistical-based approach, there remain certain research investigations among the prevailing empirical structures. These include the opportunity for improving accuracy by incorporation of significant input factors, which are absent in the existing models, proper validation check and limiting its dependency towards real-time measurable input parameters. This drives or motivates towards the formulation of an empirical model addressing the challenges as stated above. Before stepping into the formulation of an improved empirical model, the existing empirical models for prediction of irradiance and energy have to be known. There exist two basic classifications of empirical model for irradiance based on the incorporation of input parameters such as single parametric model and multi-parametric or hybrid models. Whereas, only a few polynomial regressive-based empirical models are found to be reported for energy prediction [11–13]. Hence, this chapter contributes to the formulation of empirical model for prediction of global irradiance and energy generation for solar photovoltaic system. The location of interest for the formulation of proposed empirical model was selected based on the accessibility of testing data set required for its validation. Moreover, the proposed model can further be used for other locations on altering the empirical constants embedded in the model. A schematic showing the classification of empirical model for irradiance and energy prediction is presented in Fig. 1.

1.1 Single Parametric Models for Prediction of Solar Irradiance

The single parametric models include only a single significant factor affecting irradiance which is reported to be practically measured. The commonly existing single parametric models include the sunshine-based and ambient temperature-based

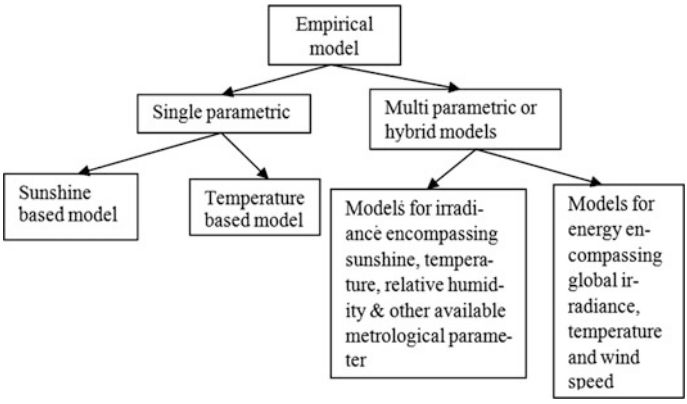

Fig. 1 Classification of empirical irradiance and energy prediction models

model. The section below describes the single parametric sunshine and temperature-based model.

1.1.1 Single Parametric Sunshine-Based Model

The sunshine-based model was first introduced by Angstrom in 1940 [14], who suggested a linear relationship between the clearness index (ratio of global horizontal irradiance to the extraterrestrial global irradiance) and the relative sunshine hour (ratio of sunshine hour to maximum possible bright sunshine hour). This was further modified by Presscott [15] to deliver Angstrom-Presscott model which supported the addition of an empirical constant to the Angstrom model. The equation of form reported by Presscott [15] is given by

$$\frac{H}{H_0} = a + b\left(\frac{S}{S_0}\right) \tag{1}$$

where H represents the monthly average daily global irradiance, H_0 represents the extraterrestrial global irradiance; S represents the monthly average daily sunshine hour and S_0 represents the maximum possible bright sunshine hour.

Having Angstrom-Prescott model as the basis several other researchers developed linear order-based sunshine model with the change in empirical constants 'a' and 'b' for certain locations of US, Zimbabwe and India [16–20]. In 1984, Benson et al. [21] proposed a seasonal specific linear order-based model for 46 stations, which experiences improved prediction accuracy than yearly based models as described in [16, 17].

Ogelmann in 1984 [22] proposed a yearly based monthly average daily quadratic model for Andana and Ankara in Turkey with a training data set of 3 years. The prediction agreement was found better than the linear based sunshine model. This occurred due to the addition of quadratic order based factor to the linear order, increasing accuracy. The regression coefficient representing closeness between the response and the input is high for a quadratic order than for a linear order factor. The basic form of quadratic order based model [22] is given by

$$\frac{H}{H_0} = a + b\left(\frac{S}{S_0}\right) + c\left(\frac{S}{S_0}\right)^2 \tag{2}$$

Furthermore, Samuel in 1991 [23] proposed a cubic model for a location with latitude 5.55°N. The MPE reflecting accuracy was reported to be 2.6 %. Thus a cubic order based empirical model would deliver better closeness between the predicted and actual value of irradiance than a quadratic and linear order. The basic form of cubic order-based model [23] is given by

$$\frac{H}{H_0} = a + b\left(\frac{S}{S_0}\right) + c\left(\frac{S}{S_0}\right)^2 + d\left(\frac{S}{S_0}\right)^3 \tag{3}$$

Ampratwum et al. in 1999 [24] compared models of linear, quadratic and logarithmic sunshine-based models. The author finally reported the usage of quadratic and logarithmic sunshine-based models for prediction of global irradiance. Further, a monthly specific quadratic order-based model for prediction of global irradiance in Sudan was proposed as in [25]. A least MPE of 0.36 % on training was observed. This occurs due to the nature of reported empirical constants, being monthly specific. Haydar et al. in 2006 [26] also experienced highly acceptable accuracy for the cubic model than the developed linear and quadratic-based sunshine models for certain provinces in Anatolia such as Afyon, Cankiri and Corum. A non-linear curve fitting model for prediction of monthly average daily global irradiance for Jeddah was reported in [27]. An acceptable prediction performance was observed due to the fact of deriving the empirical constants through curve fitting methodology than regression-based method [27]. A similar curve fitting-based methodology for gaining improved prediction accuracy, in formulation of empirical model was followed by Wanxiang et al. [28].

Finally summarizing, the single parametric-based sunshine model, improved accuracy would be rendered on employing monthly specific cubic models or curve fitting-based methodology for obtaining the empirical constants.

1.1.2 Single Parametric-Based Temperature Model

As already cited, ambient temperature also occur as a significant single parametric factor affecting global irradiance. This section cites the reported temperature-based global irradiance model with its performance comparison among sunshine-based model.

Similar to [15] which describes the basic form of sunshine model, an attempt was made in 1982 by Hargreaves and Sammi [29] to report a basic form of temperature-based model. The model reported by Hargreaves and Sammi [29] is given by Eq. (4) as follows:

$$\frac{H}{H_0} = a + b(T_{\max} - T_{\min})^{0.5} \tag{4}$$

Further modifications to the basic form of temperature model as reported in [29] model was described by few researchers as seen in literatures [30–36]. Though temperature-based models exist for prediction of global irradiance, it lies less accurate on comparison to sunshine-based models [37, 38]. Ultimately, a factor of temperature which is proven to affect the solar radiation cannot be neglected though. Hence, a hybrid model would form a better solution encompassing factors implicitly and explicitly affecting global horizontal irradiance.

1.2 Multi-Parametric or Hybrid Models for Prediction of Solar Irradiance

The hybrid parametric model evolved as the methodology for experiencing further improved accuracy than the reported sunshine and temperature-based models. The available input factors which are proved to affect the intensity of solar radiation for a desired location are considered for its prediction. The models in line with the consideration of available input factors are seen in literatures [38–43]. The reported models constitute metrological input factors such as ambient temperature (T_a), soil temperature (T_{so}), relative humidity (RH), sine of declination angle (δ), mean sea level, ambient temperature, water vapour pressure (P_v), and mean cloud cover (C_m). The basic form of the existing hybrid models as reported by cited researchers include

$$\frac{H}{H_0} = a\left((\Delta T)^b\left(1 + cP + dP^2\right)\right) \quad [39] \tag{5}$$

$$H = 4.591 - 0.1135H_0 + 2.522\left(\frac{S}{S_0}\right) + 6.1589(\sin\delta) - 0.0124(\mathrm{RH}) + 0.0187(T_{so}) - 0.052(T_a) \quad [40] \tag{6}$$

$$\frac{H}{H_0} = a + b\left(\frac{S}{S_0}\right) + cT + dV + e\mathrm{RH} + fP_v \quad [41] \tag{7}$$

$$\frac{H}{H_0} = a\ln(T_{a(\max)} - T_{a(\min)}) + b\left(\frac{S}{S_0}\right)^c + d \quad [42] \tag{8}$$

The regression coefficient marking the closeness between the desired irradiance and the input factor increases on addition of input factors affecting irradiance [38–43]. Furthermore, an exhaustive review as seen in [44] for empirical models on solar radiation prediction, reported non-linear model to be the best predictor on comparison with linear, ANN and fuzzy (complex methods) with least MPE of 0.11 %, RMSE of 0.0181 % and MBE of 0.0001 %.

Summarizing the facts delivered by hybrid model, the prediction accuracy is proved to increase on addition of significant available factors towards irradiance. The hybrid model can necessarily include the incorporation of proved significant factors of sunshine and ambient temperature towards global irradiance.

The hybrid models perform acceptably well in comparison with the single parametric model. But the prevailing challenge occurring in the present multi-parametric model is its dependence towards more number of real-time monitored input factors. These could be unavailable for stations other than its formulation or training. More simply, its reliability varies with location. Furthermore, the cost incurred in measuring the input model parameters aiding prediction of global irradiance (response) should be less than measuring the response directly. Hence

formulating a model for prediction of irradiance, whose input factor limits its dependence towards realistic measurement, is required. Similar is the case with the prediction of energy generation for a photovoltaic system.

1.3 Multi-parametric Model for Prediction of Energy Generation

The multi-parametric model for prediction of energy delivered by a typical solar photovoltaic system is given by models of kind [11–13] and [45]. These include either of the input parameters such as global irradiance, ambient temperature, module temperature and wind speed. The basic form of the reported models is given as follows:

$$P_{\mathrm{ac}} = aH + bH^2 + c\ \ln(H) \quad [11] \tag{9}$$

$$P_{\mathrm{ac}} = aH + b\left(\frac{H}{T_{\mathrm{max}}}\right)^2 + cT_{\mathrm{max}} \quad [12] \tag{10}$$

$$P_{\mathrm{ac}} = H(a + bH + cT_{\mathrm{a}} + d(WS)) \quad [13] \tag{11}$$

$$\mathrm{P_{ac}} = a + bHT_{\mathrm{m}} + cH + dH^2 \quad [45] \tag{12}$$

The performance of the prevailing models marked by absolute mean relative error varied from a minimum of 2 % to a maximum of 17 %, for the models reported as in Eqs. (9)–(12) on its application to a typical case study [13]. The prediction accuracy of the model depends on the nature of significant factors incorporated for its formulation as already cited. The generation of heat loss on power generation from a photovoltaic cell is well evident from the nature of photovoltaic effect [46] and reported research investigations [47, 48]. This significantly affects the yield or the energy generation. Hence the empirical model to be formulated for energy generation should account for the heat loss dissipated on power generation. This chapter further contributes to the evaluation of improved model for prediction of energy, generated by a typical PV system.

2 Formulation of Multi-parametric Global Irradiance Prediction Model

The formulation of an empirical multi-parametric model for prediction of global irradiance and energy involves the following sequential schematic as represented in Fig. 2. As seen, the formulation is assisted with the measured response (be it either

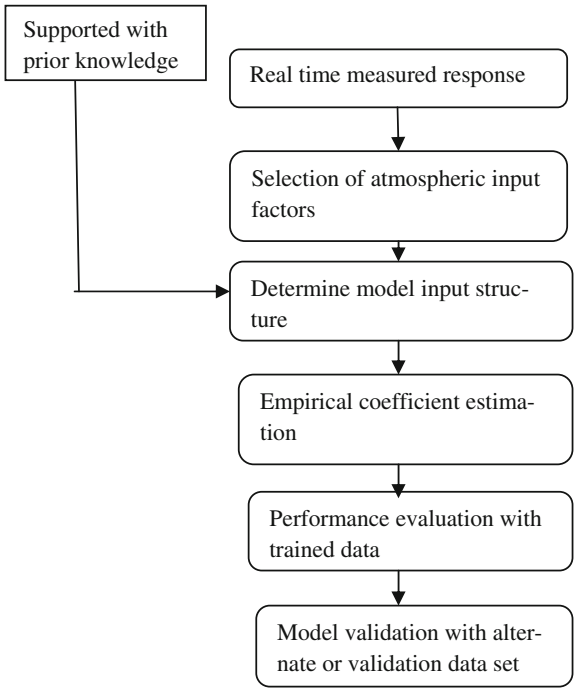

Fig. 2 Methodology for empirical model formulation

irradiance or energy) during the training period. The significant atmospheric factors affecting the spectral properties of solar irradiance or energy are related through justified or proven facts (requiring prior knowledge). The proposed model is then evaluated for its coefficients employing simpler regression methodology for a desired location, making the same to be applicable on reality.

The measured global irradiance (considering solar irradiance as the first response) for the formulation of the prediction model is inherited from the solar radiation database provided by RETscreen plus [49]. RETscreen plus provides the complied monthly average daily global irradiation data from NASA and WRDC. As the accuracy of the proposed model depends on the accuracy of the training data, a compiled input data set is preferred. The training period occurs for the duration of 1961–1990 where the monthly average daily global irradiance input set is available. The desired locations were selected based on the availability or accessibility of the validation data set. Furthermore, merely basic sunshine-based models occur for certain locations of India such as Mumbai, Kolkata, Jodhpur, Kodaikanal and Chennai, where the need for improved prediction accuracy lies important. The formulation of multi-parametric model which is believed to exhibit improved accuracy remains untested. Most particularly the state of Tamil Nadu shares about 35 % of its installed capacity from renewable source of energy [50]. The state also experiences around 300 sunny days which makes it to rely on solar power for supporting the created demand. As solar installations increase, the intermittency of

energy generation increases, ultimately creating a need for reliability. This further can be made a reality, on existence of predictive technologies. Thus certain locations of Tamil Nadu were considered in the present chapter for training and validation.

2.1 Input Factors Considered Affecting Global Solar Irradiance

The atmospheric input factors affecting the clearness index (ratio of measured global irradiance to extraterrestrial global irradiance) includes the relative sunshine hour, temperature ratio and the air mass at solar noon which are briefly described as follows.

2.1.1 Relative Sunshine Hour

The sunshine duration is defined as the length of time during which the ground is irradiated with direct solar irradiance [51]. The duration during which the ground is irradiated or the amount of daylight implicitly marks the intensity of global irradiance received by it. This duration is recommended to rely on the measurement from the sunshine recorder as suggested by several researchers, who reported sunshine-based empirical models for prediction of global irradiance. Instead of relying on real-time measurement, it can be suggested to limit the real-time dependency by theoretical assessment of sunshine hour. Thus, the equation reported as in [52] is suggested for calculation of sunshine hour duration. This reduces one of the prevailing challenges of empirical-based models. Equation (13) gives the theoretical estimation of sunshine hour [52]

$$S = \frac{h}{360} \text{arc cos}(\tan(L)\tan(23.5)\cos\left(\frac{360D_n}{365.25}\right) \tag{13}$$

where h represents hours per day; L corresponds to the latitude of the monitored site; the daily sunshine is averaged over a month to obtain monthly average daily sunshine hour (S). The maximum possible sunshine hour can be calculated by Eq. (14) as

$$S_0 = \frac{2}{15}\omega_s \tag{14}$$

where ω_s represents the hour angle in degrees. The hour angle is defined as the angular displacement of sun towards the east or west of the local meridian due to rotation of the earth on its axis at 15°/h. It is mathematically derived from declination and latitudinal angle as seen in Eq. (15).

$$\omega_s = \cos^{-1}(-\tan\ \delta\ \tan\ L) \tag{15}$$

The declination angle represented by δ is defined as the angular position of the sun with respect to the equatorial plane. This varies with the value of $\pm 23.45°$. The declination angle can be found from the approximate equation given by Cooper [53]

$$\delta = 23.45 \sin\left(360 \frac{(284 + D_n)}{365.25}\right) \tag{16}$$

The higher the sunshine duration, the more is the intensity of global irradiance received by a horizontal surface. The direct dependence of global irradiance towards sunshine hour or clearness index towards relative sunshine hour is further justified by Rahman [54]. Figure 3 shows the annual average values of clearness index for various locations such as Buenos Aries, Penang, New Delhi, Ibadan, Venezia, El Fasher, Port Sudan, Bhavnagar, Alicante, Lucknow, Abu Namma and certain other regions.

Figure 3 represents the closeness or the significance between the clearness index and relative sunshine hour, reflected through the value of regression coefficient between the same. Higher the value of regression coefficient, higher is the significance of the input factor with respect to the desired response. As the percentage contribution of relative sunshine hour towards clearness index is high as 82.9 %, the same is termed significant.

2.1.2 Temperature Ratio

The fact of sunshine duration implicitly alters the temperature of the ambient, which is incident to the radiation from the sun. This phenomenon occurs naturally and is self-evident [55]. Thus inclusion of ambient temperature towards global horizontal irradiance serves justified. Furthermore, the latitude of the location influences the amount of solar radiation. However, the pattern of temperature distribution across

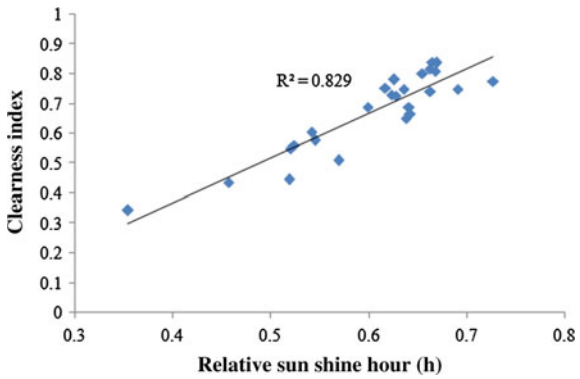

Fig. 3 Variation of clearness index with respect to relative sunshine hour as reported in [54]

the globe is also latitudinal. Thus incorporation of ambient temperature indirectly marks the inclusion of latitudinal variation across the location, making the proposed model more significant.

Besides, the consideration of ambient temperature the physical reason behind its occurrence or source of origin should also be incorporated. The source of origin is none other than the black body or the sun. Hence consideration of sun's temperature in addition to the ambient makes an empirical model physically significant. The physical significance of sun's temperature towards the intensity of radiant flux is justified by physical laws of radiation defined by Stefan-Boltzmann [56] and Planck [57].

As a ratio of measured global irradiance (H) to the maximum extraterrestrial irradiance (H_0) is found to vary linearly with a ratio of sunshine hour to maximum possible sunshine hour, the same (H/H_0) is considered to vary with the ratio of minimum temperature (ambient temperature) to the maximum temperature (sun's temperature).

2.1.3 Air Mass at Solar Noon

The solar irradiance passes through an atmospheric column of air surrounding the earth. This varies depending on the apparent position of the sun in the sky [58]. The path length of the column of air is minimum when the sun is exactly overhead (at zenith position) or at solar noon. For the instant other than solar noon, the rays have to pass through a long atmospheric air column preferably termed as optical air mass. Hence the distance between the earth and the sun decreases at solar noon increasing the magnitude of solar radiation received over the ground. Air mass is often approximated for a constant density atmosphere and is given by

$$\text{AM (at solar noon)} = \frac{1}{\cos Z}; \tag{17}$$

Z is the Zenith angle at solar noon.

$Z = 90 - \alpha$. Where $\alpha = 90 + \delta - \phi$ for Northern Hemisphere, as India lies in the Northern hemisphere.

δ, Φ and α are the declination angle, latitudinal angle and altitude angle of the site respectively.

Hence the proposed model for prediction of monthly average daily global irradiance includes the input model parameters such as relative sunshine hour, temperature ratio and air mass at solar noon. The significance of the incorporated input factor is justified by the value of regression coefficient (R^2) generated between the same and the desired global horizontal irradiance. Figure 4a–c shows or justifies the significance of the incorporated input parameters such as sunshine hour, temperature ratio and air mass towards global irradiance respectively. The value of R^2 varied from 0.71 to 0.89 marking significant contribution of input factors such as

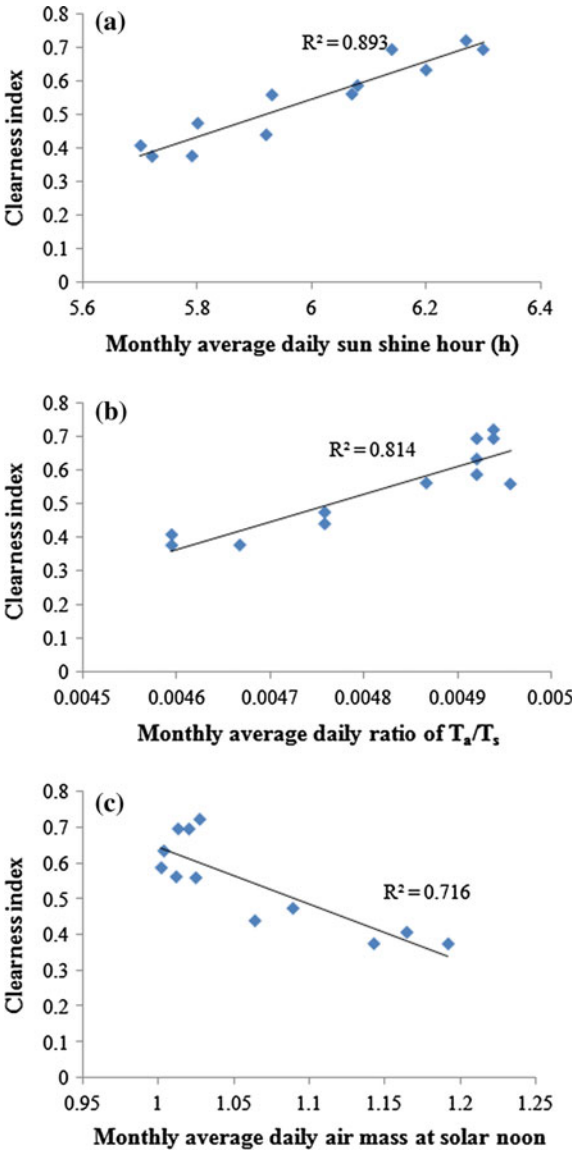

Fig. 4 **a–c** Significance of considered input factor sunshine hour, temperature ratio and air mass towards clearness index (response)

sunshine hour, temperature ratio and air mass at solar noon in prediction of global irradiance.

Thus, the section has briefly described the factors considered for modelling global horizontal irradiance with its justification towards the same. The next section follows, relating the input parameters to the response leading to the formulation of a modified multi-parametric model for global irradiance.

3 Modified Multi-parametric Empirical Model

The next step under the process of formulating an empirical model is to relate the considered input parameters towards prediction of desired response. Hence summarizing the observed relationship between the global horizontal irradiance and the input parameters, a modified multi-parametric model is formulated. The intensity of global horizontal irradiance increases for increase in sunshine hour, ambient temperature and air mass at solar noon. Hence, the form as proposed in Eq. (18) is rightly employed for the prediction of monthly average daily global irradiance.

$$\frac{H}{H_0} = a + b\left(\frac{S}{S_0}\right) + c\left(\frac{S}{S_0}\right)^2 + d\left(\frac{S}{S_0}\right)^3 + e\left(\frac{T_a}{T_s}\right) + f(\mathrm{AM}) \tag{18}$$

where *a, b, c, d, e* and *f* represents the empirical constants pertaining to a location of interest for which the model is formulated.

The proposed model incorporates explicitly the effect of sunshine, ambient temperature and air mass at solar noon. These factors implicitly mark the account of variation in latitude of the location, declination angle, altitude angle and hour angle. Thus the incorporation of more number of input parameters (multi-parametric model) either implicitly or explicitly refers to the strength of the model. The addition of significant factors also makes the model to exhibit improved prediction accuracy.

3.1 Case Studies for the Prediction of Global Horizontal Irradiance

The case studies for the applicability of the proposed irradiance model falls where the validation data set encompassing the measured global irradiance was accessible or made available. Hence the locations of Madurai/Sivagangai and Chennai were selected as case study for testing the prediction accuracy of the modified multi-parametric model. The validation data set for Madurai for which the model was formulated or trained was not available appropriately. Hence the nearest monitoring station of Sivagangai was considered for testing the model, as its validation data set was available for the duration of (2011–2013). The validation data set for Chennai was obtained from [59], who reported a basic sunshine-based model for Chennai. The validation data set for Chennai ranges from a duration of 1980–2009. The training data set for the region of Madurai is tabulated in Table 1.

The empirical constants were formulated from the training data set of model parameters covering monthly average daily data ranging for duration of 1961–1990. The least square regression-based methodology [60] was adopted for evaluation of empirical constants. The empirical constants of the proposed model for the locations of Madurai/Sivagangai are tabulated in Table 2.

Table 1 Training data set of proposed model parameters (comprising the measured and evaluated input parameters) for Madurai/Sivagangai during (1961–1990)

Training period	H/H_0	S/S_0	T_a/T_s	AM
January	0.408485	0.4981	0.004594	1.1647
February	0.475178	0.4962	0.004758	1.089
March	0.559899	0.4957	0.004957	1.0244
April	0.587719	0.4966	0.004921	1.0015
May	0.69554	0.4927	0.004939	1.0127
June	0.722052	0.4992	0.004939	1.027
July	0.695404	0.5015	0.004921	1.0199
August	0.634385	0.5035	0.004921	1.0032
September	0.562624	0.504	0.004867	1.0114
October	0.440609	0.5037	0.004758	1.0637
November	0.377241	0.5022	0.004667	1.1428
December	0.376478	0.5007	0.004594	1.1922

Table 2 Empirical constants for the proposed model for Madurai/Sivagangai

Training period	Empirical constants for Madurai/Sivagangai					
	a	*b*	*c*	*d*	*e*	*f*
January	0.3284	−0.7469	0.1224	0.6445	1.043	0.2896
February	1.6781	−1.4378	1.3805	−0.0744	−2.1012	−0.744
March	10.8872	−13.4546	−8.5434	−1.5638	−8.9353	−1.2921
April	0.6676	−0.6244	−0.1145	0.1751	1.1518	0.2310
May	−0.8909	1.2945	2.8468	−3.0847	4.4550	0.5969
June	−11.0506	5.7176	6.4529	−12.3908	−3.2989	8.6333
July	0.5529	−0.5874	0.5659	0.6156	1.1353	0.207
August	−0.6611	−0.0010	0.8371	−1.8810	−1.6701	1.3361
September	1.3152	0.2649	−0.9630	−0.8408	−0.0895	−0.5272
October	0.6667	1.0000	−0.5000	0.8333	9.07e−11	−0.6667
November	0.8113	0.2286	0.0053	0.5319	−1.3049	−0.5357
December	−0.1683	0.3910	0.0153	−0.2364	0.1970	0.3136

Similarly, the training data set for Chennai were employed in determining the empirical constants of the modified multi-parametric model. The training data set for Chennai is tabulated in Table 3 and the associated empirical constants are made available in Table 4.

The basic Angstrom-based sunshine models such as linear, quadratic and cubic were also formulated for the locations of Madurai/Sivagangai and Chennai to compare the performance accuracy of the same and the proposed multi-parametric model. The proposed Angstrom-based constants of linear, quadratic and cubic models for Madurai/Sivagangai and Chennai are tabulated in Tables 5 and 6 respectively.

Table 3 Training data set of proposed model parameters (comprising the measured and evaluated input parameters) for Chennai during (1961–1990)

Training period	H/H_0	S/S_0	T_a/T_s	AM
January	0.458509	0.4975	0.004576	1.2054
February	0.541023	0.4948	0.004812	1.1167
March	0.607537	0.4944	0.005302	1.038
April	0.683374	0.4955	0.005666	1.0031
May	0.767807	0.492	0.006083	1.0057
June	0.779793	0.4991	0.005902	1.0157
July	0.730715	0.502	0.005684	1.0105
August	0.659156	0.5046	0.005484	1.0013
September	0.584128	0.5054	0.00543	1.0202
October	0.457592	0.5045	0.005085	1.0864
November	0.394036	0.503	0.004721	1.1798
December	0.396513	0.5008	0.004576	1.2374

Table 4 Empirical constants for the proposed model for Chennai

Training period	Empirical constants for Chennai					
	a	*b*	*c*	*d*	*e*	*f*
January	−0.226	1.364	0.997	−0.035	−1.047	−0.192
February	0.841	−0.681	−0.180	−0.459	0.596	0.119
March	2.810	1.510	−1.070	−2.900	2.490	−2.270
April	0.080	−1.120	0.200	−1.600	1.260	1.290
May	1.560	−1.070	−0.980	0.140	−1.010	−0.040
June	1.130	−0.400	0.630	0.590	−0.270	−0.370
July	−0.080	−0.990	0.490	1.310	0.360	1.000
August	1.340	−0.890	0.040	−0.530	−0.320	−0.170
September	0.310	0.530	0.430	−0.790	−0.230	−0.010
October	2.550	−0.100	0.510	2.280	0.410	−2.280
November	0.100	1.391	0.728	−0.154	−0.037	−0.4842
December	0.126	−0.006	−0.510	2.990	6.9290	−0.0080

The proposed models are compared for suggesting the highly acceptable model suited for prediction of monthly average daily global irradiance tested for locations of Madurai/Sivagangai and Chennai.

3.2 Performance Study of Irradiance Prediction Models

There exist certain performance indicators for prediction models indicating its prediction accuracy. These include mean bias error (MBE), root mean square error

(RMSE), mean percentage error (MPE), mean absolute bias error (MABE) and mean absolute percentage error (MAPE). The mean bias error gives accurate information on the long-term performance of the model. This allows term by term comparison of actual deviation between the predicted and actual response [25]. A low value of MBE is always desired for better accuracy of the proposed model. A positive value of MBE shows an overestimate, while a negative value an underestimate by the model. The RMSE test gives the information on the short-term performance of the proposed model [61]. The value of RMSE is always positive. The following equations deliver the statistical performance indicators for a prediction model.

$$\mathrm{MBE} = \left(\frac{1}{N}\right) \sum \left(H_{\mathrm{pred}} - H_{\mathrm{meas}}\right) \tag{19}$$

$$\mathrm{RMSE} = \left(\left(\frac{1}{N}\right) \sum \left(H_{\mathrm{pred}} - H_{\mathrm{meas}}\right)^2\right)^{0.5} \tag{20}$$

$$\mathrm{MPE} = \left(\frac{1}{N}\right) \sum \left(\left(H_{\mathrm{pred}} - H_{\mathrm{meas}}\right)/H_{\mathrm{meas}}\right) \times 100 \tag{21}$$

On reality, prediction models usually possess low values of MBE, RMSE and MPE indicating acceptable prediction limits. The maximum deviation between the actual and the predicted response values (mean percentage error) should lie between ± 10 % for a model to satisfy predictive nature. If the mean absolute percentage error (MAPE) is ≤ 10 %, then the model has higher prediction accuracy and if $10 \leq \mathrm{MAPE} \leq 20$ means good prediction. MPE ≥ 20 indicates inaccurate prediction [62].

The values of statistical indicators are evaluated during validation and are compared for the suggested multi-parametric and sunshine-based models. The evaluated statistical indicators are compared for Madurai/Sivagangai during validation (2011–2013). The performance comparison is tabulated in Table 7.

The modified multi-parametric model encompassing significant factors proves to be better accurate and acceptable than basic sunshine based models for prediction of monthly average daily global horizontal irradiance for Madurai/Sivagangai. This is justified from Table 7, where a least MAPE of 2.29 % occurs for the modified multi-parametric model. A similar comparison of percentage error or deviation is made among the modified multi-parametric model and the existing multi-parametric models for the case of Sivagangai during training or model formulation. Selected multi-parametric models whose input parameters were found available was considered. The models which fall in this line were reported by literatures as seen in [63–65]. A performance comparison of deviation among the actual and predicted values of global irradiance obtained through the existing and the proposed multi-parametric model is made for the location of Sivagangai and is tabulated in Table 8.

Table 5 Sunshine-based empirical constants for Madurai/Sivagangai

Training period	Linear model		Quadratic model			Cubic model			
	a	*b*	*a*	*b*	*c*	*a*	*b*	*c*	*d*
January	−2.90	6.65	−3e−3	−6.3e−3	1.66	1.4e−4	1.88	−3.79	3.27
February	0.67	−0.39	2.28	−3.09	−1.09	1.00	−3.08	2.36	3.44
March	−0.57	2.29	−0.79	2.47	0.52	−3.61	6.70	2.04	2.87
April	−1.63	4.48	0.47	−0.35	1.14	0.02	0.03	1.88	0.71
May	8.80e−3	1.43	6.6e−3	1.02	1.02	0.08	1.34	−1.72	3.08
June	−16.75	35	−1.09	3.09	1.09	−3.12	5.12	3.12	4.12
July	−8.91	19.15	−0.76	2.20	1.40	0.69	0.15	0.03	−0.68
August	−0.20	1.66	0.14	0.82	0.27	1.02	−0.53	−0.17	−0.62
September	2.12	−3.1	1.34	6.94e−3	−3.10	1.00	−1.50	1.00	0.50
October	−0.67	2.20	0.59	2.11	−0.11	3.11	−4.40	−0.14	−3.27
November	7.65	−14.49	0.25	−0.5	1.5	0.06	−0.25	1.64	0.19
December	−13.46	27.65	−0.03	0.56	0.52	0.001	0.50	0.49	−0.09

Table 6 Sunshine based empirical constants for Chennai

Training period	Linear model		Quadratic model			Cubic model			
	a	*b*	*a*	*b*	*c*	*a*	*b*	*c*	*d*
January	0.16	0.6	0.608	−0.400	0.200	0.055	0.446	0.58	0.29
February	0.7825	−0.488	2.560	−4.450	0.750	0.754	−0.21	−0.77	0.66
March	1.427	−1.658	1.107	−0.612	−0.806	0.757	−0.15	0.38	−1.41
April	0.079	1.2197	0.449	0.589	−0.233	0.87	−1.30	−0.71	5.21
May	0.1883	1.1778	0.951	0.515	−1.806	−0.01	1.57	0.76	−1.53
June	1.901	−2.246	−5.6e−3	1.63	−0.12	0.98	−0.28	−0.29	0.04
July	−0.7	2.85	0.96	−0.50	0.072	−1.2	4.6	−1.0	−1.0
August	−0.1115	1.5274	3.854	−4.208	−4.208	0.57	−0.27	0.29	1.13
September	0.5123	0.1419	1.286	−0.754	−1.254	0.50	0.277	−0.14	−0.14
October	1.4740	−2.014	0.865	−1.632	1.632	−0.28	1.28	−1.28	3.28
November	1.4000	−2.000	−0.031	0.562	0.562	−0.82	1.105	1.86	1.52
December	26.06	−51.25	0.688	−0.488	−0.188	0.284	0.50	−0.20	−0.70

Table 7 Performance comparison for the proposed models during validation for Sivagangai

Statistical performance indicators	Linear	Quadratic	Cubic	Modified multi-parametric model
MBE (kWh/m^2/day)	−0.106	−0.1082	−0.1032	−0.1059
RMSE (kWh/m^2/day)	0.2533	0.2577	0.2566	0.2420
MPE (%)	1.9040	1.9430	1.8500	1.8900
MABE (kWh/m^2/day)	0.1423	0.1457	0.1437	0.1253
MAPE (%)	2.6033	2.6705	2.6284	2.2900

Table 8 Performance comparison among the existing and the reported multi-parametric models for Sivagangai

Monitored period	% error for [63] (%)	% error for [64] (%)	% error for [65] (%)	% error for proposed multi-parametric model
January	13.92731	−14.6246	2.649734	0.002878
February	−2.35788	−2.34319	1.019544	−0.01721
March	−13.9682	8.728655	1.586171	−0.03314
April	−7.61535	9.613422	2.483227	−0.00439
May	5.823812	5.004125	3.4477	0.004055
June	11.50724	1.430333	−3.79753	0.232906
July	11.17679	−0.85644	−6.35005	0.058892
August	3.219488	5.195329	−2.32099	−1.30617
September	−1.41395	10.80888	5.435546	−0.03205
October	−10.0784	−0.19466	−0.49072	−0.05847
November	−5.28594	−14.8999	−3.33001	0.190918
December	6.761487	−19.4203	−1.46601	0.017024

Table 9 Performance comparison among the existing and the reported models for Chennai during validation

Prediction Models for Chennai	MAPE (%)
Modi and Sukhatme [66]	8.87
Mani and Rangarajan [18]	9.39
Veeran and Kumar [19]	9.03
Sivamadhavi and Samuel [67] (Sunshine (linear))	4.7
Temperature (linear) [67]	11
$T_{a(min)}/T_{a(max)}$ [67]	11.3
Relative humidity (linear) [67]	10
Wind speed (linear) [67]	10.6
Precipitation (linear) [67]	8
Rainy days (linear)	7
Proposed multi-parametric model	0.07

The proposed model of the form as in Eq. (18) lies close to the actual or the measured values of global irradiance during the training. This is reflected in the least value of percentage error as seen in Table 8. Similarly, the modified multi-parametric model is also applied for Chennai with the evaluated empirical constants and testing data set. A performance comparison of MAPE is made among the existing prediction models for Chennai [18, 19, 66, 67] during validation, considered for the duration from 1980 to 2009. This comparison is made available in Table 9.

The modified multi-parametric model works out well for the prediction of global irradiance for the location of Chennai. This is made evident from Table 9, showing the multi-parametric model as in Eq. (18) to experience least MAPE of 0.07 % than the reported models. The proposed multi-parametric model possess better prediction accuracy due to the fact of encompassing significant input factors affecting global irradiance. Hence the selection of suitable model for prediction of global irradiance lie in the availability of model inputs and in the addition of significant factor justified through established physical laws.

4 Energy Prediction Model Emphasized Through Performance and Exergy Analysis

Prediction of energy delivered by a typical photovoltaic system forms a major aspect towards achieving reliability, which is one of the greatest challenge in context to power system operation. This section contributes to the formulation of energy prediction model for prediction of long term (monthly average daily) AC energy generation.

The existing Sandia inverter empirical model employs four equations which are the function of DC power input and the electric self-consumption [68]. The theoretical estimation of DC power output, further depends on models such as Sandia photovoltaic array dependent model and California Energy Commission model [5] which further lies dependent on more number of input parameters such as direct and diffuse radiation, module characteristics, array layout, diode current, reverse saturation current, series and shunt resistance increasing complexity. Thus to reduce the complexity and to make the model most applicable for pre-sizing and installation study, an empirical model independent of module system parameter is highly recommended. This forms the objective for the present section.

The evaluation of an empirical model for energy prediction follows the similar steps of methodology as adopted in formulation of global irradiance prediction. The performance analysis (electrical study) and exergy analysis (thermal study) form the preliminary study emphasizing factor addition towards empirical model formulation.

4.1 Performance Analysis of Solar PV Distribution System (Grid Connected PV System)

The performance analysis for a grid connected PV system deals with the evaluation of performance indicators such as energy generation, yield, performance ratio and efficiency for the monitored duration. Most commonly, monthly average daily based comparison for an annual period is commercially practiced. Hence monthly average prediction is rightly dealt. Furthermore, the most unique performance indicator occurs to be the AC energy generation through which the key performance indices like final yield, performance ratio and capacity factor is made available. Thus the prediction of AC energy generation for a solar photovoltaic system lies important.

The reason for the variation of key performance indices with respect to monitored input identifies the input factors affecting the same. The significant factor affecting the AC energy generation is emphasized through baseline regression analysis employed in RETscreen plus.

A typical case study of 5 MW_p PV system is considered whose energy generation is to be predicted. The plant lies operational at Sivagangai. The measured AC energy generation for the monitored duration is shown in Fig. 5. The AC energy generation varied from a minimum value of 19413.1 kWh/day (December) to 27482.8 kWh/day (September). Similarly, the monthly average daily global irradiance varies from a minimum of 4.388 kWh/m^2/day in December to 5.986 kWh/m^2/day during September. Hence the variation of AC energy generation and global irradiance occurs hand in hand. An increase in global irradiance subsequently increases the AC energy generation.

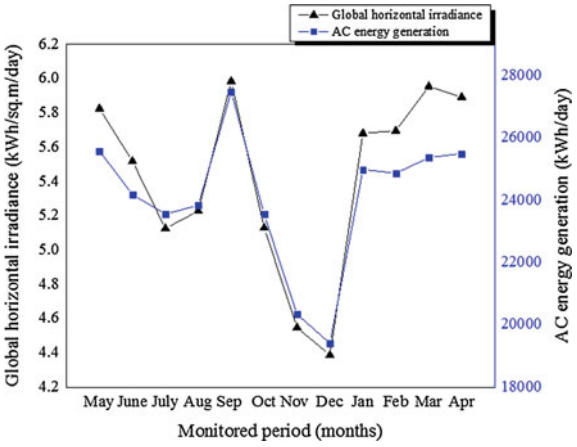

Fig. 5 Monthly average daily variation of AC energy generation and global irradiance for 5 MW_p PV

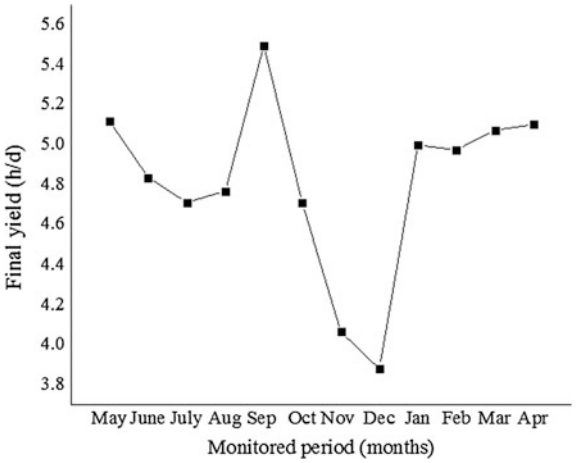

Fig. 6 Monthly average daily variation of final yield for 5 MW_p PV plant

The calculated monthly average daily variation of final yield for the monitored duration for the 5 MW_p PV plant is shown in Fig. 6. The nature of variation in final yield is similar to the annual variation of AC energy generation, which ultimately depends on the global irradiance.

Thus, the significant effect of global irradiance towards AC energy generation is emphasized by Figs. 5 and 6. Furthermore, the same is justified by adopting baseline regression analysis through RETscreen plus. The input factors such as global irradiance and ambient temperature are varied with respect to the response to be predicted or the AC energy generation. The regression coefficient occurring between their variations mark the closeness between the same. The higher the value of regression coefficient, the significant is the considered input parameter towards energy generation. Table 10 represents the effect of variation in global irradiance

Table 10 Effect of variation of H and T_a towards energy generation and efficiency

Estimated performance indicator (Y_1–Y_3)	Plot of X_1 versus (Y_1–Y_3)	Plot of X_2 versus (Y_1–Y_3)	R^2 for X_1 versus (Y_1–Y_3)	R^2 for X_2 versus (Y_1–Y_3)
E_{ac}	H versus E_{ac}	T_a versus E_{ac}	0.94	0.40
PV module efficiency η_{pv}	H versus η_{pv}	T_a versus η_{pv}	0.96	0.43
Inverter efficiency η_{inv}	H versus η_{inv}	T_a versus η_{inv}	0.68	0.49

(H) and ambient temperature (T_a) towards the key performance indices such as energy generation and efficiency as obtained from RETscreen plus.

As inferred from Table 10, the input parameter T_a is found to be less significant towards energy generation and efficiency. This lies behind the value of R^2 which varies between the ranges of 0.40 and 0.49 indicating the parameter of T_a to be less significant on comparison to global irradiance. Hence the emphasized input factor through performance analysis is the global horizontal irradiance. This is considered as one of the input factor for formulation of empirical model for energy generation.

Multi-parametric system independent energy prediction models are preferred over single parametric energy models. This is because the multi-parametric empirical prediction models experience better prediction accuracy. Hence, the formulation of multi-parametric model is followed for energy prediction too.

4.2 Exergy Analysis of Solar PV System

The effect of photovoltaic deals with the creation of power on exposure of the PV material to sunlight. During the process of power generation, there also occurs simultaneous dissipation of heat or thermal energy. The amount of thermal heat loss dissipated varies with the sizing of PV system. This loss of heat plays a significant role in affecting the performance or the energy generation of the PV system. Thus the knowledge on exergy, which accounts for the variation of thermal exergy loss towards efficiency thereby energy generation is essential for knowing its significance. The term exergy and its concept were first put forward by Gibbs in 1873 [69] and were further developed by Rant in 1956 [70]. Exergy analysis is basically derived from the second law of thermodynamics. Thus, exergy is more concentrated than energy as it considers all the irreversibility's present in the on-site operation of the plant yielding more meaningful efficiencies approaching to the ideal.

Exergy analysis plays a decisive role in analysis, improvement, design, assessment and optimization of the energy system [71]. The main key features of this analysis are to provide a true measure of actual plant performance and to identify the types, causes and location of thermodynamic losses in the system. The objective of exergy analysis in the present study is to emphasize the significance of thermal exergy loss and module temperature (resulted due to the dissipation of thermal loss) toward energy generation. Though the concept of exergy is dealt with the PV side,

the same remains unchanged on integrating the PV array system to the grid. Hence the accountability of thermal loss towards energy modelling remains important.

4.2.1 Assessment of Thermal Exergy Loss

Exergy balance of solar photovoltaic as seen in [72] can be written as

$$\text{Exergy input} - \text{Exergy output} - \text{Exergy consumption} = \text{Exergy accumulation.}$$
$$\text{(or) Exergy input} - (\text{Electrical exergy} - \text{Thermal exergy}) = \text{Energy destruction}$$

The thermal exergy loss can be theoretically evaluated [73] as given in equation

$$\text{Thermal exergy} = \text{UA}(T_\text{m} - T_\text{a})\left(1 - \frac{T_\text{a}}{T_\text{m}}\right) \tag{22}$$

U represents the overall heat loss coefficient in (W/m^2 °C). T_m represents the module temperature. The convective heat transfer coefficient 'h' is given by Boyle (2004) [74]

$$h_\text{c} = 5.7 + 3.8\upsilon_\text{s} \tag{23}$$

The radiative heat transfer coefficient is small and hence considered to be negligible.

The assessment of thermal exergy loss is carried out for the 5 MW$_\text{p}$ PV plant to justify the addition of it towards energy prediction. The evaluated monthly average daily thermal exergy loss over the monitored duration of the 5 MW$_\text{p}$ PVplant is shown in Fig. 7. The thermal exergy loss is found to increase with increase in ambient temperature. The increase in ambient temperature further increases the module temperature. Hence, as the module temperature increases the thermal exergy loss subsequently increases. Hence the module temperature, also acts as a significant factor affecting thermal exergy loss influencing energy generation.

The variation of thermal exergy loss with respect to AC energy generation for the 5 MW$_\text{p}$ PV plant is shown in Fig. 8.

The value of R^2 justifying or indicating the effect between thermal loss and AC energy generation (E_ac) is found to be 0.771. This greatly implies the justification for inclusion of thermal exergy loss for modelling energy generation. Similarly, the dependence of thermal exergy loss towards energy generation for a 160 kW$_\text{p}$ PV plant [75] is shown in Fig. 9. The variation of E_dc with respect to thermal exergy loss rightly represents the variation of E_ac with respect to Ex$_\text{th}$. The factors influencing the DC energy generation is considered influencing AC energy generation. The value of R^2 is also high amounting to 0.846 emphasizing the effect between energy generation and thermal exergy loss.

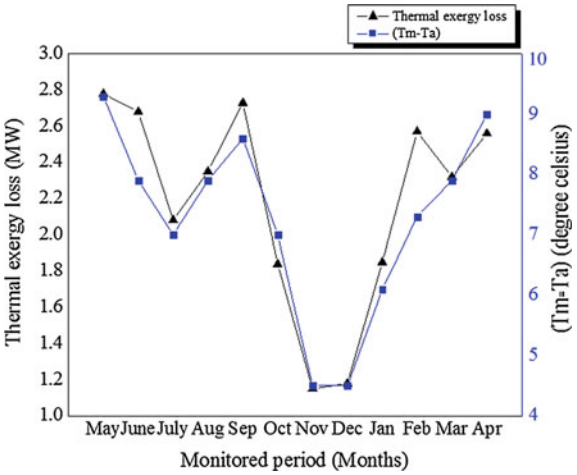

Fig. 7 Monthly average thermal exergy loss generated by 5 MW_p PV system and the monitored temperature difference

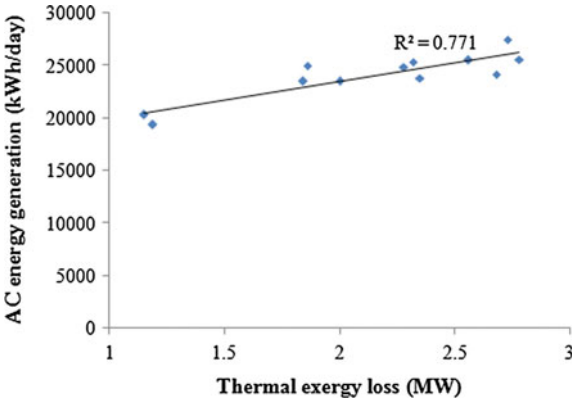

Fig. 8 Variation of thermal exergy loss over AC energy generated for a 5 MW_p PV system

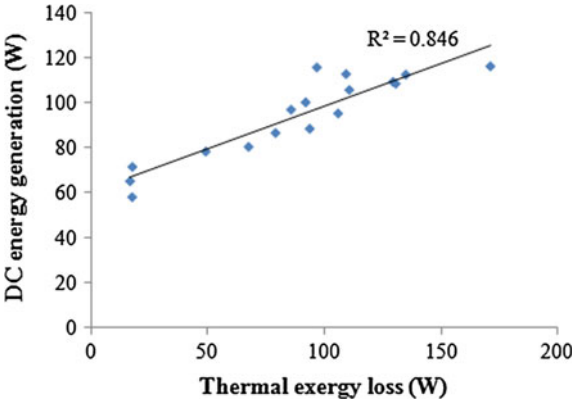

Fig. 9 Variation of thermal exergy loss over AC energy generated for a 160 kW_p PV system

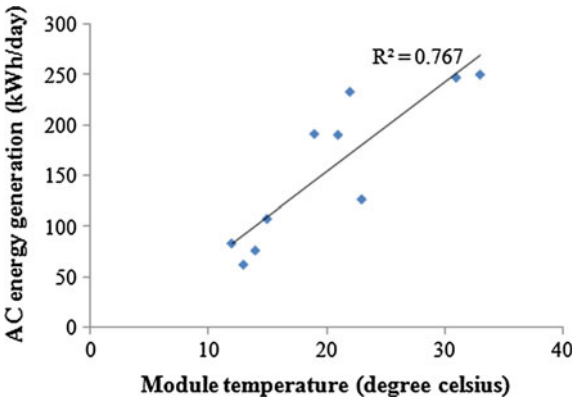

Fig. 10 T_m versus E_{ac} for 67.84 kW_p PV system [77]

Thus, the effect of thermal loss significantly affects the AC energy generation. Furthermore, the effect of module temperature also influences AC energy generation. This is justified by certain case studies which are described as follows. The effect of module temperature with respect to E_{ac} for a 1.72 kW_p roof top PV plant [76] generates the regression coefficient value between the same to be 0.734. The performance of 67.84 kW_p PV system [77] possesses an R^2 value of 0.767 as shown in Fig. 10.

The higher the value of R^2 approaching ideality, the more is the significance of response with respect to the input. Thus, the inclusion of T_m towards formulation of long-term energy prediction model is well supported by long term realistic PV plant studies.

Ultimately, the factors influencing the DC energy generation of a PV system influences the AC energy generated by the system too. The DC energy of the system varies with AC energy with an assumed constant of proportionality in most cases or the inverter efficiency.

Thus, the AC energy generated can have its dependence as

$$E_{ac} = \text{function}\,(E_{dc}, \eta_{inv}) \rightarrow E_{ac} = \text{function}\,(T_m, Ex_{th});\ [\text{from exergy analysis}] \quad (24)$$

Thus, as inferred from Eq. (24), the AC energy generated by the system is influenced by significant factors such as module temperature and thermal exergy loss as concluded from exergy analysis.

4.2.2 Formulation of Empirical Model for Energy Prediction

The input factors affecting the AC energy generation, termed significant are the global horizontal irradiance (H), module temperature (T_m) and thermal exergy loss

(Ex_{th}). These are the individual input factors contributing towards the formulation of empirical model for energy prediction.

The possible combinations of constituted input factors which are significantly affecting the energy generation include H, T_m, Ex_{th}, ($H * T_m$) ($H * Ex_{th}$), and H^2. The interactions of the main effects include ($H * T_m$) and ($H * Ex_{th}$). Thus the proposed non-linear model is of the form

$$E_{ac} = a + bH + cT_m + dEx_{th} + eHT_m + fHEx_{th} + gH^2 \quad (25)$$

The empirical coefficients in the proposed model such as *a, b, c, d, e, f* and *g* as in Eq. (25) can be calculated for a solar PV system installed at a particular location employing least square criterion. Thus the proposed model can be made applicable for a location with the assistance of certain input data set called the training data set corresponding to a location.

Thus applying Eq. (25) employing the measured and evaluated training data set the proposed equation for prediction of AC energy generated by a 5 MW_p PV plant at Sivagangai employing predicted irradiance (obtained from Eq. (18)) is given by

$$E_{ac} = -22550 - 11585H + 3590.4T_m + 5.0718Ex_{th} - 723.72HT_m - 0.302HEx_{th} + 3936.9H^2 \quad (26)$$

The proposed model is compared with the other existing models as cited in [11, 13, 45]. The absolute mean percentage error varied from a minimum to a maximum of 1.13–7.37 % for the proposed model and the same for the models proposed by Krebs and Gianolli-Rossi [11], Mayer et al. [13], International Energy Agency [45] varied from 0.3 to 24.79 %, 0.5 to 8.4 % and 0.5 to 9.47 % respectively. This is depicted in Fig. 11, which shows the proposed model to be highly acceptable for prediction of monthly average daily energy generated by a PV distribution system.

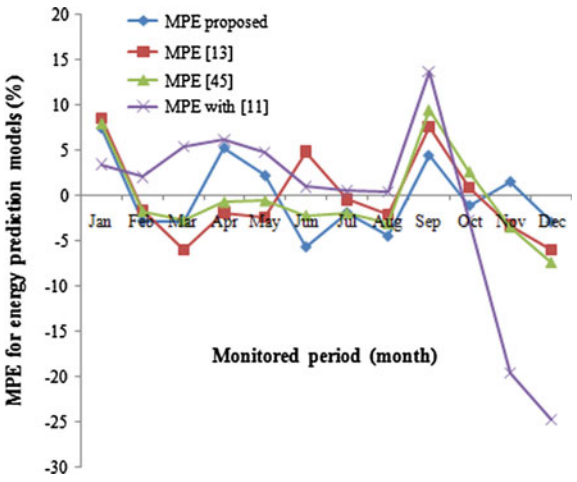

Fig. 11 Comparison of MPE for the existing with the proposed model for 5 MW_p PV plant at Sivagangai during training (2011–2012)

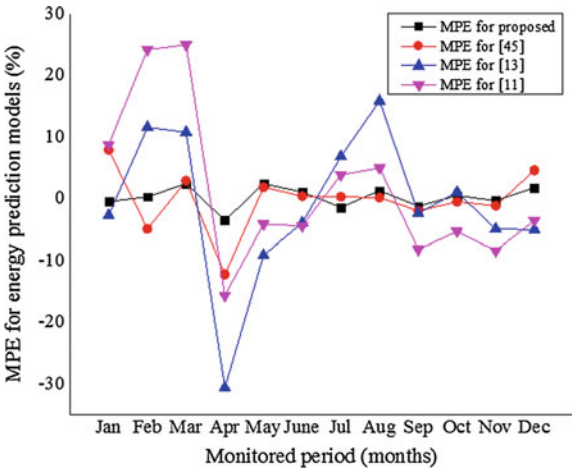

Fig. 12 MPE of the energy prediction models for a 1.72 kW_p PV plant at Durban

The modified form of energy prediction model and the existing models is also applied to a reported case study of 1.72 kW_p [76]. A performance comparison of MPE is made among the models and is represented in Fig. 12.

As seen from Fig. 12, the mean percentage error for the individual observations is least for the proposed energy prediction model than the reported energy prediction models. The adaptability of suggested energy prediction model for varying peak power capacity is also inferred on its application to PV plant at Durban.

The advantage of the modified empirical energy prediction model lies in the incorporation of system independent or metrological factors for energy prediction. Furthermore, the model is limited to real-time monitored input parameters such as ambient temperature and wind speed. In addition, the improved accuracy of the proposed model resulted due to the account of factors emphasized through performance (electrical) and exergy (thermal) analysis.

5 Summary

In order to experience improved prediction accuracy multi-parametric model is preferred over single parametric model. In addition, incorporation of significant input factors affecting energy generation also plays a vital role in yielding improved prediction accuracy. An improved empirical model for prediction of monthly average daily global horizontal irradiance tested for locations of Madurai/Sivagangai and Chennai are proposed. Furthermore, an improved energy prediction model is also formulated with predicted global irradiance for a 5 MW_p PV system whose AC energy generation is predicted over a long term horizon (monthly average daily). The advantage of the proposed models includes its limitation towards real time measured input parameters which is absent in the existing

empirical model. Moreover, the cost experienced for measuring the independent model parameters should be less than the direct measurement of the depended parameter or the desired response (global irradiance and energy generation). This becomes the adequate necessity of an empirical model. Hence, the proposed models lie in line with this adequate necessity.

References

1. Bird RE, Hulstrom RL (1980) Direct insolation models. Report SERI/TR-335–344. Solar Energy Research Institute, Golden, CO
2. Powell GL (1984) The clear sky model. Asharae J 26:27–29
3. Machler MA, lqbal M (1985) A modification of the ASHRAE clear sky irradiation model. Trans ASHRAE 91A:106–115
4. Gueymard C (2001) Parameterized transmittance model for direct beam and circumsolar spectral irradiance. Sol Energy 71:325–346
5. De Soto W, Klein SA, Beckman WA (2006) Improvement and validation of a model for photovoltaic array performance. Sol Energy 80:78–88
6. Mavromatakis F, Makrides G, Georghiou G, Pothrakis A, Franghiadakis Y, Drakakis E, Koudoumas E (2010) Modeling the photovoltaic potential of a site. Renew Energy 35:1387–1390
7. Lacour A, Duffy A, Sarah MC, Michael C (2010) Validated real time energy models for small-scale grid connected PV systems. Energy 36:4086–4091
8. King DL, Gonzalez S, Galbraith GM, Boyson W (2007) Performance model for grid-connected photovoltaic inverters, SAND2007-5036. http://www.prod.sandia.gov/cgi/bin/techlib/accesscontrol.pl/2007/075036.pdf
9. Box G, Jenkins G (1976) Time series analysis: forecasting and control. Holden Day, Oakland
10. Suykens JA, Vandewalle J (1999) Least squares support vector machine classifiers. Neural Process Lett 9:293–300
11. Krebs K, Gianolli-Rossi E (1988) Energy rating of PV modules by outdoor response analysis. In: International conference on solar energy, Florence, Italy
12. Meyer EL, Dyk EE (2000) Development of energy model based on total daily irradiation and maximum ambient temperature. Renew Energy 21:37–47
13. Mayer D, Wald L, Poissant Y, Pelland S (2008) Performance prediction of grid-connected photovoltaic systems using remote sensing. Report IEA-PVPS T2-07, p 18
14. Angstrom AS (1924) Solar and terrestrial radiation. Q J Roy Meteorol Soc 50:121–126
15. Prescott JA (1940) Evaporation from water surface in relation to solar radiation. Trans Roy Soc S Australia 64:114–118
16. Lewis G (1983) Estimates of irradiance over Zimbabwe. Sol Energy 31:609–612
17. Jain S, Jain PC (1988) A comparison of the angstrom-type correlations and the estimation of monthly average daily global irradiation. Sol Energy 40:93–98
18. Mani A, Rangarajan S (1982) Solar radiation over India. Allied Publishers, New Delhi
19. Veeran PK, Kumar S (1995) Analysis of monthly average daily global radiation and monthly average sunshine duration at two tropical locations. Renew Energy 3:935–939
20. Katiyar AK, Pandey C (2010) Simple correlation for estimating the global solar radiation on horizontal surfaces in India. Energy 35:5043–5048
21. Benson PR, Paris MV, Serry JE, Justus CG (1984) Estimation of daily and monthly direct, diffuse and global solar radiation from sunshine duration measurement. Sol Energy 32:523–535
22. Ogelman H, Ecevit A, Tasdemiroglu E (1984) A new method for estimating solar radiation from bright sunshine data. Sol Energy 33:619–625

23. Samuel TDMA (1991) Estimation of global radiation for Sri Lanka. Sol Energy 47:333–337
24. Ampratwum DB, Dorvlo ASS (1999) Estimation of solar radiation from the number of sunshine hours. Appl Energy 63:161–167
25. Elagib N, Mansel MG (2000) New approaches for estimating global solar radiation across Sudan. Energy Convers Manag 41:419–434
26. Hayer A, Balli O, Arif H (2006) Global solar radiation potential, part 1: model development. Energy Sources Part B 1:303–315
27. El-Sebaii AA, Al-Ghamdi AA, Al-Hazmi FS, Faidah AS (2009) Estimation of global solar radiation on horizontal surfaces in Jeddah, Saudi Arabia. Energy Policy 37:3645–3649
28. Wanxiang Y, Zhengrong L, Yuyan W, Fujian J, Lingzhou H (2014) Evaluation of global solar radiation models for Shanghai, China. Energy Convers Manag 84:597–612
29. Hargreaves GH, Samani A (1982) Estimating potential evapo-transpiration. J Irrig Drainage Eng 223–230
30. Bristow K, Cambell G (1984) On the relationship between incoming solar radiation and daily maximum and minimum temperature. Agric For Meteorol 31:159–166
31. Allen RG, Pereira LS, Raes D, Smith M (1998) Crop evapo-transpiration: guidelines for computing crop water requirements. J Irrig Drainage Eng 56
32. Goodin DG, Hutchinson JMS, Vanderlip RL, Knapp MC (1999) Estimating solar irradiance for crop modeling using daily air temperature. Agric For Meteorol 91:293–300
33. Meza F, Varas E (2000) Estimation of mean monthly solar global radiation as a function of temperature. Agric For Meteorol 100:231–241
34. Almorox J, Hontoria C, Benito M (2011) Models for obtaining daily global solar radiation with measured air temperature data in Madrid (Spain). Appl Energy 88:1703–1709
35. Huashan L, Weibin M, Yongwang L, Xianlong W, Liang Z (2011) Global solar radiation estimation with sunshine duration in Tibet, China. Renew Energy 36:3141–3145
36. Punnaiah V, Guduri G (2014) Analysis of yearly solar radiation by using correlations based on ambient temperature: India. Sustain Cities Soc 11:16–21
37. Mahmood R, Hubbard KG (2002) Effect of time of temperature observation and estimation of daily solar radiation for the Northern Great Plains, U.S.A. Agron J 94:723–733
38. Emmanuel K, Sofoklis K, Thales M (2009) Performance analysis of grid connected photovoltaic park on the island of Crete. Energy Convers Manag 50:433–438
39. De Jong R, Stewart DW (1993) Estimating global solar radiation from common meteorological observations in western Canada. Can J Plant Sci 73:509–518
40. Togrul IT, Onat E (2000) A comparison of estimated and measured values of solar radiation in Elazig. Renew Energy 20:243–252
41. Trabea AA, Mosalam Shaltout MA (2000) Correlation of global solar radiation with meteorological parameters over Egypt. Renew Energy 21:297–308
42. Rensheng C, Kang E, Jianping Y, Shihua L, Wenzhi Z (2006) Estimating daily global radiation using two types of revised models in China. Energy Convers Manag 47:865–878
43. Muyiwa SA (2012) Estimating global solar radiation using common meteorological data in Akure, Nigeria. Renew Energy 47:38–44
44. Teke A, Basak H, Celik O (2015) Evaluation and performance comparison of different models on solar radiation. Renew Sustain Energy Rev 50:1097–1107
45. IEA International Energy Agency (2008) Performance prediction of grid connected photovoltaic systems using remote sensing. Report IEA PVPS T2-08, pp 1–44
46. Becquerel Edmond (1839) Mémoire sur les effets électriques produits sous l'influence des rayons solaires (In French). Comptes Rendus 9:561–567
47. Igzi E, Akkaya YE (2013) Exergo-economic analysis of a solar photovoltaic system in ˙Istanbul, Turkey. Turkish J Electr Eng Comput Sci 21:350–359
48. Rusirawan D (2012) Energy modelling of photovoltaic modules in grid connected PV systems. Ph.D Dissertation
49. Minister of Natural Resources Canada (2003) RETscreen engineering and cases textbook, 3rd edn
50. Athena Infonomics India Private Limited (2011) Power scenario in Tamil Nadu: a comparative analysis. pp 1–27

51. Measurement of sunshine duration and solar radiation, pp 1–14. www.jma.go.jp/jma/jma-eng
52. Taylor W (1996) www.taylormade.com.au/billspage/sunshine/sunhine.html
53. Cooper PI (1969) The Absorption of Solar Radiation in Solar Stills. Sol Energy 12:3
54. Rahman MM (2000) Site independent global solar radiation correlation with bright sun shine hours. Int J Radio Space Phys 29:285–290
55. Kunt M (2008) The daily temperature amplitude and surface solar radiation. Ph.D Dissertation, University of Zurich
56. Stefan J (1879) On the relationship between heat radiation and temperature. 79:391–428
57. Planck M (1914) The theory of heat radiation, 2nd edn
58. Tyagi AP (2009) Solar radiant energy over India. Indian Metrological Department, Ministry of Earth Sciences
59. Sivamadhavi V, Samuel Selvaraj R (2012) Prediction of monthly mean daily global solar radiation using artificial neural network. J Earth Syst Sci 121:1501–1510
60. Per Christian H, Victor P, Godela S (2013) Least square data fitting with applications. The John Hopkins University Press, Baltimore
61. Tarhan S, Ahmed S (2005) Model selection for global and diffuse radiation over the central black sea (CBS) region of Turkey. Energy Convers Manag 46:605–613
62. Amit KY, Chandel SS (2014) Solar radiation prediction using artificial neural network techniques: a review. Renew Sustain Energy Rev 33:771–781
63. Magrabhi AH (2009) Parameterization of a simple model to estimate monthly global solar radiation based on meteorological variables, and evaluation of existing solar radiation models for Tabouk. Saudi Arabia Energy Convers Manage 50:2754–2760
64. Swartman RK, Ogunlade O (1967) Solar radiation estimates from common parameters. Sol Energy 11:170–172
65. Abdalla YAG (1994) New correlation of global solar radiation with meteorological parameters for Bahrain. Int J Solar Energy 16:111–120
66. Modi V, Sukhatme SP (1979) Estimation of daily total and diffuse insolation in India from weather data. Sol Energy 22:402
67. Sivamadhavi V, Samuel R (2012) Robust regression technique to estimate global radiation. Int J Radio Space Phys 41:17–25
68. Nathan B, Mark M, Craig C (2008) Modeling photovoltaic and concentrating solar power trough performance, cost, and financing with the solar advisor model. In: American solar energy society conference
69. Gibbs JW (1873) A method of geometrical representation of the thermodynamic properties of substances by means of surfaces. Trans Connecticut Acad 2:382–404
70. Rant Z (1956) Exergy, a new word for technical available work. Forschung auf dem Gebiete des Ingenieurwesens 22:36–37 (in German)
71. Sahin A, Dincer I, Rosen MA (2007) Thermodynamic analysis of solar photovoltaic cell systems. Solar Energy Mater Solar Cells 91:153–159
72. Wong KFV (2000) Thermodynamics for engineers. CRC Press LLC, University of Miami, Boca Raton, USA
73. Petala R (2003) Exergy of undiluted thermal radiations. Sol Energy 74:469–488
74. Boyle G (2004) Renewable energy power for a sustainable future, 2nd ed. Oxford: Oxford University Press
75. Pandey A, Tyagi VK, Tyagi SK (2012) Exergetic analysis and parametric study of multi-crystalline solar photovoltaic system at a typical climatic zone. Clean Technol Environ Policy 15:333–343
76. Ayompe LM, Duffy A, McCormack SJ, Conlon M (2011) Measured performance of a 1.72 kW roof top grid connected photovoltaic system in Ireland. Energy Convers Manag 52:816–825
77. Drif M, Perez PJ, Aguileria J, Almonacid G, Gomez P, De la Casa J, Aguilar JD (2007) A grid connected photovoltaic system of 200 kWp at Jean university: overview and performance analysis. Solar Energy 91:670–683

A Study of Islanding Mode Control in Grid-Connected Photovoltaic Systems

Wei Yee Teoh, Chee Wei Tan and Mei Shan Ngan

Abstract This paper reviews the recent trend and development of control techniques for islanding mode particularly for photovoltaic (PV) grid-connected systems. Grid-connected system has gained vast popularity over the past years. Therefore, it is essential to ensure ultimate safe interaction between distribution generations and utility grid. One of the major safety issues is the unintentional activities carried out by maintenance workers within the grid-connected PV system during the islanding operation mode. There are two types of islanding mode, namely the intentional and unintentional. This paper only focuses on the detection methods for unintentional islanding. Anti-islanding detection methods are generally categorized into two groups, namely the Local Islanding Detection Technique and the Remote Islanding Detection Technique. Each detection group consists of several specific techniques that apply different methodologies or algorithms. The fundamental concept and theory of operation of popularity used anti-islanding detection methods are described. In addition, the advantages and disadvantages of each control method have been highlighted. The operation characteristics and system parameters of each detection techniques are analyzed and discussed. Moreover, the comparison of islanding detection method based on various characteristics has been detailed. It can be concluded that anti-islanding detection methods are greatly governed by the nature of system application as well as the scale of the system. Finally, this chapter also explains construction of the simulation

W.Y. Teoh · C.W. Tan (✉)
Department of Electrical Power Engineering (POWER), Faculty of Electrical Engineering, Universiti of Teknologi Malaysia (UTM), Johor Bahru, Malaysia
e-mail: cheewei@utm.my

W.Y. Teoh
e-mail: weiyee11722@hotmail.com

M.S. Ngan
Department of Electrical and Electronics Engineering, Faculty of Engineering and Information Technology, Southern University College, Skudai, Malaysia
e-mail: msngan@sc.edu.my

M.R. Islam et al. (eds.), *Advances in Solar Photovoltaic Power Plants*,
Green Energy and Technology, DOI 10.1007/978-3-662-50521-2_7

of the PV grid-connected anti-islanding detection method in MATLAB/Simulink simulation software. The chapter ends with the simulation results of both passive and active methods as well as the results, discussion, and analysis.

Keywords Photovoltaic (PV) grid-connected system · Islanding detection · Passive method · Active method · Hybrid method · Communication-based method

1 Introduction

Over the past decades, the quick growth of industries due to the rapid development of new technology has significantly increased the worldwide energy demand [1]. Moreover, it is projected by the U.S. Energy Information Administration (U.S.EIA) that the world energy consumption is still increasing and anticipated to reach a growth of 53 % from year 2008 to 2035 [2]. To date, the generation of main power supply is still heavily reliant on fossil fuel, such as coal and natural gas [3]. However, the production of electricity using fossil fuels is known to emit hazardous greenhouse gases which may harm the environment [4, 5]. It has been reported in Ref. [6] that, based on the consumption trend of fossil fuels from 1980 to 2006, natural oil is estimated to run out to approximately 40 years. As fossil fuels become scarce, the price of energy will continue to soar in the upcoming decades [1, 6, 7]. Therefore, the world is in urgent need of alternative resources, and related technologies have been focused and developed intensively for the past few years [8].

With the growth of renewable energy, the importance of Microgrids has also relatively increased. This is because Microgrids is part of power distribution system that contained DGs, energy storage device, and intergrading loads as shown in Fig. 1

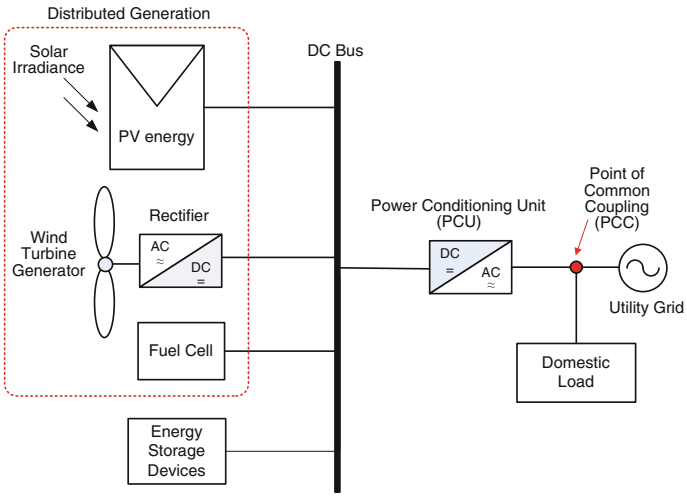

Fig. 1 The overview block diagram of Microgrids connected to utility grid

[9, 10]. DGs are small-scale power generation plants located near the loads they are feeding and interact with the utility grid to import or export energy [11, 12]. Typically, DGs generate power from a few kilowatts upto 50 MW (a block diagram of multiple DGs system connected to the utility grid is shown in Fig. 1). Thanks to their proximity, transmission losses are reduced. This could effectively decrease the size and the number of power lines that are put up to deliver the output to the consumer. Additionally, the use of DGs helps to reduce greenhouse emissions, minimize peak loads, improve the system security, and ultimately reduce the vulnerability to simultaneous system failures [3, 11]. Nevertheless, in order to meet the targeted goals, the DGs system connected to the utility grid must comply with the DGs interconnection standards imposed by the national electrical rules and regulations to ensure substantial safety and prevent performance implication [13–18].

Photovoltaic (PV) energy has become one of the most promising renewable energies in DGs [3, 11]. This is due to the fact that PV energy is free, environmentally friendly, and sustainable [11, 12, 19]. However, at present, the high cost of PV material and grid interconnection policies have restricted its vase development in energy generation. Consequently, solar energy can only help to reduce the dependency on conventional power generation. Therefore, a big challenge remains to enhance the PV technologies and to clarify the grid interconnections requirements, in order to make PV as the primary energy resource in the near future [20].

The interconnection of PV, power conditioning unit (PCU), and the utility grid in grid-connected PV systems has to meet the specified technical requirements to ensure high power quality and reliability. For that reason, abnormal operating conditions that could influence the operation of grid-connected PV systems should be avoided [16]. For instance, unintentional operation in islanding mode is a major system reliability issue that could seriously affect the system stability due to the loss of grid synchronization. Unintentional islanding causes the voltage and frequency of DG to deviate from the tolerated range which may harm the component in the system within the islanded section. More importantly, the safety of maintenance workers will be threatened as they may not be aware of the occurrence of islanding in their service section [21]. Therefore, it is vital to apply anti-islanding control in all grid-connected PV systems.

A good islanding mode control is compulsory to ensure the safety of maintenance workers as well as to prevent a potential damage to end user's equipment. Several anti-islanding algorithms have been proposed and published over the past decades [22]. Based on the gathered literatures, there is no specific islanding detection method that is considered ideal. Typically, the drawbacks of those detection methods are as follows:

1. the occurrence of a non-detected zone (NDZ), which may lead to failure of anti-islanding detection.
2. the degradation of power quality and the system stability.
3. the malfunction in multiple DGs.
4. the need of extra circuitry or apparatus.
5. high capital and maintenance cost [23].

To the best of the author's knowledge, there are more than 25 anti-islanding methods that have been proposed but not all methods are suitable for PV grid-connected systems. Moreover, the peer-reviewed literature on PV-related anti-islanding is limited. Hence, recent trends in the proposed anti-islanding control techniques are worth to review and compile. This paper is compiled and analyzed commonly on applied and recently developed anti-islanding detection techniques, especially for PV grid-connected systems. The fundamentals of islanding conditions are described and the available islanding detection methods are also reviewed and revised. In addition to that, a comprehensive comparison among the studied methods has been made. Finally, summary and conclusions of this review are drawn.

2 The Principle of Islanding in Distribution Generation Systems

Islanding is a phenomenon that refers to a fault that occurs in the utility grid or DG due to various factors, causing the DG to disconnect from the utility grid. If the DG source did not detect or recognize the fault, it will not terminate the electricity supplied to the local loads, although the DG has lost connection with the grid. Being isolated from the DG, the utility grid will lose control to the DG system without reference parameters, such as RMS voltage and/or frequency from the utility grid [13, 14] (DG system will continue to operate in stand-alone conditions).

The fundamental idea of islanding concept is shown in Fig. 2, where the DG with PV as a distribution source owned by a utility customer is connected to a utility via a PCU. PCU interfaces the DG with the utility through the Point of Common Coupling (PCC) in between the utility and the local loads. The main function of the PCU is to perform Maximum Power Point Tracking (MPPT) and DC–AC inversion features [24]. Islanding occurs when the utility circuit breaker opens, but the PV continues to supply power to the section of the utility system between the utility circuit breaker and the PCC.

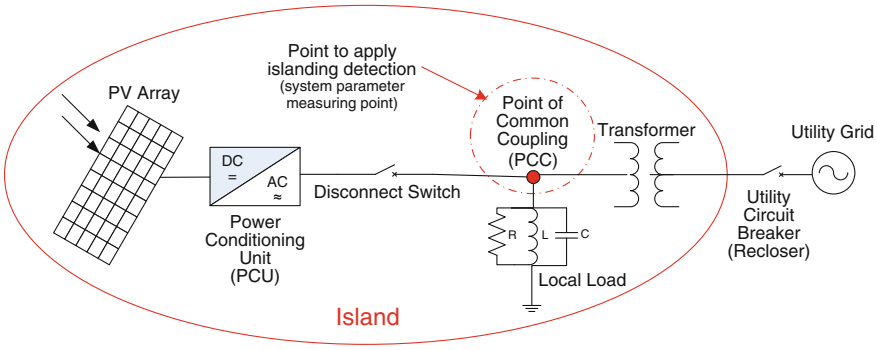

Fig. 2 The grid-connected PV system at the PCC where anti-islanding control is present

This section normally consists of a transformer, utility equipment, and a local load. During islanding, the system loses solid voltage and frequency references from the utility. Equipment and other connected electrical devices may suffer damages due to asynchronous voltage and frequency. Worst, safety hazard is now present. The technical team assigned to this section may not be aware of the danger resulting from the continuous energizing, even though the utility is no longer connected to it. For this reason, islanding needs to be detected as soon as possible in order to alert all the control systems which in turn will discontinue the energy production. This action is referred to as "Anti-islanding" and is usually performed at the PCC [25, 26].

2.1 Types of Islanding

Generally, islanding mode is classified into intentional (planned) and unintentional (unplanned) modes. The former islanding aims to sectionalize the utility system during disturbances to create power "islands." This mode is commonly used during maintenance. When disturbances occur in a utility distribution, this island can maintain a constant supply to local loads within, as planned by the energy management procedure, until the utility is ready to be re-synchronized with the DG. Typically, intentional islanding has no negative consequences as it will be handled during or after the grid's disconnection [17, 18, 27].

The latter islanding mode is caused by unpredictable disturbances in the utility. The DG is automatically disconnected from the utility to avoid damages to the source and/or to the loads. This results in a severe impairment of the power system stability due to the loss of grid synchronization. In addition, unintentional islanding can be hazardous to the maintenance team, who may not be aware that the islanding area is still powered even though the power from the grid was tripped. Hence, high concern is given to the possible occurrence of unintentional islanding in a distribution system with distributed resources as loads and generations [17, 18, 28]. Unintentional islanding may occur as a consequence of any of the following phenomena:

1. a fault has been detected by the utility, such as blackout, voltage shutdown, short circuit, etc., leading to the opening of the protection devices in order to disconnect the supply; however, the disconnection failed to be detected by the DG site protection devices or the PV inverter.
2. an accidental opening of the normal utility supply due to equipment failure.
3. the utility switching of the DG system and loads.
4. an intentional disconnection for maintenance purposes either at a point on the utility grid or at the service entrance.
5. sudden changes in the electric distribution systems and loads.
6. a human error or a malicious mischief.
7. vandalism or act of nature.

2.2 The Needs of Islanding Prevention

The grid-connected PV systems must adhere to the voltage and frequency characteristics of the utility supply. In the case of islanding, the PV generators should be disconnected from the local loads immediately. However, if the PV system accidentally reconnected during islanding, an asynchronous condition will occur, which allow transient overcurrents to flow through the PV system. Damages due to the inverters and/or to the protective equipment such as circuit breakers as well as to sensitive electrical equipment may occur [13].

Islanding control can be achieved through inverters or via the distribution network [29]. Inverter controls can be designed for the detection of grid voltage or measurements of impedance, frequency variations, or harmonics. There are many reasons that islanding should be prevented in a PV grid-connected system or in any other distributed energy generation such as to ensure the high quality of power provided. Thus, the utility requires the implementation of anti-islanding controls on any grid-connected PV system. Possible consequences of an undetected islanding include:

1. a possible damage to the customer's equipment as the utility would not be able to control the voltage and frequency of power supply in the island.
2. both the utility as well as the PV distributed resource owner could be found liable for electrical damage to customer's equipment due to voltage or frequency excursion outside of the acceptable ranges.
3. islanding may present an electrical hazard to the utility line-workers or to the public who assumes a line had been disconnected from all energy sources, while, in fact, it had not.
4. re-closing into an island may result in re-tripping the line or damaging the distributed resource equipment or other connected equipment, due to out of phase closure.
5. islanding may interfere with the manual or automatic restoration of the power supply by the utility [30].

Due to the abovementioned reasons, additional research and study needs to be carried out to help mitigating the drawback of the existing anti-islanding detection algorithm.

3 Anti-islanding Detection Methods

The NDZ and Quality factor (Q factor) are two major features to emphasize in this section. This is to promote a better understanding of the islanding detection technique discussed in the next section. Both the NDZ and Q factor have been widely cited as the criteria to evaluate the efficiency of islanding detection [31, 32]. The NDZ represents the interval of islanding failed to be detected by the DG once

an islanding occurred [23]. The NDZ corresponds to the power mismatch between the power supplied by DG and the local load. This in turn creates the real power variation (ΔP) and the reactive power variation (ΔQ). These variations should be large enough so that the algorithm can detect islanding within an adequate interval of time. In short, the NDZ is also known as the evaluation index [31]. The Q factor is the product of two pi (π) and the ratio of the maximum energy stored to the energy dissipated per cycle, at a given frequency [13]. It represents the relative amount of energy stored and energy dissipated in an RLC circuit. In another word, only low value of Q factor can ensure the high effectiveness of islanding detection [22]. The local load is typically modeled as a parallel RLC to demonstrate a high Q factor scenario, as expressed in

$$Q_{\mathrm{f}} = R\left(\frac{C}{L}\right)^{\frac{1}{2}} \tag{1}$$

where Q_{f} is the Q factor, R is resistive loads, C is capacitive loads, and L is inductive loads. The higher the Q factor, the more difficult an islanding is detected. Comparatively, nonlinear loads such as harmonics producing loads and constant power loads do not increase the difficulty to detect islanding. The Q factor is directly proportionate to the NDZ, hence a smaller NDZ is desired [24]. In particular, most of the islanding methods have to cope with the NDZ problem, especially when using passive islanding detection methods. Consequently, it can be deduced that minimizing the NDZ and shortening the response time of islanding detection are the main objectives that need to be researched [31, 32].

The control techniques of anti-islanding for PV grid-connected DG can be grouped into two: the first is the local islanding detection techniques that rely on the measurement of the system parameters at the DG site; the second is the remote islanding detection techniques based on the communication between the utility grid and the DG. Figure 3 shows the classification of islanding and anti-islanding detection techniques. Local detection technique can further be classified into:

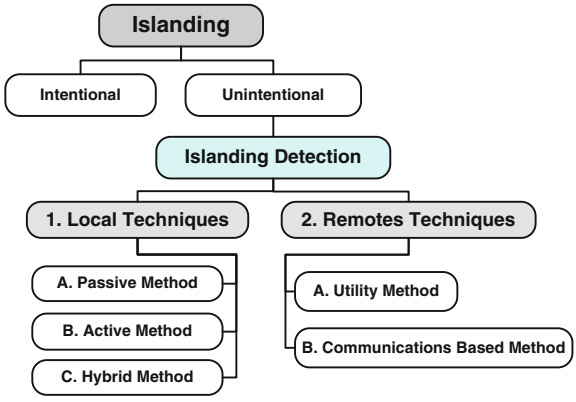

Fig. 3 The classification of anti-islanding detection techniques

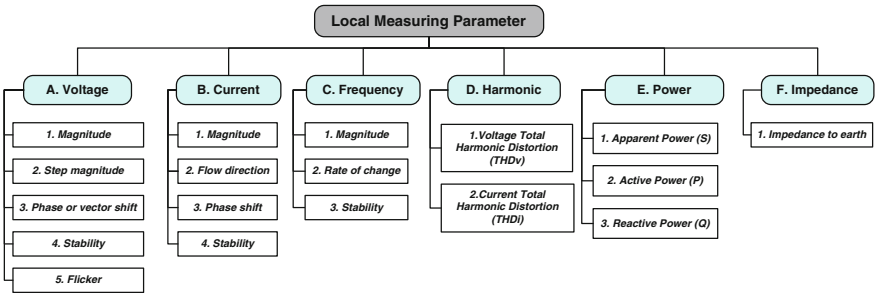

Fig. 4 Local measuring parameters of local anti-islanding detection method

passive method, active method, and hybrid method. On the other hand, remote detection technique can be classified into: utility method and communications based method.

3.1 Local Anti-islanding Detection Method

The local islanding detection technique is based on the measurement of the system parameters at the PCC and at the DG site. These parameters (voltage, frequency or other parameters) can be measured to detect an islanding as shown in Fig. 4. Most of the islanding detection techniques rely on more than a single parameter in order to determine an islanding occurrence [27, 28, 33]. Local islanding detection techniques can be further classified into three methods: passive, active, and hybrid as shown in Fig. 3.

3.1.1 Passive Method

Passive islanding detection methods rely on the measurement of the system parameters. These parameters can be the variations in voltage, frequency, harmonic distortion, etc. [34]. As shown in Fig. 2, these parameters vary greatly at the PCC when the system is islanded. To differentiate a grid-connected condition from an islanding, one needs to assess the threshold settings of these parameters [35]. The setting of the threshold values should be made very carefully in order to effectively distinguish an islanding from other disturbances in the system. Passive techniques have minimal response time and do not introduce disturbances in the system. However, these have a large NDZ that could cause detection failures [36]. There are various passive islanding detection methods. Some of the most commonly used grid-connected PV system are shown in Fig. 5 together with their alternative naming according to the similarities of their principle of operation. Figure 6 illustrates the flowchart of a passive islanding detection.

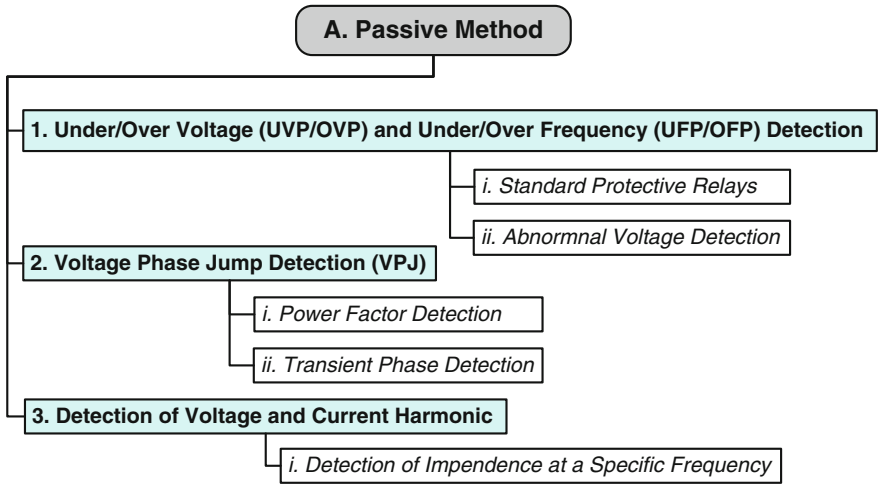

Fig. 5 The passive islanding detection methods

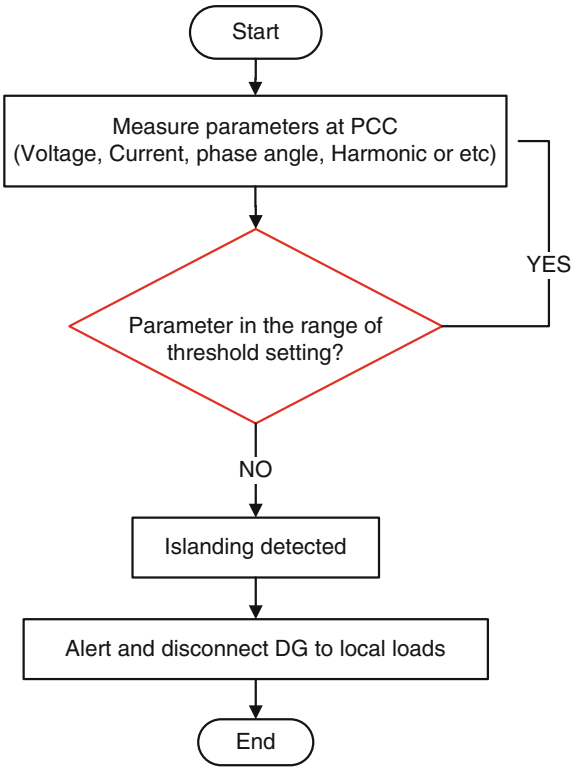

Fig. 6 The flowchart of the passive islanding detection method

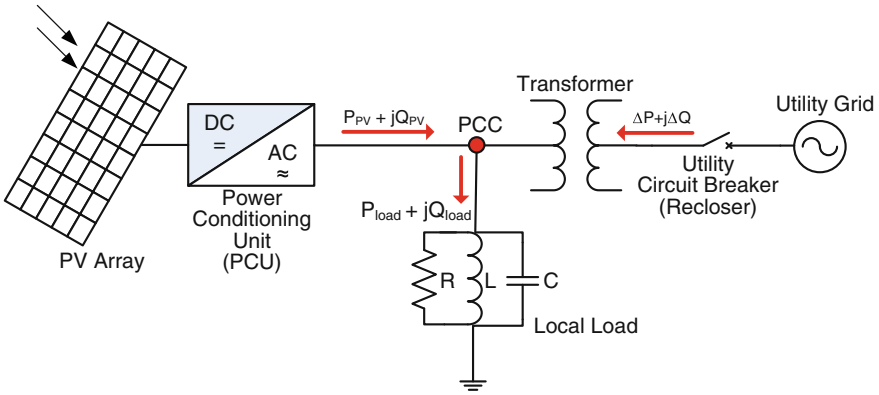

Fig. 7 The power flow in a PV grid-connected system under a normal operating condition

Voltage Protection and Frequency Protection

Under/over frequency protection (UFP/OFP) and under/over voltage protection (UVP/OVP) methods are also known as Standard Protective Relay or Abnormal Voltage Detection [13]. Implementation of these methods is usually regulatory mandated as this is the basic protection for a PV grid-connected system. In the event that the amplitude of the V_{PCC} or the frequency exceeds the defined thresholds, these measures kick in to prevent the DG from supplying power to the utility. The same methodology can be used for islanding detection [29, 34, 37]. Figure 7 shows the power flow in a PV grid-connected system under normal conditions. The node PCC depicts the PCC between the utility grid and the PCU.

Consider the configuration shown in Fig. 7. The PCC node is the PCC between the utility grid and the PCU in a PV DGs. When the recloser is closed and the utility is connected, the power flow in the interconnected system can be described by the following equations [38].

The power delivered by the inverter is (2)

$$S_{PV} = P_{PV} + jQ_{PV} \tag{2}$$

where P_{PV} is the real power and jQ_{PV} is the reactive power flowing from the PV DG. The power consumed by the load is (3).

$$S_{load} = P_{load} + jQ_{load} \tag{3}$$

where P_{load} is the real power and jQ_{load} is the reactive power flowing from the PCC to the load. We can derive the portion of power delivered by the grid by summing the power flows at the PCC, as shown in (4) and (5).

$$P_{\text{load}} = P_{\text{PV}} + \Delta P \tag{4}$$

$$Q_{\text{load}} = Q_{\text{PV}} + \Delta Q \tag{5}$$

where ΔP is the real power and ΔQ is the reactive power flowing into the PCC from the utility grid. Hence, ΔP (6) can be derived from (4) and ΔQ (7) from (5).

$$\Delta P = P_{\text{load}} - P_{\text{inv}} \tag{6}$$

$$\Delta Q = Q_{\text{load}} - Q_{\text{inv}} \tag{7}$$

In case of an islanding, the real power consumed by the load is expressed in an Eq. (8). It is a function of voltage:

$$P_{\text{load}} = \frac{V_{\text{pcc}}^2}{R_{\text{load}}} \tag{8}$$

where V_{pcc} is the voltage at the PCC and R_{load} is the local resistive loads. And reactive power is expressed in Eq. (9), it is a function of the voltage and the frequency.

$$Q_{\text{load}} = \frac{V_{\text{pcc}}^2}{\frac{1}{X_L} - \frac{1}{X_C}} = \frac{V_{\text{pcc}}^2}{\omega L\left[1 - \left(\frac{\omega}{\omega_R}\right)^2\right]} \tag{9}$$

where $\omega_{\text{R}} = \frac{1}{(LC)^{\frac{1}{2}}}$ is the resonant frequency, L is the load inductance, and C is the load capacitance.

Equations (8) and (9) describe the active and reactive power consumed by RLC load. If the active power demand for the local load and the active power generated from the PV system are not equal in instance, the utility circuit breaker opens, where $P_{\text{PV}} < P_{\text{load}}$ next the V_{pcc} must increase until $P_{\text{PV}} = P_{\text{load}}$. If $P_{\text{PV}} > P_{\text{load}}$, then V_{pcc} will decrease until $P_{\text{pv}} = P_{\text{load}}$. Correspondingly, if the reactive power demands of the local load and the reactive power generated do not match at the instance the grid is disconnected, then the frequency, ω at the PCC must change until $Q_{\text{PV}} = Q_{\text{load}}$. The PV inverter will continue to adjust the frequency until the phase angle of the power at the PV is in synchronization with the local load. Hence once the utility circuit breaker is opened, i.e., islanding occurs, the resulting voltage and frequency change can be detected by the over/under frequency/voltage relays in the system [27].

In another perspective, the islanding behavior of the system when the utility circuit breaker opens will depend on ΔP and ΔQ at the instant before the switch opens. If $\Delta P \neq 0$, the amplitude of the V_{PCC} changes and the over/under voltage and over/under frequency relays to detect the change, an islanding can be prevented. By OVP/UVP protection, the inverter monitors the RMS voltage of the

utility and disconnects if the values go across the thresholds. This offers a protection during brown-outs and utility drops [39]. If $\Delta Q \neq 0$, then the V_{load} will result in a sudden shift in phase. Then the inverter's control system will induce the frequency of the inverter to be closer to that of the output current's, and thus the frequency of V_{PCC} to approach $\Delta Q = 0$. This change in frequency is detected by the over/under voltage and over/under frequency relays [13, 14].

Due to the small values of ΔP and ΔQ, when the local load demand and the PV generation are similar, it created difficulties to detect an islanding phenomenon. In an NDZ, the values are insufficient for the frequency or voltage changes to be detectable by an over/under voltage and over/under frequency relays. Hence, OVP/UVP protection will not trip to prevent islanding. It is necessary to develop islanding techniques that are suitable in such cases when the powers of the PV and the local load demand closely match. It is the target of all islanding detection methods to reduce the non-detection zone to as close to zero as possible [13, 14].

Voltage Phase Jump Detection

Phase jump detection (PJD) is a method of anti-islanding. It is performed by monitoring the phase difference between the inverter's terminal voltage (V_{pcc}) and inverter's output current (I_{PV_inv}) in order to detect a sudden phase jump as present in Fig. 8 [22, 28, 40]. In case of an islanding, during the transition from a grid-connected condition to islanding occurrences, the phase angle of V_{pcc} will shift to match the phase angle of the local load. This phase shift results in a sudden phase change at the PCC point. Hence, the PJD method will detect for this sudden change of phase angle in order to notice an islanding happened. In addition, it is in the nature of the loads to have imperfect power factors, which means that the total voltage from the utility grid is not completely absorbed but is slightly impeded. It is a crucial requirement for the grid-connected inverters to have a unity power factor

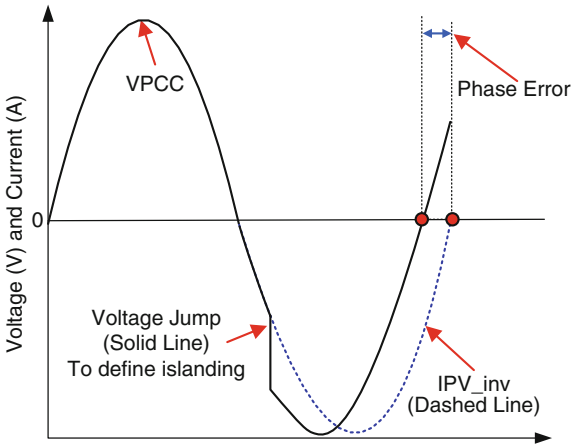

Fig. 8 The operation of voltage phase jump detection

(pf) because the NDZ of a PJD depends on the pf. The NDZ can change if the inverter is not operating in unity with power factor. Hence, the PJD is also called Power Factor Detection or Transient Phase Detection [13].

Generally, the inverter in a PV system tracks the phase of the grid signal using a Phase Locked Loop (PLL). For more studies about PLL and PJD please kindly refer to [41–48]. In a current-source inverter, the output current waveform is synchronized with the utility voltage. This is done by detecting the rise or fall of the V_{PCC} at its zero crossings at the PCC in a normal operation. This is generally accomplished by using an analog or digital PLL. However, in a voltage-source inverter, the role of the voltage and current are inverted. This is similar in a current-source inverter [30]. For the current-source inverter, the V_{pcc} has lost control by the utility voltage source when the utility grid is no longer connected. While the I_{PV_inv} is fixed, it still follows inherently the waveform template provided by the PLL in the inverter. This is due to the synchronization between the I_{PV_inv} and the V_{pcc} and occurs only at the zero crossings of the V_{PCC}. Between the zero crossings, the inverter is essentially operating in an open-loop mode. Therefore, the I_{PV_inv} turns to become a fixed-phase reference. But, as the frequency has not yet changed, the phase angle of the load must be the same as the utility's phase angle just before it disconnects and as a result the V_{pcc} must "jump" to this new phase as shown in Fig. 8. At the next zero crossing of the V_{pcc}, this will result in a phase error between the "new" V_{pcc} and the I_{PV_inv} which can be used to detect an islanding. If this phase error is over the setting threshold values, the controller can stop the operations of the inverter [15]. Hence, the difficulty comes in the threshold selection as the NDZ of the PJD depends on pf and the pf in the island depends on the local load in the island [30].

Detection of Voltage and Current Harmonic

The Detection of Voltage and Current Harmonic technique is based on the measurement of the Total Harmonic Distortion (THD) at the PCC. A comparison is made between the measured values and the defined threshold, the inverter's operation will cut off in case when the measured value exceeded the defined threshold [38].

When the utility grid is connected, the V_{pcc} refers to the grid voltage. This forces a low-distortion sinusoidal voltage across the load terminal which, in turn, induces the linear load to draw an undistorted sinusoidal current. Therefore, harmonic currents produced by the inverter will flow into the low impedance grid through PCC. This harmonic current is kept small and the utility impedance is generally low. The interaction of this harmonic current with the minimal utility impedance will only produce a very small amount of distortion at the V_{pcc}. Normally, the THD of the V_{pcc} is below the detection point when the inverter is connected to the utility grid [30]. For that reason, the harmonic distortion can be considered as negligible (THDv $\approx$ 0) in this condition.

However, when an islanding condition takes place, the current harmonics produced by the inverter is transmitted to the load which ordinarily bears higher impedance than the grid. The interaction of the harmonic currents and the utility impedance generates a great, measureable distortion at the V_{pcc}. Thus, the THD variations exceeded the defined thresholds and can be used to detect an islanding [39]. There are two mechanisms that can cause the harmonics in V_{pcc} to increase during an islanding. The first mechanism is the switching process of the PV inverter itself. The PV inverter will produce current harmonics in its AC output current as a nature of all switching power converters. Hence, it is typical to expect a grid-connected PV inverter to produce a THD of less than 5 % of its full rated current. Second, when the utility grid disconnects, the harmonic currents interacting with the larger load impedance will produce a larger voltage harmonic in V_{pcc} [40]. This is due to the fact that the low utility impedance has been disconnected and only the local load impedance remains. In general, the load impedance is higher than the utilities. The harmonic currents produced by the inverter will flow into the local load leading to an increase in harmonics at the PCC. These voltage harmonics, or the change in their levels, can be detected by the inverter. This will trigger the operation to be discontinued [30].

When an islanding occurs, the THD of the local load will naturally increase to that of the inverters themselves. This offers a very secure method of detection of an anti-islanding because, commonly, there are no other sources of THD that would match the inverter. This method is advantageous due to the fact that its effectiveness is preserved even with multiple inverters. Yet, as a drawback, this method will induce high quality loads to filter out the distortion. If this filtering effect is strong enough, the distortion response will be too small which, in turn, may reduce the THD below the islanding trigger thresholds. The detection is more difficult in a system without a transformer inside the disconnected point. This is because the transformer has nonlinear effects that produce unique 2nd and 3rd harmonics, which are easily measurable. However, the largest problem is that the modern inverters attempt to lower the THD as much as possible, in some cases to immeasurable limits. Thus, they are sensitive to the grid perturbations which render the threshold establishment more difficult for an islanding detection. In addition, with nonlinear loads, the voltage distortion at the PCC can be so high that a fault may be mistakenly detected even if the grid is present. Conversely, with linear loads, the THD variation may be too low to be detected [49].

Other Passive Islanding Detection Methods

Apart from the aforementioned methods, many other passive methods have been developed. For example, a new islanding detection was proposed by authors in [50]. Based on State Estimators method, this proposed islanding detection method is concerned with the application of a voltage-oriented control combined with

resonant controllers. The algorithm is based on a grid voltage control without sensors, which is ordinarily sensitive to the system perturbations. This algorithm, integrated in a grid voltage estimator on the controller, detects the variations of the estimated harmonic content and the real harmonic content. Furthermore, Kalman filters algorithm is implemented in this method in order to estimate the 3rd and the 5th harmonics of the grid voltages. The corresponding energy mismatch between the estimated 3rd and 5th harmonics and the measured values are used to detect an islanding condition [49].

Authors of [51] reported a new passive method known as the Detection of Voltage Unbalance and Total Harmonic Distortion. Two newly proposed system parameters are used in the detection of an islanding, namely the voltage unbalances and the THD of the current. Nevertheless, the voltage magnitude used in the conventional islanding detection methods is also used here. This new method diagnoses the operating condition of the DG by monitoring the change of these three parameters. This method detects an islanding effectively and is not affected by the variations of the DG loads as it has a good selectivity for islanding and non-islanding conditions. However, this method does not solve the issues and the difficulties found in the high Q factor detection, and the threshold is still difficult to be determined [37].

3.1.2 Active Method

Active islanding detection methods involve the injection of a small disturbance signal to certain parameters at the PCC. Then, the response of the DG is monitored at the time the disturbance signal is injected [37]. The concept of this method is based on the relative significance of a weak signal at two instances: (1) grid is supplying power to the load and (2) grid no longer supplies power to the load. To be exact, a small disturbance signal will become significant once the utility is no longer connected and ceased acting as the reference power, which in turn will trigger the inverter to cease power conversion. The values of system parameters will also vary during the cessation of power conversion. By measuring specific corresponding system parameters, islanding event can be detected [26]. Active methods involve some feedback control technique to detect the changes in the parameters such as the frequency or the voltage at the PCC [25].

Active method can detect islanding accurately due to the method reduced or even eliminate the NDZ effectively. However, the complexity of an implementation increase because of the additional circuit required to create suitable disturbances. On the other hand, the additional circuit may create problems on the power quality, for example, the deterioration of the grid voltage quality and the system instability [13, 14].

There are many active islanding detection methods. Some of the most popular ones are used in the grid-connected PV systems as shown in Fig. 9, together with

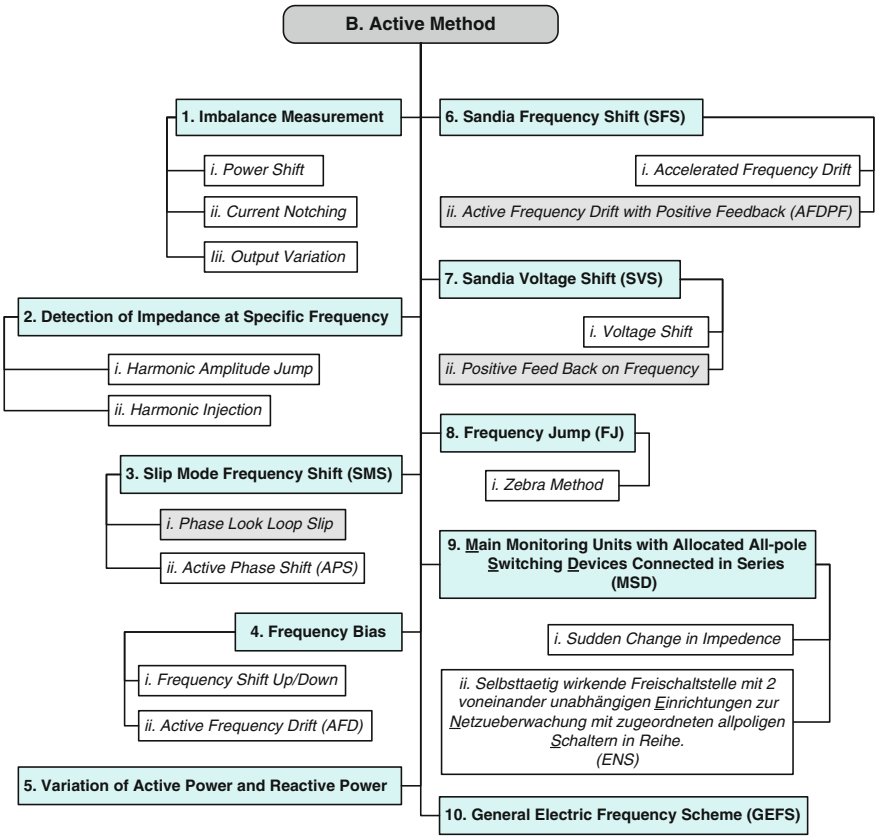

Fig. 9 The active islanding detection methods

their alternative names based on similarity of their principle of operation. The basic operation flow of an active islanding detection procedure is shown in Fig. 10.

Impedance Measurement

An Impedance Measurement measures the overall impedance of the circuit fed by the inverter. The inverter supplies a current source I_{PV_inv} to the utility and injects excessive current that acts as disturbance signals at specific times [13]. The frequency of this excessive current is different from the one of the utility grids under normal circumstances. When the grid is connected normally, it would have no effect on the measured voltage at the PCC because, as an effective infinite current source, the utility grid will absorb the excess current and tolerate the small frequency difference [37], as shown in Fig. 11a. However, in an islanding event, where the grid is disconnected, excessive current flows through the RLC load, as shown in

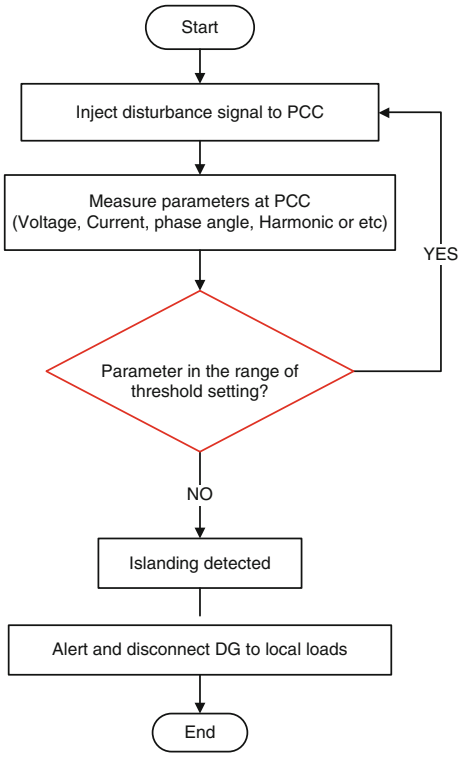

Fig. 10 The flowchart of the active islanding detection method

Fig. 11b. This will induce a voltage change in the PCC. Once a disturbance (voltage change) occurs, the detection of an islanding becomes permissible since even small disturbances are relatively significant once the grid is disconnected [34].

When the PV inverter behaves as a current source, it supplies the current (10) to the utility.

$$i_{\mathrm{PV\_inv}} = I_{\mathrm{PV\_inv}} \sin(\omega_{\mathrm{PV}} t + \phi_{\mathrm{PV}}) \tag{10}$$

where $I_{\mathrm{PV\_inv}}$ is the inverter's current amplitude ($i_{\mathrm{PV\_inv}} = I_{\mathrm{PV\_inv}} + I_{\mathrm{disturbance}}$), ω_{PV} is the frequency, and ϕ_{PV} is phase angle. These three parameters can vary and modify or be set as a disturbance signal. A disturbance is normally added to the inverter output current ($I_{\mathrm{PV\_inv}}$). This will induce the output voltage at the PCC to suffer from the changes when the grid is disconnected. This variation is observed by the inverter when measuring the $\mathrm{d}V_{\mathrm{PCC}}/\mathrm{d}i_{\mathrm{PV\_inv}}$, hence this method is called Impedance Measurement method. In addition, this method is also called Output Variation method, Current Notching method, or Power Shift method [15]. Figure 11 shows the power flow of the Impedance Measurement method. This power flow can actually represent the power flow of most active islanding detection methods.

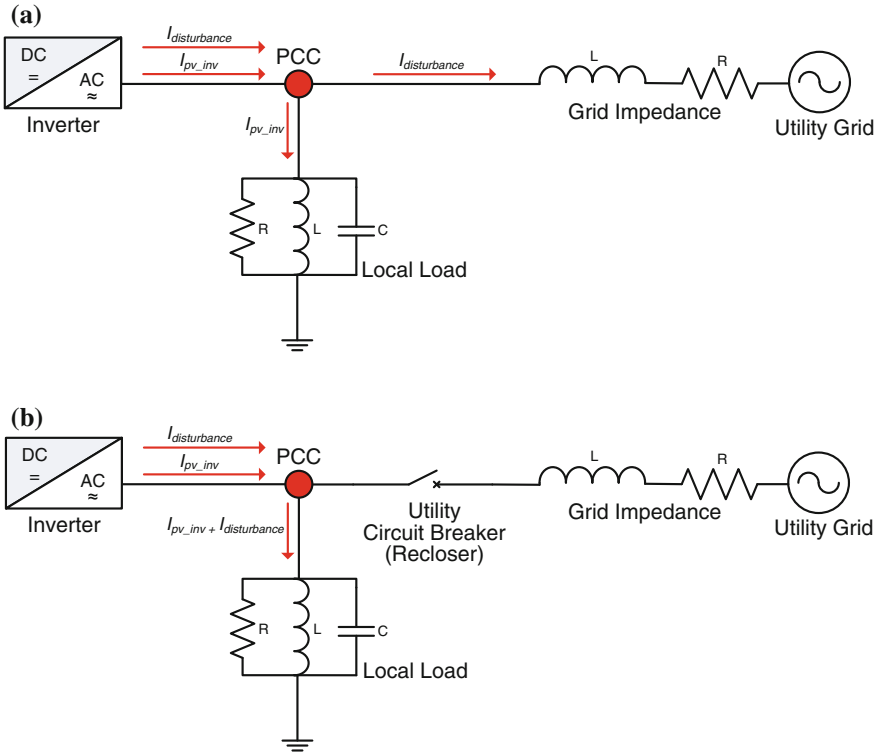

Fig. 11 The path of the disturbance signals during an islanding condition, **a** before the circuit breaker is opened and **b** after the circuit breaker is opened

Frequency Bias

Frequency Bias is a method that injects a minimal frequency bias signal into the grid via the PCC but recovers it at the end of every half cycle by jumping back into phase when the voltage passes the zero crossing. This method is also known as Active Frequency Drift (AFD) where the method uses a positive feedback by creating a slightly misaligned phase angle of the inverter output current. However, the power factor remains closer to the utility grid and resets itself every half cycle as shown in Fig. 12. The inverter phase angle is given by (11) [39, 52].

$$\phi_{\mathrm{PV}} = \pi f t_{\mathrm{Z}} = \frac{\pi \delta_{\mathrm{f}}}{f_{\mathrm{n}} + \delta_{\mathrm{f}}} \tag{11}$$

where t_{Z} is a dead time or zero time, δ_{f} is forcing current frequency, and f_{n} is nominal Frequency.

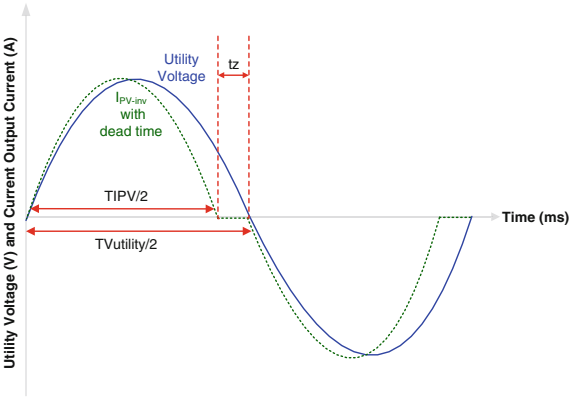

Fig. 12 Frequency bias islanding detection method: distorted current waveform

As refer to Fig. 12, T_{IPV} is the period of one cycle of the sinusoidal inverter current output waveform ($I_{\mathrm{PV\_inv}}$) and T_{Vutility} is the period of one cycle of the sinusoidal utility voltage waveform. The Chopping Fraction (cf) is defined as (12) [30].

$$\mathrm{cf} = \frac{2t_{\mathrm{Z}}}{T_{\mathrm{Vutility}}} \tag{12}$$

During the first half cycle, the $I_{\mathrm{PV\_inv}}$ is a sinusoid with a frequency slightly higher than the utility voltage. When the $I_{\mathrm{PV\_inv}}$ reaches the zero crossing, it remains at zero for the time t_{Z}, before beginning the second half cycle. At the first part of the second half cycle, the PV inverter output current ($I_{\mathrm{PV\_inv}}$) is in the negative half of the sine wave from the first half cycle. When the $I_{\mathrm{PV\_inv}}$ again reaches zero, it remains at this level until the rising zero crossing the utility voltage. It is important to note that the zero time in the second half cycle is not fixed and needs not to equals t_{Z} [30].

When the utility grid is connected, cf is low because the utility grid will stabilize the V_{PCC} by providing a solid phase and a frequency reference. Once the utility grid is disconnected, there is a phase error between V_{pcc} and $i_{\mathrm{PV\_inv}}$ waveforms [37]. The PV inverter will increase the frequency of $i_{\mathrm{PV\_inv}}$ in order to eliminate the phase error. The zero crossing of the voltage response of the load again advances in time with respect to where it was expected to be, and the PV inverter will still detect a phase error and will increase its frequency accordingly [13]. This repetitive cycle result in a constant increase in the value of cf, until the frequency has drifted far enough from ω_0 to be detected by the over/under frequency protection (OFP/UFP). This will finally trigger a stop in the inverter operation. For more details about AFD, please refer to [52].

Sandia Voltage Shift

Sandia Voltage Shift (SVS) uses the Positive Feedback, based on the amplitude of the voltage at the PCC, to prevent an islanding. When the utility grid is connected, the effect on the power of the system will be very small or none at all. But once the utility is disconnected, there is a reduction in the V_{pcc}. According to the load impedance's relationship, this reduction will continue and, as a result, the current and the power output will deteriorate. This reduction in the amplitude of the V_{PCC} will be significant enough to be detected by the UVP. At this point, it is possible either to increase or decrease the power output of the inverter, leading the OVP/UVP to trip and stop the inverter operations [13, 30, 37].

Sandia Frequency Shift

Sandia Frequency Shift (SFS) method, commonly known as Active Frequency Drift with Positive Feedback (AFDPF), is an improvement of the AFD method [39, 52]. The SFS creates a slightly misaligned phase angle at inverter output current while adding truncations—or "dead times"—to the current's waveform as shown in Fig. 13. Hence, the inverter's output current frequency will be forced to a different value than the grid's frequency [53–56]. The chopping frequency expressed in (13) is considered as being a function of error in the grid's frequency.

$$\mathrm{Cf} = \mathrm{Cf_o} + K(f_a - f_{line}) \tag{13}$$

where $\mathrm{Cf_o}$ is the chopping, K is an accelerating gain, f_a is the measured frequency of the V_{pcc}, and f_{line} is the line frequency.

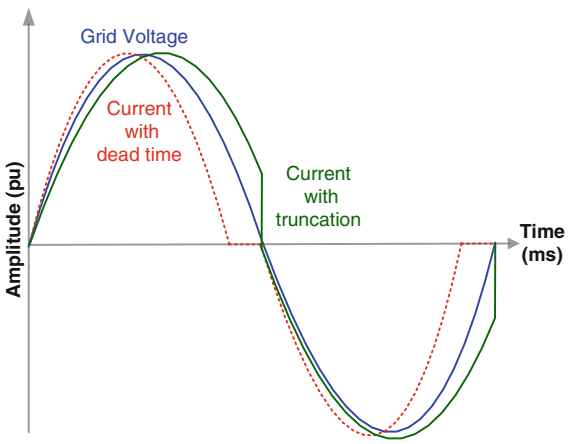

Fig. 13 The SFS islanding detection method: current waveform with dead time and truncation

When the utility grid is connected, the Cf is low because the utility grid stabilizes the V_{pcc} by providing a solid phase and a frequency reference. Once the utility grid is disconnected, a phase error arises between the V_{PCC} and the i_{PV_inv} waveforms [37]. This causes the PV inverter to increase the frequency of the i_{PV_inv} in order to eliminate the phase error. The voltage response of the load, again, has its zero crossing advanced in time with respect to where it was expected to be. At this time, the PV inverter continues to detect a phase error and continues to increase its frequency [13]. This result an increase in the value of the Cf until the frequency has drifted far enough from ω_0 to be detected by the OFP/UFP. Once this is detected it will stop the inverter operation.

Other Active Islanding Detection Methods

Numerous others active islanding methods have been reported in the literature. For instance, the Detection of Impedance at Special Frequency method is done by injecting a current harmonic of a specific frequency intentionally into the PCC via the PV inverter [30, 36]. Slip Mode Frequency Shift (SMS) is a method that forces the phase of the inverter's output to be slightly misaligned with the grid in order to cause a variation in the inverter current [22, 30, 34, 37]. Frequency Jump (FJ) is a modification of the Frequency Bias method. The FJ method relies on the insertion of a dead zone into the output current waveform on a specific number of cycles [13, 36]. Main Monitoring Units with Allocated All-pole Switching Devices Connected in Series (MSD) is a multiple detection method. It relies on the detection of the grid impedance by using two monitoring devices simultaneously [13, 49]. Variation of Active Power and Reactive Power method involves the injection of an active and reactive power from the inverter into the utility system [13, 49]. Active Current-disturbing Method by adding a periodical current without generating harmonic current to the system [57]. An Intelligent Islanding Technique Considering Load Balance with DGs for Distribution System is a method based on wide area measure and control aided by the pre-fault real time sampling [58].

3.1.3 Hybrid Anti-islanding Method

Hybrid anti-islanding methods have evolved from the need of overcoming a combination of both active and passive detection methods [34, 37, 59]. The hybrid methods involve two stages of detection procedures to overcome the problems of passive methods and active methods in order to achieve higher effectiveness [59]. During the detection procedure, passive detection method is used as a primary protection, then the active detection method is activated when an islanding situation is suspected by the passive method [34]. Figure 14 shows the basic operation flow for the hybrid islanding detection procedures.

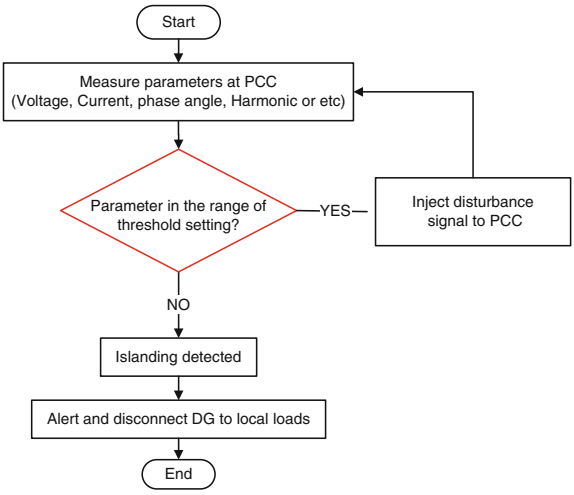

Fig. 14 The flowchart of the hybrid islanding detection method

Based on current researches on hybrid anti-islanding detection methods, it can be seen that most of those proposed in the literatures are applied in synchronous machines and three-phase systems, e.g.: the hybrid methods proposed in [21, 56, 59, 60, 61, 62]. Some other hybrid methods employ multiple system parameters to identify any possibility of an islanding operation based on data mining and artificial intelligence such as the methods proposed in [59, 62]. The islanding detection system proposed in [63] consists of a combination of UFP/OFP, UVP/OVP, SFS, and SVS methods. Another hybrid control algorithm proposed in [64] combines the advantage of SFS anti-islanding detection method with a Rate of Change of Frequency (RoCoF) detector relay. Although hybrid methods provide better effectiveness by detecting an islanding, at the present, only Japan requires renewable energy source DG systems to have at least one passive and one active islanding detection method implemented in a DG system [15]. This is because most of the proposed methods are still in the research and development stage and are yet to reach practical implementation in real systems.

3.2 Remote Anti-islanding Detection Method

Remote islanding detection methods are based on the communication between the utilities and the DGs, but the detection algorithm is typically situated at the utility side [30, 37, 49]. In most cases, communication between devices installed at both the utility side and the DG side must be maintained; a stoppage would alert the utility side of a possible islanding occurrence. The NDZ of remote methods is negligible. However, the higher reliability of these techniques relative to the local techniques comes at a cost; they are expensive to implement due to the need of

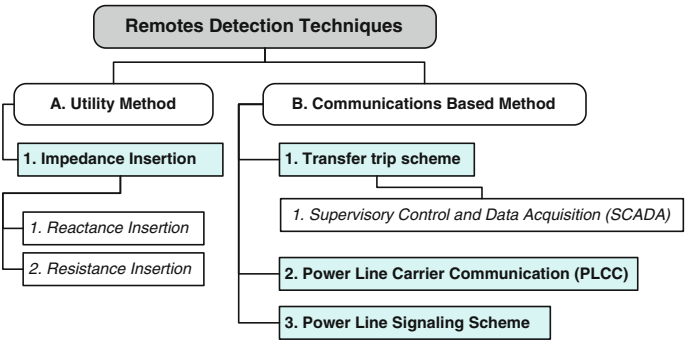

Fig. 15 Classification of remote islanding detection method

communication equipment. Hence, this method is only implemented in large-scale systems and/or in the presence of sensitive equipment. As shown in Fig. 15, two types of remote techniques are identified and classified, namely utility methods and communication-based method.

3.2.1 Utility Method

Utility methods require the installation of specific equipment at the utility side. Commonly, these are devices that modify the impedance that can be observed at the PCC during an islanding occurrence. Impedance insertion is an example of a utility method [30, 37, 49].

Impedance Insertion

Impedance insertion method involves the insertion of a low value impedance load at the head-end on the utility side, which remains disconnected from the PCC unless an islanding occurs, i.e., load is disconnected from the utility [65]. As a consequence to the insertion of the low impedance load, the power balance between generation and local load is modified [13, 14, 49]. However, there must be a sufficient delay between the instance and the utility is disconnected from the PCC and the instance, the impedance load, and the PCC is connected. This creates a significant interference in phase and the resonance frequency can be detected by the UFP limits. The topology of this method is presented in Fig. 16. A capacitor bank, the typically used impedance load, is added to point **a**, and the connectivity is controlled by a switch (**Switch a**). When an islanding happens, **Switch a** will close and the capacitor bank will be connected to the PCC after a delay.

It is necessary to have a short delay between the circuit interruption and the switching of the capacitor bank, because it is theoretically possible for a large capacitor to compensate an inductive load. As a result, the loads will be balanced and

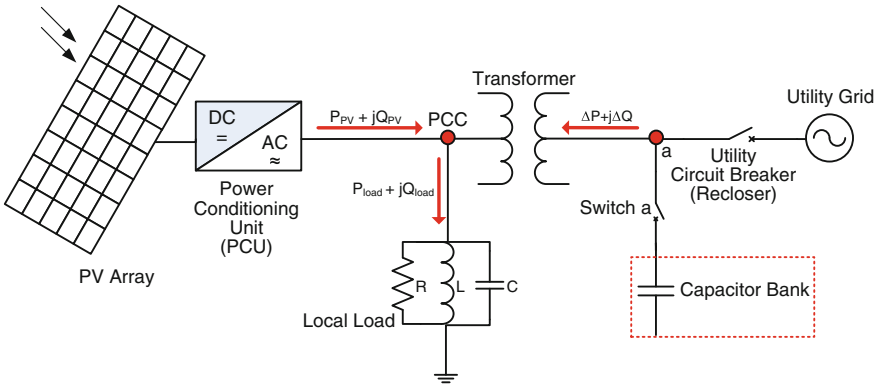

Fig. 16 Topology of Impedance Insertion Method, where a low value impedance load had been added to the utility

will cause islanding detection failure. By delaying the switching of the capacitor bank, the load would be highly inductive before connected to the capacitor bank and create a large frequency deviation upon disconnection. Hence, the short delay allows sufficient time for this frequency deviation to be detected [13].

Moreover, it is possible to use other similar methods in terms of operation principle called Reactance, Insertion, and Resistance Insertion. Instead of using a capacitive load, a resistive load and inductive load could also be used to cause significant change in voltage at **a**. Nevertheless, a capacitor bank is preferred because it is readily available and can be used simultaneously for reactive power support [13].

3.2.2 Communication Anti-islanding Method

As this method depends on the communication means, any issue occurring in the communication equipment will jeopardize the islanding detection. Communication base methods require additional devices to be installed at the utility end and at the DG end. Islanding detection is reliant on the constant communication between the paired devices at utilities side and at every inverter at the DG side [34]. When an islanding is detected, the device at the DG side would be triggered by default or by activation to cut off power to the local load. Implemented properly, NDZ in communication anti-islanding detection techniques can be eliminated completely. These techniques are more robust, accurate, and have a better reliability compared to any other local islanding detection technique. However, the communication equipments required for this method are uncommon and are extremely expensive. This makes these methods uneconomical to be implemented on small-scale DG systems [63]. As this method depends on the communication medium, any issue occurring in the communication equipment will jeopardize the islanding detection performance.

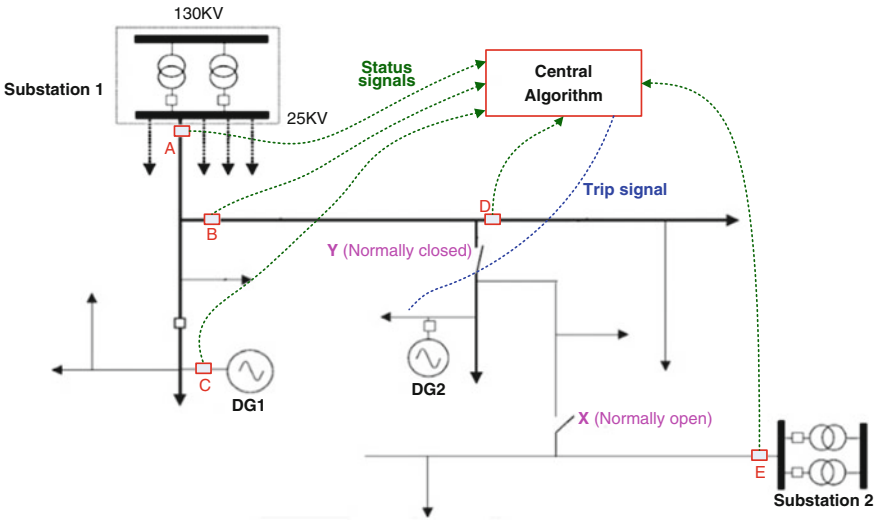

Fig. 17 The illustration of Transfer Trip Scheme in a distribution system [23]

Transfer Trip Scheme

The Transfer Trip Scheme works in conjunction with the Supervisory Control and Data Acquisition (SCADA) system to report the status of the circuit breakers and reclosers at the utility grid to the DG control system [66]. Hence, this method is also known as SCADA Islanding Detection method [13]. This method requires a reliable communication channel (radio communication, telephone line, internet broadband, wireless communication, fiber optic Ethernet, satellite communication and etc.) between the utility and the DG so that necessary actions can be taken within a stipulated time frame in the event of any abnormality in the system [37]. When a PV inverter is installed, the mechanism utilized by SCADA for an islanding prevention is straightforward. As shown in Fig. 17 it is implemented by connecting all the voltage-sensing devices installed at all local parts in the grid-connected PV system to a central algorithm [65]. When the DG is disconnected from the grid, the sensor at the particular islanded area will send a status signal to the central algorithm. Next, central algorithm will trigger alarms to alert the DG, and the power from the PV to the local load will be cut off. In addition, the same system can be used to synchronize the power at both ends of the system for reconnection once the fault clearance is confirmed [67].

Power Line Carrier Communication (PLCC)

Similar to Transfer Trip Scheme, PLCC system relies on the constant communication between devices installed at the utility side and at the costumer side (DG). However, the communication channel in PLCC is the utility power line, i.e., using

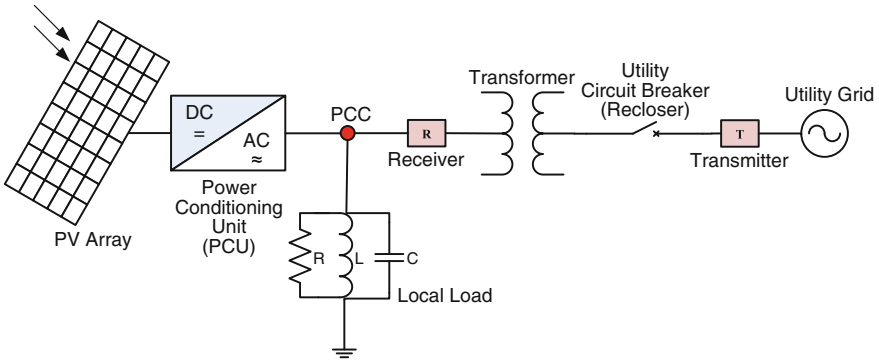

Fig. 18 Topology of power line carrier communication control with transmitter (T) and receiver (R) added to the system

the power line as a signal carrier, hence the name PLCC is given or called Distribution Line Carrier (DLC) [65]. As an additional bonus, it is possible to use the PLCC signal to perform a continuity test of the utility side and the DG side.

The basic operation of the PLCC is to send a low-energy signal between the transmitters (T) installed on the utility side and receiver (R) installed on the DG side [67]. When islanding occurs, the power and signal are simultaneously cut off from the DG. Hence the receiver (R) will fail to receive any communication signal from the utility. This will trigger a stopping signal from the receiver (R) to the PCU or to a switch to isolate the load from the DG [68, 69].

Figure 18 shows the typical system configuration for a PLCC islanding detection method. A device acting as a transmitter is installed between the utility circuit breaker or recloser and the utility grid. Another device acting as a receiver is installed between the PCC and the utility grid. A signal is sent from the transmitter (T) along the power line to the load and detected by the receiver. When a PLCC signal is lost, i.e., not detected by the receiver when it is supposed to, a break in the continuity of the line is suspected and the PCU will be instructed to cease operation or opens its own switch to isolate the load from DG [17, 67, 70].

One of the advantages for using this method is that it allows the use of an existing utility PLCC signal for the islanding prevention. It can be implemented without interfering with the normal utility use and without degradation to the information in the signal. The use of the PLCC method has been proposed as a way to solve many of the problems associated with inverter based islanding prevention methods [68, 69].

One of the similar methods to the PLCC that were developed is the Signal Produced by Disconnect (SPD). SPD differs from the PLCC method as it does not rely on the power line as it acts as the communication channel. Instead, the transmission of the signal from utility to DG is done via microwave link, telephone link, or other communication channels [30].

Other Communication Islanding Detection Methods

There are also several new communication-based islanding detection methods proposed in [35, 71, 72, 73]. The focus in researches nowadays is the communications between intelligent electronics devices (IEDs), in which IEDs are the microprocessor-based controllers of the power grid equipment [9]. Methods using synchro-phasors for islanding detection proposed in [5, 72, 73]. Distributed controlled islanding detection proposed in [71] is a combination of a vertical inter-substation BST (Binary Signal Transfer) signaling with a horizontal IEC 61850 GOOSE and messaging at the substation level [71].

4 Comparisons and Discussions

The available anti-islanding detection methods for islanding have been analyzed based on the characteristics such as local/remote, passive/active/hybrid, utility-based/communication-based, as presented in Table 1. In selecting a suitable islanding detection method, consideration should be focused on the different characteristics among the available detection methods. As can be seen from Table 1, each islanding detection method has its own advantages and disadvantages under different factor of considerations. A combination of two or more anti-islanding methods would give better solution for islanding detection in grid-connected PV systems. Nevertheless, detection times of all the discussed methods are within the standard, established in IEEE 929 and IEEE 1547. Other requirements of the standards are discussed in detail in [13, 16, 17, 18, 23, 74, 75].

A passive islanding detection method is a local detection method that does not affect the power quality, is relatively easy to install and does not require expensive equipment. Only a monitoring device is required at the PCC and a mechanism to cut off power from the DG when any irregularity power flow is detected. However, the NDZ using a passive islanding detection method is relatively large resulting in less effective detection. The threshold for cutting power supply from DG is also not easy to set as a high threshold might fail to detect an occurrence of islanding, while a low threshold could lead to false positives. Moreover, the reliability of passive islanding detection method is reduced in certain loads condition, most notably in a load-source balance condition. The passive islanding detection methods are preferred in larger PV grid-connected systems due to its ‘silent’ operation, i.e., does not affect the system stability and power quality. However, solely using passive islanding detection method is rarely adequate as the NDZ is large.

An active islanding detection method is a detection method that has a much smaller NDZ, especially when the Q factor load is low. In fact, some active islanding detection method can eliminate NDZ completely under favorable conditions. However, active islanding detection method means that one or more forms of disturbances must be introduced into the system before any islanding can be observed. Thus, this method causes degradation in power quality and system

Table 1 Comparison of islanding detection method based on various characteristics

Characteristics	Local method			Remote method	
	Passive	Active	Hybrid	Utility	Communication
Principle of operation	Uses monitoring of local parameter (voltage, current, frequency) detecting at PCC	Uses injection of external disturbance signal to PCC in order to drive the system operating point toward the threshold	Uses the principle of both active and passive methods	Uses additional element such as impedance at the point of utility to alter the impedance, so that the impedance seen from PCC is modified during islanding	Based on the bridge (communication) between the grid and DGs by using communication equipment
NDZ	Large	Small	Small	None	None
Response time	Fast	Slightly faster than passive method	Slower than active method	Fast (depends on the size of capacitor)	Very fast
Operation failure	Possibility is high without proper setting of tripping threshold, especially true for a small mismatch of power between utility grid and the local load	Possible in high Q factor	Possibility lower than only use passive or active method	Possible if the value of impedance is out of the minimum phase variation	Impossible unless damage on communication equipment
Effect on distribution system	None	Impact to power system	The impact is lower than active method	None	None
Implementation cost	Cheap (least hardware)	Moderate (additional devices and circuitries required)	Expensive (consist of hardware required at passive and active methods)	Very expensive (reactive power and active power compensator such like capacitor bank required)	Extremely expensive (dedicated communication system required)

(continued)

Table 1 (continued)

Characteristics	Local method			Remote method	
	Passive	Active	Hybrid	Utility	Communication
Effectiveness	Depends on consumption and supply condition (less efficient on source-load balanced condition)	Effective (can detect islanding even in source-load balance condition)	Very effective	Very effective	The most effective
Allow multiple DGs operation	Possible	Not possible	Possible	Possible	Possible
Influence by the number of connected inverter	None	Yes	Yes	None	None
Degradation of power quality	None	Yes	Yes (lower than active method)	None	None

stability to a varying degree. The issue becomes more significant as more inverters are connected to the DG. Most of the active islanding detection methods are only applicable to small-scale PV grid-connected systems. At present, many researchers focus heavily on improving active islanding detection methods as shown in Fig. 9. Among the active islanding detection methods, the SVS and SFS methods are highlighted for their ability to effectively detect islanding with the least power degradation and are relatively easy to implement [26].

A communication-based islanding detection method provides the best performance in terms of effectiveness and efficiency among the discussed detection methods. The monitoring and control devices are installed and maintained by the utility side rather than at the PV owner. In general, communication-based islanding detection method has no NDZ and has been satisfying response time, but is extremely dependent on the seamless communication between each paired devices at the utility side and the DG side. Thus, the cost of implementation is substantially higher than multiple expensive telecommunications devices and sensors are required for this method. Because of this, communication-based method is only used when the utility prioritizes system stability and power quality over the islanding detection system cost, i.e., large-scale systems with sensitive loads.

In each method discussed above there are limitations such as the reliability of detection, perseverance of power quality, and cost of implementation. In order to overcome these weaknesses, hybrid systems consisting of two or more of the aforementioned methods have been proposed. Even so, hybrid islanding detection systems are still at its infancy. Such systems put in the real world grid-connected PV system is only found in Japan [76]. As such, more research and development efforts on islanding detection systems have to be done in order to provide an affordable, safe, and reliable way to prevent and resolve islanding in a grid-connected PV system.

5 Simulation of Islanding Mode Control

5.1 Simulation of the Voltage and Frequency Protection

The simulation was conditioned by referring to the Malaysian Standard, namely MS IEC 61727 and MS IEC 62116 [77, 78], where the normal operating voltage at the PCC is between 85 and 110 % of the grid voltage; the frequency at the PCC is in the range of 98–102 % of grid frequency. As shown in Table 2, the operation window is in a grid with based voltage of 230 V is 196–253 V, so voltage protection is minimum and maximum tripping point will be set at 195 and 254 V, respectively. The minimum and maximum frequency test points for determining proper operation of the frequency trip function should be 48 and 52 Hz, respectively. The simulation model has been developed to test the frequency (FPCC) and the root mean square voltage (VRMS) at the PCC, where the grid disconnection

Table 2 Voltage and frequency limits for VFP under standard MS IEC 61727 and 62116

Standard	Voltage at PCC		Clearing time (s)	Frequency at PCC	Clearing time (s)	Quality factor	Power quality	
	V_{RMS}			Utility frequency 50 Hz		Q_f	THD_v (%)	THD_i (%)
System $\leq$ 10 kVA	Base voltage %	Base voltage 230 V						
MS IEC 61727:2010	$V < 50$	$V < 115$	0.1		0.2		<5	<5
	$50 \leq V < 85$	$115 \leq V < 196$	2	$f < 49$ Hz		1		
	$85 \leq V \leq 110$	$196 \leq V \leq 253$	Normal	$f > 51$ Hz		MS IEC 62116:2012		
	$110 < V < 135$	$253 < V < 311$	2					
	$135 \leq V$	$311 \leq V$	0.05					

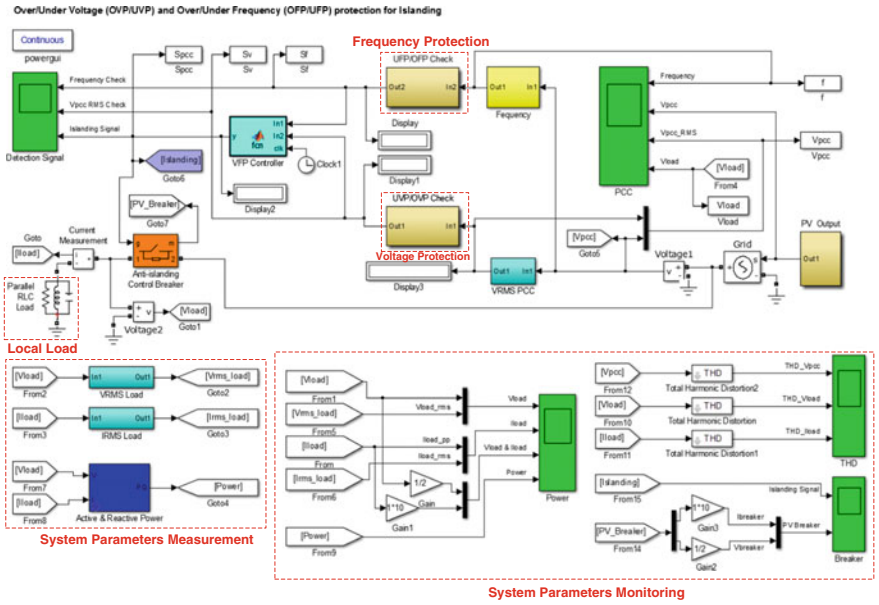

Fig. 19 The VFP simulation model in MATLAB/Simulink

Table 3 VFP method simulation parameters

V_{ref}	V_{min}	V_{max}	f_{ref}	f_{min}	f_{max}	Q_f	Power
V_{rms} (V)			Hz				
230	196	253	50	49	51	1.0	P = 1000 W
							Q_L = 1000 VAR
							Q_C = 1000 VAR
						2.5	P = 1000 W
							Q_L = 2500 VAR
							Q_C = 2500 VAR

was set at t = 0.2 s. Therefore, the clearing time for UFP/OFP detection must be less than t = 0.4 s, and the UVP/OVP detection time must be less than t = 2.2 s.

Figure 19 shows the complete simulation model of the VFP method. The control system is designed to monitor the RMS voltage and frequency at the PCC. In the case when either or both the RMS voltage or frequency exceeded the limits as indicated in Table 3, it will stop supplying power to the local load by triggering the PV breaker.

The simulation is involved by gradually changing the frequency. This caused the appearance of ripples in the output of the RMS due to the fundamental frequency which is identified to be 50 Hz. The occurrence of Hysteresis error due to this ripple will result in error detections of OVP/UVP.

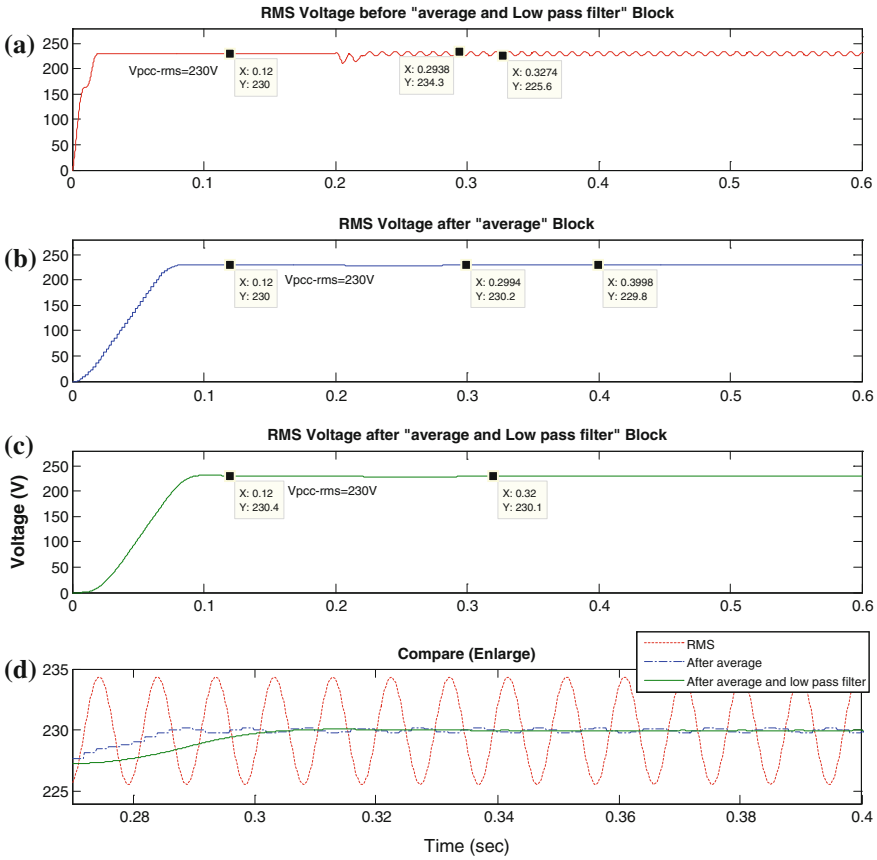

Fig. 20 The RMS voltage when the frequency of the instantaneous voltage input is increasing from 50 to 52 Hz at t = 0.2 s: **a** before filter or before the Average and low pass filter block; **b** after the Average blocks; **c** after filter or the Average and low pass filter block; **d** comparisons of (**a**–**c**)

Figure 20a shows the RMS voltage when the frequency of the instantaneous voltage input was increased from 50 to 52 Hz at t = 0.2 s. The ripple voltage is 3.78 % after the frequency changes. The output voltage after adding the average blocks is shown in Fig. 20b. The ripple is significantly reduced compared to the previous conditions, where the ripple voltage is 0.17 %. Finally, a Discrete second-order filter blocks, which is defined as a low pass filter used to enhance the output of the RMS value. Figure 20c shows the RMS voltage after the block Average and low pass filter; thus the ripple voltage is almost eliminated. Figure 20d shows an enlarged portion of the ripple voltage under the three different conditions.

For Q_f = 1.0, the simulated output waveforms for normal operation are shown in Fig. 21. The output waveforms for the cases of under frequency are shown in Fig. 22, while the results for the cases of over frequency are presented in Fig. 23.

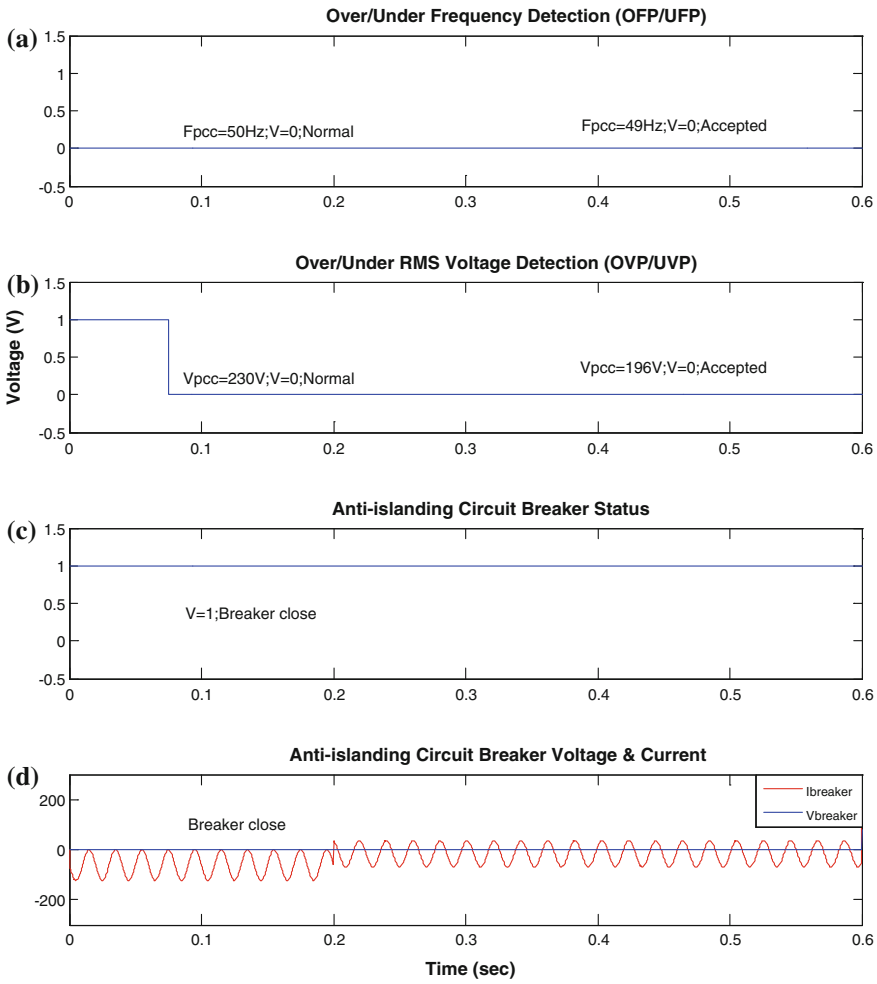

Fig. 21 The detection signals for VFP under the normal operation, V_{pcc} = 196 V and F_{pcc} = 49 Hz: **a** OFP/UFP checker, $V = 0$; **b** OVP/UVP checker, $V = 0$; **c** VFP controller, $V = 1$; **d** circuit breaker maintains at closed status

The waveform pattern for different groups and cases are similar, while the value differs according to parameters in each case.

5.2 *Simulation of the Active Frequency Drift*

Figure 24 shows the entire simulation model for the AFD anti-islanding control. This control is designed to monitor the V_{pcc} and F_{pcc}.

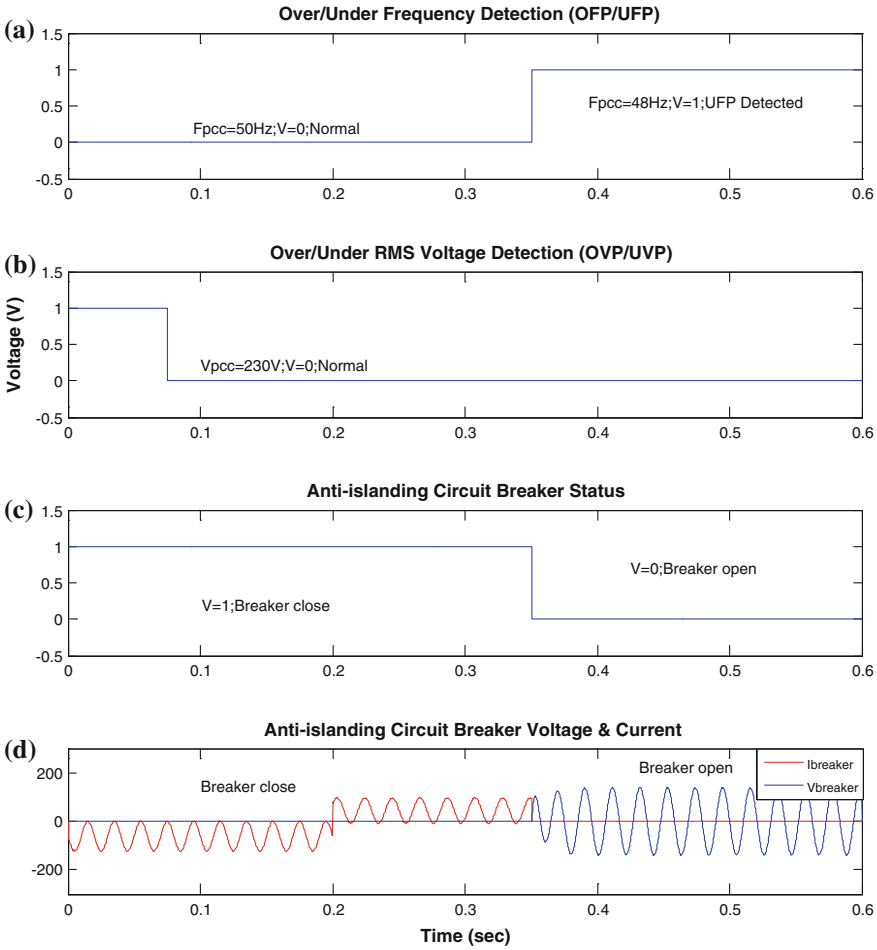

Fig. 22 The detection signals for VFP under the UFP operation, V_{pcc} = 196 V and F_{pcc} = 48 Hz: **a** OFP/UFP checker trigger UFP at t = 0.3504 s, V = 1; **b** OVP/UVP checker, V = 0; **c** VFP Controller detects islanding at t = 0.3506 s, V = 0; **d** circuit breaker opens at t = 0.3506 s

The simulation module included an inverter circuit connected to a utility grid control and AFD islanding detection section at the PCC. The V_{PCC} and I_{pv_inv} are in phase in the initial setting. The grid supply is set to 110 Vrms/50 Hz. By using the Step block, the circuit breaker is set to disconnect the grid from the local load at t = 0.1 s. The RL filter is set to L = 6 mH and R = 0.01 Ω, respectively.

The AFD anti-islanding method determines the occurrence of islanding based on the logical path in the figure. First, the frequency data is taken and tested against the

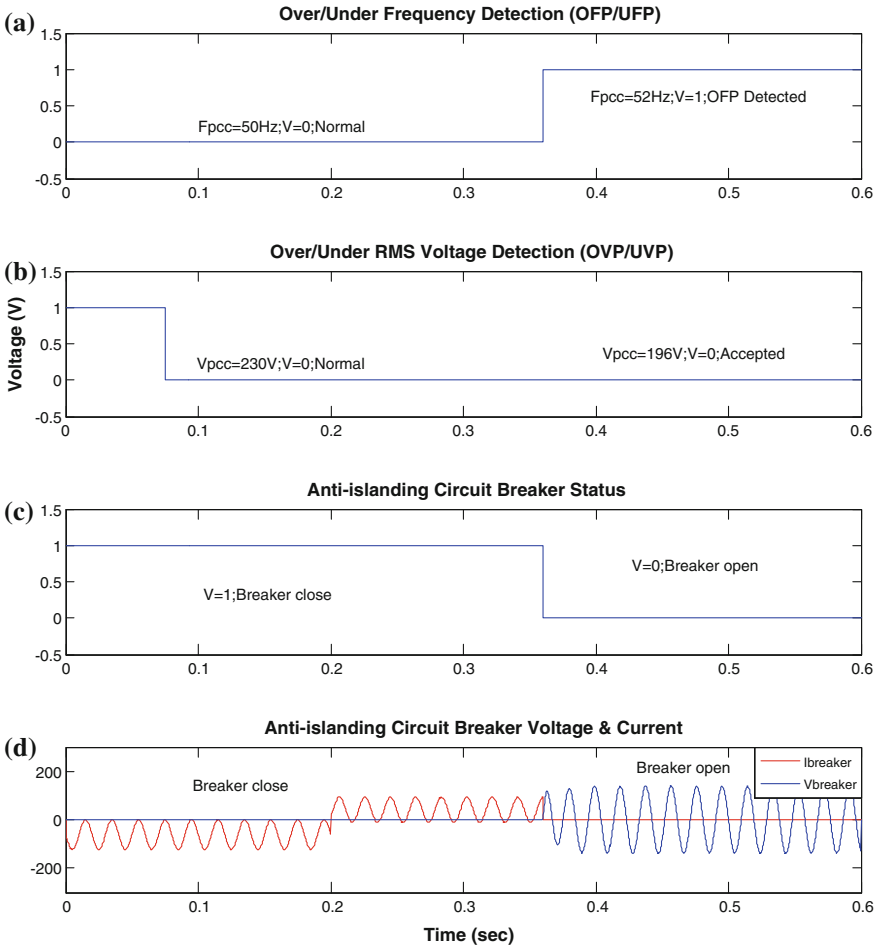

Fig. 23 The detection signals for VFP under the OFP operation, V_{pcc} = 196 V and F_{pcc} = 52 Hz: **a** OFP/UFP checker trigger OFP at t = 0.3602 s, V = 1; **b** OVP/UVP checker, V = 0; **c** VFP Controller detects islanding at t = 0.3602 s, V = 0; **d** circuit breaker opens at t = 0.3602 s

UFP/OFP threshold. If it is out of the threshold, then islanding definitely occurred. Otherwise, further testing using AFD is required because islanding within NDZ may have occurred but not detected. In order to proceed, a source with frequency modified by the cf is then injected into the inverter output current every half cycle and every full cycle to produce a t_Z on the output current waveform. In case of islanding, the value of the cf will slightly increase every half cycle to drift the current frequency from voltage frequency until islanding is detected. Then, a signal

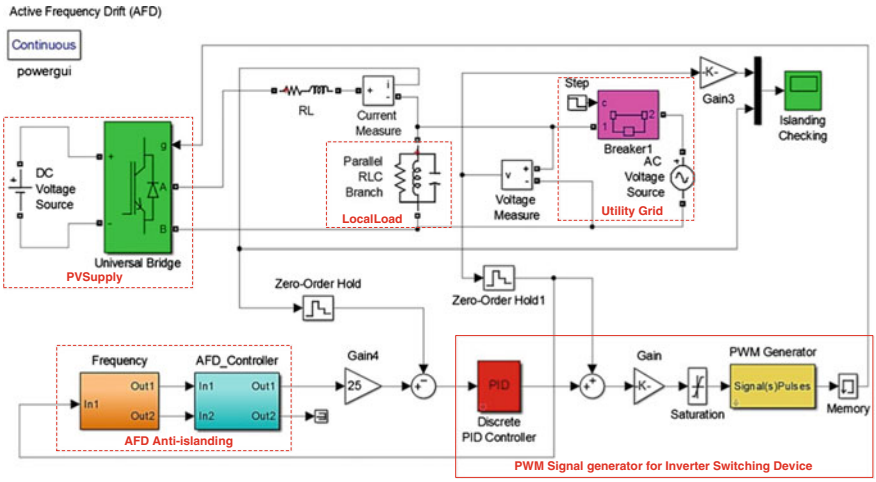

Fig. 24 The AFD simulation model in Simulink

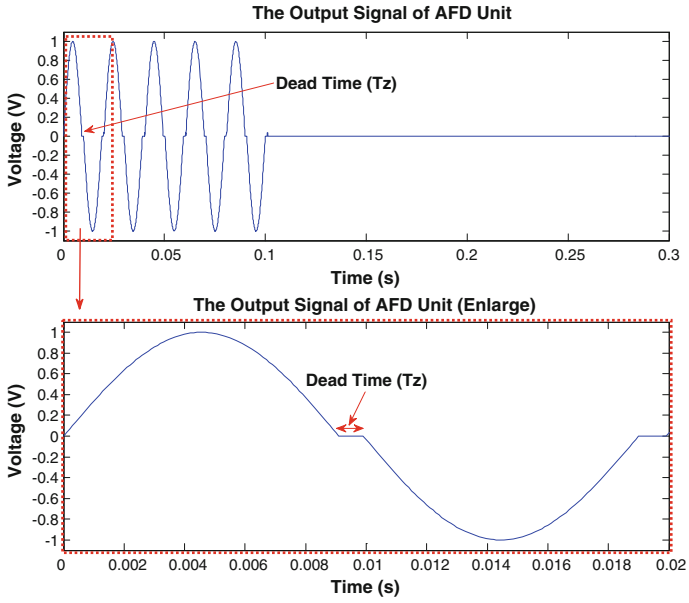

Fig. 25 The AFD signal generated from the AFD Controller

will be sent to stop the inverter from operating. If there is no islanding occurred, the cf is small enough to be simply absorbed by the grid. Figure 25 shows the AFD signal.

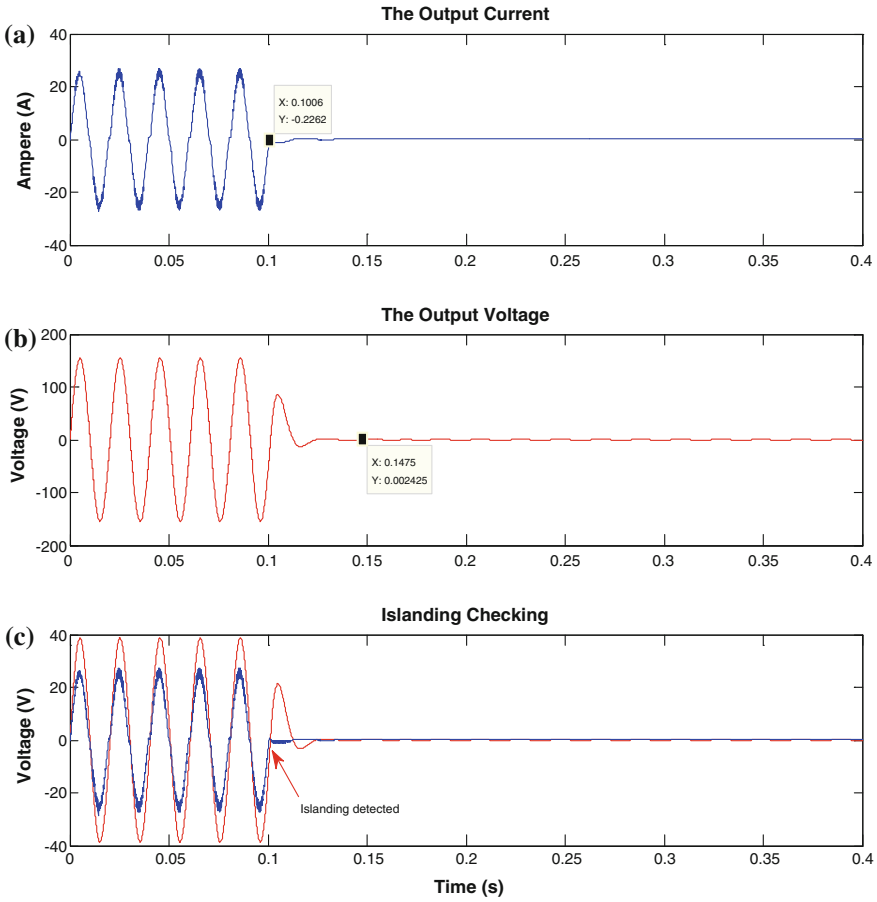

Fig. 26 The simulation output of AFD for F_{pcc} = 49.4 Hz, cf = 0.049: **a** islanding detection time, t = 0.1006 s; **b** the load V_{pcc} stop at t = 0.1475 s; **c** islanding detected

A few simulation cases have been conducted using the simulation model as shown in Fig. 24. All the cases are tested in both Q_f = 1.0 and Q_f = 2.5.

Figures 26, 27, and 28 show the simulation output of AFD, where (a) is the islanding detection time detect by AFD, (b) is the load voltage stop time, and (c) is the inverter output current injected by a disturbance signal delaying the phase angle compared to the voltage output. This disturbance signal became significant once the grid was disconnected, then the AFD detected the occurrence of islanding and signaled the PV to disconnect from the local load.

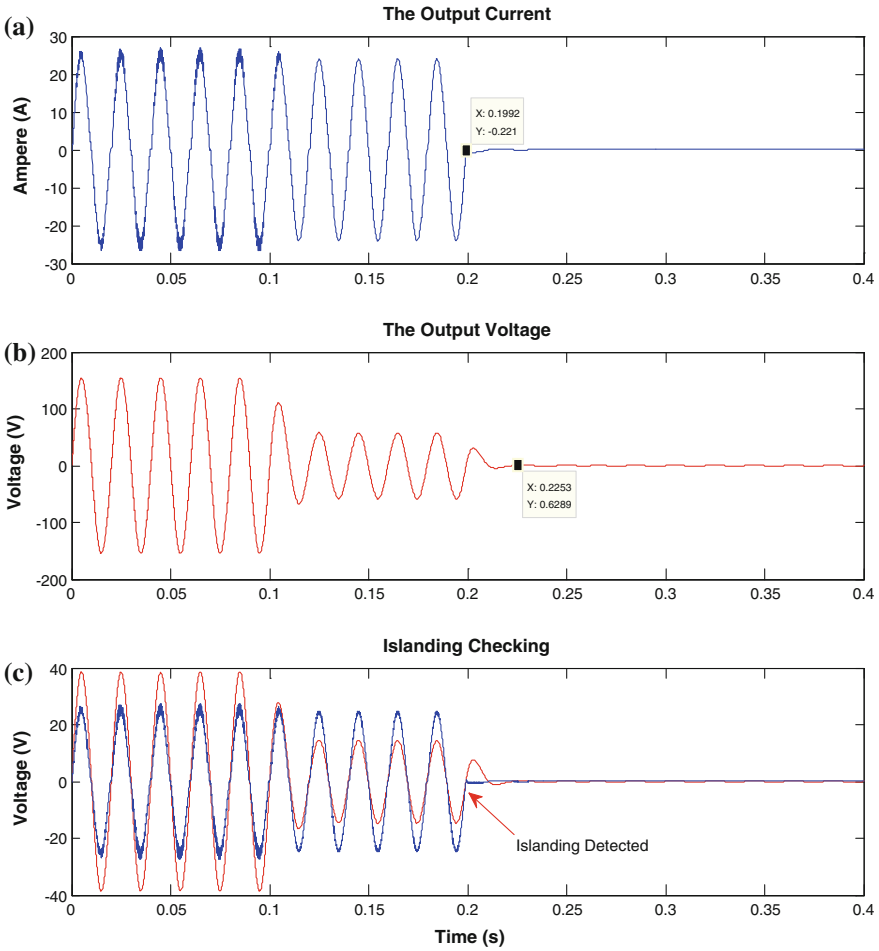

Fig. 27 The simulation output of AFD for F_{pcc} = 50.0 Hz, cf = 0.05: **a** islanding detection time, t = 0.1992 s; **b** the load V_{pcc} stop at t = 0.2253 s; **c** islanding detected

Figure 26 shows the results for, when F_{pcc} = 49.4 Hz, cf = 0.0494, and Q_f = 1.0, islanding detection time, t = 0.1006 s and V_{pcc} fully stopped at t = 0.1475 s with THD_i = 8.95 % and THD_v = 0.02 %. Figure 28 shows the results for, when F_{pcc} = 50.0 Hz, cf = 0.05 and Q_f = 1.0, the islanding detection time, t = 0.1992 s and load V_{pcc} fully stopped at t = 0.2253 s with THD_i = 6.98 % and THD_v = 0.01 %. Figure 29 shows the results for, when F_{pcc} = 50.4, cf = 0.0504 and Q_f = 1.0, the detection time t = 0.1008 s and V_{pcc} fully stop at t = 0.1455 s with the THD_i = 6.14 % and THD_v = 0.01 %.

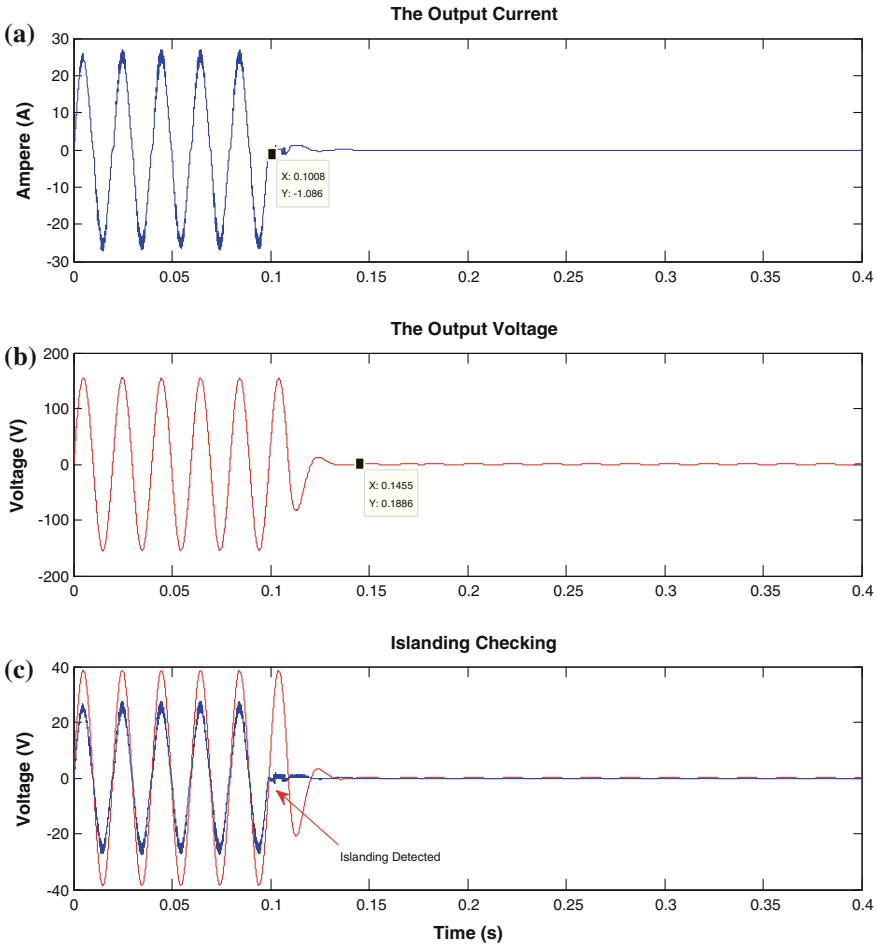

Fig. 28 The simulation output of AFD for F_{pcc} = 50.4 Hz, cf = 0.0504: **a** islanding detection time, t = 0.1008 s; **b** the load V_{pcc} stop at t = 0.1455 s; **c** islanding detected

Besides, the simulation results also show that longer time are required to trigger an islanding detection for frequencies with values close to the reference value. As shown in Fig. 29, the detection time took about 0.01 s longer when F_{pcc} = 50 Hz (t = 0.1992 s) is compared with F_{pcc} = 49.4 Hz (t = 0.1006 s) and F_{pcc} = 50.4 Hz (t = 0.1008 s).

In addition, Fig. 30 shows that the run on time is proportional to the Q_f. Take case 5 (F_{pcc} = 50.4 Hz, and cf = 0.0504) as an example, the voltage transient stop at t = 0.1455 s for Q_f = 1.0, however, the voltage transient stop at t = 0.1902 s for Q_f = 2.5. V_{pcc} took a longer time to completely stop in the case Q_f = 2.5 as compared with the case of Q_f = 1.0.

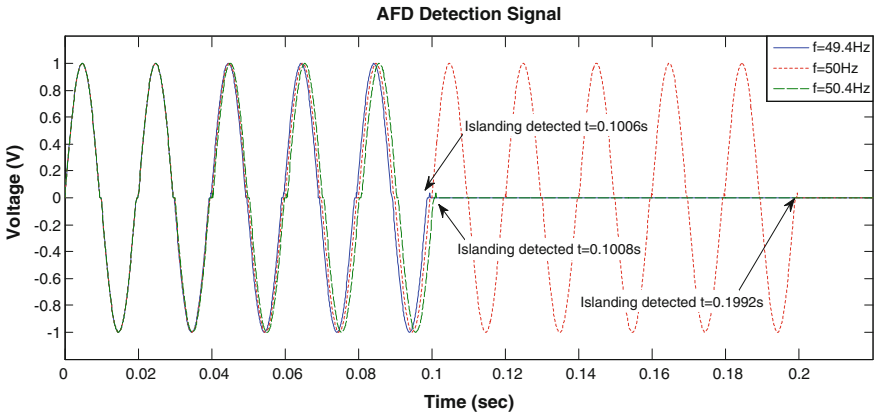

Fig. 29 Comparison of detection time with various frequency for case, Q_f = 1.0: F_{pcc} = 49.4 Hz (*blue line*); AFD islanding detection at t = 0.1006 s. F_{pcc} = 50.0 Hz (*red dotted line*); AFD islanding detection at t = 0.1992 s. F_{pcc} = 5.04 Hz (*green dotted line*); AFD islanding detection at t = 0.1008 s

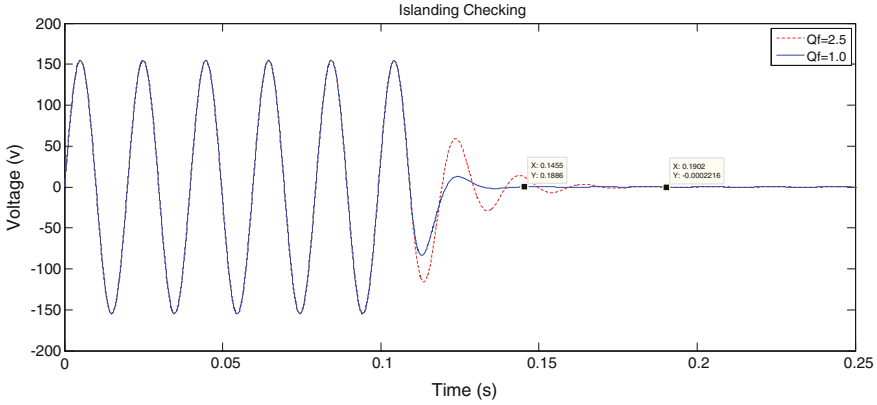

Fig. 30 Comparison of run on time with different Q_f for the case F_{pcc} = 50.4 Hz, cf = 0.0504: Q_f = 1.0 (*blue line*), the voltage transient stop at t = 0.1455 s; Q_f = 2.5 (*red dotted line*), the voltage transient stop at t = 0.1902 s (Color figure online)

6 Conclusion

This paper summarized the fundamental principle and operation of available anti-islanding methods that are suitable for PV grid-connected systems. It also outlines the advantages and disadvantages of each reviewed methods. In general, anti-islanding methods can be classified into four major groups, which include passive, active, communication-based methods, and hybrid methods. Active anti-islanding methods have been preferred over the years due to its small NDZ

when implemented for a small-scale distribution generation. The passive methods are typically affordable to implement and simple to install compared to active methods. However, DG systems using passive islanding detection methods suffer from large NDZ that severely affects the system performance. In contrast, the communication-based methods inherit the advantages between active and passive methods. Communication methods are less destabilizing to the power system and more significantly, these methods have negligible NDZ. The only drawback of communication methods is the high implementation cost. The hybrid method is another detection method that is evolved from the combination of both active and passive methods. This method has been proven to achieve more effective and efficient anti-islanding detection by many researchers, as compared to active or passive method that act alone. In short, it is not wise to define a generic method for a specific application (islanding detection in grid-connected PV systems) because each detection method is governed by its nature of application and associated system elements. Besides that, the setup and operation cost is also a vital factor when selecting a suitable method to implement practically in a real system. Therefore, the selection of islanding detection method has to be made based on the understanding of the actual probability of islanding occurrence in a particular system, and also the risks and costs associated with the deployment of each method. This is to ensure that the detection and control system is reliable, as well as to minimize system cost and to maintain the system quality and safety. Most importantly, the selection of suitable anti-islanding methods must comply with the islanding detection and control requirements established by each country's national electrical rules and regulations. Due to the stringent conditions set by the authorities, most researches are essential to develop better islanding detection methods to meet the requirements. The chapter ends with the simulation results of both passive and active methods as well as the results discussion and analysis. From analysis of the simulation results, we can conclude that the VFP method is heavily dependent on the monitoring of frequency and RMS voltage at the PCC, and the accuracy of both these parameters are key factors to determine the reliability of the VFP method.

References

1. Asif M, Muneer T (2007) Energy supply, its demand and security issues for developed and emerging economies. Renew Sustain Energy Rev 11(7):1388–1413
2. US Energy Information Administration (2011) International energy outlook
3. Pepermans G, Driesen J, Haeseldonckx D, Belmans R, D'haeseleer W (2005) Distributed generation: definition, benefits and issues. Energy Policy 33(6):787–798
4. Christopher D, Lenzen M (2000) Greenhouse gas analysis of electricity generation systems. ANZSES solar 2000 conference, Griffith University, Queensland, pp 658–668
5. Norton B, Eames PC, Lo SNG (1998) Full energy chain analysis of greenhouse gas emissions for solar thermal electric power generation systems. Renew Energy 15(1–4):131–136

6. Shafiee S, Topal E (2009) When will fossil fuel reserves be diminished? Energy Policy 37(1):181–189
7. Van Ruijven Bas, Vuuren DPV (2009) Oil and natural gas prices and greenhouse gas emission mitigation. Energy Policy 37(11):4797–4808
8. Mohd IA (2010) Green energy and technology: issues and challenges. In: International conference on advances in renewable energy technologies (ICARET), Cyberjaya Malaysia
9. Lidula NWA, Rajapakse AD (2011) Microgrids research: a review of experimental microgrids and test systems. Renew Sustain Energy Rev 15(1):186–202
10. Llaria A, Curea O, Jimenez J, Camblong H (2011) Survey on microgrids: unplanned islanding and related inverter control techniques. Renew Energy 36(8):2052–2061
11. Ackermann T, Andersson G, Soder L (2001) Distributed generation: a definition. Electr Power Syst Res 57(3):195–204
12. Blaabjerg F, Teodorescu R, Liserre M, Timbus AV (2006) Overview of control and grid synchronization for distributed power generation systems. IEEE Trans Industr Electron 53(5):1398–1409
13. Ward B, Ropp M (2002) Evaluation of islanding detection methods for photovoltaic utility interactive power systems. IEA International Energy Agency, Task V report IEA PVPS T509
14. Wei YT, Chee WT (2011) An overview of islanding detection methods in photovoltaic systems. Int J Electr Comput Energ Electron Commun Eng 5(11)
15. IEA (International Energy Agency), Verhoeven B (1998) Utility aspects of grid connected photovoltaic power systems. Task V report IEA PVPS T5-01
16. IEEE (1987) IEEE recommended practice for utility interface of residential and intermediate photovoltaic (PV) systems. ANSI/IEEE Std 929-1988: 01
17. IEEE (2003) IEEE standard for interconnecting distributed resources with electric power systems. IEEE Std 1547-2003, pp 1–16
18. IEEE (2009) IEEE application guide for IEEE std 1547, IEEE standard for interconnecting distributed resources with electric power systems. IEEE Std 1547.2-2008, pp 1–207
19. Lior Noam (2010) Energy resources and use: the present (2008) situation and possible sustainable paths to the future. Energy 35(6):2631–2638
20. Ngan MS, Tan CW (2012) Assessment of economic viability of PV/wind/diesel hybrid energy system in southern Peninsular Malaysia. Renew Sustain Energy Rev 16(1):634–647
21. Mulhausen J, Schaefer J, Mynam M, Guzman A, Donolo M (2010) Anti-islanding today, successful islanding in future. In: 63rd annual conference on protective relay engineers
22. Singam B, Hui LY (2006) Assessing SMS and PJD schemes of anti-islanding with varying quality factor. In: IEEE international conference on power and energy conference PECon'06
23. Xu W, Mauch K, Martel S (2004) An assessment of distributed generation islanding detection methods and issues for Canada. Report # CETC-Varennes 2004-074(TR), CANMET Energy Technology Centre, Varennes, Natural Resources Canada 53
24. Abdullah MA, Yatim AHM, Tan CW, Saidur R (2012) A review of maximum power point tracking algorithms for wind energy systems. Renew Sustain Energy Rev 16(5):3220–3227
25. Funabashi T, Koyanagi K, Yokoyama R (2003) A review of islanding detection methods for distributed resources. In: Power tech conference proceedings, IEEE Bologna
26. Noor F, Arumugam R, Vaziri MY (2005) Unintentional islanding and comparison of prevention techniques. In: Power symposium proceedings of the 37th annual North American
27. Skocil T, Gomis-Bellmunt O, Montesinos-Miracle D, Galceran-Arellano S, Rull-Duran J (2009) Passive and active methods of islanding for PV systems. In: 13th European conference on power electronics and applications EPE'09
28. Aljankawey AS, Morsi WG, Chang L, Diduch CP (2010) Passive method based islanding detection of renewable based distributed generation: the issues. In: Electric power and energy conference (EPEC). IEEE, pp 1–8
29. Chowdhury SP, Chowdhury S, Chui FT, Crossley PA (2008) Islanding protection of distribution systems with distributed generators—A comprehensive survey report. Power and Energy Society General Meeting—Conversion and Delivery of Electrical Energy in the 21st century. IEEE, pp 1–8

30. Ward Bower and M Ropp (2002) Evaluation of islanding detection methods for utility-interactive inverters in photovoltaic systems. SAND2002-3591 unlimited release
31. Xuancai Z, Chengrui D, Guoqiao S, Min C, Dehong X (2009) Analysis of the non-detection zone with passive islanding detection methods for current control DG system. In: Applied power electronics conference and exposition twenty-fourth annual IEEE
32. Zhihong Y, Kolwalkar A, Yu Z, Pengwei D, Reigh W (2004) Evaluation of anti-islanding schemes based on nondetection zone concept. IEEE Trans Power Electron 19(5):1171–1176
33. De Mango F, Liserre M, Aquila AD, Pigazo A (2006) Overview of anti-islanding algorithms for PV systems. Part I: passive methods. In: 12th international conference on power electronics and motion control
34. Pukar M, Chen Z, Birgitte B-J (2008) Review of islanding detection methods for distributed generation. In: Third international conference on electric utility deregulation and restructuring and power technologies
35. Timbus A, Oudalov A, Ho CNM (2010) Islanding detection in smart grids. In: Energy conversion congress and exposition (ECCE). IEEE, pp 3631–3637
36. Trujillo CL, Velasco D, Figueres E, Garcera G (2010) Analysis of active islanding detection methods for grid-connected microinverters for renewable energy processing. Appl Energy 87(11):3591–3605
37. Kunte RS, Wenzhong G (2008) Comparison and review of islanding detection techniques for distributed energy resources. In: Power symposium NAPS 40th North American
38. Doumbia ML, Agbossou K, Bose TK (2004) Islanding protection evaluation of inverter based grid-connected hybrid renewable energy system. In: Electrical and computer engineering Canadian conference
39. Beltran H, Gimeno F, Segui-Chilet S, Torrelo JM (2006) Review of the islanding phenomenon problem of connection of renewable energy systems. In: International conference on renewable energies and power quality
40. Kobayashi H, Takigawa K, Hashimoto E, Kitamura A, Matsuda H (1991) Method for preventing islanding phenomenon on utility grid with a number of small scale PV systems. In: Photovoltaic specialists conference. Conference record of the twenty second IEEE
41. Arruda LN, Silva SM, Filho BJC (2001) PLL structures for utility connected systems. In: Industry applications conference, thirty-sixth IAS annual meeting. Conference record of the 2001 IEEE
42. Best R (1993) Phase-locked loops: theory, design, and applications, 2nd edn. McGraw-Hill Inc., New York
43. Brennan PV (1996) Phase-locked loops: principles and practice. MacMillan Press Ltd
44. Ciobotaru M, Agelidis V, Teodorescu R (2008) Accurate and less disturbing active anti-islanding method based on PLL for grid-connected PV inverters. In: Power electronics specialists conference
45. Ciobotaru M, Agelidis VG, Teodorescu R, Blaabjerg F (2010) Accurate and less-disturbing active anti-islanding method based on PLL for grid-connected converters. IEEE Trans Power Electron 25(6):1576–1584
46. Guan-Chyun H, Hung JC (1996) Phase-locked loop techniques—A survey. IEEE Trans Industr Electron 43(6):609–615
47. Lindsey WC, Chak Ming C (1981) A survey of digital phase-locked loops. Proc IEEE 69 (4):410–431
48. Rey TJ, Lindsey WC, Chak Ming C (1982) Comments on "A survey of digital phase locked loops". Proc IEEE 70(2):201–202
49. Velasco D, Trujillo CL, Garcera G, Figueres E (2010) Review of anti-islanding techniques in distributed generators. Renew Sustain Energy Rev 14(6):1608–1614
50. Liserre M, Pigazo A, Dell'aquilla A, Moreno VM (2006) An anti-islanding method for single phase inverters based on a grid voltage sensorless control. IEEE Trans Industr Electron 53(5):1418–1426

51. Jang SI, Kim KH (2004) An islanding detection method for distributed generations using voltage unbalance and total harmonics distortion of current. IEEE Trans Power Delivery 19(2):745–752
52. Lopes LAC, Huili Sun (2006) Performance assessment of active frequency drifting islanding detection methods. IEEE Trans Energy Convers 21(1):171–180
53. Liu F, Kang Y, Duan S (2007) Analysis and optimization of active frequency drift islanding detection method. In: Applied power electronics conference twenty second annual IEEE
54. Ropp ME, Begovic M, Rohatgi A (1999) Analysis and performance assessment of the active frequency drift method of islanding prevention. IEEE Trans Energy Convers 14(3):810–816
55. Yu GJ, So JH, Jung YS, Choi JY, Jeong SG, Kim KH, Lee KO (2005) Boundary conditions of reactive power variation method and active frequency drift method for islanding detection of grid-connected photovoltaic inverters. In: Photovoltaic specialists conference. Conference record of the thirty-first IEEE
56. Jung Y, Choi J, Yu G (2007) A novel active anti-islanding method for grid-connected photovoltaic inverter. J Power Electron 7(1):64–71
57. Zhang C, Liu W, San G, Wu W (2006) A novel active islanding detection method of grid-connected photovoltaic inverters based on current-disturbing. In: CES/IEEE 5th international power electronics and motion control conference
58. LuY, Yi X, Wu J, Lin X (2006) An intelligent islanding technique considering load balance for distribution system with DGs. IEEE Power Engineering Society general meeting, vol 5
59. Chang WY (2010) A hybrid islanding detection method for distributed synchronous generators. In: 2010 international conference on power electronics
60. Ghazi R, Lotfi N (2010) A new hybrid intelligent based approach to islanding detection in distributed generation. In: 45th international conference on universities power engineering
61. Yin J, Chang L, Diduch C (2006) A new hybrid anti-islanding algorithm in grid-connected three-phase inverter system. In: 37th IEEE power electronics specialists conference
62. Menon V, Nehrir MH (2007) A hybrid islanding detection technique using voltage unbalance and frequency set point. IEEE Trans Power Syst 22(1):442–448
63. Robitaille M, Agbossou K, Doumbia ML, Simard R (2011) Islanding detection method for a hybrid renewable energy system. Int J Renew Energy Res 1(1):41–53
64. Mayr C, Brundlinger R (2007) Optimized destabilizing islanding detection scheme for grid-tied inverters insensitive to short term network disturbances. In: European conference on power electronics and applications, pp 1–9
65. Etxegarai A, Eguia P, Zamora I (2011) Analysis of remote islanding detection methods for distributed resources. In: International conference on renewable energies and power quality
66. Redfern MA, Usta O, Fielding G (1993) Protection against loss of utility grid supply for a dispersed storage and generation unit. IEEE Trans Power Delivery 8(3):948–954
67. Xu W, Zhang G, Li C, Wang W, Wang G, Kliber J (2007) A power line signalling based technique for anti-islanding protection of distributed generators—Part I: scheme and analysis. IEEE Trans Power Delivery 22(3):1758–1766
68. Ropp ME, Aaker K, Haigh J, Sabbah N (2000) Using power line carrier communications to prevent islanding. Photovoltaic specialists conference. Conference record of the twenty-eighth IEEE
69. Ropp M, Larson D, Meendering S, Mcmahon D, Ginn J, Stevens J, Bower W, Gonzalez S, Fennell K, Brusseau L (2006) Discussion of a power line carrier communications based anti-islanding scheme using a commercial automatic meter reading system. Photovoltaic energy conversion. Conference record of the IEEE 4th world conference
70. Wang W, Kliber J, Zhang G, Xu W, Howell B, Palladino T (2007) A power line signalling based scheme for anti-islanding protection of distributed generators—Part II: field test results. IEEE Trans Power Delivery 22(3):1767–1772
71. Olli Rintamaki and Kimmo Kauhaniemi (2009) Applying modern communication technology to loss of mains protection. In: 20th international conference and exhibition on electricity distribution—Part 1, pp 1–4

72. Best RJ, John Morrow D, Laverty DM, Crossley PA (2010) Synchrophasor broadcast over internet protocol for distributed generator synchronization. IEEE Trans Power Delivery 25(4):2835–2841
73. Schweitzer EO III, Whitehead D, Zweigle G, Ravikumar KG (2010) Synchrophasor-based power system protection and control applications. In: 63rd annual conference on protective relay engineers, pp 1–10
74. IEEE (1986) IEEE recommended criteria for terrestrial photovoltaic power systems. ANSI/IEEE Std 928-1986, pp 1–10
75. IEEE (2000) IEEE recommended practice for utility interface of photovoltaic (PV) systems. IEEE Std 929-2000
76. IEA (International Energy Agency), Cullen N, Thronycroff J, Collinson A (2002) Risk analysis of islanding of photovoltaic power systems within low voltage distribution networks. Task V Report IEA PVPS T508:2002
77. Department of Standards Malaysia (2010) Photovoltaic (PV) systems—Characteristics of utility interface (IEC 61727:2004.IDT). MS IEC 61727:2010
78. Department of Standards Malaysia (2012) Test procedure of islanding prevention measures for utility-interconnected Photovoltaic inverters (IEC 62116:2008.IDT). MS IEC 62116:2012

Stability Assessment of Power Systems Integrated with Large-Scale Solar PV Units

Naruttam Kumar Roy

Abstract Renewable energy sources are proficient in reducing greenhouse gas emission in the world. Among various renewable energy sources, solar photovoltaic (PV) generation is gaining its popularity day by day. Unlike conventional generating units, PV plants do not have inertias. Therefore, the increasing penetration of PV may impact a system's oscillations negatively as PV units add additional dynamics to power systems. Therefore, it is essential to analyze a system's behavior before replacing conventional generators by large-scale solar PV units. This chapter analyzes the impacts of increasing penetration of PV units on power systems. The effect of control mode of PV generator on the system's stability is investigated. Both static and dynamic stability analysis methods are conducted to find out the critical issues. The simulation results effectively identify the impact of high PV penetration on the stability of the studied system which show that voltage control mode of PV generator can improve the performance of a system. However, high penetration of PV can interact negatively with the system in certain cases.

Keywords Renewable energy · Dynamic stability · Static voltage stability · Power–voltage curve · System inertia

1 Introduction

Most of the developed countries around the world have set their mandatory targets to produce electricity from renewable energy sources in the coming years [1, 2]. Among various renewable energy sources, the grid integration of solar photovoltaic (PV) systems is gaining more interest than traditional stand-alone systems because of the following benefits [3]:

N.K. Roy (✉)
Department of Electrical and Electronic Engineering, Khulna University of Engineering and Technology, Khulna 9203, Bangladesh
e-mail: nkroy@eee.kuet.ac.bd

M.R. Islam et al. (eds.), *Advances in Solar Photovoltaic Power Plants*,
Green Energy and Technology, DOI 10.1007/978-3-662-50521-2_8

- a grid-connected PV system can supply the excess power to the utility grid;
- it is comparatively easy to install as the grid is used as a backup; and
- storage costs and losses are not incurred.

The fundamental operation of solar PV units differs from conventional synchronous generators. Solar cells convert sunlight into DC power and DC power is then converted into AC power through a power electronic-based converter. Thus, they do not have inertia and their dynamic behavior depends on the characteristics and controls of inverters.

Due to the economic factors modern power systems operate close to their voltage stability limits. Replacing conventional synchronous generators by inverter connected solar PV units will change the dynamics of power systems. The impact of high PV penetration on small signal stability of power system is studied in [4], which shows that high PV penetration affects the critical mode of the system. The simulation results in [5] demonstrate that solar PV generation can either have beneficial or detrimental effect on small signal stability depending on its location and penetration level.

A pseudo power point tracking system is introduced in [6], which provides frequency regulation functionality to PV systems. It can control the amount of active power injected into the grid for frequency regulation. In a large system, high penetration of PV can reduce system inertia and alter power flow patterns when that replaces a portion of conventional generation sources. At some penetration levels, overvoltages are observed at transmission level buses which can cause disconnection of PV units according to grid regulation of utilities [7]. It is observed that systems with high PV penetration levels cause larger voltage dips following most of the disturbances [7].

It is expected that within a few years, inverter-based PV generation will displace a significant amount of conventional generation. With the increasing penetration of PV units, the effectiveness of PV units will heavily rely on their control structure [8]. High penetration levels of PV generation may strongly affect power system stability. The impact of centralized and distributed solar PV units in a real system is studied in [9], which concludes that distributed solar PV generators are significantly more advantageous, from the stability point of view, than large centralized solar PV units. Distributed PV units are modeled as constant PQ negative loads as they are operated at unity power factor due to regulatory issue. On the other hand, centralized PV units can be modeled as constant PV or PQ generators depending on the chosen control mode of the inverters [9].

Although there are rich literature available on the modeling of PV units [10–12], literature on the impact of control modes of solar PV generation on power system stability is not readily available. Therefore, the analysis of impact of the high penetration of PV on the stability has become a very important issue to ensure reliable operation of power systems.

The main contributions of this chapter are: (a) investigating the operating mode of solar PV generator on the voltage profile and power loss of a system; (b) investigating the static voltage stability of distribution networks through PV analysis

for different modes of operation; and (c) examining the dynamic performance of the system with various PV penetrations.

The chapter is organized as follows. The system models for impact studies are presented in Sect. 2. Section 3 provides static analysis of the system. Dynamic simulation results are discussed in Sect. 4. Summary is provided in Sect. 5.

2 System Description

In this chapter, the Western System Coordinating Council (WSCC) 9-bus test system shown in Fig. 1 is used. The test system data is given in Table 1. Bus 1 is considered as slack bus. Two synchronous generators which supply a real power output of 1.63 and 0.85 pu are connected at bus 2 and bus 3, respectively. The system has 3-loads connected at bus 5, bus 6, and bus 8 which are modeled as constant impedance load for simplicity.

2.1 Synchronous Generator

Synchronous generators are modeled as PV bus for load flow study and a fourth order model of synchronous generator with automatic voltage regulator is used for dynamic simulation. The dynamics of synchronous generator is governed by the following equations [13]:

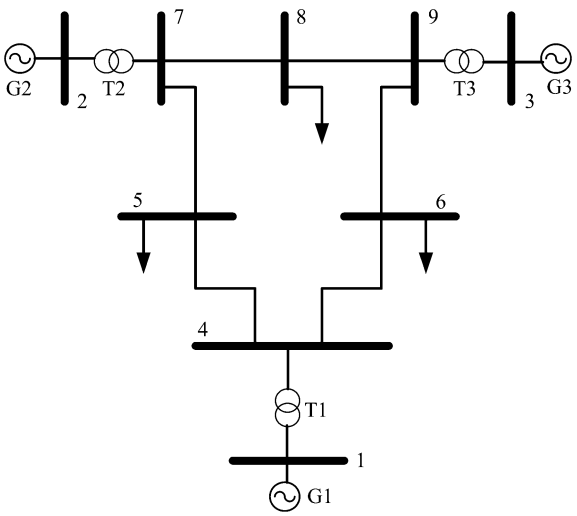

Fig. 1 WSCC 9-bus test system

Table 1 Data of WSCC 9-bus system

Line no.	From bus–To bus	Resistance, R (pu)	Reactance, X (pu)	Susceptance, B (pu)
1	7–8	0.0085	0.072	0.149
2	6–9	0.039	0.170	0.358
3	5–7	0.032	0.161	0.306
4	4–5	0.01	0.085	0.176
5	4–6	0.017	0.092	0.158
6	8–9	0.0119	0.1008	0.209

$$\dot{\delta} = \Omega_b(\omega - 1) \tag{1}$$

$$\dot{\omega} = (P_m - P_e) - D(\omega - 1)/M \tag{2}$$

$$\dot{e}'_q = (-f_s(e'_q) - (X_d - X'_d)i_d) + E_f)/T'_{d0} \tag{3}$$

$$\dot{e}'_d = \left(-e'_d + (X_q - X'_q)i_q\right)/T'_{q0} \tag{4}$$

Algebraic equations are

$$0 = v_q + r_a i_q - e'_q + X'_d i_d \tag{5}$$

$$0 = v_d + r_a i_d - e'_d + X'_q i_q \tag{6}$$

where, Ω_b is the base frequency in rad/s, ω is the rotor speed, P_m is the input mechanical power, P_e is the output electrical power, M is the machine inertia, f_s is the system frequency, X'_d and X'_q are the d- and q-axis transient reactances, respectively, X_d and X_q are the d- and q-axis synchronous reactances, respectively, e'_d and e'_q are the d- and q-axis transient voltages, respectively, E_f is the field voltage, r_a is the stator resistance and i_d and i_q are the d- and q-axis stator currents, respectively.

2.2 Solar PV Generator

A solar PV generator can be run in the following two ways [13, 14].

a. Constant P and constant Q mode (PQ mode)
b. Constant P and constant V mode (PV mode)

In PQ mode, a constant power factor is maintained and in PV mode, reactive power is generated to keep the bus voltage constant. The block diagram of PQ and PV mode is shown in Figs. 2 and 3, respectively.

The dynamics of the solar PV generator depends on the dc to ac power converter. Figures 4 and 5 show the block diagram of the PQ and PV model with converter [9]. In PQ mode, *d*- and *q*-axis reference currents are obtained based on the desired active and reactive powers and measurements of terminal voltage in the dq reference frame. In PV mode, the reference value for reactive power is obtained based on the reference and actual voltage values using a *PI* controller.

Using the above models, the power injections into the ac bus system are [13]:

$$P = v_d i_d + v_q i_q \tag{7}$$

$$Q = v_q i_d - v_d i_q \tag{8}$$

Reference currents are generated based on the active and reactive power references as follows [13, 14]:

$$\begin{bmatrix} i_{d\text{ref}} \\ i_{q\text{ref}} \end{bmatrix} = \begin{bmatrix} v_d & v_q \\ v_q & -v_d \end{bmatrix}^{-1} \begin{bmatrix} P_{\text{ref}} \\ Q_{\text{ref}} \end{bmatrix} \tag{9}$$

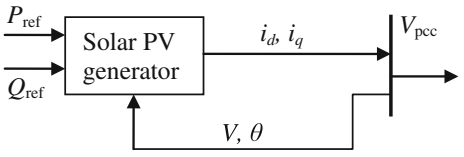

Fig. 2 Constant *P*, constant *Q* model

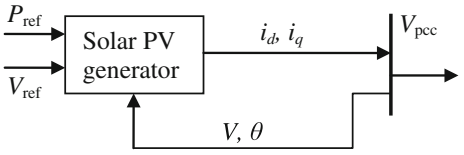

Fig. 3 Constant *P*, constant *V* model

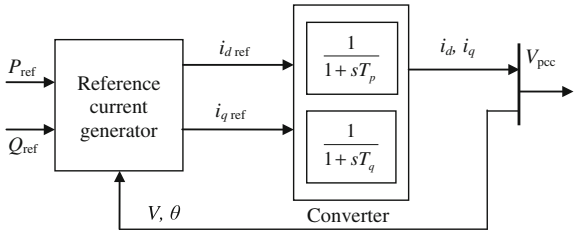

Fig. 4 Constant *P*, constant *Q* model with converter

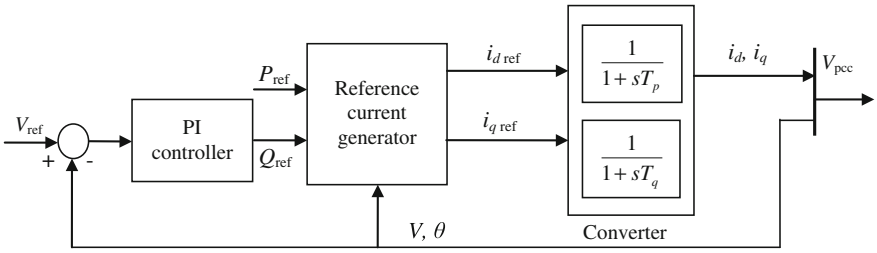

Fig. 5 Constant P, constant V model with converter

The PV penetration level is defined as the ratio of total PV generation to total system load, as expressed in the following equation:

$$\text{PV penetration}\,(\%) = \frac{\text{Total PV generation}\ (\text{MW})}{\text{Total load}\,(\text{MW})} \times 100 \tag{10}$$

3 Static Analysis

To study the steady-state behavior of the power systems under different control modes of PV generator, it is essential to conduct the load flow. A load flow study for the considered test system is conducted using Newton–Raphson method [15]. For this analysis, the synchronous generator at bus 3 is replaced by a same size solar PV generator. The solar PV generator is run in its both operating modes to investigate the impacts of control modes on voltage profile, power loss, and static voltage stability of the system.

3.1 Voltage Profile of the System

To ensure the reliable operation of power system, it is essential to keep the nodal voltages within a range which is ±10 % for most of the utilities around the world. The bus voltages of the test system are shown in Fig. 6, where it can be observed that the PV mode of solar PV unit keeps the system voltages within the permissible limit. In this mode, reactive power is generated based on the difference between reference and actual voltage and thus, regulates the system voltage. However, the PQ mode of the solar generator violates the voltage limit at bus 3 and bus 9. It is to be noted that not only the solar connecting bus, but also its nearest buses have voltage rise from that solar generator. This is because, an excess of reactive power causes overvoltage in some points of the network.

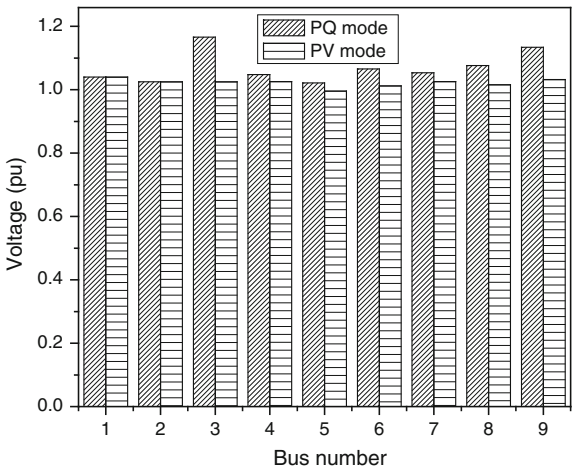

Fig. 6 Bus voltage of the system in different modes

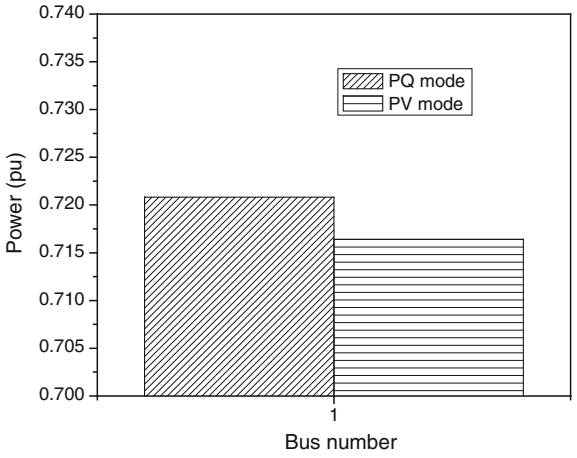

Fig. 7 Power imported from the grid

3.2 Power Loss of the System

Minimizing power loss is an important objective for efficient operation of power systems. The system loss is calculated for PQ and PV mode of solar PV generator. It is found that the system loss for PQ mode of operation is 0.05083 pu and PV mode is 0.04641 pu. The real power drawn by the system from main grid is shown in Fig. 7. As PQ mode has more loss, in this mode, the system draws more power from the main grid to support the loss.

3.3 Static Voltage Stability of the System

Static voltage stability of a system can be determined from the static analysis. To analyze the static voltage stability generally power–voltage (P–V) curves are used which determine the maximum loading limit of a system. Here, this curve has been produced by using a series of power flow solutions for different load levels using Matlab-based power system analysis toolbox (PSAT) [13]. PSAT provides with a complete set of user-friendly graphical user interface (GUI) for simulation. The GUI setting for continuation power flow (CPF) is shown in Fig. 8. The CPF algorithm determines a normalized tangent vector and a corrector step which can be obtained using local parameterization or a perpendicular intersection [13, 16]. The base case (with synchronous generator at bus 3) P–V curve for all the buses is shown in Fig. 9. The variations in load bus voltages with the loading factor are obtained for different control modes of solar PV unit and summarized in Table 2 from which it can be seen that a PV system in its PV mode has the same loading margin like base case. It is to be expected as in the load flow solar PV generator is modeled like a synchronous generator with voltage regulation capability. On the other hand, a solar PV unit in its PQ mode reduces the maximum loading point (MLP) compared to the base case. A PV mode has superior performance in maintaining MLP of the system due to its voltage control capability.

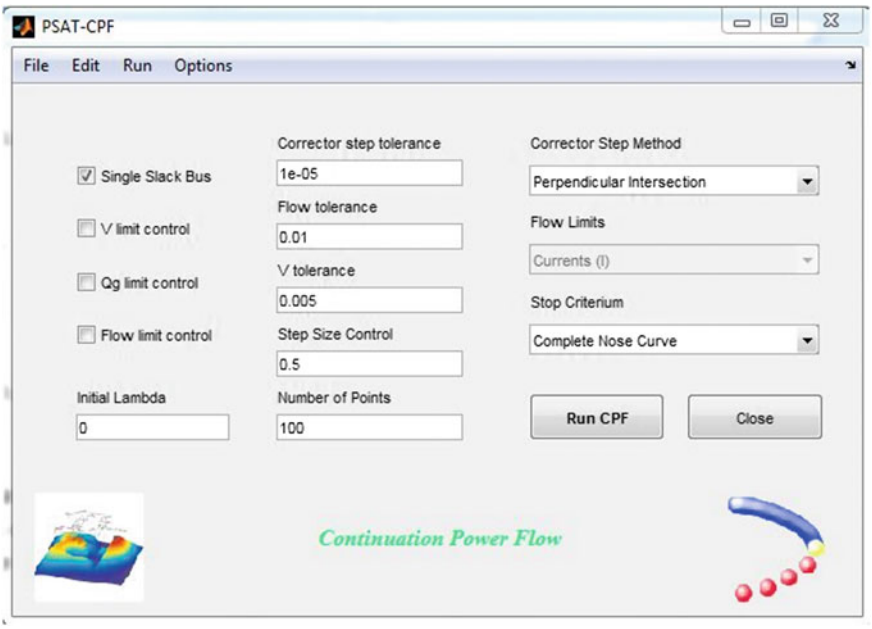

Fig. 8 GUI for continuation power flow settings in PSAT

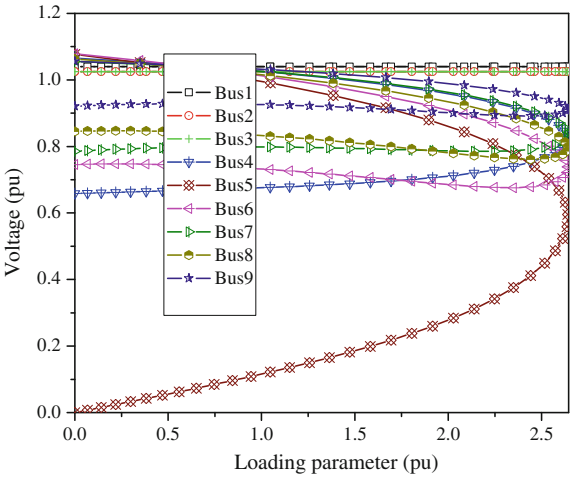

Fig. 9 *P–V* curve under base case

Table 2 MLP of the system

Operating mode	Maximum loading point (MLP), pu
Base case (PV)	2.6407
PQ mode	2.4957
PV mode	2.6407

4 Dynamic Analysis

A time domain analysis was performed to examine the detrimental impacts of high PV penetration during the system transients. The goal of dynamic simulations is to study the effectiveness of the control methods in mitigating the voltage fluctuation problems that arise when sudden changes occur in the system. Following cases are investigated to understand the performance of PV integrated system.

4.1 Case 1: Sudden Disconnection of Line

In order to investigate the dynamic performance of the system, the line connecting bus 2 and 5 is disconnected at 1 s. The bus voltages of the system under this condition are shown in Fig. 10 from which it can be visualized that all the bus voltages in the system have large oscillations.

Under the same condition, the speed deviation of synchronous generator connected at bus 2 and power output of it is shown in Figs. 11 and 12, respectively. From these figures, it can be observed that the connection of PV impacts the dynamics of nearby synchronous generator. The frequency of the generator buses of the considered system is shown in Fig. 13.

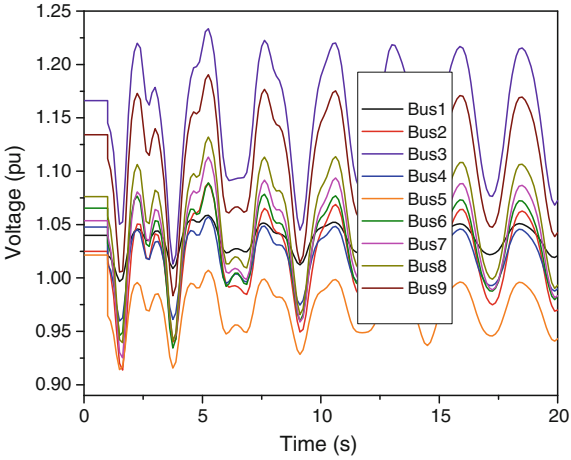

Fig. 10 Bus voltages of the system (PQ mode)

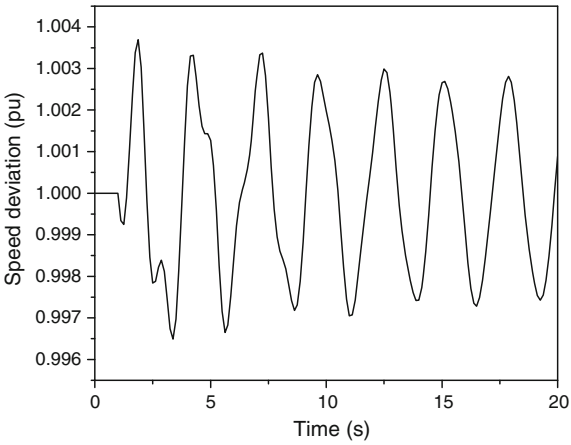

Fig. 11 Speed deviation of synchronous generator connected at bus 2

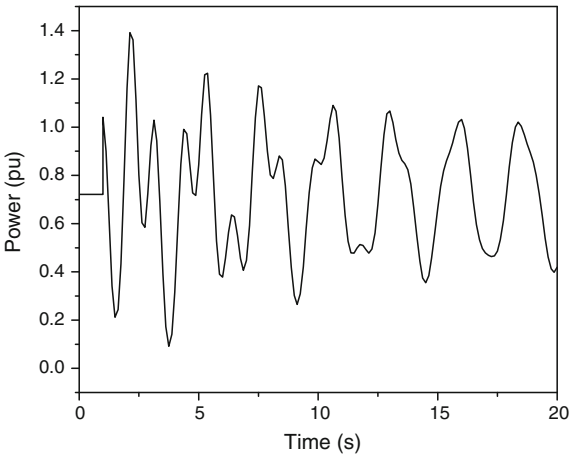

Fig. 12 Power output of synchronous generator connected at bus 2

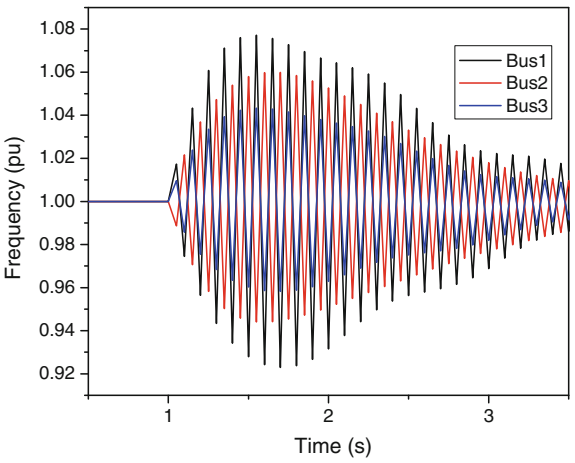

Fig. 13 System frequency measured at bus 1, 2, and 3

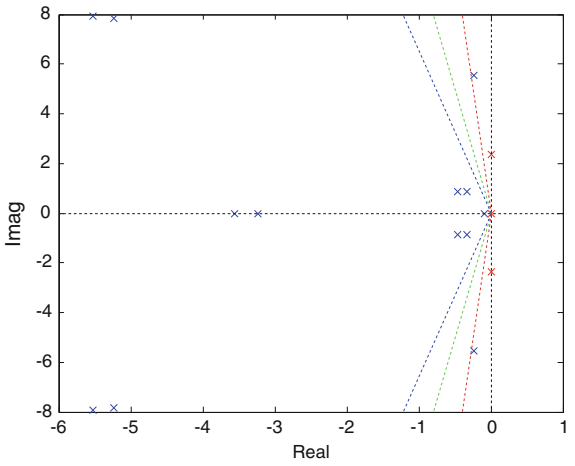

Fig. 14 Eigenvalues of the solar PV integrated system

The reason of this instability can be easily understood from linear analysis. Some of the dominating eigenvalues of the linearized system are shown in Fig. 14 which signifies that the system is marginally stable in its PQ mode and may become unstable under disturbance. It can also be observed from Fig. 15 which shows the MLP of the system during the line between bus 2 and 5 is disconnected. It is seen that under contingencies the static voltage stability of the system reduces significantly compared to the base case (2.6407 pu).

Moreover, unlike conventional synchronous generators, PV units have no rotating part which means that no inertial response can be provided during major disturbances in the system. It is well known that the lower the system inertia, the faster the system oscillations [17]. The average inertia constant for a power system can be determined by the following equation [18]:

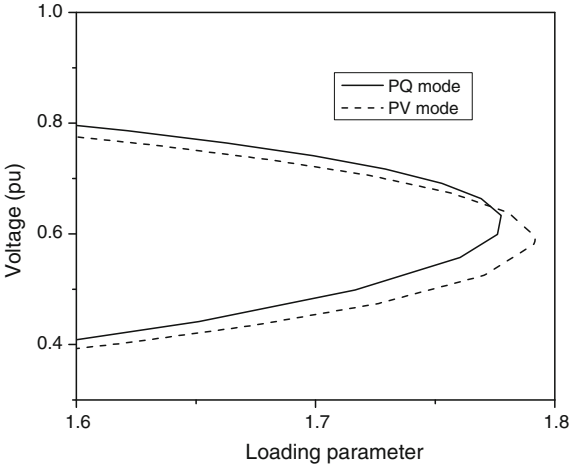

Fig. 15 Loading parameter versus voltage curve under contingency

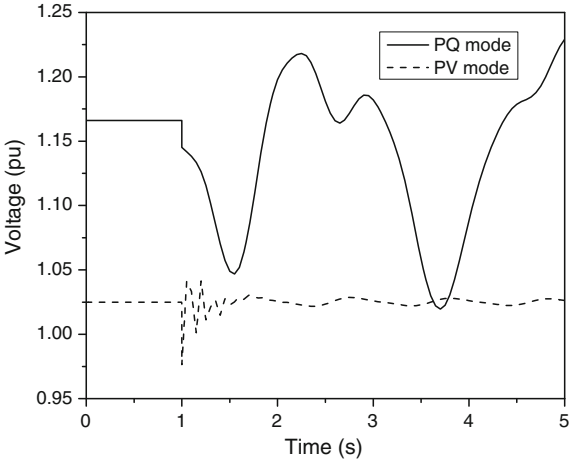

Fig. 16 Voltage at bus 3

$$H_{\text{sys}} = \frac{\sum_{i=1}^{n} S_i H_i}{\sum_{i=1}^{n} S_i} \tag{11}$$

where H_i and S_i are the inertia constant and the nominal power of generator i, respectively.

Replacing the conventional synchronous generator by solar PV units reduces the average inertia of the system and thereby, increasing oscillations.

However, in PV mode generator can easily balance the reactive power to restore the nodal voltage to its prefault value as shown in Fig. 16. This is because PV mode has higher voltage stability limit under contingency compared to PQ mode. The frequency response of the system under the same fault is shown in Fig. 17 from which it can be seen that the system also balances the real power demand quickly in this mode due to less power loss and keep the system frequency constant.

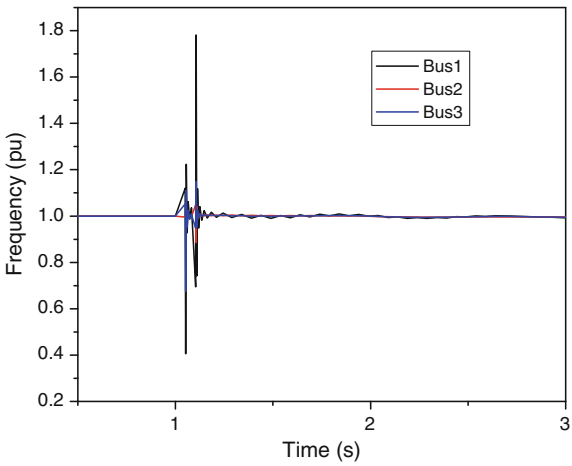

Fig. 17 System frequency measured at bus 1, 2, and 3

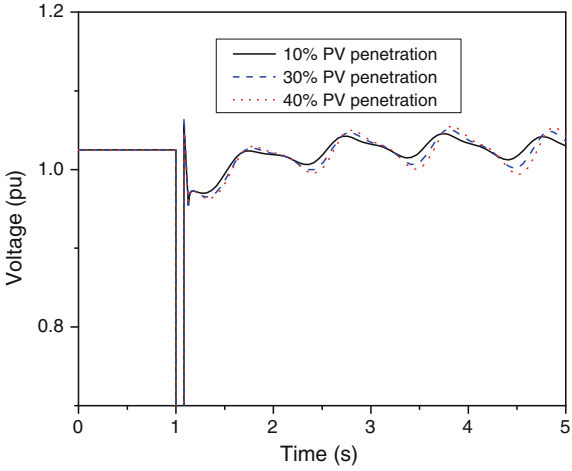

Fig. 18 Voltage at bus 2

4.2 Case 2: Short Circuit Fault

It is important to investigate the ability of PV generation system to maintain stability of the system when subjected to severe disturbance such as three-phase short circuit fault on transmission facilities. The effects of the presence of increasing penetration of PV generator in its PV mode have been simulated here.

A solid three-phase short circuit fault at bus 2 is applied at 1 s and removed at 1.083 s. The voltage profile of the system at bus 2 is shown in Fig. 18 for different PV penetration levels. It can be observed that increasing the PV penetration reduces the damping of the dominating mode of the system. The dominant mode of the system for 10 % PV penetration is found to be $-0.2352 \pm j7.90$. The speed deviation of the synchronous generator connected at bus 1 for 40 % PV penetration

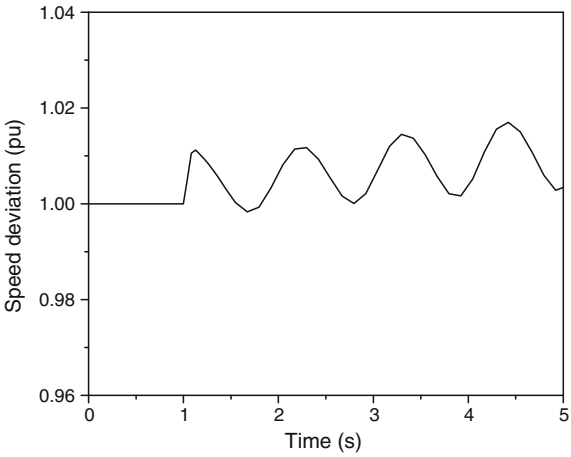

Fig. 19 Speed deviation of synchronous generator 1

is shown in Fig. 19 in which oscillation is observed. Therefore, it can be said that nonlinear interactions of PV converter to the system with synchronous generator creates oscillations and as the penetration of solar PV is increased the average inertia of the system is reduced which impacts the system oscillations negatively by reducing the damping of the critical mode. Thus, with the increasing of PV capacity in the power system, the transient stability of the conventional synchronous generator affected pessimistically due to the lower system inertia.

5 Summary

This chapter investigates the impact of PV generation on power system stability. It is shown that fault on a power system with high PV penetration can be a risk for the system stability. From the analysis, following conclusions can be made:

- The control mode of solar PV unit has a large impact on the system's performance. A PQ control mode causes overvoltage at certain buses in the system. However, PV control mode can keep the bus voltages within permissible limit. Moreover, less system loss occurs in PV mode compared to the PQ mode of operation.
- A PV control model provides higher loading margin than a PQ control model.
- A solar PV generator impacts the dynamics of the nearby synchronous generators connected to the system. Voltage oscillations in the system are prominent in PQ mode due to the mismatch in reactive power after a disturbance. Transient stability of the system is also affected due to the lower inertia of the system.
- The integration of PV generators tends to make the system less stable following a severe disturbance. As the penetration of PV generator increases, it deteriorates the damping performance of the system.

Finally, it can be concluded that if solar PV generation is implemented on a large-scale, there is a need to utilize the PV control mode of the solar units to support network voltage. However, the use of supplementary controller to improve the damping performance of the system should be investigated.

Acknowledgement This work is supported by a University Grants Commission funded aid from the Committee for Advanced Studies & Research, Khulna University of Engineering & Technology, Bangladesh.

References

1. Renewable energy target scheme, Report of the expert panel, Commonwealth of Australia (2014)
2. IRENA, Renewable Energy Target Setting (2015)
3. Roy NK, Pota HR (2014) Integration of green energy into power distribution systems: study of impacts and development of control methodology. Renewable Energy Integration: Challenges and Solutions, Chapter 10, Springer
4. Eftekharnejad S, Vittal V, Heydt GT, Keel B, Loehr J (2013) Small signal stability assessment of power systems with increased penetration of photovoltaic generation: a case study. IEEE Trans Sustain Energy 4(4):960–967
5. Liu H, Jin L, Le D, Chowdhury AA (2010) Impact of high penetration of solar photovoltaic generation on power system small signal stability. In: International conference on Power System Technology (POWERCON). pp 1–7. 24–28 Oct 2010
6. Pappu VAK, Chowdhury B, Bhatt R (2010) Implementing frequency regulation capability in a solar photovoltaic power plant. In: North American Power Symposium (NAPS), pp 1–6, 26–28 Sept 2010
7. Eftekharnejad S, Vittal V, Heydt GT, Keel B, Loehr J (2013) Impact of increased penetration of photovoltaic generation on power systems. IEEE Trans Power Systems 28(2):893–901
8. Roy NK, Pota HR, Mahmud MA, Hossain MJ (2013) D-STATCOM control in distribution networks with composite loads to ensure grid code compatible performance of photovoltaic generators. IEEE Conference on Industrial Electronics and Applications (ICIEA), Melbourne, Australia, 19–21 June 2013
9. Tamimi B, Cañizares C, Bhattacharya K (2013) System stability impact of large-scale and distributed solar photovoltaic generation: the case of Ontario, Canada. IEEE Trans Sustain Energy 4(3):680–688
10. Weixiang S, Hoong CF, Peng W, Chiang LP, Yang K (2011) Development of a mathematical model for solar module in photovoltaic systems. In: 6th IEEE conference on industrial electronics and applications, Beijing, China, pp 2056–2061, 21–23 June 2011
11. Molina MG, Mercado PE (2008) Modeling and control of grid-connected photovoltaic energy conversion system used as a dispersed generator. In: IEEE/PES transmission and distribution conference and exposition, Latin America, Bogota, pp 1–8, 13–15 Aug 2008
12. Tan YT, Kirschen DS, Jenkins N (2004) A model of PV generation suitable for stability analysis. IEEE Trans Energy Convers 19(4):748–755
13. Milano F (2005) An open source power system analysis toolbox. IEEE Trans Power Syst 20 (3):1199–1206
14. Tamimi B, Cañizares C, Bhattacharya K (2011) Modeling and performance analysis of large solar photo-voltaic generation on voltage stability and inter-area oscillations. IEEE PES Gen Meet Jul 2011:1–6

15. Balagurusamy E (1999) Numerical methods. New Delhi, Tata Mc-Graw-Hill
16. Cañizares C (2002) Voltage stability assessment: concepts, practices and tools. IEEE/PES Power System Stability Subcommittee, Final document, Tech. Report
17. Lalor G, Mullane A, O'Malley M (2005) Frequency control and wind turbine technologies. IEEE Trans Power Syst 20:1905–1913
18. Rahmann C, Castillo A (2014) Fast frequency response capability of photovoltaic power plants: the necessity of new grid requirements and definitions. Energies 7:6306–6322

Energy Storage Technologies for Solar Photovoltaic Systems

Anjon Kumar Mondal and Guoxiu Wang

Abstract Among various renewable energy resources, solar energy has gained tremendous attention for future energy because of its cleanliness, availability and environmental friendliness. Many countries around the globe are intensely considering solar energy technologies for their future energy expansion. The major disadvantage for use of solar technology is its intermittent and unpredictable nature. This influence the power quality and consistency of the power grid, particularly at large-scale solar energy systems. Solar power is the conversion of sunlight into electricity, either directly using photovoltaic (PV) or indirectly using concentrated solar power. The variation of sun light may lead to over-production of electricity at one time and lack of production at another time. The variable nature of solar power causes significant challenges for the electric grid operators. To smooth out the intermittency of solar energy production, electrical energy storage technology will become necessary. In order to increase the solar energy penetration with appropriate reliability, this chapter presents a range of energy storage systems that could technically and economically be used in association with solar photovoltaic energy.

Keywords Energy storage · PV system · Energy density · Power density · Renewable energy · Battery

1 Introduction

One of the most important challenges to modern society is the availability of energy at a reasonable cost without adverse environmental consequences. The worldwide energy demand is projected to double by the middle of the century and triple by the

A.K. Mondal (✉) · G. Wang
Center for Clean Energy Technology, University of Technology Sydney, Broadway, NSW 2007, Australia
e-mail: Anjon.Mondal@uts.edu.au

G. Wang
e-mail: Guoxiu.Wang@uts.edu.au

M.R. Islam et al. (eds.), *Advances in Solar Photovoltaic Power Plants*, Green Energy and Technology, DOI 10.1007/978-3-662-50521-2_9

end of the century as because billions of third world consumers gaining access to modern services and products. Major sources of energy for human activity are fossil fuels and nuclear sources. Currently, the burning of fossil fuels for thermal power plants, transportation and domestic heating represents more than 80 % of the world energy production. We nearly reach 87 % by the addition of nuclear sources and it is expected to peak around the year 2050 [1, 2]. Although the stored carbon fossil has some advantages including high energy density and stability but our planet will not support for much longer such massive energy consumption from this resource. The massive utilization has induced two major disadvantages: The first one is that the availability of fossil fuel is limited and eventually it will be exhausted. The second one is even more serious and concerns anthropogenic heavy greenhouse gas emissions, carbon dioxide in particular. Every kWh of electricity production by burning fossil carbon (coal) generates an average 1000 g CO_2, a greenhouse gas that is generally considered as the primary contributor to global warming [3].

To reduce greenhouse gas (GHG) emissions, many countries already implemented emission regulations. The issues of carbon footprint and carbon tax, in the context of pollution caused by fossil fuels are vigorously debated and truly controversial. If we do not think to control those CHG emissions we will have to face the penalties of an abnormally high concentration of CHGs in the Earth atmosphere, which will lead to deep alteration of the climate and particularly global warming [4]. To date most reports forecast an increase in temperature from 2 to 3 °C by the end of twenty-first century, suggesting dramatic changes on the environment, such as the rise in sea level [5]. From August 1992 to April 1999, the Topex–Poseidon satellite has been recorded an annual average sea level rise of 3.1 mm [6]. Clearly, climate change could entirely reshuffle our natural features within a few decades. However, we cannot expect immediate change of this complex situation. If it takes 4–8 years for CO_2 to spread into the atmosphere, it will take 50–100 years to get clear of half of it.

The constant increase in the world population and in order to reach the living standard of modern societies, mankind will face the fundamental challenge in the twenty-first century, which is definitely energy supply, its storage and conversion. The finite supply of conventional energy sources and constantly increasing energy demand in the context of environmental pollution, have stimulated the development of alternative, sustainable and clean energy technologies. Renewable energy sources, such as solar, wind, geothermal and tidal energy have been developed. Among various renewable energy sources, the solar energy is most abundant and potentially readily available. The solar radiation energy the Earth receives in 1 h is enough to meet worldwide energy consumption for a year. Currently, the output from PV module installations is growing 40 % per year globally [7]. In the coming decades, the solar energy is expected to play a fundamental role in the massive generation of decarbonized electricity. However, the solar energy is generated only in day time and often relies on the weather or climate to work effectively. It exhibits large fluctuations in power output in monthly or even annual cycles. Thus, energy from this source must be stored when excess is produced and then released, when production levels are less than the required demand. Therefore, energy storage technologies are an integral and indispensable part for a reliable and effective solar PV system.

2 Electricity and Its Storage

As shown in Fig. 1, various technologies have been developed within the energy framework, which includes mechanical, electrical, thermal, chemical, radiant and nuclear energy. Among the different forms of energy, electricity is the most convenient form of energy, which is easy to distribute by simple conversion processes without any strong harmful scattering. The physical access to electricity through

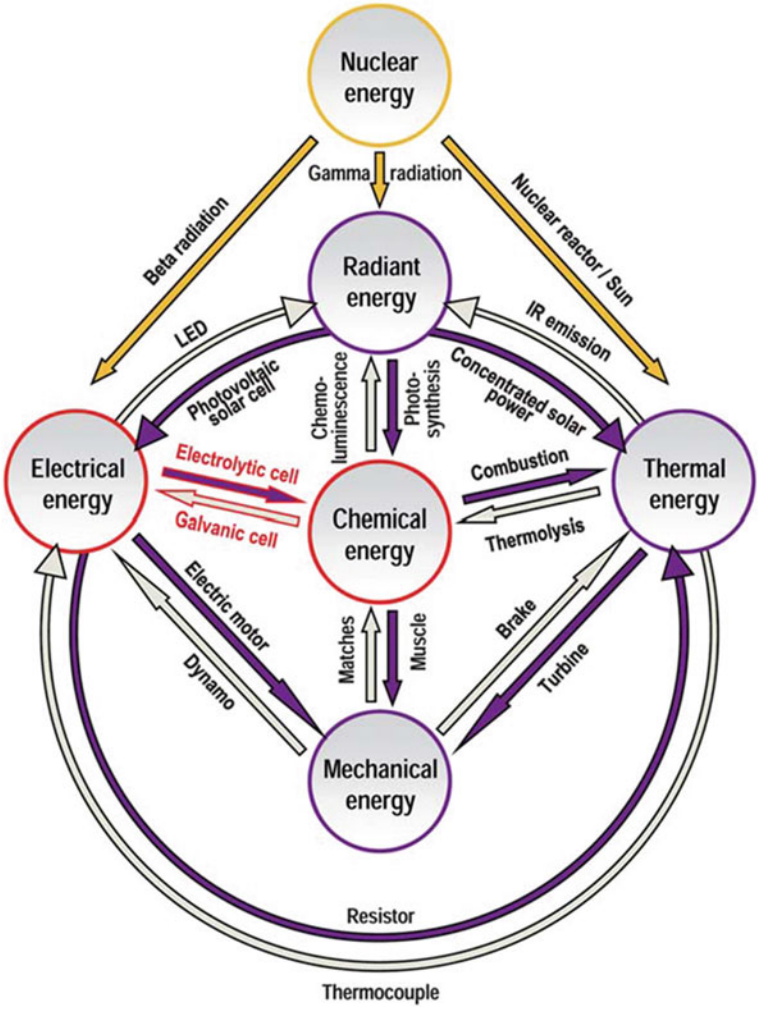

Fig. 1 Illustration of the six forms of energy and related examples of their inter-conversions [9]

power grid or mobile sources particularly increases the standard of living [8]. The blackout episode on August 2003 and the recent September 2011 power failure which extended from southern California to Mexico and Arizona are two of the more widely publicized examples in which 50 million people were in a critical situation demonstrating how life get somewhat cumbersome without electricity.

Such power outage events highlight the complex set of issues associated with the generation and use of electricity: the use of fossil fuels and related carbon emissions, the reliability of grid, the development of electric vehicles to decrease dependence of foreign oil and the increased deployment of renewable energy resources. Besides, most of the issues are international in scope as previously mentioned that worldwide demand for electricity is projected to double by 2050. Electrical energy storage (EES) cannot possibly address all of these problems. However, energy storage can offer a well-established approach for improving grid reliability and overall use of the entire power system (generation, transmission and distribution). As illustrated in Fig. 2, EES can be employed for providing many grid services, including a set of ancillary services such as (1) frequency regulation and load following, (2) cold start services, (3) contingency reserves and (4) energy services that shift generation from peak to off-peak periods. Moreover, it can provide services to solve more localized power quality issues and reactive power support.

3 Renewable Energy from PV Generation and Storage

The development and use of renewable energy from PV generation has experienced rapid growth over the past few years. Electrical production from PV source yields a more assured supply for consumers with less environmental hazards. As previously mentioned the major problem of this resource is its fluctuation from demand. Although it is abundant and conversion systems are becoming more and more reasonable, significant contribution to sustainable energy use will, however, require considerable further development of energy storage systems. Energy storage represents the ultimate solution to the problem of intermittent generation. Energy storage and its utilization in the electrical grid add value to renewable energy sources such as solar energy, allowing for more intense use of these technologies. Its use includes applications in load levelling, integration of renewable sources, peak-shaving and energy trading, making the system more stable and reliable. Figure 3 shows a schematic diagram of PV systems connected to the grid with and without energy storage systems, which show the undeniable increase in flexibility with the insertion of the energy storage system [11]. Generally, energy storage increases the usefulness of PV in the way that it absorbs excess PV and allows PV energy to be used when it is not produced in the evenings, on cloudy days etc. This will open up a new field of application, especially due to the growth of electrical production from solar PV, along with decentralized production.

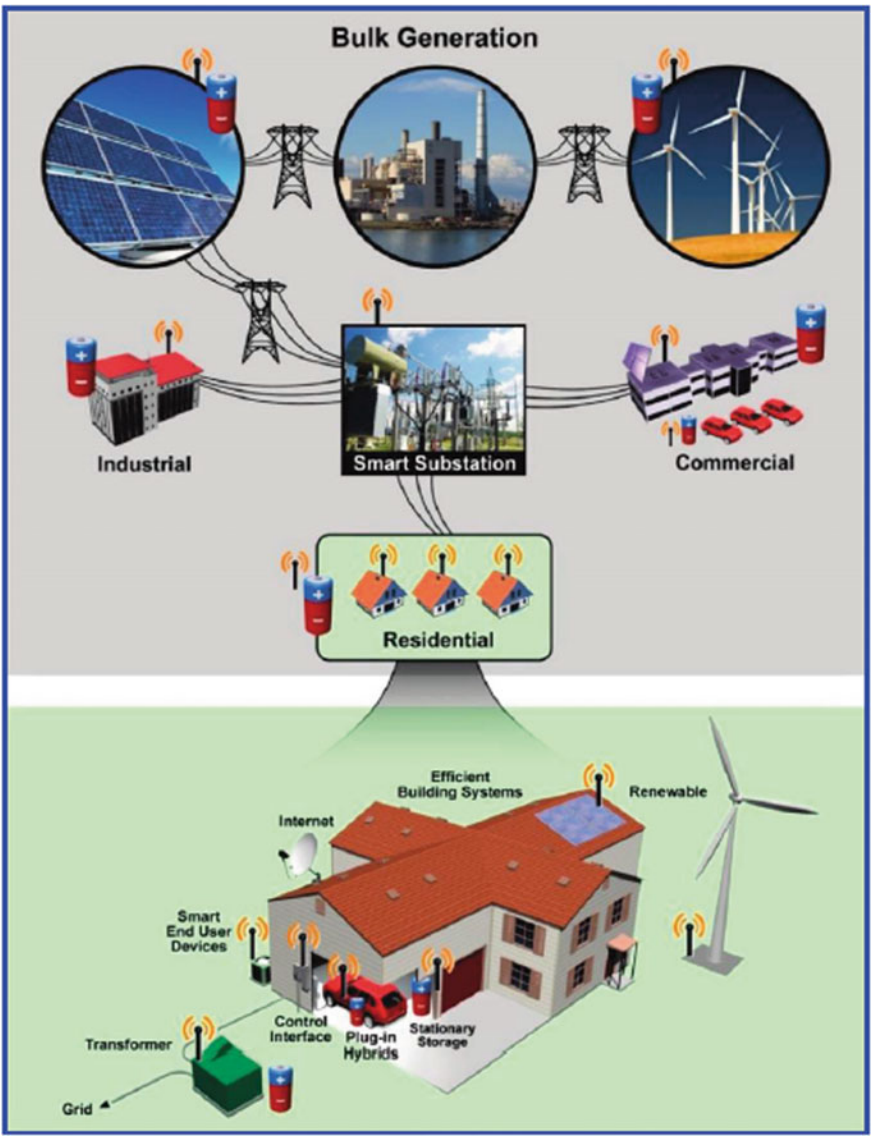

Fig. 2 Schematic of applications of electricity storage for generation, transmission, distribution, and end customers and future smart grid that integrates with intermittent renewables and plug-in hybrid vehicles through two-way digital communications between loads and generation or distribution grids [10]

4 Energy Storage Technologies

The history of the stationary EES dates back to the turn of the twentieth century, when power stations were often shut down overnight, with lead–acid accumulators supplying the residual loads on the direct current networks [12]. Electrical energy storage systems are devices that store electricity after its conversion in some other forms of energy that can be converted back to electricity when needed. This process enables electricity to be produced at times of either low generation cost, low demand or from intermittent energy sources and to be used at times of high generation cost, high demand or when no other generation is available [13]. There are many possible techniques for energy storage, found in practically all forms of energy: mechanical, electrical and chemical. The storage technologies that answer to specific technical and economic criteria, which vary considerably as a function of the applications and requirements, will obviously be of different types. A number of utility-scale energy storage systems are currently deployed such as, pumped hydro storage (PHS) and compressed air energy storage (CAES). Both technologies are generally large scale (tens to hundreds of MW) and have unique geological and geographic requirements [14]. Batteries are more scalable in size and do not depend on availability of water or air storage. The efficiency of these technologies ranges from 70 to 95 % [15]. Table 1 presents the main features of selected EES systems.

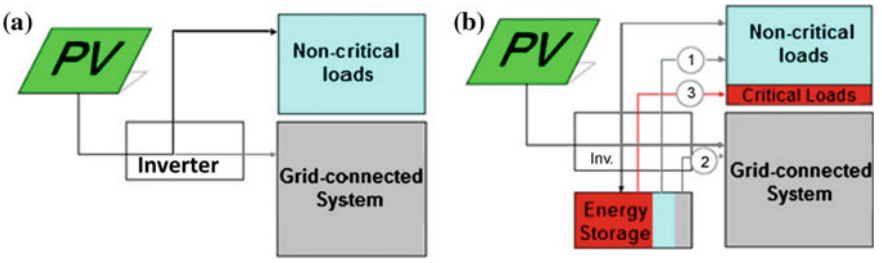

Fig. 3 Photovoltaic systems interconnected to the grid: **a** without energy storage, **b** utilizing energy storage with the different options *1* local load management, *2* load management for the utility, and *3* considering critical emergency loads [11]

Table 1 Energy storage technologies

Technology	Energy density (Wh/kg)	Power density (W/kg)	Efficiency (%)	Cycle life (cycles)	Self-discharge
Pumped hydro	0.3	–	70–85	>20 years	Negligible
CAES	10–30	–	70–89	>20 years	–
Supercapacitors	<50	4000	95	>50,000	Very high
Pb–Acid	20–35	25	70–90	200–2000	Low
Ni–Cd	40–60	140–180	70–90	500–2000	Low
NaS	120	120	70	2000	–
Li-ion	100–200	360	90–95	500–2000	Medium

In terms of their applications, the energy storage technologies are divided in two categories:

- Low to medium power applications where the energy could be stored as kinetic energy (flywheel), compressed air, chemical energy, hydrogen (fuel cells) or in supercapacitors.
- Large-scale power applications where the energy could be stored as potential energy, thermal energy, chemical energy (batteries) or compressed air.

Storage technologies are characterized by factors such as storage capacity, available power, depth of discharge, discharge time, cycling performance, self-discharge, efficiency, mass and volume densities of energy, reliability, operational constraints and environmental aspect. The size of an energy storage system has two components: energy (how much energy may be stored) and power (what is the rate of charge and discharge). The relative size of the energy and power components may be independent of one another, depending on the storage technology. The relationship between energy and power in an energy storage system may be expressed by the energy/power ratio. Energy storage can increase performance ratio of the PV system. Energy storage helps to reduce power injection to the grid during the peak times.

5 Role of Energy Storage Technology

For decades, people have argued that electricity differs from all other products and markets because it cannot be stored. This is basically correct, but future developments have the prospective to remove this limitation and to combine storage with other energy technologies, e.g. solar PV to create a new energy pattern. Energy storage and demand side management are two options that can be used to increase the penetration level of grid-connected distributed generation. The fact is that energy generation from solar PV is seldom constant over time and also electricity demand is never constant. Thus, using an energy storage technology into solar PV generating system is important. Energy storage technologies provide opportunity for the generation side to meeting the level of power quality as well as consistency needed by the demand side. Energy storage can also offer emergency power and peak saving opportunity. Energy storage is especially important for decentralized power supply system by giving the more load-following capability, which is an important factor from generation side management.

6 Different Energy Storage Technologies

As previously mentioned, electricity is not easy to be stored cheaply but it can be easily stored in other forms and converted back to electricity when required. Different storage technologies are discussed in the following sections.

6.1 Mechanical Energy Storage

6.1.1 Pumped Hydroelectric Storage

PHS is the most widely implemented large-scale EES. The main advantage of this technology is that it is readily available. This technology is currently the most used for high power applications. It uses the power of water, a highly concentrated renewable energy sources. As shown schematically in Fig. 4, this system generally consists of (1) two reservoirs located at different elevations, (2) a unit to pump water to the high elevation and (3) a turbine to generate electricity with the water returning to the low elevation. During periods when demand is low, these stations use electricity to pump the water from low reservoir to the upper reservoir. When demand is very high, the water flows out of the upper reservoir and activates the turbines to generate high-value electricity for peak hours. Clearly, the amount of stored energy is proportional to the height difference of between the two reservoirs and the volume of water stored. Pumped hydroelectric storage is a mature technology with large volume, long storage period, high efficiency and relatively low capital cost per unit of energy. The conversion efficiency of PHS is about 70–85 %, which depends on equipment characteristics. Owing to the small evaporation and penetration, the storage period of PHS can be varied from typically hours to days and even years. The typical rating of PHS is about 1000 MW (100–3000 MW) and facilities continue to be installed worldwide at a rate of 5 GW per year. The major shortcoming of this technology is the need for available sites for two large reservoirs. A high cost (typically hundreds to thousands of million US dollars) and long lead time ($\sim$10 years) for construction and environmental issues (e.g. removing trees and vegetation from the large amounts of land prior to the reservoir being flooded) [16].

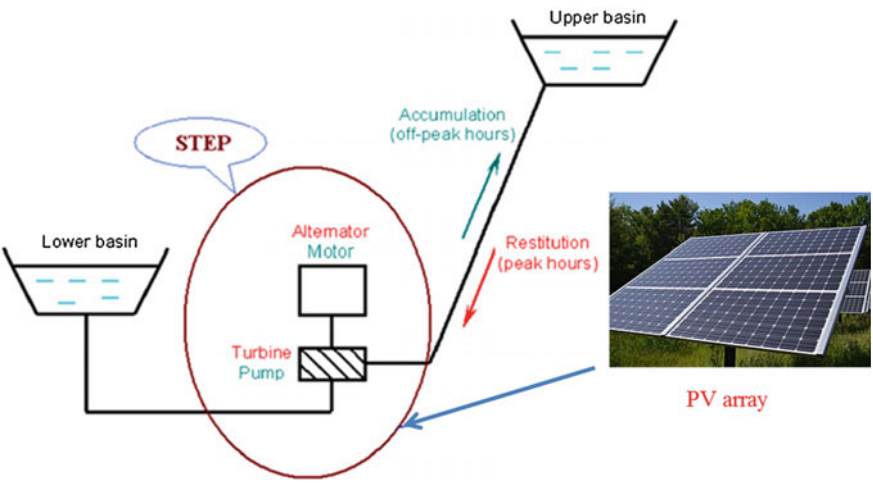

Fig. 4 Illustration of pumped hydro storage with the pumping energy supplied by PV array [17]

6.1.2 Compressed Air Energy Storage

CAES is a technology that stores energy as compressed air for later use. Besides the PHS, the CAES is only other commercially available technology, which is capable of providing very large energy storage deliverability (above 100 MW with single unit). Figure 5 presents a schematic diagram of a CAES system. It consists of five major components: (1) Air compressor of two or more stages with inter-coolers and after-coolers to achieve economy of compression and reduce the moisture content of the compressed air. (2) A cavity or container for storing compressed air. (3) A turbine train, containing both high and low pressure turbines. (4) A motor/generator that employs clutches to provide alternate engagement to the compressor or turbine trains. (5) Equipment controls and auxiliaries, such as fuel storage and heat exchanger units.

It works on the basis of conventional gas turbine generation. It decouples the compression and expansion cycles of a conventional gas turbine into two separated processes and stores the energy in the form of elastic potential energy of compressed air. When demand is low, energy is stored by compressing air into an airtight space, typically 4.0–8.0 MPa. To extract the stored energy, compressed air is drawn from the storage vessel, heated and the expanded through high pressure turbine, which captures some of the energy in the compressed air. The air is then mixed with fuel and combusted with the exhaust expanded through a low pressure

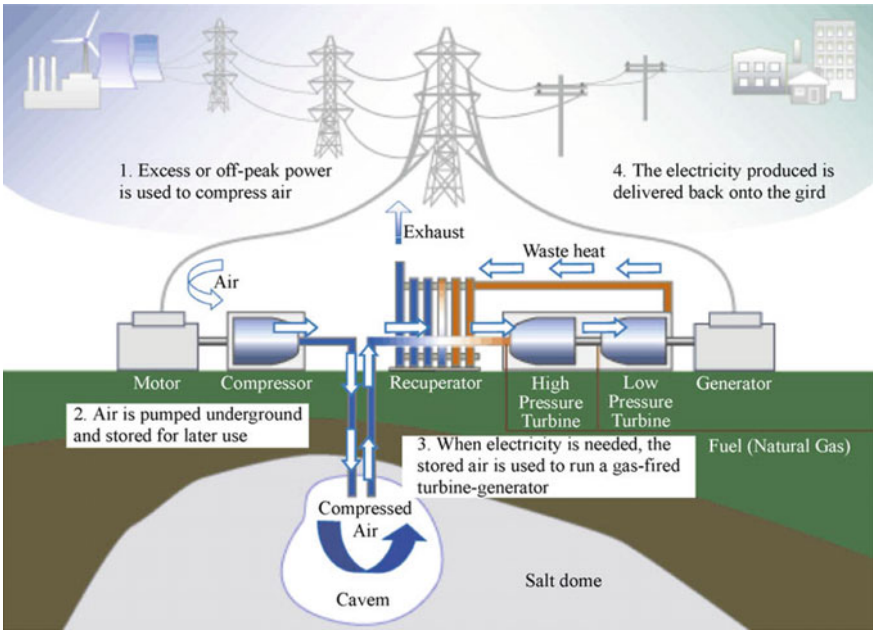

Fig. 5 Schematic diagram of compressed air energy storage [18]

turbine. Both the low and high pressure turbines are connected to a generator to produce electricity. The waste heat of the exhaust is potentially captured via recuperator before being released.

CAES systems have been considered for a number of applications, most notably for electric grid support for load-levelling applications. In such systems, energy is stored during periods of low demand and then converted back to electricity when the electricity demand is high. CAES systems are designed to cycle on a daily basis and to operate efficiently during partial load conditions. Compared to the conventional intermediate generating units, CAES systems have improved environmental characteristics. CAES has low capital cost, high storage efficiency (70–89 %) and relatively long storage period. The typical rating for a CAES system is in the range of 50–300 MW, which is much higher than other storage technologies except for the PHS. The major barrier to the implementation of CAES is the reliance on favourable geography, hence it is only economically feasible for the power plants that nearby rock mines, salt caverns, aquifer or depleted gas fields. In addition, it is not an independent system and has to be associated with a gas turbine plant.

6.2 *Electrical Energy Storage*

6.2.1 Superconducting Magnetic Energy Storage

Superconducting magnetic energy storage (SMES) systems store energy in the magnetic field created by the flow of direct current through a superconducting coil of nearly zero resistance. This is the only technology which store electrical energy directly into electric current [19]. A typical SMES system includes three parts: superconducting coil, cryogenically cooled refrigerator and power conversion system as shown in Fig. 6. To maintain the inductor (coil) in its superconducting state, it is immersed in liquid helium (at 4.2 K or super fluid helium at 1.8 K) contained in a vacuum-insulated cryostat. The inductor is generally made of

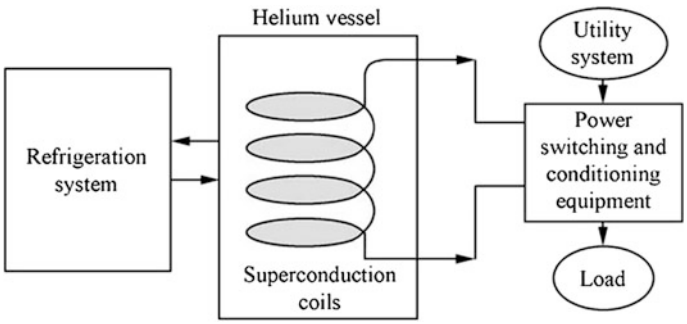

Fig. 6 Supermagnetic energy storage system [20]

niobium-titanium (NbTi), that operate cryogenically cooled (−270 °C) temperature. Once the superconducting coil is charged, the current will not decay and the magnetic energy can be stored indefinitely. The stored energy can be released back to the network by discharging the coil.

Compared to the other methods of energy storage, SMES loses the least amount of electricity in the energy storage process. SMES provides one of the highest densities of any power storage method. Its main advantage is high energy storage efficiency (>95 %). The energy output of an SMES system is much less dependent on the discharge rate compared with batteries. It also has a high cycle life and suitable for applications that require constant, full cycling and a continuous mode of operation. These features make SMES suitable for use in solving voltage stability and power quality problems for large industrial consumers. The energy stored in the SMES coil can be calculated by $E = 0.5LI^2$, where L is the inductance of the coil and I is the current passing through it [21]. However, the major problem confronting the implementation of SMES units are the high cost and the environmental issues associated with strong magnetic fields.

6.2.2 Electrochemical Capacitors (Supercapacitors)

Electrochemical capacitors (also called supercapacitors or ultracapacitors) are passive and static electrochemical devices for storing and releasing energies rapidly and reversibly [22]. This is another form of energy storage devices with high power density and long life cycle. Supercapacitors have higher energy densites (about 5 Wh kg^{-1}) than conventional capacitors. Although supercapacitors have the lower energy densities than popular lithium-ion batteries, their ultrafast charged and discharged capability leads to high power densities (10 kW kg^{-1}). The principle of energy storage in a supercapacitor is through the ion adsorption on an electrode/electrolyte interface which make electric double layer [electrical double layer capacitors (EDLC)] or due to electron transfer between the electrolyte and electrode through fast Faradic redox reaction (pseudocapacitors) [23].

Electric Double Layer Capacitors

EDLCs store electrical energy using reversible adsorption of ions from an electrolyte on the electrodes to form an electric double layer at an electrode/electrolyte interface. Supercapacitors that only involve physical adsorption, in which there is no electrochemical reactions on the electrode material (e.g. carbon) while charging and discharging process (Fig. 7a) are called EDLC. In this type of supercapacitors, no charge transfers across the electrode/electrolyte interface, and no net ion exchanges occur between the electrode and the electrolyte [23]. This implies that the electrolyte concentration remains constant during the charging and discharging processes. Since there is no physical change in the electrodes during charge/

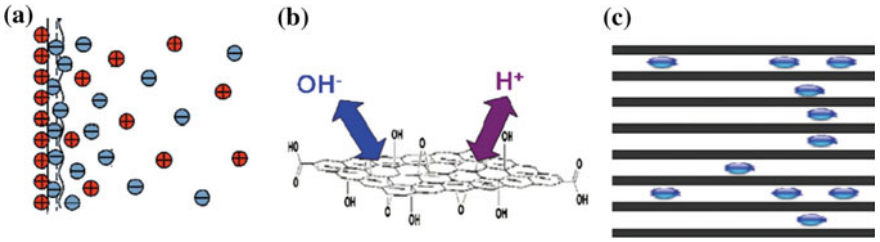

Fig. 7 The working principle of supercapacitors. **a** Electric double layer, **b** redox reaction on the surface and **c** redox reaction in bulk [24]

discharge process, EDLCs can sustain millions of cycles. The model of energy storage could be defined by the following equation:

$$E = 1/2\, CV^2 \tag{1}$$

where E is the entire energy delivered, C denotes the specific capacitance and V is the potential window.

However, due to the electrostatic surface charging mechanism, EDLCs suffer from a limited energy density and scientific research mainly emphasises to improve energy performance. The materials for EDLCs should be highly conductive large specific surface area. Different carbon materials, such as activated carbon, carbon nanofibres, carbon nanotubes are considered to be best electrode materials for EDLCs.

Pseudocapacitors

The pseudocapacitors are different from EDLC in the way in which charge is stored. Pseudocapacitive charge storage fundamentally relies on redox reactions between electrode materials and electrolyte ions. The electric energy is generated by fast Faradic redox reaction, which produces pseudocapacitance. Materials undergoing such redox reactions include conducting polymers and several metal oxides (RuO_2, MnO_2, Co_3O_4 etc.) [25]. Depending on the location of these redox reactions, the pseudocapacitive charge storage can be categorized into surface charge storage and bulk charge storage (Fig. 7 b and c). These pseudocapacitors can be superimposed on any electric double layer capacitors. In systems, where multiple oxidation states can be accessed, the pseudocapacitors often provide a higher energy density than EDLCs. Since the electrochemical processes occur both on the surface and in the bulk near the surface of the solid electrode, pseudocapacitors exhibit higher specific capacitance and energy density than EDLCs. However, pseudocapacitors suffer from relatively lower power density than EDLC because Faradic processes are normally slower than non-faradic processes. Moreover, due to the physical changes of the electrodes during redox reactions, pseudocapacitors have poor cycling stability compared with EDLCs [25].

Supercapacitors show potential applications in electronics, transportation, communication and aviation. It can also be used in a wide range of energy capture and storage applications either by themselves as a primary power source or in combination with batteries and fuel cells. Supercapacitors can be used as uninterrupted power supplies (back-up supplies used to protect against power disruption) and load-levellers (back-up power for memories, microcomputers, clocks, system boards etc.). In combination with batteries and fuel cells, supercapacitors are likely to be used for powering HEVs and EVs [26].

6.3 Chemical Energy Storage (Batteries)

Batteries are rechargeable electrochemical systems used to store energy. These are the oldest and most established form of electricity storage, which store electricity in the form of chemical energy [27]. Among the different types of storage methods, systems based on chemical energy storage are very attractive. A battery comprised of single or multiple electrochemical cells, connected in series or in parallel or both depending on the desired output voltage. As presented in Fig. 8, each cell consists of

- The anode is the negative electrode of a cell associated with oxidative chemical reactions that release electrons into the external circuit.
- The cathode is the positive electrode of a cell associated with reductive chemical reactions that gain electrons from the external circuit.
- An electrolyte is a material that provides the medium for transfer of electrons between the positive and negative electrodes of a cell.

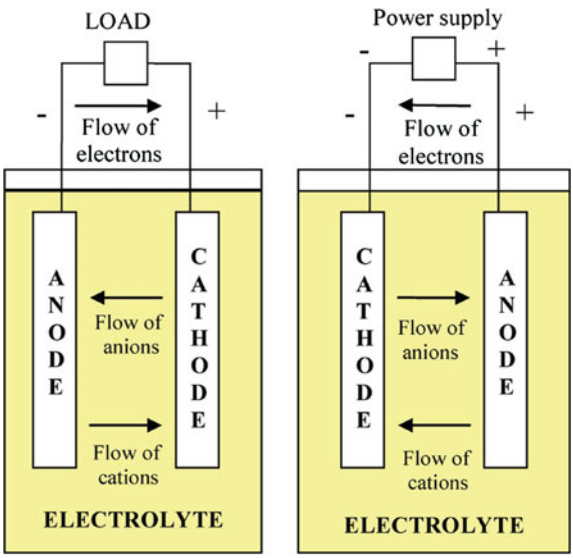

Fig. 8 Rechargeable cell/battery diagram [28]

- A separator is a physical barrier between the positive and negative electrodes incorporated into most cell designs to prevent electrical shorting. The separator can be a gelled electrolyte or a microporous plastic film or other porous inert material filled with electrolyte. Separators must be permeable to the ions and inert in the battery environment.

During discharge electrochemical reactions occur at the two electrodes generating a flow of electrons through an external circuit. The reactions are reversible, allowing the battery to be recharged by applying an external voltage across the electrodes. The batteries are rated in terms of their energy and power capacities. For most of the battery types, the energy and power capacities are not independent and are fixed during the battery design. Some of the other essential features of a battery are cycle life, efficiency, depth of discharge, operating temperature, self-discharge and energy density. At present, significant development is going on in battery technology. Different types of batteries are being developed of which some are available commercially while some are still in the experimental stage [29]. They not only provide environmental advantages and fuel flexibility, but also offer a number of important advantages to the electricity utility. They can respond very quickly to load changes and accept co-generated and/or third-party power, thus enhancing the system stability. Various battery technologies for power system applications are discussed in the following sections.

6.3.1 Lead–Acid Battery

Over the past hundred years, lead–acid battery technology has been the most widely used of any electrochemical storage medium. Lead–acid batteries that store and release electricity via a reversible electrochemical conversion. It is made of stacked cells, immersed in a dilute solution of sulfuric acid (H_2SO_4) as an electrolyte. The positive electrode (Cathode) of each cell is composed of lead dioxide (PbO_2), while the negative electrode (anode) is sponge lead (Pb). On discharging, both electrodes are converted into lead sulphate ($PbSO_4$). During charge, both electrodes return to their initial state. The electrochemical reactions are

(I) Anode:

$$Pb + SO_4^{2-} \leftrightarrow PbSO_4 + 2e \tag{2}$$

(II) Cathode:

$$PbO_2 + SO_4^{2-} + 4H^+ + 2e^- \leftrightarrow PbSO_4 + 2H_2O \tag{3}$$

These batteries have been applied to almost every area of industry, and their sales constitute 40–45 % of all battery sales in the world [30]. Since their availability, lead–acid batteries have been tested for utility applications, especially for power quality, reliability control and power regulation. There are two major types

of lead–acid batteries: flooded batteries, which is the most common topology, and valve regulated batteries, which are subject of extensive research and development. Lead–acid battery has low cost and a high reliability with a round trip efficiency of 70–90 %. It is a popular storage choice for uninterrupted power supply (UPS), power quality and some spinning reserve applications. However, lead–acid batteries have a short cycle life of 500–1000 cycles and low energy density (30–50 Wh/kg), which limits its application for energy management. Lead–acid batteries also have a poor low temperature performance. In reality, high operation temperature (up to 45 °C) can improve the battery performance in terms of higher capacity, but reduce the life time of the system [28].

6.3.2 Nickel–Cadmium Battery

Development of nickel–cadmium (Ni–Cd) rechargeable batteries has been carried out since 1950. The main components of Ni–Cd batteries are nickel hydroxide (positive electrode), cadmium hydroxide (negative electrode), a separator and an alkaline electrolyte (KOH) [31]. During discharge, $Ni(OH)_2$ is the active material of the positive electrode, and $Cd(OH)_2$ is the active material of the negative electrode. During charge cycle, nickel oxyhydroxide (NiO(OH)) is the active material of positive electrode and metallic Cd is the active material of the negative electrode. The overall electrochemical reaction is

$$2NiO(OH) + Cd + 2H_2O \leftrightarrow 2Ni(OH)_2 + Cd(OH)_2 \quad (4)$$

This type of battery can be found in two different forms, depending on the application: (i) sealed form in portable equipment and (ii) flooded form in general industrial applications. Ni–Cd batteries have a higher energy density (50–75 Wh/kg) and robust reliability. They have longer cycle life (more than 3500 cycles) than lead–acid batteries combined with very low maintenance requirements. These advantages over lead–acid batteries make them favourable for emergency lighting, UPS, power tools, generator starting and telecoms. The major drawbacks of Ni–Cd batteries are their toxicity and the fact that they suffer from the "memory effect". Cadmium is a toxic heavy metal which can cause health risk of humans.

6.3.3 Sodium–Sulphur Battery

Sodium–sulphur batteries (NaS) are one of the promising options for high power energy storage applications. As shown in Fig. 9, the NaS batteries consist of liquid (molten) sulphur as the positive electrode and liquid (molten) sodium as the negative electrode [32]. A solid ceramic Beta alumina (Al_2O_3) acts as both the separator and the electrolyte simultaneously. During the discharge cycle, the metallic sodium is oxidized, releasing Na^+ ions. The electrolyte enables the transfer of sodium ions to the cathode where they combine with sulphur to form sodium

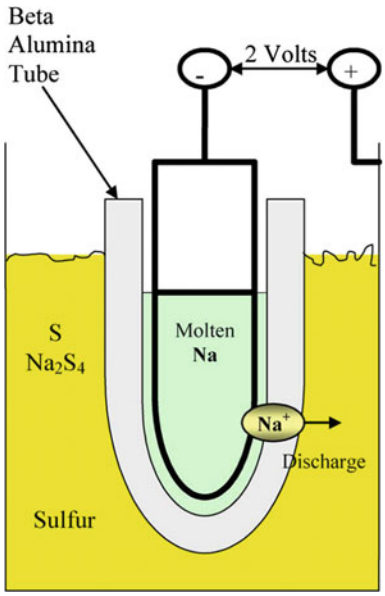

Fig. 9 NaS battery [28]

polysulfides: $2Na + S \leftrightarrow Na_2S_4$. During the charge cycle, the sodium polysulphide is decomposed into sodium and sulphur. The battery operating temperature is in the range of 300–350 °C. Therefore, NaS batteries need to be heated externally for optimal operation.

NaS batteries exhibit high energy density (150–240 Wh/kg) and power density (150–230 W/kg), good temperature stability, high Coulombic efficiency (75–95 %), long cycle life (~2500 cycles), good safety and inexpensive. These batteries can be used for load levelling, UPS applications, emergency power supply, being suitable to a number of markets, such as industrial applications and wind power generating systems. The batteries are made of abundant and low-cost materials, making them suitable for large-scale industrial production. However, the major disadvantage is that an external heat source is required to operate NaS batteries, which partially reduces the battery performance. NaS batteries are currently used in electricity grid-related applications such as peak-shaving and improving power quality.

6.3.4 Sodium Nickel Chloride Battery

Sodium nickel chloride battery is a high temperature (~300 °C) system and also known as ZEBRA battery [33]. In this system, nickel chloride is used as the positive electrode. The chemical reaction occurring in a ZEBRA battery is

$$2NaCl + Ni \leftrightarrow NiCl_2 + 2Na \quad (5)$$

Compared to NaS batteries, ZEBRA batteries can withstand limited overcharge and discharge and have potentially better safety characteristics and high cell voltage (2.58 V). The drawbacks with respect to NaS batteries are their low energy density ($\sim$120 Wh/kg) and power density ($\sim$150 W/kg). Another disadvantage is that only one company (Beta R&D, UK) is trying to develop this technology. At present, Beta R & D is developing a high power version of the ZEBRA battery for hybrid electric vehicles, a high energy version for storing renewable energy and a load-levelling battery for industrial applications [33].

6.3.5 Lithium-Ion Battery

Lithium-ion batteries store electrical energy in electrodes made of lithium intercalation (or insertion) compounds. Lithium intercalation compounds are used as positive and negative electrode materials in lithium-ion batteries [34]. In a typical lithium-ion cell, graphite and lithium metal oxide ($LiCoO_2$) are used as a negative electrode (anode) and a positive electrode (cathode), respectively. A non-aqueous Li^+ conducting medium is used as electrolyte. The positive and negative electrodes are separated by an electrolyte-filled porous polymer membrane that allows lithium-ion transfer but prevents electrolyte from direct contact. The lithium ions are shuttled between two host electrodes (anode and cathode) during the charge–discharge process. When the battery is discharging, Li^+ ions de-intercalate from the anode, pass through the electrolyte and intercalate into the cathode. Meanwhile, the electrons pass through the external circuit from the negative electrode to the positive electrode. On charging, the process is reversed when an external voltage is applied to the battery. During charge–discharge process, Li ions move between the negative and positive electrode, empowering the conversion of chemical energy into electrical energy and storage of electrochemical energy within the battery.

Figure 10 illustrates the basic lithium-ion battery system that leads the current battery market. The cell reactions are reversible lithium-ion intercalation and de-intercalation cycles between two layered structures. The redox reactions involved in $LiCoO_2$/graphite cell are presented as follows [35]:

Cathode:

$$LiCoO_2 \leftrightarrow Li_{1-x}CoO_2 + xLi^+ + xe^- \quad (1 < x < 0) \quad (6)$$

Anode:

$$6C + xLi^+ + xe^- \leftrightarrow Li_xC_6 \quad (1 < x < 0) \quad (7)$$

Among rechargeable batteries, lithium-ion batteries have become popular with many advantages such as high energy density, low maintenance, long cycle life, no

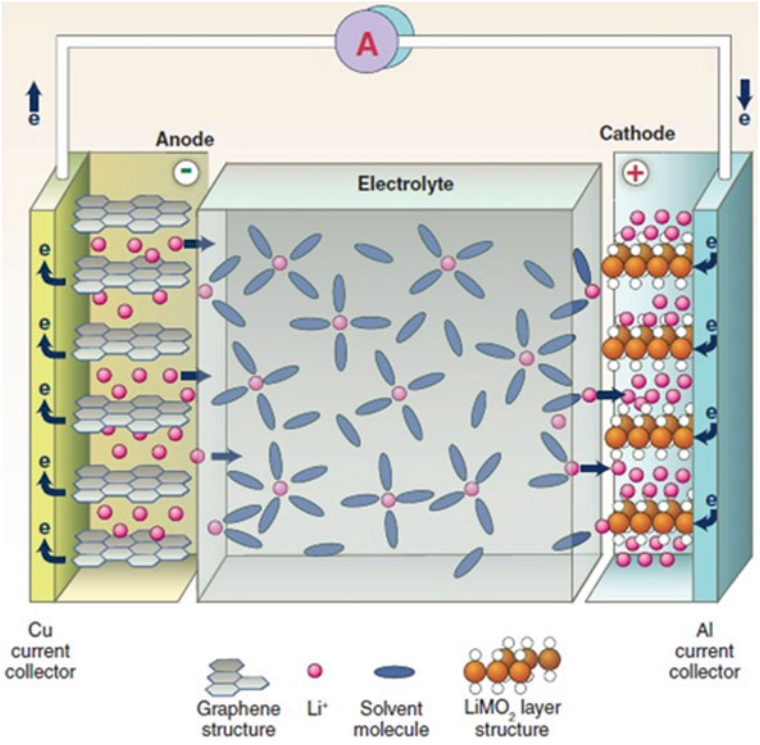

Fig. 10 Schematic of a LIB [36]

memory effect and low self-discharge. In the past two decades since the first commercial products manufactured by SONY, lithium-ion batteries (LIBs) have been widely applied for portable electronic devices. These include notebook computers, cell phones, digital cameras, etc. Its energy density is 2–3 times and power density 5–6 times higher than traditional nickel–metal hybrid, nickel–-cadmium and lead–acid batteries. The advantages in high energy capacity and power over other technologies have made lithium-ion batteries the most promising option for transportation application. Extensive research and development were carried out in the past decades. Significant progress has been made in materials and chemistries to improve the battery technologies for the applications. The worldwide market of lithium-ion batteries is valued at 10 billion US dollars per annum. Lithium-ion batteries are now being intensively pursued upcoming large-scale transportation applications including hybrid electric vehicles (HEV), plug-in hybrid electric vehicles (PHEV) and electric vehicles (EV) [37]. They are also seriously considered for the efficient storage and utilization of intermittent renewable energies such as, solar and wind.

Referring the disadvantages of lithium-ion batteries, it can be mentioned that the lithiated graphite electrode operates at a potential close to that of metallic lithium,

leading to Li-dendrite growth and potential electrical shorting. In the presence of flammable organic electrolyte solvents currently in use, there is a risk of heat generation, thermal runway and fire. An additional challenge is the high cost that may not be critical to small portable electronic applications but is very important for large-scale applications. There are some other battery technologies, including lithium sulphur batteries, sodium ion batteries, lithium oxygen batteries are in experimental stage. Many research groups and industries around the globe are continuing intensive research to develop new environmentally benign battery technologies for large-scale energy storage applications.

7 Conclusions and Future Perspective

Today climate changes and energy storages are confronting our society with considerable technological, economic, safety, health, and national security challenges. The current trend towards reducing greenhouse gas emission and increasing penetration of renewable energy, along with growing demands of high-quality power, calls for urgent development and implementation of EES systems. EES systems are the key enabling technologies for utility and transport applications. In particular, the proliferation of energy storage will enable the integration and dispatch of renewable PV generation. Without suitable EES, the current electrical grid could allow for only limited level of penetration of renewable energy generation from PV. Storage is a key element for the growth of renewable energies, particularly for PV generation. Installing EES into the grid would not only facilitate increasing penetration of renewable energy, but insure quality power for a society. Implementing EES would help to reduce greenhouse gas emissions by replacing fossil-burning turbines currently employed to stabilize the grid.

The success of these applications of energy storage will depend on how well storage technologies can meet key expectations. The most important of these are low installed cost, long life, high efficiency and high reliability. A number of potential technologies for EES exist and some of these have demonstrated for utility applications. However, these technologies are facing either challenges in meeting the performance and economic matrix for the stationary applications, or limits in environment, site selection etc. This also calls for both basic and applied research to further develop current technologies and discover new technologies that can address the requirements for renewable and utility applications.

References

1. Whitesides GM, Crabtree GW (2007) Don't forget long-term fundamental research in energy. Science 315:796–798
2. Key World Energy Statistics, International Energy Agency, Paris, 2009, http://www.iea.org/textbase/nppdf/free/2009/key_stats_2009.pdf. Accessed June 2010

3. Meier PJ, Wilson PPH, Kulcinski GL, Denholm PL (2005) US electric industry response to carbon constraint: a life-cycle assessment of supply side alternatives. Energy Policy 33:1099–1108
4. Levitus S, Antonov JI, Wang J, Delworth TL, Dixon KW, Broccoli AJ (2001) Anthropogenic warming of Earth's climate system. Science 292:267–270
5. Assessment Report (AR4), Climate Change 2007: Synthesis Report, Summary for Policymakers, IPCC Plenary XXVII, Valence, Spain, 12–17 Nov 2007. http://www.ipcc.ch/pdf/assessment-report/ar4/syr/ar4_syr_spm.pdf. Assessed June 2010
6. The Topex/Poseidon satellite was launched on 10 August 1992 with the objective of "observing and understanding the ocean circulation". A joint project between NASA, the US space agency, and CNES, the French space agency, see http://topex-www.jpl.nasa.gov/. Accessed June 2010
7. Ginley D, Green MA, Collins R Solar energy conversion toward 1 terawatt. MRS Bull 33:355–364
8. Alam MS, Roychowdhury A, Islam KK, Huq AMZ (1998) A revisited model for the physical quality of life (PQL) as a function of electrical energy consumption. Energy 23:791–801
9. Poizot P, Dolhem F (2011) Clean energy new deal for a sustainable world: from non-CO_2 generating energy sources to greener electrochemical storage devices. Energy Environ Sci 4:2003–2019
10. Yang Z, Liu J, Baskaran S, Imhoff CH, Holladay JD (2010) Enabling renewable energy-and the future grid-with advanced electricity storage. JOM 62:14–23
11. Toledo OM, Filho DO, Diniz ASAC (2010) Distributed photovoltaic generation and energy storage systems: a review. Renew Sust Energ Rev 14:506–511
12. Baker JN, Collinson A (1999) Electrical energy storage at the turn of the millennium. Power Eng J 6:107–112
13. Walawalkar R, Apt J, Mancini R (2007) Economics of electric energy storage for energy arbitrage and regulation. Energy Policy 5:2558–2568
14. Denholm P, Kulcinski GL (2004) Life cycle energy requirements and greenhouse gas emissions from large scale energy storage systems. Energ Convers Manage 45:2153–2172
15. Linden D, Reddy TB (2002) Handbook of Batteries, 3rd edn. Mcgraw-Hill, New York
16. Denholm P, Holloway T (2005) Improved accounting of emissions from utility energy storage system operation. Environ Sci Technol 39:9016–9022
17. Ibrahim H, Ilinca A, Perron J (2008) Energy storage systems-characteristics and comparison. Renew Sust Energ Rev 12:1221–1250
18. Jewitt J (2005) Impact of CAES on wind in Tx and NM, In: Annual peer review meeting of DOE energy systems research. San Francisco, USA, pp 1–16, 20 Oct 2005
19. Boom RW (1990) Superconductive magnetic energy storage for electric utilities-a review of the 20 year Wisconsin program. In Proceedings of 34th International Power Sources Symposium, Cherry Hill, NJ, pp 1–4, 25–28 Jun1990
20. http://www.beaconpower.com/products/EnergyStorageSystems/DocsPresentations.htm. 20 Mar 2007
21. Chen H, Cong TN, Yang W, Tan C, Li Y, Ding Y (2009) Progress in electrical energy storage system: a critical review. Prog Nat Sci 19:291–312
22. Burke A (2007) Ultracapacitors: why, how and where is the technology. J Power Sources 91:37–50
23. Conway BE (1999) Electrochemical supercapacitors, scientific fundamentals and technological applications. Kluwer Academic Publishers/Plenum Press, New York
24. Liu C, Li F, Ma LP, Cheng HM (2010) Advanced materials for energy storage. Adv Mater 22: E28–E62
25. Wang GP, Zhang L, Zhang J (2012) A review of electrode materials for electrochemical supercapacitors. Chem Soc Rev 41:797–828
26. Kotz R, Carlen M (2000) Principles and applications of electrochemical capacitors. Electrochim Acta 45:2483–2498

27. Winter M, Brodd RJ (2004) What are batteries, fuel cells, and supercapacitors? Chem Rev 104:4245–4269
28. Hadjipaschalis I, Poullikkas A, Efthimiou V (2009) Overview of current and future energy storage technologies for electric power applications. Renew Sust Energ Rev 13:1513–1522
29. Linden D, Reddy TB (2002) Handbook of batteries. The McGraw-Hill Companies Inc., New York
30. Parker CD (2001) Lead-acid battery energy-storage systems for electricity supply networks. J Power Sources 100:18–28
31. Moriokaa Y, Narukawab S, Itou T (2001) State-of-the-art of alkaline rechargeable batteries. J Power Sources 100:107–116
32. http://www.electricitystorage.org/tech/technologies_technologies.htm. 20 Mar 2007
33. Galloway RC, Dustmann C (2003) ZEBRA battery-material cost availability and recycling. In: Proceeding of international electric vehicle symposium (EVS-20), Long Beach, Canada, pp 1–9, 15–19 Nov 2003
34. Tarascon JM, Armand M (2001) Issues and challenges facing rechargeable lithium batteries. Nature 414:359–367
35. Yang Z, Zhang J, Kinter-Meyer MCW, Lu X, Choi D, Lemmon JP, Liu J (2011) Electrochemical energy storage for green grid. Chem Rev 111:3577–3613
36. Dunn B, Kamath H, Tarascon JM (2011) Electrical energy storage for the grid: a battery of choices. Science 334:928–935
37. Goodenough JB, Kim Y (2010) Challenges for rechargeable Li batteries. Chem Mater 22:587–603

Superconducting Magnetic Energy Storage Modeling and Application Prospect

Jian-Xun Jin and Xiao-Yuan Chen

Abstract Superconducting magnetic energy storage (SMES) technology has been progressed actively recently. To represent the state-of-the-art SMES research for applications, this work presents the system modeling, performance evaluation, and application prospects of emerging SMES techniques in modern power system and future smart grid integrated with photovoltaic power plants. A novel circuit-field-superconductor coupled SMES energy exchange model is built and verified to bridge the applied superconductivity field to the electrical engineering and power system fields. As an emerging SMES application case to suit photovoltaic power plants, a novel low-voltage rated DC power system integrated with superconducting cable and SMES techniques is introduced and verified to implement both the high-performance fault current limitation and transient power buffering functions. Four principal SMES application schemes of a sole SMES system, a hybrid energy storage system (HESS) consisting of small-scale SMES and other commercial energy storage systems, a distributed SMES (DSMES) system, and a distributed HESS (DHESS) are proposed and compared for achieving efficient and economical power management applications in future photovoltaic power plants.

Keywords Energy storage · Superconducting magnetic energy storage · Energy exchange modeling · Superconducting AC loss · Circuit-field-superconductor coupled analysis · Microphotovoltaic grid · Smart grid

J.-X. Jin (✉)
School of Electrical Engineering and Automation, Tianjin University, Tianjin, China
e-mail: jxjin@tju.edu.cn

X.-Y. Chen
School of Engineering, Sichuan Normal University, Chengdu, China

M.R. Islam et al. (eds.), *Advances in Solar Photovoltaic Power Plants*,
Green Energy and Technology, DOI 10.1007/978-3-662-50521-2_10

1 Introduction to Energy Storage

The alternatives for the continued availability of highly reliable and inexpensive power supply in future smart grid include the deployment of clean coal generation, nuclear power generation, renewable energy generation, and other generation resources. It is expected to combine with centralized and distributed power generation for developing the modern resource-saving and environment-friendly power systems. The main role of the energy storage systems (ESSs) is to increase the penetration of renewable energy sources such as photovoltaic power plants, to level the load curve, to contribute to the frequency control, to upgrade the transmission line capability, to mitigate the voltage fluctuations, and to increase the power quality and reliability, etc. Various ESSs can be used to allow increased capacity and stability to be derived from any given quantity of physical resources like photovoltaic power plant, and should be considered as a strategic choice that allows for optimum use of existing and new resources of all kinds [1–6].

According to the energy forms of the currently available ESSs, they are mainly divided into chemical energy storage and physical energy storage, as shown in Fig. 1. For the chemical energy storage, the mostly commercial branch is battery energy storage, which consists of lead-acid battery, sodium-sulfur battery, lithium-ion battery, redox-flow battery, metal-air battery, etc.

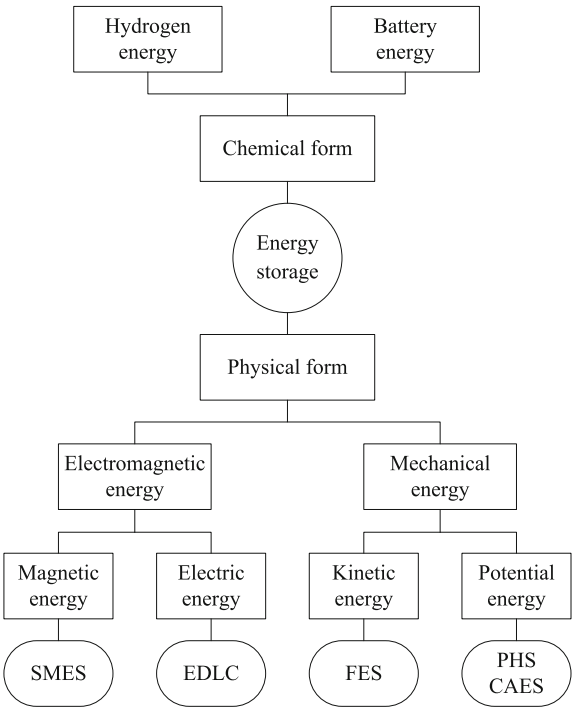

Fig. 1 Classification of energy storage systems

The use of lead-acid batteries for energy storage dates back to mid-1800s. Lead-acid battery consists of spongy lead as the negative active material, lead dioxide as the positive active material, immersed in diluted sulfuric acid electrolyte, and lead as the current collector. It is most widely used due to its low capital cost and mature production techniques; however, it also has serious shortcomings such as low storage efficiency and performance degradation under the fast repeated charge–discharge operations.

Sodium-sulfur battery consists of molten sulfur at the positive electrode and molten sodium at the negative electrode separated by a solid beta alumina ceramic electrolyte. It is known for its strong cycle life, decent energy efficiency, and specific energy 3–4 times that of lead-acid battery. Moreover, it is able to provide short power bursts (about 30 s) that are 6 times of the rated continuous power, making it particularly suitable in short-time power quality maintenance.

Lithium-ion battery is a typical new-type high-energy and high-efficiency batteries. Its positive electrode is made of a lithium metal oxide, and the negative electrode is composed of layered graphitic carbon. Thanks to its extremely high efficiency as well as high energy density, power density, cell voltage, and long cycle life over other batteries, lithium-ion battery has become popular in various advanced equipment applications such as electric vehicle, computer, and cell phone. However, its special packaging of overcharge protection circuit causes the high production cost, which eventually prevents many large-scale systems from being developed and industrialized.

Another promising environment-friendly hydrogen energy storage branch has three fundamental forms of compressed gaseous hydrogen (CGH_2), liquid hydrogen (LH_2), and solid-state absorbers [7, 8]. The mostly commercial CGH_2 is operated at 35–70 MPa and room temperature, while the promising LH_2 with much higher energy density and no high-pressure risk is operated at 0.5–1 MPa and 20–30 K. The solid state absorbers of hydrogen include hydrides and high-surface materials, which offer very high volumetric hydrogen density on a materials basis.

The physical energy storage can be further divided into mechanical energy storage and electromagnetic energy storage. Among the mechanical energy storage systems, there are two subsidiary types, i.e., potential-energy-based pumped hydro storage (PHS) and compressed air energy storage (CAES), and kinetic-energy-based flywheel energy storage (FES).

Pumped hydro storage system consists of two reservoirs with a height differential and a penstock or pipe connecting them. To produce electrical energy, water is allowed to flow from the upper reservoir down the pipe through a water turbine and into the lower reservoir. Its simplicity of design, relatively low cost, and similarity in operation to hydroelectric power has made it the industry standard for storage for a century. However, its practical installation requires very specific geographic conditions and high capital cost, and might cause some undesirable environmental impacts.

Compressed air energy storage system consists of air compressor, air recuperator, and air storage place, which can be in a geologic formation such as salt caverns from mining, impervious rock formations, porous rock aquifers, and depleted oil or

gas wells. Once the air is compressed and stored, electrical energy is extracted using a standard gas turbine. Thanks to its similarity to standard combustion turbine systems, compressed air energy storage systems are easily integrated into the existing power systems.

Flywheel energy storage system stores kinetic energy in a rotatory disc in the form of angular momentum. It has high power density, high energy density, and virtually infinite number of charge–discharge cycles. Recent advances in power electronics and bearing material engineering have made this technology attractive for a number of other applications such as frequency regulation and power quality improvement. Moreover, the promising superconducting suspended bearings have significantly reduced the self discharge due to the frictional losses.

In practice, the electromagnetic energy storage systems consist of electric-energy-based electrochemical double-layer capacitor (EDLC), which is also called super capacitor or ultra capacitor, and magnetic-energy-based superconducting magnetic energy storage (SMES).

Electrochemical double-layer capacitor uses high-permittivity dielectric with a very high electrode surface area. The electrode surface area is maximized by using porous carbon as the current collector, allowing a relatively large amount of energy to be stored at the collector surface. The two electrodes are separated by a very thin porous separator and immersed in an electrolyte such as propylene carbonate. Electrochemical double-layer capacitor has the ability to charge and discharge more quickly over electrochemical batteries, and can practically be charged at any rate within an available temperature range from about −55 to 85 °C. However, due to the high permeability and close proximity of the electrodes, EDLC has a low-voltage-withstand capability, e.g., 2–3 V. This can be a serious problem to achieve the current and voltage balances within the hundreds to thousands of series-parallel-connected EDLC units for high-voltage applications.

Superconducting magnetic energy storage system can store electric energy in a superconducting coil without resistive losses, and release its stored energy if required [9, 10]. Most SMES devices have two essential systems: superconductor system and power conditioning system (PCS). The superconductor system mainly consists of (i) superconducting magnet (SM), (ii) cryogenic Dewar, (iii) refrigeration system, (iv) quench protection system, (v) persistent current switch, and (vi) current leads. The PCS mainly consists of (i) current-voltage (I-V) chopper, (ii) DC-link capacitor, (iii) DC-AC bidirectional converter, and (iv) AC filter. As compared to other ESSs, it has advantages: (i) fast response speed, (ii) high power density, (iii) high storage efficiency, (iv) long life-time, and (v) little environmental pollution. In addition, several subsidiary benefits from the SMES technology can be also derived (i) to lower the consumption of fossil resources, (ii) to increase the operation efficiency and lifetime of generators, (iii) to defer the power generation and transmission capacities, and (iv) to increase the availability of renewable energy sources such as photovoltaic power plants.

2 SMES Modeling and Verification

2.1 Energy Exchange Circuit

The PCSs for SMES applications mainly include [11–14] thyristor-based, current source converter (CSC-based, and voltage source converter (VSC)-based topologies, which can be used to develop various power conversion, compensation, and control equipments, e.g., (i) flexible AC transmission systems (FACTS) for power transmission, (ii) distributed FACTS (DFACTS) for power distribution, and (iii) uninterrupted power supplies (UPSs) for power end-users.

Figure 2 shows a typical VSC-based PCS. It mainly includes an SM in the cryostat, a current/voltage (I/V) chopper, a DC-link capacitor, a DC/AC converter, and an AC filter. The PCS can be connected in series or in parallel with the AC grid. Figure 3 shows three basic FACTS and DFACTS schemes, i.e., (i) series-type static synchronous series compensator (SSSC), (ii) parallel-type static synchronous compensator (STATCOM), and (iii) series-parallel-type unified power flow controller (UPFC) formed by the combination of a SSSC and a STATCOM. For the applications in high-voltage alternating-current (HVAC) and high-voltage direct-current (HVDC) transmissions, large-scale PCSs consisting of multilevel choppers and converters are needed. In various DC applications such as DC output-type distributed generators and DC distribution network, the SMES has

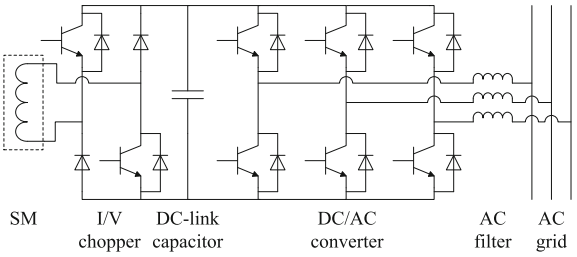

Fig. 2 Topology of a typical VSC based PCS

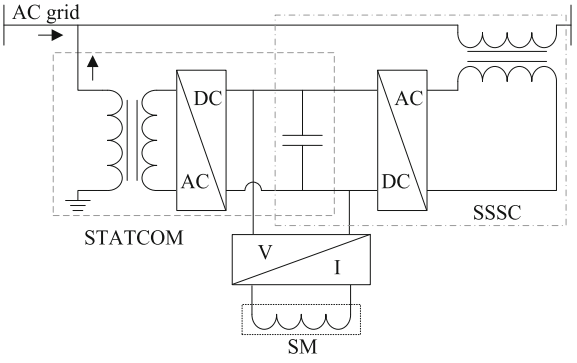

Fig. 3 Topologies of three basic FACTS and DFACTS schemes

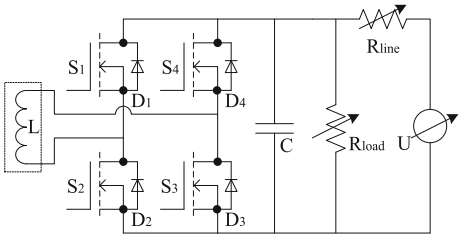

Fig. 4 Energy exchange circuit with a brige-type chopper

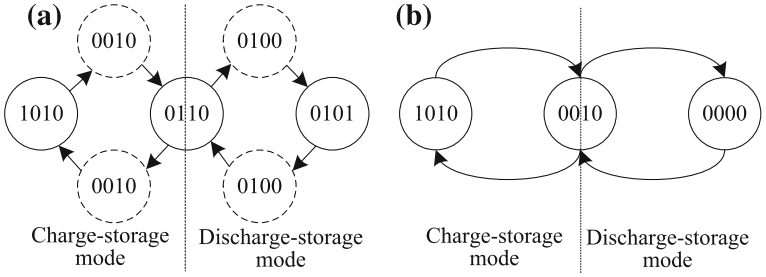

Fig. 5 Digital state diagrams of the two I-V choppers: **a** Bridge-type chopper; **b** Conventional chopper

simpler system topology and easier control requirement. Only an I/V chopper is needed to link the SC to the DC bus for online power flow regulation.

For the SM used in a SMES device, the targeted power system applications can be transformed into equivalent energy exchange demands. To simplify the relatively complex system topology and relevant control strategies, an equivalent load network is therefore introduced to build an energy exchange circuit, as shown in Fig. 4 [15–18]. A controllable voltage source U is used to imitate the external power fluctuations, a power-line resistor R_{line} is used to imitate the consumed power from the step-up power transformer, AC filter, and DC/AC converter in a practical PCS, while a power-load resistor R_{load} is used to imitate the external load fluctuations. To maintain the voltage $U_{\text{R}}(t)$ across the power-load resistor around its rated voltage, the SM should carry out the dynamic energy exchanges through the online conversions of the operation state of the chopper used. Thus, the external power system problems to be solved can be equivalently achieved by adjusting the above three controllable parameters.

As for the energy exchange control, a bridge-type I-V chopper formed by four MOSFETs S_1–S_4 and two reverse diodes D_2 and D_4 is introduced [15–18]. By defining the turn-on or turn-off status of a MOSFET as "1" or "0," all the operation states can be digitalized as "$S_1S_2S_3S_4$." As shown in Fig. 5, the charge-storage mode ("1010" → "0010" → "0110" → "0010" → "1010") and the discharge–storage mode ("0101" → "0100" → "0110" → "0100" → "0101") correspond to

the control schemes for the power absorption operation and the power compensation operation, respectively. To carry out the comparative analyses, two MOSFETs S_1 and S_3 and two reverse diodes D_2 and D_4 are also introduced to form a conventional chopper.

When the operation voltage $U_R(t)$ across the power-load resistor R_{load} is between a minimum reference voltage U_{min} and a maximum reference voltage U_{max}, i.e., $U_{min} \leq U_R(t) \leq U_{max}$, the power-load resistor is assumed to operated in a rated voltage state, and thus the I-V chopper is operated in the energy storage state. The system current and voltage equations can be expressed by

$$U = I(t)R_{line} + I_R(t)R_{load} \tag{1}$$

$$U_0 + \frac{1}{C}\int_0^t I_C(t)\mathrm{d}t = I_R(t)R_{load} \tag{2}$$

$$I(t) = I_R(t) + I_C(t) \tag{3}$$

where $I(t)$, $I_R(t)$, and $I_C(t)$ are the currents through the power-line resistor, power-load resistor, DC-link capacitor and SM; U_0, the initial voltage across the power-load resistor and DC-link capacitor; C, the capacitance of the DC-link capacitor.

When $U_R(t) > U_{max}$, the power-load resistor is operated in a voltage swell state, and the I-V chopper is operated in the energy charge state. The system current and voltage equations can be expressed by (1), (4), and (5)

$$L\frac{\mathrm{d}I_L(t)}{\mathrm{d}t} + I_L(t)R_{SC} = U_0 + \frac{1}{C}\int_0^t I_C(t)\mathrm{d}t = I_R(t)R_{load} \tag{4}$$

$$I(t) = I_L(t) + I_R(t) + I_C(t) \tag{5}$$

where L is the inductance of the SM; $I_L(t)$, the coil current; I_0, the initial coil current; R_{SC}, the equivalent lossy resistance, which mainly comes from the I-V chopper and current leads.

When $U_R(t) < U_{max}$, the power-load resistor is operated in a voltage sag state and the I-V chopper is operated in the energy discharge state. The system current and voltage equations can be expressed by (1), (6), and (7)

$$-L\frac{\mathrm{d}I_L(t)}{\mathrm{d}t} - I_L(t)R_{SC} = U_0 + \frac{1}{C}\int_0^t I_C(t)\mathrm{d}t = I_R(t)R_{load} \tag{6}$$

$$I(t) + I_L(t) = I_R(t) + I_C(t) \tag{7}$$

2.2 Superconducting AC Loss Calculation

The sample SC used is a 0.2 H Bi-2223 solenoid coil having three same axial coil units in series [15]. Each unit is wounded by 21 layers with 35 turns per layer. The average gap width between the adjacent units is about 6 mm. The average gap width between the adjacent layers in one coil unit is about 2.7 mm. A 2D axisymmetric simulation model is built by using COMSOL software, as shown in Fig. 6. It consists of 63 coil layer units, and each unit formed by 35 turns has radial width of 12.6 mm and axial height of 4.2 mm. The inner and outer radii of each unit are 68 and 80.6 mm, respectively. The Bi-2223 tapes used are the AMSC high-strength tapes, whose average width is—4.2 mm, average thickness—0.28 mm, critical current—145.8 A at 77 K and self field. The filamentary thickness d_c and width w_c are 0.18 and 3.8 mm. The perpendicular and parallel time constants $\tau_{\perp}$ and $\tau_{//}$ are 33.07 and 0.93 ms, respectively.

In the 0.2 H Bi-2223 coil, the parallel component accounts for the vast majority of the total magnetic field distributed in the inner cavity area. However, the perpendicular component becomes larger as the location gets closer to two coil ends, as shown in Fig. 7. Due to the anisotropy, the turns located at two coil ends have

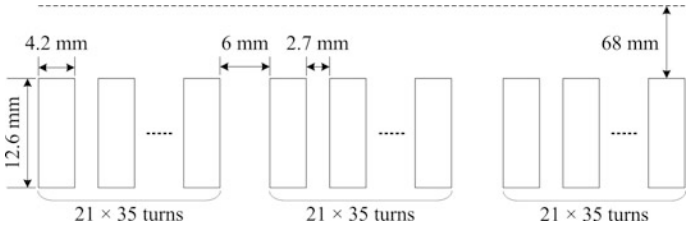

Fig. 6 2D axisymmetric model of the 0.2 H Bi-2223 solenoid coil

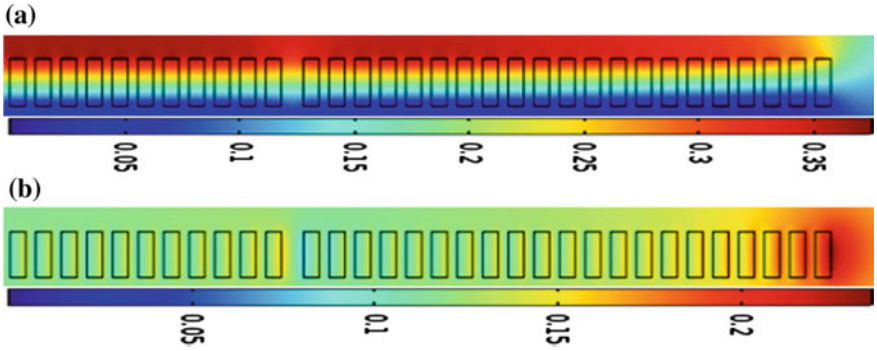

Fig. 7 Magnetic field distributions of the 0.2 H Bi-2223 solenoid coil when $I(t)$ is 60 A: **a** parallel magnetic field; **b** perpendicular magnetic field

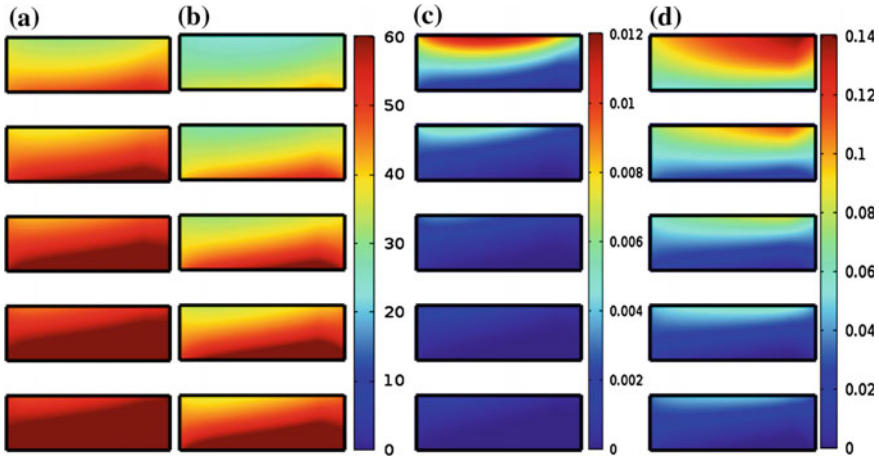

Fig. 8 Critical current and flux flow loss distributions of the five upper coil layers: **a** critical current distributions when $I_L(t)$ = 40 A; **b** critical current distributions when $I_L(t)$ = 60 A; **c** flux flow loss distributions when $I_L(t)$ = 40 A; **d** flux flow loss distributions when $I_L(t)$ = 60 A

lower critical current and higher flux flow loss as compared to those located at the middle coil part. Figure 8 shows the critical current and flux flow loss distributions of the five upper coil layers. To make all the coil turns of the 0.2 H Bi-2223 coil work at superconducting state, the calculated $I_c(B_{//}, B_{\perp})$ is about 40 A.

Besides the mentioned flux flow loss above, the superconducting tapes in the SC will also generate a certain amount of hysteresis loss, coupling current loss, and eddy current loss due to the real-time changes of the coil current and magnetic field during the energy exchange operations.

From the top to bottom of the 63 coil layers, they are defined as N_{layer} = 1, N_{layer} = 2, …, N_{layer} = 63, respectively. The top coil layer (N_{layer} = 1) generates the maximum perpendicular hysteresis loss and perpendicular coupling current loss, while the middle coil layer (N_{layer} = 32) generates the maximum parallel hysteresis loss and parallel coupling current loss, as shown in Figs. 9 and 10. The left side of each layer in Figs. 9 and 10 is located in the inner wall of the coil.

Based on the FEM calculations in Fig. 11, the total hysteresis loss $P_{hys}(t)$, flux flow loss $P_{flow}(t)$, coupling current loss $P_{coup}(t)$, and eddy current loss $P_{eddy}(t)$ can be fitted into four coil-current-dependent formula, as depicted by [19]

$$P_{hys}(t) = P_1 \times a_1 \times \left[\frac{I_m(t)}{I_1}\right]^{a_2} \times \frac{f(t)}{10 \times f_1} \tag{8}$$

$$P_{flow}(t) = P_1 \times b_1 \times \left[\frac{I_L(t)}{I_1}\right]^{b_2} \tag{9}$$

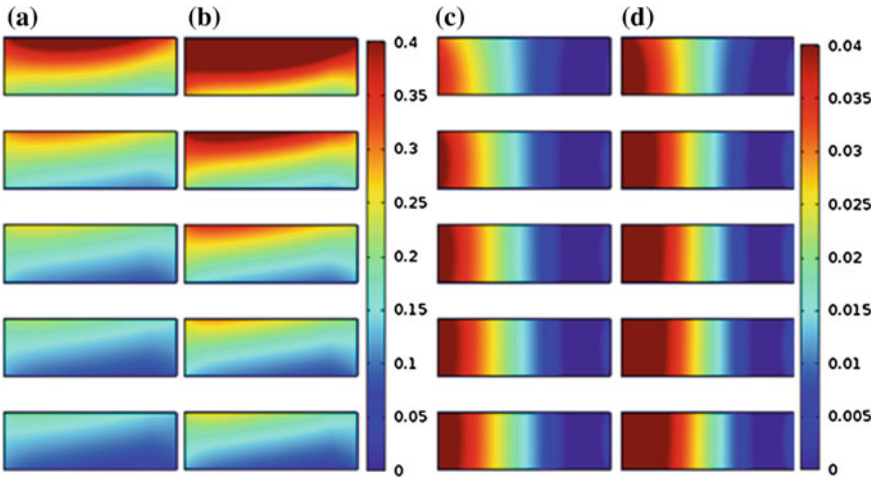

Fig. 9 Perpendicular and parallel hysteresis loss distributions: **a** $P_{hys\perp}$, $N_{layer} = 1$ to $N_{layer} = 5$, $I_m = I_{dc} = 15$ A, $f = 10$ Hz; **b** $P_{hys\perp}$, $N_{layer} = 1$ to $N_{layer} = 5$, $I_m = I_{dc} = 20$ A, $f = 10$ Hz; **c** $P_{hys//}$, $N_{layer} = 30$ to $N_{layer} = 34$, $I_m = I_{dc} = 15$ A, $f = 10$ Hz; **d** $P_{hys//}$, $N_{layer} = 30$ to $N_{layer} = 34$, $I_m = I_{dc} = 20$ A, $f = 10$ Hz

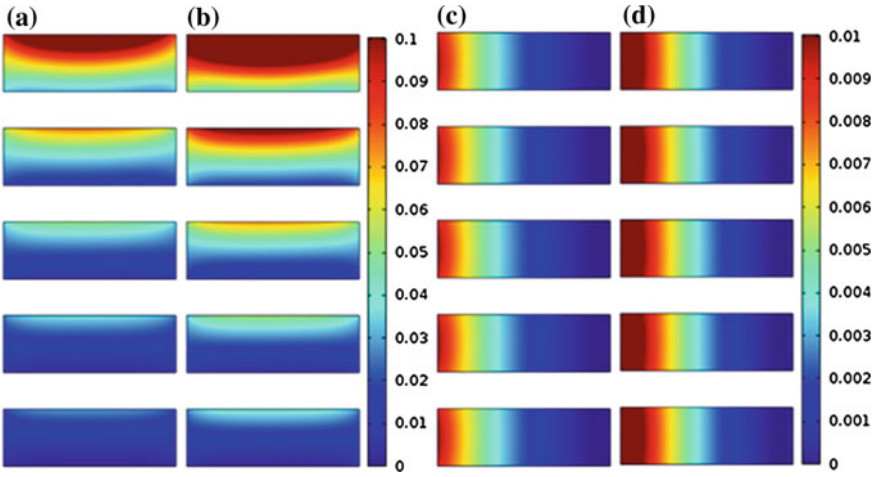

Fig. 10 Perpendicular and parallel coupling current loss distributions: **a** $P_{coup\perp}$, $N_{layer} = 1$ to $N_{layer} = 5$, $S(t) = 50$ A/s; **b** $P_{coup\perp}$, $N_{layer} = 1$ to $N_{layer} = 5$, $S(t) = 60$ A/s; **c** $P_{coup//}$, $N_{layer} = 30$ to $N_{layer} = 34$, $S(t) = 50$ A/s; **d** $P_{coup//}$, $N_{layer} = 30$ to $N_{layer} = 34$, $S(t) = 60$ A/s

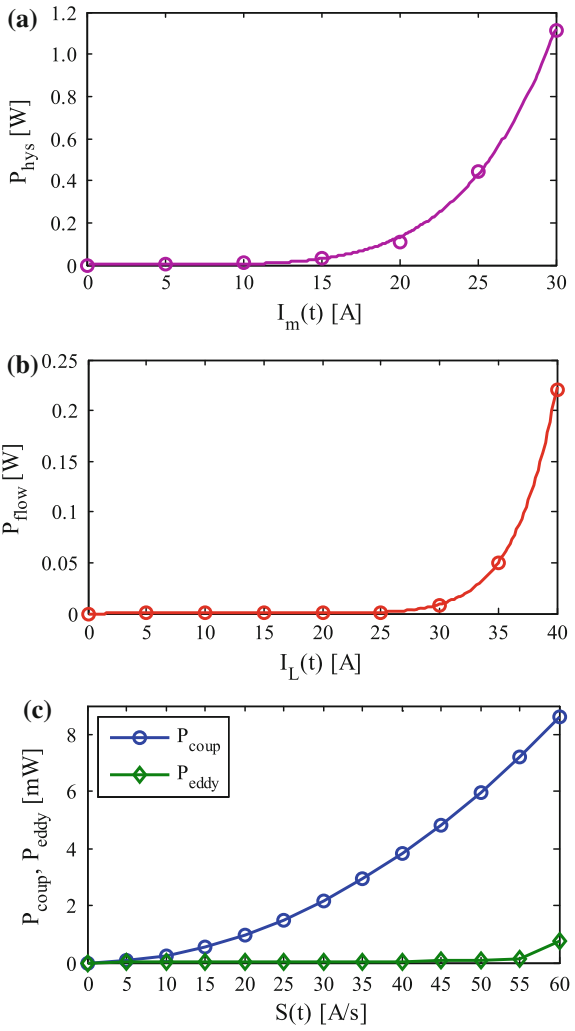

Fig. 11 Calculated and fitted AC loss of the whole coil: **a** hysteresis loss; **b** flux flow loss; **c** coupling current loss and eddy current loss

$$P_{\text{coup}}(t) = P_1 \times c_1 \times \left[\frac{1}{60} \times \frac{S(t)}{S_1}\right]^2 \tag{10}$$

$$P_{\text{eddy}}(t) = P_1 \times d_1 \times \left[\frac{1}{60} \times \frac{S(t)}{S_1}\right]^2 \tag{11}$$

where $I_{\text{m}}(t)$ and $f(t)$ are the peak current and operation frequency of the AC coil current; a_1, a_2 b_1, b_2, c_1, d_1, the coil-structure-dependent parameters; I_1, P_1, f_1, S_1, the normalizing constants of 1 A, 1 W, 1 Hz, 1 A/s. For the 0.2 H Bi-2223 coil, the fitted parameters $a_1 = 1.841 \times 10^{-5}$, $a_2 = 5.269$, $b_1 = 3.048 \times 10^{-19}$, $b_2 = 11.151$, $c_1 = 8.61$, $d_1 = 0.75$.

According to (10) and (11), both the coupling and eddy current loss distributions are similar. It can be seen that the total coupling current loss is about 11.5 times of the total eddy current loss. When the current changing rate $S(t)$ = 60 A/s, the total coupling current loss is about 8.3 mW, while the total eddy current loss is only about 0.7 mW.

2.3 Circuit-Field-Superconductor Coupled Model

In the past decades, the researchers in the applied superconductivity field have developed a number of superconducting magnet (SM) models based on the numerical and finite element algorithms to calculate and optimize the AC loss features of the SM itself. Due to its relatively complex system topologies and control strategies of a practical PCS, the most models [20] employed simple triangle or trapezoid coil current waves, which are insufficient to match with the practical coil current waves with high precision under dynamic energy exchange operations. On the other side, the researchers in the electrical engineering field have developed a number of PCS models, in which the SM is just utilized as an ideal lossless inductor to evaluate the energy exchange performance for the external system [21, 22].

To have both the superconducting AC loss and energy exchange features integrated in one model, this work proposes a new superconducting magnetic energy exchange (SMEE) model based on a circuit-field-superconductor coupled method. The PCS is simplified into an equivalent energy exchange circuit model for use in the AC loss calculations, while the superconductor system provides a coil-current-dependent SM model for use in the energy exchange performance evaluations.

The four main AC losses of the SM in a SMES device are simply calculated by four coil-current-dependent formulas (8)–(11), while the real-time coil current is equivalently obtained by solving the system current and voltage equations (1)–(7) of the equivalent energy exchange circuit. Thus, the coil current can be served as an intermediate link to bridge the applied superconductivity field with the electrical engineering field.

The basic principle of the circuit-field-superconductor coupled analysis is shown in Fig. 12. The SM is controlled to carry out the bi-directional energy exchanges with the external system through the equivalent energy exchange circuit. These will

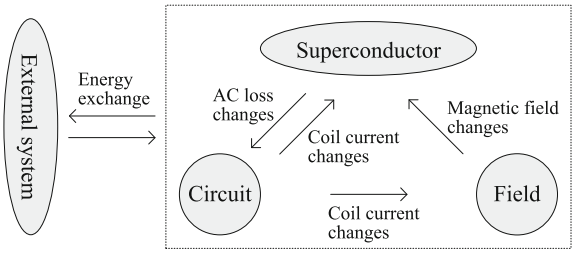

Fig. 12 Principle of circuit-field-superconductor coupled method

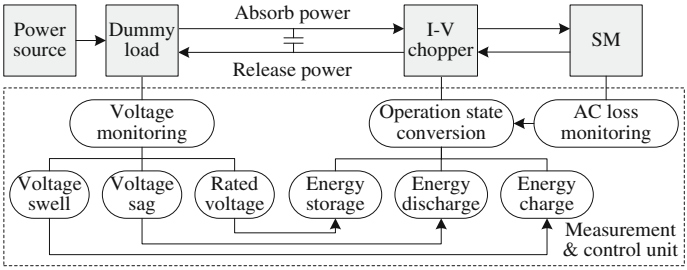

Fig. 13 Scheme of the SMEE model

cause the real-time changes of the coil current in the SM, and thus generate the varying magnetic field around the SM. The changes of both the coil current and magnetic field result in varying AC losses and thus diminish the stored magnetic energy in the SM and its corresponding coil current.

Based on the circuit-field-superconductor coupled method, a new SMEE model is built, as shown in Fig. 13 [19]. It mainly consists of one controllable voltage source, one dummy load, one DC-link capacitor, one I-V chopper, one SM, and one measurement and control unit. The dummy load corresponds to the combination of the power-line resistor and power-load resistor in Fig. 4. The measurement and control unit is used to implement the online state conversion of the I-V chopper based on the power and voltage monitoring of the dummy load. In addition, an AC loss monitoring module is also added to limit the total AC loss P_{ac} within the maximum cooling power P_{max} in the practical refrigeration system. If the generated AC losses exceed the upper limitation in any case, the operation state of the I-V chopper should be converted into the energy storage state immediately to avoid the quench of the SM.

The SMEE model has the potentials to evaluate the AC loss features under a given energy exchange condition and to evaluate the energy exchange features with a designed or developed SM prior to its practical application. The main input parameters include: (i) Energy exchange parameters—U, U_{min}, U_{max}, R_{line}, R_{load}, C; (ii) SM parameters—L, I_0, S_m, P_m, a_1, a_2, b_1, c_1, d_1, d_2. The main output parameters include: (i) Energy exchange parameters—$U_R(t)$, T_{ch}, T_{dis}; (ii) SM parameters—$I_L(t)$, $I_m(t)$, $f(t)$, $S(t)$, $I_c(t)$, $P_{hys}(t)$, $P_{flow}(t)$, $P_{coup}(t)$, $P_{eddy}(t)$, $P_{ac}(t)$. T_{ch}, and T_{dis} are the charging and discharging time durations from the initial coil current I_0 to a reference value.

2.4 Simulation Analysis

Based on the developed SMEE model, a Matlab/Simulink simulation model is built. The energy exchange circuit is used to simulate the buffering effects for compensating a voltage sag. The main simulation parameters are as follows: U = 300 V,

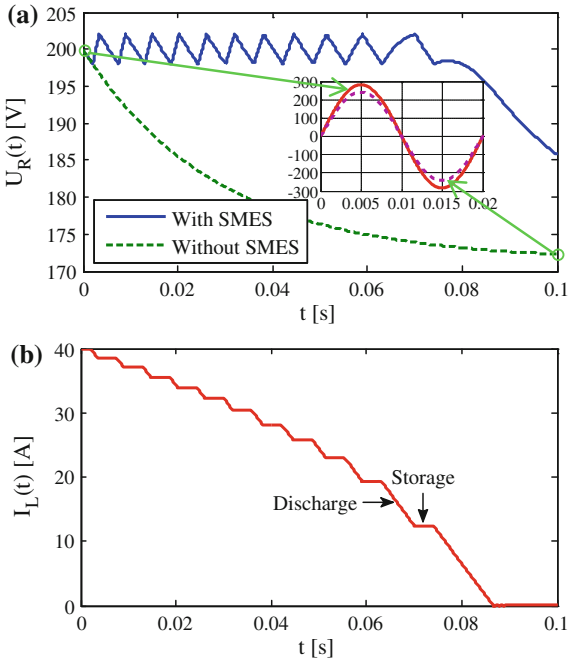

Fig. 14 Simulated load voltage and coil current: **a** $U_R(t)$ versus t; **b** $I_L(t)$ versus t

U_{max} = 202 V, U_{min} = 198 V, R_{line} = 5 Ω, R_{load} = 20/3 Ω, L = 0.2 H, I_0 = 40 A, and C = 10 mH. The power-load resistor R_{load} is assumed to converted from 10 to 20/3 Ω when the time t = 0 s, thus the real-time load voltage $U_R(t)$ will drop gradually to about 171 V without SMES, as shown in Fig. 14a. It should be noticed that the above DC voltage sag corresponds to an AC voltage sag from $200\sqrt{2} \times \sin(2\pi ft)$ V to $171\sqrt{2} \times \sin(2\pi ft)$ V, as shown in the insertion of the Fig. 14a—red line and purple line, respectively. f is the power frequency in the modern power systems, e.g., 50 or 60 Hz.

In the case of the 0.2 H/40 A SMES is applied, the operation state of the I-V chopper is converted between the energy discharge state and energy storage state to discharge the shortfall power from the power-load resistor. Thus $U_R(t)$ is kept within the voltage range from 198 to 202 V for 0.07 s, i.e., T_{dis} = 0.07 s. This compensation time value is the same as that in the above equivalent AC voltage sag.

The four coil-current-dependent formulas are used to calculate the hysteresis loss, flux flow loss, coupling current loss, and eddy current loss. The whole coil current curve in Fig. 14b is equivalent to half a charge–discharge cycle with f = 5.7 Hz and $I_{dc} = I_m$ = 20 A. The calculated hysteresis loss P_{hys} and its generated energy consumption Q_{hys} are about 60.4 mW and 5.2 mJ, respectively. Figure 15 shows the flux flow loss P_{flow} and its generated energy consumption Q_{flow} during the whole voltage sag compensation period. The generated energy consumption Q_{flow} value is about 3.2 mJ.

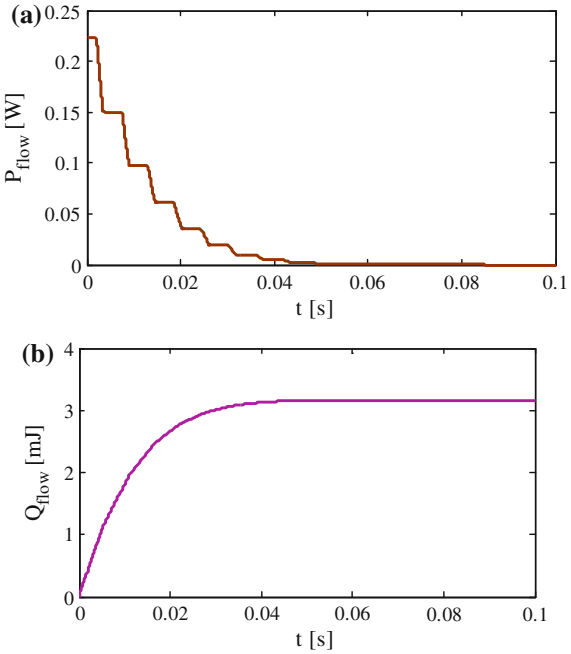

Fig. 15 Simulated flux flow loss and energy consumption: **a** $P_{\text{flow}}(t)$ versus t; **b** $Q_{\text{flow}}(t)$ versus t

Table 1 Simulation results for coupling and eddy current losses

$I_{\text{L}}(t)$ (A)	T_{dis} (ms)	$S(t)$ (A/s)	P_{coup} (W)	P_{eddy} (W)	Q_{coup} (mJ)	Q_{eddy} (mJ)
40.0	1.378	1000.82	2.395	0.208	3.302	0.288
38.6	1.444	1000.81	2.395	0.208	3.459	0.301
37.2	1.517	1000.80	2.395	0.208	3.635	0.317
35.6	1.613	1000.79	2.395	0.208	3.864	0.337
34.1	1.724	1000.79	2.395	0.208	4.130	0.360
32.2	1.873	1000.79	2.395	0.208	4.487	0.391
30.4	2.054	1000.79	2.395	0.208	4.922	0.429
28.2	2.341	1000.83	2.395	0.208	5.608	0.489
25.8	2.774	1000.90	2.396	0.208	6.648	0.579
23.0	3.605	1001.11	2.397	0.209	8.641	0.753
19.4	6.968	1002.69	2.404	0.209	16.755	1.460
12.4	12.555	986.85	2.329	0.203	29.243	2.547

Table 1 shows the simulation results for the coupling and eddy current loss calculations. The coil current decreases gradually while the discharge time T_{dis} in one energy discharge state increases for achieving the condition of 198 V ≤ $U_{\text{R}}(t)$ ≤ 202 V. During the 11 discharge–storage cycles in Fig. 14b, the total energy consumption Q_{coup} from the coupling current loss and total energy

consumption Q_{eddy} from the eddy current loss are 65.4 and 5.7 mJ, respectively. In the following energy discharge period from 12.4 to 0 A, they are 29.2 and 2.5 mJ, respectively.

2.5 Experimental Verification

Figure 16 shows the schematic diagram and overall experiment setup of the energy exchange prototype [15–17, 23]. Four OptiMOS™ MOSFETs are introduced to develop the bridge-type and conventional choppers, with the power lines among the four MOSFETs formed by silvered copper bars. The MOSFET parameters are as follows: drain-source breakdown voltage $V_{DSmax} = 30$ V, turn-on resistance $R_{on} \approx 0.65$ mΩ. Thirty-two conductive polymer aluminum solid electrolytic capacitors with ultra-low equivalent series resistance $R_{esr} \approx 11$ mΩ are connected in parallel to serve as the DC-link capacitor. The power-line resistor R_{line} is combined by three independent 0.5 Ω resistors. The power-load resistor R_{load} has three parallel resistor branches of R_2, R_3, and R_4. The available resistors in each branch are one 1 Ω resistor and two 2 Ω resistors. Each branch can be connected or disconnected to the power-line resistor by controlling its series-connected MOSFET. The high-temperature superconducting (HTS) coil is a 0.2 H Bi-2223 solenoid coil immersed in liquid nitrogen (LN_2). It consists of three solenoids in series for reducing the internal connections. The HTS coil is connected to the bridge-type chopper through two copper current leads. When the chopper is operated in the storage state, the total lossy resistance in series with the HTS coil is about 3.2 mΩ.

The main operation processes of the prototype are described as follows: (i) Close S_1, S_3 and S_5, the coil current $I_L(t)$ is firstly charged gradually to a pre-set initial current value I_{L0}. (ii) Open S_1, and then close S_2, the two choppers are operated in the storage state. (iii) Open S_5, and then close one, two or three branched MOSFETs of S_6–S_8, the corresponding branched resistors are connected to the controllable power source through the power-line resistor. (iv) Finally, a MCU MSP430 and CPLD EPM240 joint measurement and control module is to implement the online voltage monitoring of $U_R(t)$, and thus to change the next operation state of the choppers accordingly.

In the experiment, the controllable power source $U = 15$ V is first applied to the power-line resistor $R_1 = 0.5$ Ω and two branched power-load resistors $R_2 = R_3 = 1$ Ω. Each branched resistor is operated at its rated voltage $U_r = 10$ V. Assuming that one branch and three branches of $R_2 = R_3 = R_4 = 1$ Ω are connected with the power-line resistor successively, a voltage swell status and a voltage sag status will be appear accordingly. When the 0.2 H Bi-2223 coil is applied, it should be controlled to absorb a mean surplus power $P_{swell} = 100$ W and to compensate a mean shortfall power $P_{short} = 100$ W, respectively. As shown in Fig. 17, a whole 100 W energy exchange cycle can be divided into four different segments.

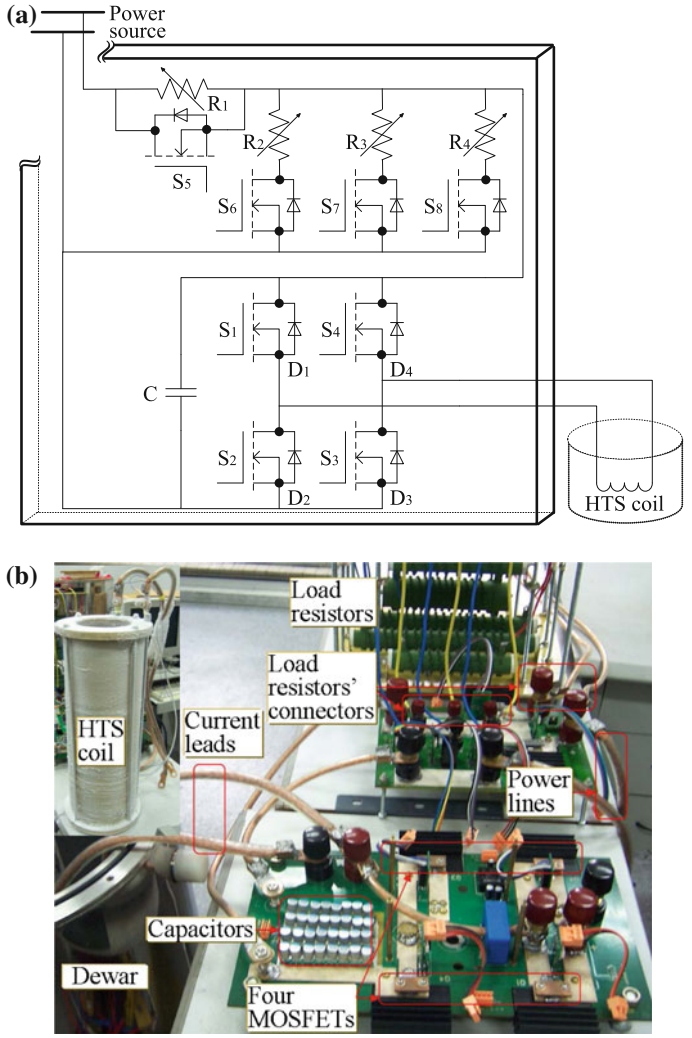

Fig. 16 Developed SMES prototype: **a** schematic diagram; **b** experiment setup

The first one is an incomplete absorption segment when $I_L(t) < 10$ A, the two choppers are operated in the charge state until $U_R(t)$ drops to 10 V. The second one is a complete absorption segment when $10 \text{ A} \leq I_L(t) \leq 60$ A, the two choppers are operated in the charge storage mode to maintain $U_R(t)$ around 10 V. Once $I_L(t)$ reaches its rated operation current $I_{Lr} = 60$ A, the third process enters into a complete compensation segment. In this segment, the two choppers are operated in the discharge–storage mode to maintain $U_R(t)$ around 10 V until $I_L(t)$ drops to 10 A. The fourth one is an incomplete compensation segment when $I_L(t) < 10$ A, the two choppers are operated in the discharge state to release a decreasing power.

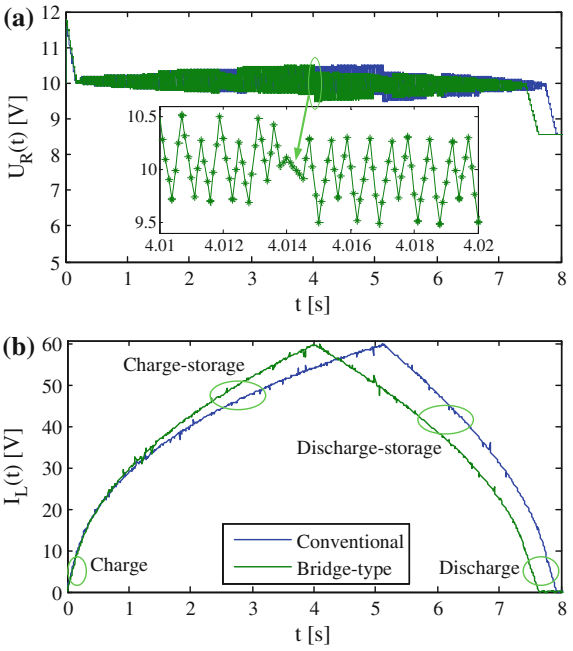

Fig. 17 Measured results of $U_R(t)$ and $I_L(t)$ during a 100 W energy exchange cycle: **a** $U_R(t)$ versus t; **b** $I_L(t)$ versus t

To evaluate the performance of SMES before its practical applications, the surplus or shortfall power demands from the external system can be simply transformed into the combinations of U and R_1—R_4. Thus the buffering effects of SMES for the given power fluctuations could be obtained equivalently in the above four segments.

Since the consumed power from the used OptiMOS™ MOSFETs is much lower over their reverse diodes [18], the bridge-type chopper has shorter absorption time T_{abs} and longer compensation time T_{com} as compared to the conventional one. This means that the bridge-type chopper has higher charge–discharge efficiency η_{total}, which is defined by $\eta_{total} = (P_{swell} \times T_{abs})/(P_{short} \times T_{com})$. From the measured results of Fig. 17, the η_{total} values of the bridge-type and conventional choppers are about 0.876 and 0.526, respectively. Therefore, the bridge-type chopper is more suitable to apply in the low-voltage end-user applications for high-efficiency SMES operations. Figure 18a shows the measured and calculated results of η_{total} versus I_{L0}. In the 100 W energy exchange cycle, $I_L(t)$ increases from I_{L0} to 60 A, and then decreases from 60 A to I_{L0}. It can be seen that η_{total} decreases along with the increment of I_{L0}. This is because the consumed power from the MOSFETs is in direct proportion to the square of the coil current. Figure 18b shows the measured and calculated results of η_{total} versus P_{ref}. P_{ref} is assumed to be equal to both the P_{swell} and P_{short}. It can be seen that η_{total} increases with a reduced rising slope as P_{ref} increases.

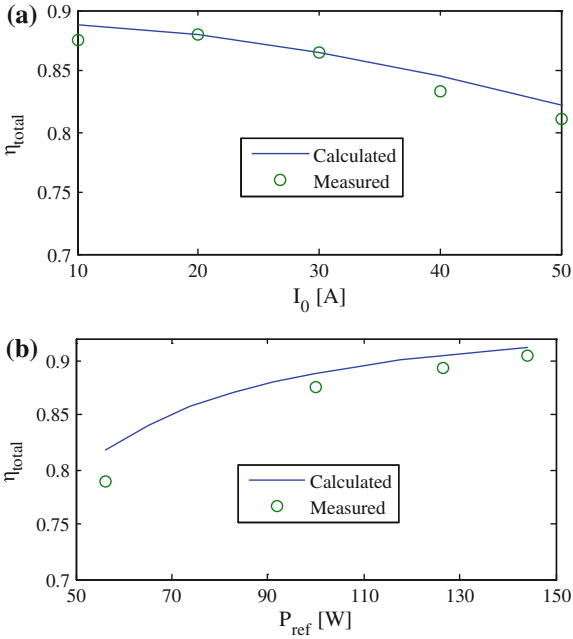

Fig. 18 Measured and calculated results of η_{total} during a 100 W energy exchange cycle: **a** η_{total} versus I_0; **b** η_{total} versus P_{ref}

Besides the independent charge and discharge tests, the prototype can also be used to carry out multicycle energy exchange tests to simulate a variety of application conditions. Figure 19a, b shows the measured results of $U_R(t)$ and $I_L(t)$ during five charge–discharge cycles. The 0.2 H Bi-2223 coil is applied to absorb a mean surplus power P_{swell} = 100 W during the first half cycle, and then to compensate a mean shortfall power P_{short} = 100 W during the residual half cycle.

Due to the energy consumptions from the conduction losses of the MOSFETs and magnetization loss of the Bi-2223 coil itself, $I_L(t)$ decreases continuously after each charge–discharge cycle. From Fig. 19b, $I_L(t)$ at the ends of the first cycle to fifth cycle are reduced to 24.78, 19.66, 13.69, 5.74, and 0.21 A, respectively. It is noticed that an incomplete compensation segment and an incomplete absorption segment appear successively within the time range from about 19.91 to 20.09 s. The corresponding lowest and highest offset voltage values are about 9.41 and 10.72 V, respectively.

Figure 19c, d shows the total AC loss $P_{mag}(t)$ and energy consumption $Q_{mag}(t)$. The calculated root-mean-square (RMS) values from the first cycle to fifth cycle are 1.21, 0.78, 0.52, 0.36, and 0.26 W, respectively. The corresponding $Q_{mag}(t)$ values are 6.02, 9.92, 12.53, 14.35, and 15.66 J, respectively.

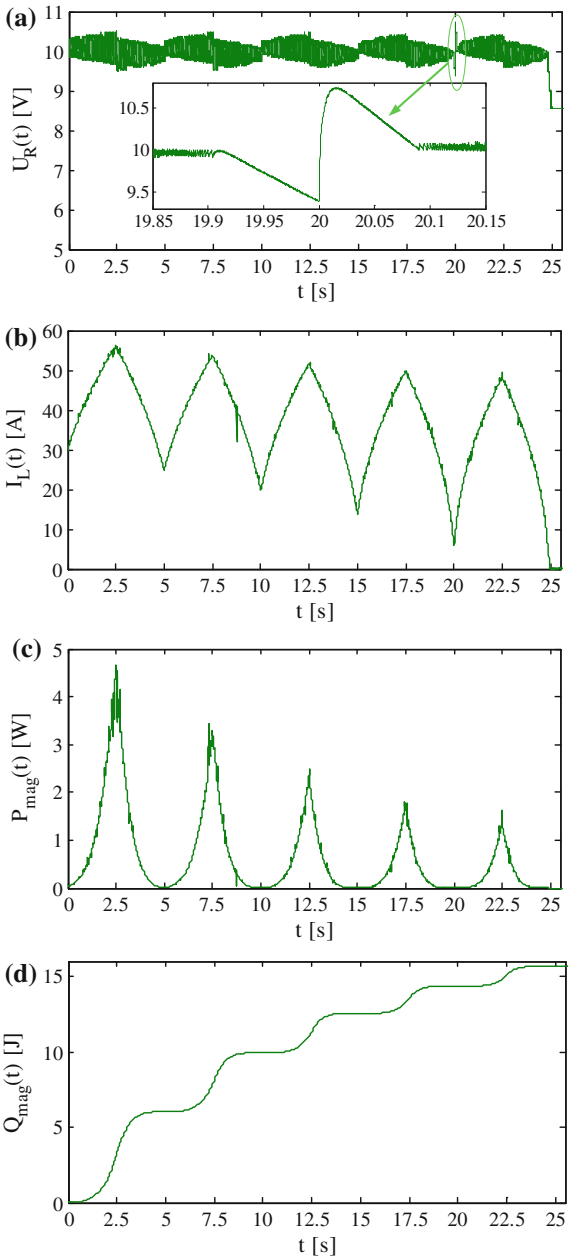

Fig. 19 Measured and calculated results during five 100 W energy exchange cycle: **a** $U_R(t)$ versus t; **b** $I_L(t)$ versus t; **c** $P_{mag}(t)$ versus t; **d** $Q_{mag}(t)$ versus t

3 SMES-Based Microphotovoltaic Grid

3.1 Principle and System Description

Due to the energy intermittency from the photovoltaic power plants, various energy storage systems are utilized to allow increased power capacity and stability. As compared to other energy storage schemes, emerging SMES technique is significantly highlighted for fast speed response and high power density. A number of SMES devices and systems have been studied and verified to apply in the modern power systems with or without the penetrations of the photovoltaic power plants [11–14, 24–26].

In addition, superconducting cables (SCs) are with the advantages of high transport current capability, no resistive loss and compact system, therefore high-power and high-efficiency transmissions for delivering the electric power directly from distant photovoltaic power plants to local power consumers can be achieved [27–29]. Besides the high-capacity electricity transmission, the SC can also serve as a self-acting fault current limiter for its power system auto protection because its resistance characteristic is similar to that in a resistive-type superconducting fault current limiter. Based on the self-acting fault-current-limiting (FCL) feature, the so-called FCL SC can achieve favorable grounding fault current limitation effect; meanwhile, it also has the significant potential to enhance the fault ride-through (FRT) capability of all the in-grid photovoltaic power plants.

To integrate the self-acting FCL feature from the FCL SC and the fast-response grid voltage protection feature from the SMES in one power system, this work proposes a novel low-voltage direct-current (LVDC) micro photovoltaic grid by applying multiple FCL SCs and SMES devices [30, 31]. The concept to form the novel LVDC microphotovoltaic grid is to implement the hybrid energy transfer of the hydrogen and electricity. As shown in Fig. 20, the most generated electricity from the photovoltaic power plants and utility grid supplies the distant power loads, while the surplus electricity produces the LH_2 by using water electrolyzers and liquefying devices. For the SC system, a main FCL SC is used to transfer the electricity to local residential and industrial areas, while multiple branch FCL SCs are used to distribute the electricity to various distributed loads.

For the SMES system, it can be divided into three different types: (i) The first type connected with the photovoltaic power plants is used to locally compensate the transient output power and voltage fluctuations; (ii) The second type connected with the AC loads, DC loads, and electric vehicles (EVs) is used to serve as fast-response uninterruptible power supplies (UPSs) for improving the local power quality; (iii) The third type connected with the bus line between the main FCL SC and multiple branch FCL SCs is used to bridge the photovoltaic power plants with various distributed loads, and thus to buffer the power and voltage fluctuations from the photovoltaic power plants and to compensate the load fluctuations from the distributed loads.

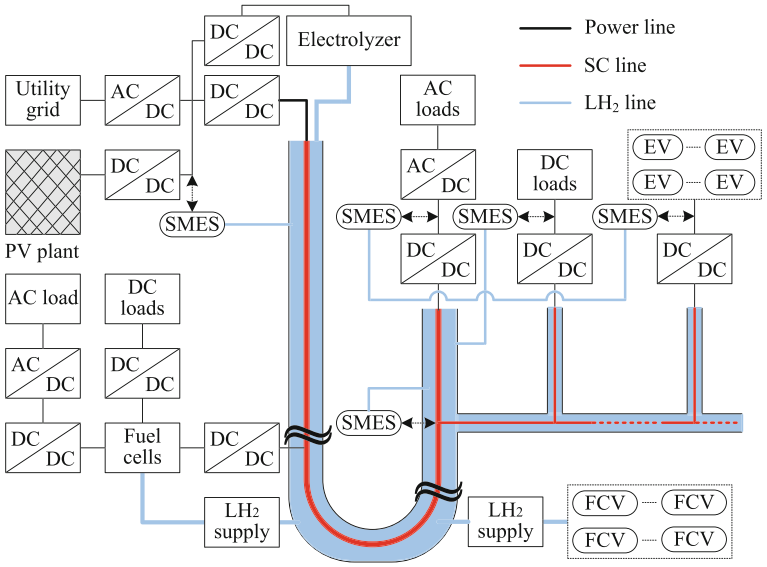

Fig. 20 Sketch of the LVDC micro photovoltaic grid

As an alternative cooling method, the LH_2 transferred can not only be used to provide hydrogen energy for the fuel cells (FCs) and FC vehicles (FCVs), but also can be used as the refrigeration fluid for cooling the FCL SC and SMES systems. In addition to supply the off-grid AC and DC loads, the generated electricity from the FCs can also provide demanded power feedback to the LVDC network.

3.2 Simulation Model and Implementation

To evaluate the performance of the integrated FCL SC and SMES systems during a grounding fault, a simulation model is built in Simulink, as shown in Fig. 21. A controllable voltage source (CVS) is used to simulate the electricity from the photovoltaic power plants. One 200-V/100-kA/20-MW main FCL SC and five 200-V/20-kA/4-MW branch FCL SCs is used to form the FCL SC model system. Five 200-V/20-kA/4-MW resistive loads from load 1 to load 5 are used to simulate the distributed loads located in the terminals from the branch FCL SC 1 to branch FCL SC 5. One second-type 0.06-H/15.5-kA/7.2-MJ SMES A is installed near the bus line between the main FCL SC and branch FCL SCs, while one third-type 0.06-H/15.5-kA/7.2-MJ SMES B is installed near the critical load 1.

The PI section line block is adopted to build an approximate SC circuit model, as shown in Fig. 22. It mainly consists of one distributed inductor with its inductance of L, two distributed capacitors with their capacitances of $C/2$, and one equivalent lossy resistor with its resistance of $R(t)$. The cable inductance and cable capacitance

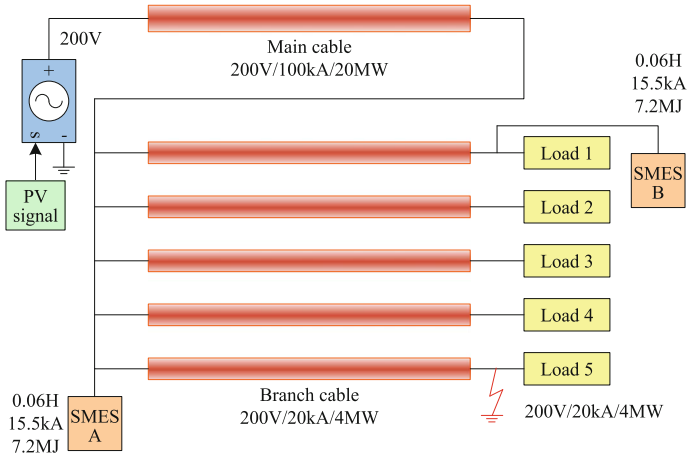

Fig. 21 Simulation model of the LVDC micro photovoltaic grid

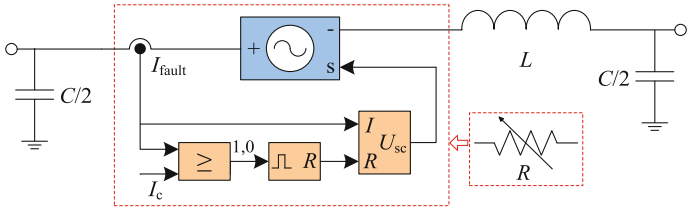

Fig. 22 FCL SC circuit model

per unit length are 2 mH/km and 8.6 pF/km as standard, respectively. The total lengths of the main cable and each branch cable are 10 and 1 km, respectively.

The lossy resistance characteristic of the SC is similar to the resistive-type superconducting fault current limiter [32]: (i) When the grounding fault current $I_{fault}(t)$ exceeds the critical current I_c of the SC, a quench state starts, and thus $R(t)$ increases exponentially to a maximum value of R_m, i.e., $R(t) = R_m \times [1 - \exp(-t/\tau_1)]$; (ii) Subsequently when the grounding fault disappears, a recovery state starts, and thus $R(t)$ decreases exponentially to zero, i.e., $R(t) = R_m \times \exp(-t/\tau_2)$. τ_1 and τ_2 are the time constants of the quench period and recovery period, respectively. The dynamic changes of $R(t)$ ensures the self-acting FCL feature of the SC.

The SMES system is divided into twenty SMES units in parallel, with each unit consists of one 1.2-H/775-A/360-kJ SMES coil unit [33] and one bridge-type chopper unit [15–18], as shown in Fig. 23. The bridge-type chopper is formed by four MOSFETs S_1-S_4 and two diodes D_2, D_4. As compared to the conventional chopper formed by two MOSFETs S_1, S_3 and two diodes D_2, D_4, the bridge-type one has higher energy utilization efficiency in the LVDC network. To further

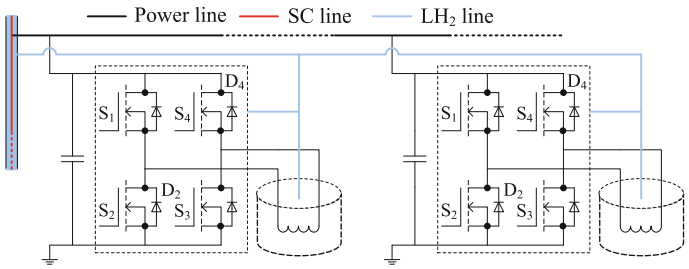

Fig. 23 SMES circuit model

improve the efficiency, cryogenic MOSFET units cooled by the low-temperature gas hydrogen from the SMES Dewar are the available options. As for the SMES control, all the operation states are digitalized as "$S_1S_2S_3S_4$" by defining the turn-on or turn-off status of a MOSFET as "1" or "0". The charge–storage operation mode ("1010" → "0010" → "0110" → "0010" → "1010") and the discharge–storage operation mode ("0101" → "0100" → "0110" → "0100" → "0101") correspond to the control schemes for the power absorption and compensation operations, respectively.

3.3 SMES Coil Design

To further improve the allowable coil critical current in a solenoidal SMES coil, the simplest method is to adopt two or more parallel pancake coils which served as one coil unit located at two coil ends. However, it needs more tape usage and higher capital cost. A number of feasible optimization methods such as electromagnetic field analyses, simulated annealing algorithm, adaptive genetic algorithm, continuum sensitivity approach, sequential quadratic programming approach are consequently studied for structural optimizations. Among the most literatures related to the coil optimizations, they are aiming to achieve a maximum energy storage capacity with a determined tape usage, or achieve a reference energy storage capacity with a minimum tape usage. For instance, Noguchi et al. [34, 35] propose a steps-shaped cross-sectional shape having several stepped coil units to reduce about 24 % in tape usage. By considering the ratio between the critical current and tape usage in the mentioned optimization methods above, the step-shaped shape has a maximum value. Therefore, it is preferable to achieve a very high critical current with a determined tape usage, and thus used to carry out the conceptual design of the 0.06-H/15.5-kA/7.2-MJ SMES coil in the proposed LVDC micro photovoltaic grid.

The designed coil assembly has 20 1.2-H/775-A/360-kJ solenoidal units in parallel, as shown in Table 2. Each unit is connected to the bus line between the main cable and five branch cables through one bridge-type chopper unit. Critical

Table 2 Specifications of the magnet assembly and coil units

Items	Coil unit	Magnet assembly
Inductance	1.2 H	0.06 H
Critical current	880 A	17.6 kA
Rated current	775 A	15.5 kA
Rated energy	360 kJ	7.2 MJ
Rated power	150 kW	3 MW
Rated voltage	200 V	200 V

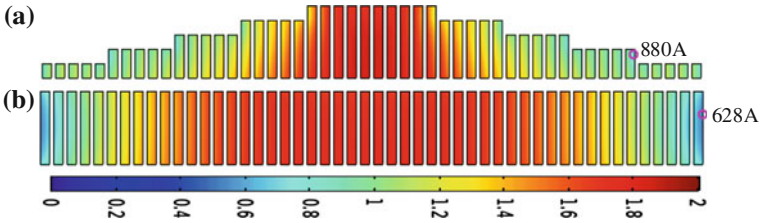

Fig. 24 Critical current (kA) distributions of **a** *rectangular-shaped* coil and **b** *step-shaped* coil

Table 3 Specifications of the 1.2 H SMES coil

N_{disk}	N	r_{inner} (mm)	r_{outer} (mm)	h (mm)	S_{tape} (m)
1–5	10	278	285	32.5	168.2
6–10	20	271	285	32.5	336.3
11–15	30	264	285	32.5	504.5
16–20	40	257	285	32.5	672.7
20–25	50	250	285	32.5	840.9

current (kA) distributions of the rectangular-shaped coil and the step-shaped coil are shown in Fig. 25 [30, 31]. Benefited from the reduced perpendicular magnetic fields located at two coil ends, the critical current and tape usage requirement of the step-shaped coil are about 1.4 times and 0.6 times of those of the rectangular-shaped coil.

The 1.2 H step-shaped coil can be divided into two axisymmetric left and right parts. Each part consists of five stepped coil units with each unit having five disks, as shown in Fig. 24. The average width w and average thickness t of the used DI-BSCCO tapes are 4.5 and 0.3 mm, respectively. Two stacked tapes are used to wind the coil so as to achieve a high critical current of 880 A at 20 K. The gap between two adjacent turns in the same disk is 0.1 mm. The gap between two adjacent disks is 2 mm. From the right to left of the 50 coil layers, they are defined as $N_{disk} = 1$, $N_{disk} = 2$, …, $N_{disk} = 50$, respectively. Table 3 summarizes the coil turns N, inner radius r_{inner}, outer radius r_{outer}, height h, and tape usage S_{tape} of the five stepped coil units.

3.4 Performance Evaluation

In the simulations, the three 200-V/10-kA/2-MW resistive loads are connected or disconnected to the cable terminal by controlling the three series-connected breakers. Three operation states of the connected resistive load(s) are consequently achieved: (i) When one of the three breakers closes, the connected resistive load is operated in a power swell state; (ii) When two of the three breakers close, the connected resistive loads are operated in a rated power state; and (iii) When all the three breakers close, the connected resistive loads are operated in a power sag state.

Figure 25 shows the simulated load voltage $U_{load}(t)$ during the power sag period from 0.5 to 3 s. If the SMES system is not applied, the load voltage $U_{load}(t)$ will decrease rapidly to about 183.8 V at 1.5 s and then increase gradually. At the time t = 3 s when two of the three breakers close, $U_{load}(t)$ increases exponentially to about 203.3 V at 3.8 s. In the case of the SMES system is applied, the twenty bridge-type chopper units are operated in the discharge–storage mode to compensate the shortfall power from the bus line. As a result, $U_{load}(t)$ is maintained around its rated voltage with a maximum voltage ripple of about 198.8 V at 3 s. Accordingly, the coil current $I_L(t)$ decreases to about 9.8 kA at 3 s, as shown in Fig. 26.

Figure 27 shows the simulated load voltage $U_{load}(t)$ during the power swell period from 0.5 to 3 s. If the SMES system is not applied, the load voltage $U_{load}(t)$ will increase rapidly to about 218.3 V at 1.6 s and then decrease gradually. At the time t = 3 s when two of the three breakers close, $U_{load}(t)$ decreases exponentially to about 196.1 V at 6 s. In the case of the SMES system is applied, the 20 bridge-type chopper units are operated in the charge-storage mode to absorb the surplus power from the bus line. As a result, $U_{load}(t)$ is maintained around its rated voltage with a maximum voltage ripple of about 201.4 V at 2 s. Accordingly, the coil current $I_L(t)$ increases to about 15.6 kA at 3 s, as shown in Fig. 26. Therefore, the SMES system can protect the load voltage effectively under both power sag and power swell conditions.

To evaluate the fault current limitation (FCL) characteristic of the superconducting cable, an additional breaker is used to simulate a short-circuit fault in the branch cable 5. In the simulations, the cable inductance and cable capacitance per

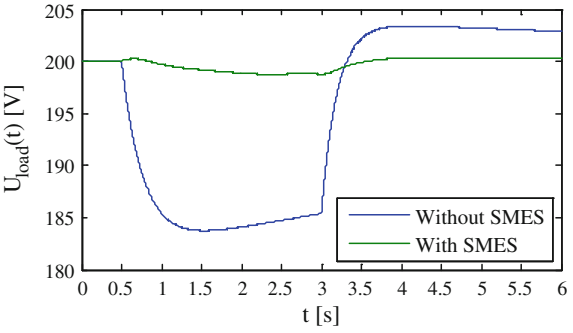

Fig. 25 Load voltage $U_{load}(t)$ during a power sag period

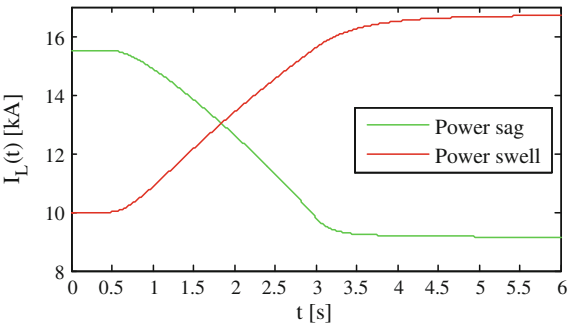

Fig. 26 Coil current $I_L(t)$ during a power swell period and a voltage sag period

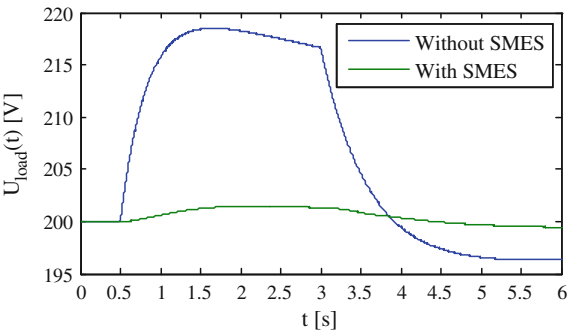

Fig. 27 Load voltage $U_{load}(t)$ during a power swell period

unit length are set as 2 mH/km and 8.6 pF/km, respectively. The total lengths of the main cable and each branch cable are set as 10 and 1 km, respectively. From the simulation results and analyses under a short-circuit fault condition, the DC SC having the self-acting FCL characteristic can simultaneously protect the load voltage and current of the adjacent branch cables, but there are still unavoidable load voltage and current drops after the fault occurrence. This is because the quenching degree becomes increasingly serious as the fault current rises, and thus the resulting superconducting resistance increases exponentially from zero to a maximum value along with the quenching time.

To achieve a better protection effect, the SMES is applied to cooperate with the DC SC. The basic cooperative operation principle of the FCL SC and SMES is shown in Fig. 28. The FCL SC branch 5, SMES A and SMES B are equivalent to one fault-current-dependent increased voltage source U_{sc} and two load-voltage-dependent decreased current sources (I_A, I_B), respectively. Two load-voltage-dependent switches (S_A, S_B) are closed to switch on the SMES A and SMES B when the bus voltage U_{bus} and load voltage U_{load} are lower than their rated values. Thus, the increased U_{sc} offsets the line voltage to limit the fault current through the FCL SC branch 5, while the discharging currents from the SMES A and SMES B prevent the voltage and current drops across the adjacent branch FCL SCs.

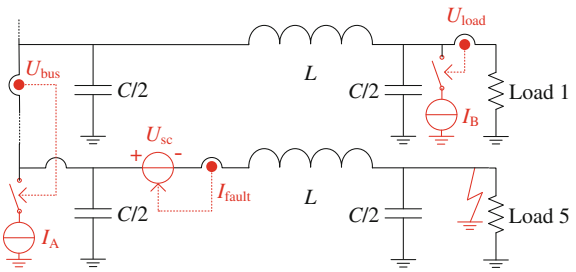

Fig. 28 Basic cooperative operation principle of the FCL SC and SMES

To further enhance the FRT capability of the in-grid photovoltaic power plants, the SMES A is applied to cooperate with the FCL SC. As shown in Fig. 29a, b, the fault current is significantly limited due to the self-acting FCL resistance $R(t)$, and thus the load voltage $U_{load}(t)$ remains around 200 V from 0.5 to 1 s. This means that the grounding fault has virtually no impact on the adjacent FCL SC branches if the fault time duration is less than 0.5 s. However, if other energy storage systems such as electrochemical cells are applied, their slow start-up time will cause relatively obvious load voltage drop after 0.5 s. From the green line in Fig. 29a, when the start-up time is 25, 50, and 100 ms, the corresponding load voltage reduces to about 198.3, 196.8, and 193.7 V. From 1 to 3 s, $U_{load}(t)$ drops gradually to a minimum value of 180 V and then remains nearly unchanged. Accordingly, the coil current $I_A(t)$ in Fig. 29c decreases to about 8.6 kA at 3 s and then remains unchanged. As compared to the load voltage curve with the FCL function only, the load voltage reduction decreases from 20 to about 10 %.

When the time t = 3 s, the grounding fault removes. The FCL SC branch 5 is still operated in the quench state until $I_{fault}(t)$ decreases to 30 kA at about 3.15 s. After that, a recovery state starts, and $R(t)$ decreases exponentially to zero. Due to the high transient current through the FCL SC branch 5, $U_{load}(t)$ increases rapidly to a maximum value and then decreases to 200 V. With the SMES A, the maximum load voltage after the fault disappearance drops from 210 to about 205 V, and the voltage recovery time reduces from 27 to about 22 s. Therefore, the SMES A has a positive effect on grid voltage stability and enhances the FRT capability.

Although 10 % reduction in the load voltage with the cooperative operation of the FCL SC and SMES A is enough to achieve the practical FRT of the in-grid photovoltaic power plants, it is not allowed by the critical load 1 located in the terminal of the branch FCL SC 1. To obtain a longer voltage protection time duration, the SMES B installed near the critical load 1 should be applied after the time t = 1 s. As shown in Fig. 30a, the load voltage $U_{load1}(t)$ through the FCL SC branch 1 can further maintain around 200 V for about 4 s. Due to the existence of an inevitable control system time delay including a sampling time of the load voltage, a computing time of the digital control system, and an on-off implementing time of the MOSFETs, the practical control signals for the SMES charge–discharge

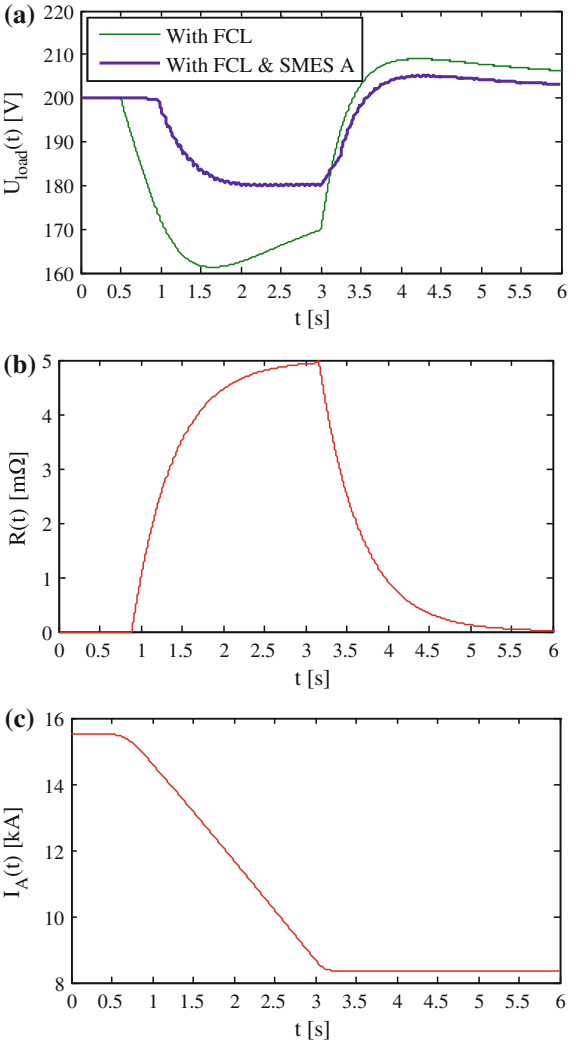

Fig. 29 Simulated results during a grounding fault: **a** $U_{load}(t)$ versus t; **b** R (t) versus t; (c) $I_A(t)$ versus t

operation lag behind the changes of the load voltage. This will result in some undesired voltage overshoots accordingly. In addition, with the cooperative operation of the SMES A and SMES B, the minimum load voltage $U_{load2}(t)$ through the FCL SC branch 2 increases from 180 to about 184 V. Accordingly, the coil currents $I_A(t)$ and $I_B(t)$ decreases to 2.3 and 9.5 kA at 5 s, as shown in Fig. 30b.

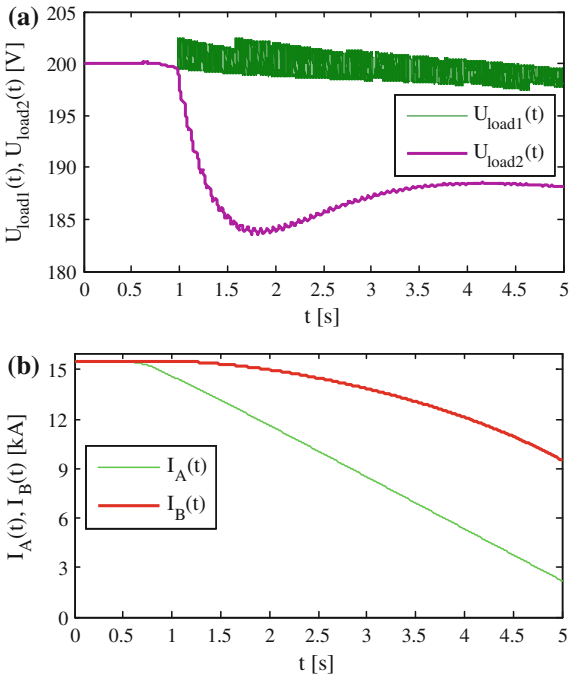

Fig. 30 Simulated results with the cooperative operations of FCL SC branch 5, SMES A and SMES B: **a** $U_{load1}(t)$, $U_{load2}(t)$ versus t; **b** $I_A(t)$, $I_B(t)$ versus t

4 Summary and Application Prospect

In most smart grid plans integrated with photovoltaic power plants, one of the most principal development goals is to intelligently supply the highly customizable electricity with high quality and reliability. Due to the rapid load fluctuations from the power end-users and intermittent power fluctuations from the photovoltaic power plants, various ESSs are expected to integrate into the power generation, transmission, distribution, and utilization systems to achieve a good supply–demand balance. They are controlled to absorb the surplus electricity when a power swell occurs, and to release the shortfall electricity when a power sag occurs. The overview and application analyses of the current SMES technology conclude that SMES with the outstanding advantages of fast response speed, high power density, and high storage efficiency has the significant potentials to combine with, even replace other conventional ESSs in the modern power system and future smart grid. It can be well expected that the future SMES devices are not only essential to improve the power quality with small-scale or medium-scale energy storage capacity but also ensure the daily load leveling and overall reliability of the power systems with large-scale energy storage capacity.

The main SMES application schemes and their basic functions are as follows: (i) SMES devices installed near the large-scale centralized generators (CGs) are used to balance the output power and to achieve daily load leveling; (ii) SMES

devices installed in the transmission lines (TLs) are used to form FACTS devices for compensating the load fluctuations and maintaining the grid frequency stability; (iii) SMES devices installed in the distribution lines (DLs) are used to form DFACTS devices for improving the power quality; (iv) SMES devices installed near the distributed generators (DGs) are used to reduce the impacts from the intermittent renewable energy sources so as to facilitate the grid integration; and (v) SMES devices installed near the power end-users are used to form SMES-based UPSs for protecting the critical loads. In the above five application schemes, a number of SMES devices are distributed in the multiarea interconnected networks with the same voltage level on the one hand, on the other hand, they are also distributed in the multivoltage-level interconnected networks including the CGs, TLs, DLs, DGs, and end-users. Therefore, SMES devices in future smart grid integrated with photovoltaic power plants are expected to intelligently handle with the external power exchange demands through the joint efforts with each other.

Besides the sole SMES scheme with full energy storage scale, three feasible application schemes of SMES should also be considered. The sole SMES scheme has one advantage of high storage efficiency for large-scale energy storage, while it has two advantages of fast response speed and high power density for small-scale energy storage. But both the large-scale and small-scale SMES devices are suffered from high capital cost as compared to other commercial ESSs with the same capacity. The SMES-based hybrid energy storage system (HESS) scheme reduces the required energy storage capacity of SMES, but the practical system topologies and relevant control strategies of HESS are more complex over the sole SMES. The distributed SMES (DSMES) scheme has two advantages of high mobility and high expandability because the DSMES units in the trucks are easy to install in arbitrary locations once they arrive on site. To achieve efficient stability and reliability of the whole power system, various distributed HESS (DHESS) units with different energy storage capacities and power ratings should be installed in the power generation, transmission, distribution, and utilization systems. The novel concept of SMES-based HESS scheme utilizes various energy storage technologies efficiently and thus enhances the flexibility and economy of SMES greatly in future photovoltaic power plants. With the rapid development and research of superconducting materials and superconducting power applications, emerging SMES systems and devices have promising potentials to replace or cooperate with other commercial energy storage systems on the one hand; on the other hand, they are also well expected to integrate with other superconducting power devices such as superconducting generator, superconducting cable, superconducting transformer, and superconducting fault current limiter, with essential aims to develop various high-performance, high-efficiency, and high-economy photovoltaic power plants in future smart grid.

References

1. Castillo A, Gayme DF (2014) Grid-scale energy storage applications in renewable energy integration: a survey. Energy Convers Manag 87:885–894
2. Vazquez S, Lukic SM, Galvan E, Franquelo LG, Carrasco JM (2010) Energy storage systems for transport and grid applications. IEEE Trans Industr Electron 57(12):3881–3895
3. Bradbury K (2010) Energy storage technology review. Duke University
4. Kondoh J, Ishii I, Yamaguchi H, Murata A, Otani K, Sakuta K, Higuchi N, Sekine S, Kamimoto M (2000) Electrical energy storage systems for energy networks. Energy Convers Manag 41(17):1863–1874
5. Yoon JY, Lee SR, Hwang IT (2013) A quantitative analysis on future world marketability of HTS power industry. IEEE Trans Smart Grid 4(1):433–436
6. Jin JX, Xin Y, Wang QL, He YS, Cai CB, Wang YS, Wang ZM (2014) Enabling high-temperature superconducting technologies toward practical applications. IEEE Trans Appl Supercond 24(5):5400712
7. von Helmolt R, Eberle U (2007) Fuel cell vehicles: status 2007. J Power Sources 165:833–843
8. Durbin DJ, Malardier-Jugroot C (2013) Review of hydrogen storage techniques for on board vehicle applications. Int J Hydrogen Energy 38:14595–14617
9. Stekly ZJJ (1963) Magnetic energy storage using superconducting coils. In: Proceedings of pulse-power conference, pp 53
10. Peterson HA, Mohan N, Boom RW (1975) Superconductive energy storage inductor-converter units for power system. In: IEEE Trans Power Appar Syst PAS-94(4):1337–1346
11. Ali MH, Wu B, Dougal RA (2010) An overview of SMES applications in power and energy systems. IEEE Trans Sustain Energy 1(1):38–47
12. Jin JX (2011) High temperature superconducting magnetic energy storage: principle and applications. Science Press, Beijing
13. Jin JX, Chen XY (2012) Study on the SMES application solutions for smart grid. Phys Procedia 36:902–907
14. Chen XY, Jin JX, Xin Y, Shu B, Tang CL, Zhu YP, Sun RM (2014) Integrated SMES technology for modern power system and future smart grid. IEEE Trans Appl Supercond 24 (5):3801605
15. Zhang JY, Jin JX, Chen XY, Zhou X, Ren AL, Gong WZ, Xin Y (2014) Electric energy exchange and applications of superconducting magnet in an SMES device. IEEE Trans Appl Supercond 24(3):5700704
16. Chen XY, Jin JX, Xin Y, Guo YG, Xu W, Wen L, Zhu JG (2014) Energy exchange experiments and performance evaluations using an equivalent method for a SMES prototype. IEEE Trans Appl Supercond 24(5):5701005
17. Jin JX, Xu W, Chen XY, Wen L, Wang SC (2014) Flux flow loss of HT-SMES coil during energy exchange. IEEE Trans Magn 50(11):9000604
18. Jin JX, Chen XY, Wen L, Wang SC, Xin Y (2015) Cryogenic power conversion for SMES application in a liquid hydrogen powered fuel cell electric vehicle. IEEE Trans Appl Supercond 25(1):5700111
19. Jin JX, Chen XY, Qu R, Xin Y (2015) A superconducting magnetic energy exchange model based on circuit-field-superconductor coupled method. IEEE Trans Appl Supercond 25 (3):5700906
20. Grilli F, Pardo E, Stenvall A, Nguyen DN, Yuan W, Gömöry F (2014) Computation of losses in HTS under the action of varying magnetic fields and currents. IEEE Trans Appl Supercond 24(1):8200433
21. Hamajima T, Amata H, Iwasaki T, Atomura N, Tsuda M, Miyagi D, Shintomi T, Makida Y, Takao T, Munakata K, Kajiwara M (2012) Application of SMES and fuel cell system combined with liquid hydrogen vehicle station to renewable energy control. IEEE Trans Appl Supercond 22(3):5701704

22. Shim JW, Cho YH, Kim SJ, Min SW, Hur K (2013) Synergistic control of SMES and battery energy storage for enabling dispatch ability of renewable energy sources. IEEE Trans Appl Supercond 23(3):2062–2065
23. Wen L, Jin JX, Chen XY, Jiang L (2014) A universal LabVIEW-based HTS device measurement and control platform and verified through a SMES system. IEEE Trans Appl Supercond 24(5):9002705
24. Luongo CA, Baldwin T, Ribeiro P, Weber CM (2003) A 100 MJ SMES demonstration at FSU-CAPS. IEEE Trans Appl Supercond 13(2):1800–1805
25. Shikimachi K, Hirano N, Nagaya S, Kawashima H, Higashikawa K, Nakamura T (2009) System coordination of 2 GJ class YBCO SMES for power system control. IEEE Trans Appl Supercond 19(3):2012–2018
26. Sander M, Gehring R, Neumann H (2013) LIQHYSMES—A 48 GJ toroidal MgB_2-SMES for buffering minute and second fluctuations. IEEE Trans Appl Supercond 23(3):5700505
27. Grant PM (2005) The SuperCable: dual delivery of chemical and electric power. IEEE Trans Appl Supercond 15(2):1810–1813
28. Jin JX (2007) High efficient DC power transmission using high-temperature superconductors. Physica C 460–462:1443–1444
29. Yamada S, Hishinuma Y, Uede T, Schippl K, Yanagi N, Mito T, Sato M (2010) Conceptual design of 1 GW class hybrid energy transfer line of hydrogen and electricity. J Phys Conf Ser 234:032064
30. Jin JX, Chen XY, Qu R, Fang HY, Xin Y (2015) An integrated low-voltage rated HTS DC power system with multifunctions to suit smart grids. Physica C (Amsterdam, Neth) 510:48–53
31. Jin JX, Chen XY (2015) Cooperative operation of superconducting fault-current-limiting cable and SMES systems for grounding fault protection in a LVDC network. IEEE Trans Ind Appl 51(6):5410–5414
32. Ngamroo I, Karaipoom T (2014) Cooperative control of SFCL and SMES for enhancing fault ride through capability and smoothing power fluctuation of DFIG wind farm. IEEE Trans Ind Appl 24(5):5400304
33. Chen XY, Jin JX (2014) Evaluation of step-shaped solenoidal coils for current-enhanced SMES application. IEEE Trans Appl Supercond 24(5):4603404
34. Noguchi S, Yamashita M, Yamashita H, Ishiyama A (2001) An optimal design method for superconducting magnets using HTS tape. IEEE Trans Appl Supercond 11(1):2308–2311
35. Noguchi S, Yamashita H, Ishiyama A (2002) An optimal design method for SMES coils using HTS tapes. IEEE Trans Appl Supercond 12(1):1459–1462

Recycling of Solar Cell Materials at the End of Life

Teng-Yu Wang

Abstract Although solar energy is a green energy, it can produce a significant amount of waste. Some types of solar cells use rare elements or precious metals as the component material. Therefore, the recycling of PV modules is necessary for environmental and economic purposes. The recycling process for PV modules includes chemical and physical treatment methods, which have been successfully used in other recycling industries, such as electronics or hardware recycling. The use of these mature technologies can decompose and recycle PV module materials. There are still some differences between PV module recycling and electronic recycling. A solar cell module contains several encapsulating plastic materials, such as ethylene vinyl acetate (EVA) and polyvinyl fluoride (PVF). In recycling programs, removing the plastic materials is the first step. In this chapter, several types of recycling processes are introduced, which correspond to different types of PV modules. These methods have been validated and successfully implemented in PV module recycling plants.

Keywords Recycle · Silicon · Cadmium telluride · Gallium arsenide · Copper indium gallium selenide · PV module

1 Introduction

Solar energy is a green technology. Solar cells can convert the sunlight into electricity with a conversion efficiency of approximately 10–40 %, depending on their type. With the rapid growth of the PV industry, its production scale has increased every year. In 2014, the global solar PV installations increased by 21 % to reach 45 GW from 37 GW in 2013 [1]; the majority of these were silicon-wafer-based solar cells. However, with the growth of the PV industry, the associated

T.-Y. Wang (✉)
Green Energy and Environment Research Laboratories,
Industrial Technology Research Institute, Hsinchu 31040, Taiwan
e-mail: tengyuwang@itri.org.tw

M.R. Islam et al. (eds.), *Advances in Solar Photovoltaic Power Plants*,
Green Energy and Technology, DOI 10.1007/978-3-662-50521-2_11

environmental problems have become a concern. PV modules are designed to generate clean, renewable energy, and to have a long lifetime of over 25 years. Therefore, the waste from end-of-life modules and PV scrap is expected to substantially increase in 25 years, [2]. Figures 1 and 2 show the global PV annual installation and cumulative installation rates [3]; the projected waste is based on calculations. At the beginning of the twenty-first century, the number of global PV installations was low. After 2007, it exhibited a rapid growth and has sharply increased every year. Assuming crystalline silicon solar modules as the calculation reference, a 250 W PV module weighing 20 kg will contribute 0.8 kg waste per

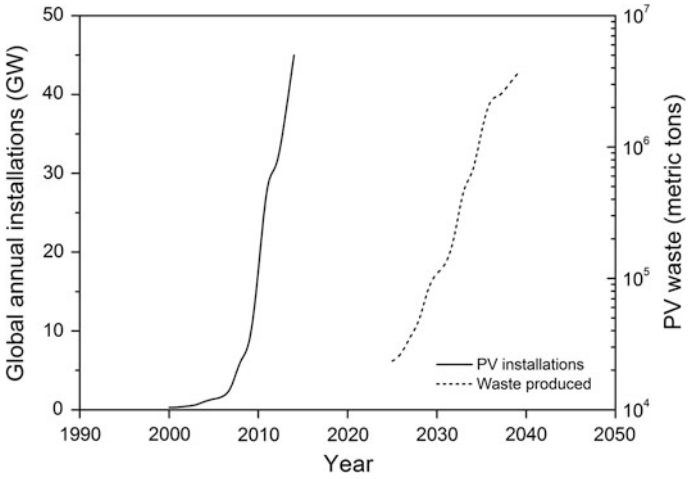

Fig. 1 Solar PV global annual installations and projected waste

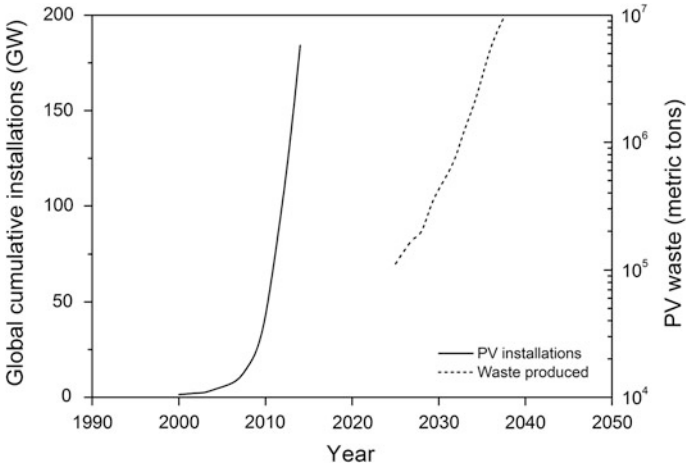

Fig. 2 Solar PV global cumulative installations and projected waste

Watt. Consequently, 80 metric tons of PV waste will be produced from 1 MW of end-of-life PV modules. Because the lifetime of a PV module is 25 years, large amounts of PV waste will begin to appear from 2023. The PV waste will increase from 20,000 metric tons to 3.6 million metric tons in 10 years. Therefore, the establishment and implementation of a recovery process for PV module waste is imperative.

This chapter is organized as follows: the lifetime and the degradation model of a PV module are presented in Sect. 2. Section 3 describes the composition of different types of PV modules. The recycling processes for the different types of PV modules are presented in Sect. 4. The benefits of PV module recycling are summarized in Sect. 5. Finally, the chapter is concluded in Sect. 6.

2 Lifetime of PV Cells

One of the advantages of PV modules is their long lifetime. All PV manufacturers claim that their products have 25 years of warranted long-term power-output. Two factors determine the lifetime of a PV module: reliability and durability. The reliability indicates whether the product is prone to premature failure. The durability determines its slow degradation until the output power of the solar module is below the acceptable limits. The reliability and lifetime of a PV module depend on its degradation modes. There are four factors affecting the degradation of a PV

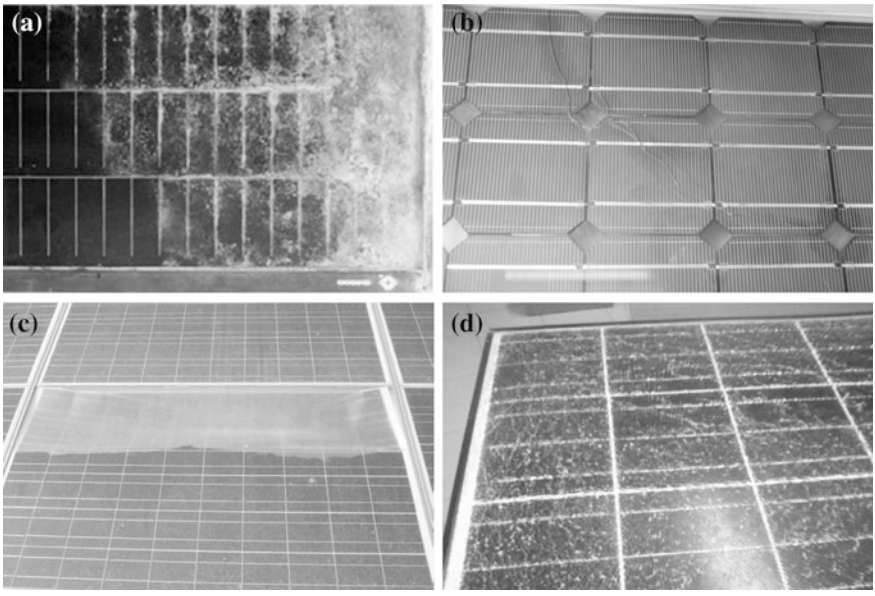

Fig. 3 Degradation of PV modules: **a** corrosion, **b** discoloration, **c** delamination, **d** breakage and cracking [5–8]

module: irradiation, temperature, humidity, and mechanical shock [4]. Each of these factors induces PV module degradation. There are several types of degradation: corrosion, discoloration, delamination, and breakage (Fig. 3) [5–8]. Figure 4 shows the relations between the degradation factors and the degradation model.

2.1 Corrosion of PV Modules

The main factors that cause corrosion are humidity and temperature. Under high temperature and high humidity, the permeability of the back sheet of a PV module increases. Moisture enters the module from its edge and causes corrosion; it attacks the metal materials inside the PV module and sometimes degrades the adhesion materials between the solar cells and the contact metal. The corrosion increases the leakage current and induces the degradation of the PV module. Besides moisture, oxygen causes the corrosion of silicon junctions.

2.2 Discoloration of PV Modules

The main factor that causes discoloration is irradiation. In PV modules, discoloration is predominantly induced by UV rays. The most commonly used encapsulating material for PV modules is ethylene vinyl acetate (EVA). UV rays cause the degradation of EVA and change its color from transparent to yellow, even to brown. The discoloration of the encapsulating materials increases the optical transmission loss and induces performance loss of the PV module.

2.3 Delamination of PV Modules

The main factors that cause delamination are humidity, temperature, and irradiation. Under high temperature and high humidity, the moisture that penetrates into the PV module causes corrosion of the metal materials. The corrosion sometimes induces delamination between the solar cells and the encapsulating polymer. The irradiation causes the deterioration of the EVA. The adhesion loss between the solar cells and the front glass or the encapsulating polymer materials changes the optical transmission of the PV module and the optical loss reduces the performance of the PV module.

2.4 Breakage and Cracking of PV Modules

Breakage is predominantly caused by mechanical shock. The breakage of the front glass changes the optical transmission and causes optical loss. Furthermore, the

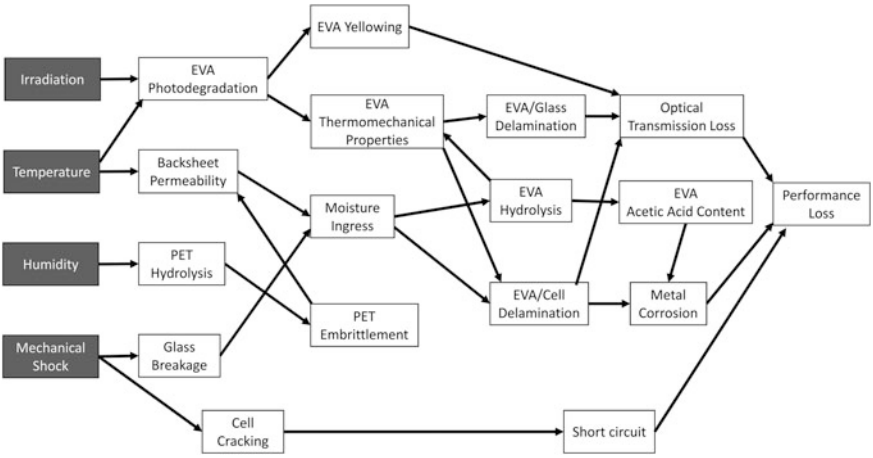

Fig. 4 PV module performance degradation pathways [4]

performance of the PV module is reduced by cracking of the solar cells. Sometimes, cracked solar cells cause short circuits. Corrosion, discoloration, and delamination usually follow the breakage and cracking of the PV module.

3 Composition of PV Modules

The main components of a PV module are solar cells. Based on the application, different types of solar cells are selected to compose the PV module. Solar cells can be divided into three types: silicon-based, compound, and organic. Figure 5 shows the classification of solar cells. 90 % of commercial PV modules are fabricated with silicon-based solar cells, including single-crystalline and multi-crystalline silicon solar cells, because of their low cost and the availability of mature industry technology. The HIT (heterojunction with intrinsic thin layer) solar cell has high energy conversion efficiency. However, its market share is only 2.3 % because of its high product technique. The electronic performance of the silicon thin-film (amorphous silicon or microcrystalline silicon) solar cell is lower than that of crystalline silicon solar cells. Therefore, it is not commonly used in large-scale applications, such as electric power plants, but it is suitable for rooftop and small-device applications. The other 7 % of PV modules in the market are cadmium telluride (CdTe) and copper indium gallium selenide (CIGS) modules. The III–V solar cell has very high energy conversion efficiency and is used for concentrator photovoltaic (CPV) applications (Table 1).

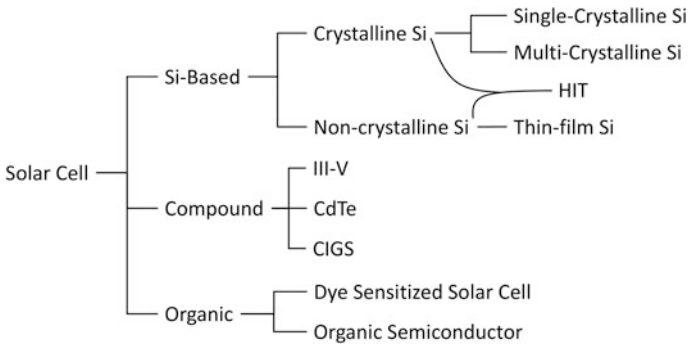

Fig. 5 Classification of solar cells

Table 1 The market share of PV module [9]

PV type	Production (GWp)	Market share (%)
Single-crystalline Si	13	33.6
Multi-crystalline Si	21.3	55
HIT	0.9	2.3
Amorphous Si	0.8	2.1
CdTe	1.9	4.9
CIGS	0.8	2.1

3.1 Crystalline Silicon PV Modules

The several types of crystalline silicon PV modules have similar structures; their only difference is the structure of the component solar cells. There are several types of crystalline silicon solar cells: commercial solar cells, selective-emitter (SE) solar cells, metal-wrap-through (MWT) solar cells, interdigitated back-contact (IBC) solar cells, bifacial solar cells, and passivated-emitter rear cells (PERC) [10]. The commercial solar cell is a simple p-n junction with an antireflection layer and a metal contact layer. The SE solar cell has an additional *n*+ region under the front metal contact, which can reduce the contact resistance of the front electrode. A laser hole through the MWT solar cell replaces the front bus bar, which can increase the area of light absorption. The metal electrode of the IBC solar cell is only on the rear-side surface and there is no shading on the front surface. The bifacial solar cell allows the absorption of light entering from the front and back sides. The PERC solar cell is the evolved form of an SE cell with better surface passivation. The local back contact and passivation layer on the rear side can also enhance the solar cell efficiency. Figure 6 shows the structures of the different solar cell types. All solar cell types can be fabricated with single-crystalline or multi-crystalline silicon wafers.

After fabrication, all PV modules have similar appearances. Figure 7 shows the structure of a PV module. The illuminated side is a transparent glass. The solar cells

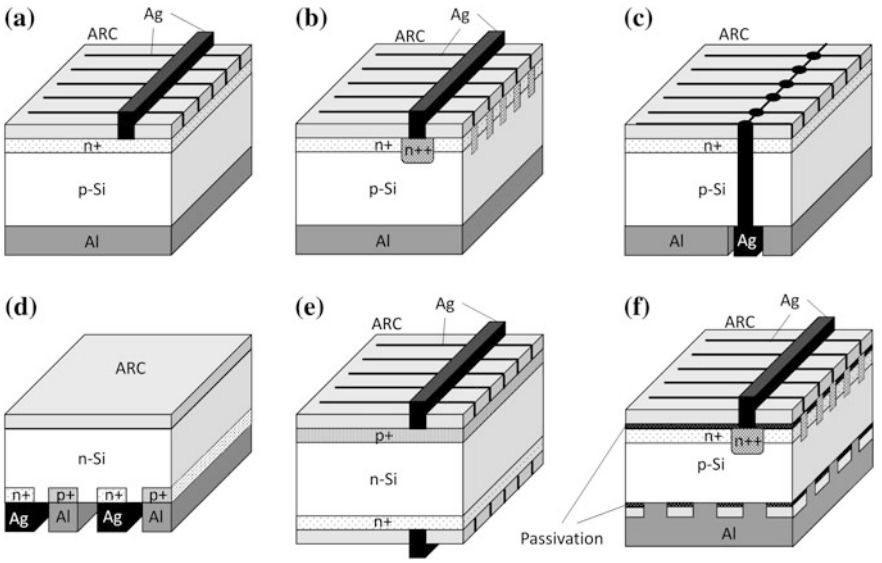

Fig. 6 Structure of silicon solar cells: **a** commercial solar cell, **b** SE solar cell, **c** MWT solar cell, **d** IBC solar cell, **e** bifacial solar cell, **f** PERC solar cell

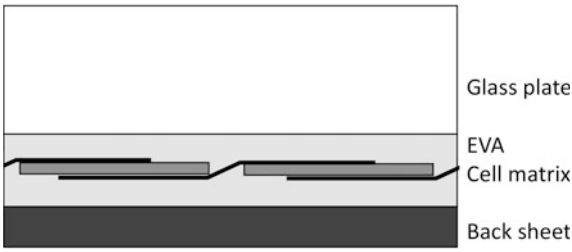

Fig. 7 Structure of commercial silicon PV modules

are connected by a ribbon and encapsulated in EVA. The rear side of the PV module is a back sheet made of plastic material. The PV module is enclosed in an aluminum frame. Each module has a junction box behind the module. Table 2 shows the main components of a crystalline silicon PV module. Most of the weight is contributed by the glass layer. The weight contribution of the solar cells contained in the module is approximately 3 wt%. For commercial silicon PV modules, the thickness of the glass plate is 3.2 mm.

The distinction between the different types of crystalline silicon PV modules is the way in which the solar cells are connected. Figure 8 shows the structure of different PV module types. If the solar cells have only a back contact, such as MWT or IBC, the ribbon is in contact only with the rear side of the solar cells. For the bifacial PV module, a transparent back sheet is used. Otherwise, a second glass plate is used as the back sheet. However, the total weight of the PV module increases to 60 wt% when two glass plates are used.

Table 2 The components of a crystalline silicon PV module

Components	6 × 10 cells module		6 × 12 cells module	
	Weight (kg)	Ratio (wt%)	Weight (kg)	Ratio (wt%)
Glass plate	12.8	67.4	15.4	68.4
Solar cell	0.6	3.1	0.7	3.1
Ribbon	0.2	1.0	0.3	1.3
EVA	1.4	7.4	1.7	7.6
Back sheet	0.7	3.7	0.8	3.6
Junction box	0.3	1.6	0.3	1.3
Aluminum frame	3.0	15.8	3.3	14.7
Total	19	100	22.5	100
Example: XS-60 and XS-72 PV module (Motech Ind.)				

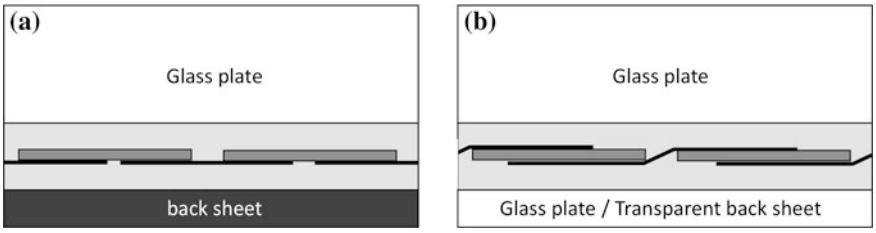

Fig. 8 Structure of PV modules with different solar cell types: **a** rear-contact solar cells, **b** bifacial solar cells

3.2 Noncrystalline Silicon PV Modules

Compared to the crystalline silicon PV module, the silicon thin-film PV module has a simpler structure. However, the energy conversion efficiency of a silicon thin-film solar cell is lower than that of a crystalline silicon solar cell. Furthermore, most of the companies that produced silicon thin-film solar cells are terminated; only one company, Kaneka Corp. Japan, is still operating. Figure 9 shows the structure of the

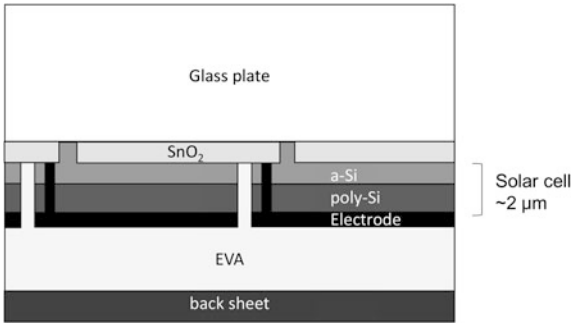

Fig. 9 Structure of a silicon thin-film PV module

Hybrid PV panel, fabricated by Kaneka Corp. [11]. The solar cell is constructed by depositing an amorphous silicon layer and a microcrystalline silicon layer directly on the glass layer. The front electron is gathered by the transparent conducting oxide (TCO) layer. The rear contact metal is fabricated by chemical vapor deposition (CVD) with laser patterning. Because the hybrid module can be integrated by laser scribing, no ribbon is needed. The rear side is protected by the EVA and the back sheet. The temperature during the fabricating process is below 350 °C. Table 3 shows the components of the silicon thin-film PV module fabricated by Kaneka Corp. Because the solar cell is positioned directly on the glass plate, only one EVA sheet is needed for the encapsulation process. The thickness of the solar cell is only 2 μm and the glass plate contributes most of the weight to the PV module. In this case, the thickness of the glass plate is 5 mm. Table 4 provides a list of PV power plants installed by Kaneka Corp. worldwide. There are still several PV power plants in operation.

The HIT PV module is similar to the crystalline silicon PV module. The HIT solar cell is fabricated from a crystalline silicon wafer using thin-film processing and equipment [12]. Because there is an intrinsic amorphous silicon layer between the emitter and the base silicon, the temperature tolerance of the HIT solar cell is limited to less than 300 °C. The encapsulation method is the same as that used for

Table 3 The components of a silicon thin-film PV module

Components	Quantities	
	Weight (kg)	Ratio (wt%)
Glass plate	14.5	79.3
Solar cell	~0.005	~0
EVA	0.5	2.7
Back sheet	0.5	2.7
Junction box	0.3	1.6
Aluminum frame	2.5	13.7
Total	18.3	100
Example: Hybrid PV panel (Kaneka Corp.)		

Table 4 The PV power installations constructed by Kaneka Corp.

Country	Location	Capacity (MW)
USA	Santee, San Diego	0.862
USA	Richmond, California	0.09
USA	Davis, California	0.06
Bulgaria	Paunovo, Ihtiman Municipality	1
Spain	Valencia	4
Germany	Haunsfeld	1.67
Germany	Solar Park Kleinleitzkau	1.5
Germany	Morbach	1.07
UK	Birmingham	0.102
Czech	Vrany, Kladno	1.4

Table 5 The components of HIT PV module

Components	Quantities	
	Weight (kg)	Ratio (wt%)
Glass plate	10.0	66.7
Solar cell	0.2	1.3
Ribbon	0.3	2.0
EVA	1.1	7.3
Back sheet	0.5	3.3
Junction box	0.3	2.0
Aluminum frame	2.6	17.3
Total	15	100
Example: HIT PV panel (Panasonic Corp.)		

crystalline silicon PV modules. The illuminated side is a transparent glass. The solar cells are connected by a ribbon and encapsulated in EVA. The rear side of the PV module is a back sheet made of plastic material. The PV module is enclosed in an aluminum frame. Each module has a junction box on its back side. Table 5 shows the components of the HIT PV module. The HIT solar cell has a bifacial structure; a back sheet with good reflection is used to increase the module efficiency when the product is a mono-facial module. For the construction of a bifacial module, two glass plates are used.

3.3 CdTe PV Modules

The CdTe PV module is fabricating by thin-film processing. Figure 10 shows the structure of the CdTe PV module [13]. First, the TCO layer (SnO_2) is deposited on the substrate glass. The emitter (CdS) and absorber layers (CdTe) are deposited on

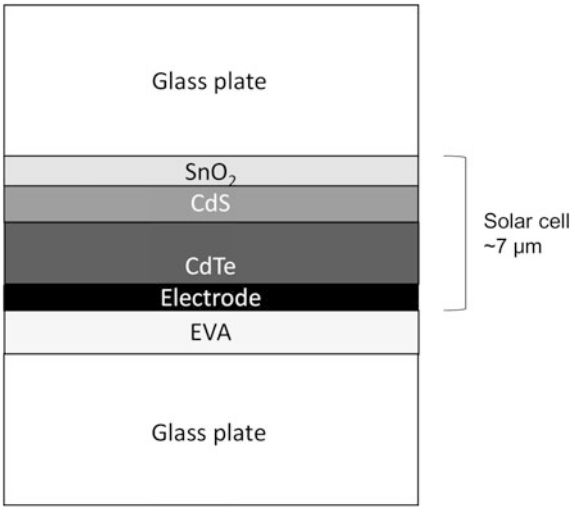

Fig. 10 Structure of the CdTe PV module

Table 6 The components of the CdTe PV module

Components	Quantities	
	Weight (kg)	Ratio (wt%)
Glass plate	11.3	94.0
Solar cell	~0.03	0.2
EVA	0.4	3.3
Junction box	0.3	2.5
Total	12	100
Example: Series 4^{TM} PV module (First Solar Inc.)		

the TCO layer by a CVD process. The thickness of CdS and CdTe is 0.1 and 5 μm, respectively. The back electrode is deposited by a sputter process. Because the CdTe module can be integrated by laser scribing, no ribbon is needed. After solar cell fabrication, the rear side is encapsulated in EVA and another glass plate. Table 6 shows the main components of a CdTe PV module. Because the CdTe PV module is a bifacial module and does not have an aluminum frame, 94 wt% of the module weight corresponds to the glass plate whereas the solar cells only contribute 0.2 wt%.

First Solar Inc. is a typical company that produces CdTe PV modules. Table 7 presents a list of PV power installations constructed by First Solar Inc. The biggest

Table 7 The PV power installations constructed by First Solar Inc.

Country	Location	Capacity (MW)
USA	San Luis Obispo County, California	550[a]
USA	Riverside County, California	550[a]
USA	Yuma County, Arizona	290
USA	Monterey County, California	280[a]
USA	Moapa, Nevada	250[a]
USA	Los Angeles, California	230[a]
USA	Boulder City, Nevada	58
USA	Tuson, Arizona	25
USA	Blythe, California	21
Canada	Ontario	80
Chile	Copiapó	141
Japan	Kitakyushu City	1.3
Germany	Templin, Brandenburg	128
Germany	Leipzig	40
Germany	Lieberose Photoviltaic Park	53
Germany	Trier	8.4
Israel	Ramat Hovav	37.5
United Arab Emirates	Seih Al Dahal, Dubai	13
Australia	Geraldton	10
Australia	New South Wales	159[a]

[a]Under construction

CdTe PV power plate has 290 MW capacity and is located in Arizona, USA. Until 2015, more than 10 GW of PV power was installed by First Solar Inc. and some solar power plants are still under construction. The market share of CdTe modules has been approximately 5 % in recent years.

3.4 III–V PV Modules

The III–V solar cells hold the world record for the highest efficiency; however, the materials used for constructing III–V solar cells are usually expensive. Therefore, III–V solar cells were only used in space applications in the past. Until the concentrator solar cell represent the cost of III–V solar cells is acceptable for concentrations above 400 suns, concentrator PV systems with III–V solar cell are used for power generation on earth. GaAs is a commonly used material in multi-junction solar cells of solar panels, especially for concentrating solar power. Figure 11a shows the structure of a GaInP/GaAs/Ge solar cell with a germanium substrate. Three solar cells with different band gaps are fabricated on the substrate by metal organic chemical vapor deposition (MOCVD). The thickness of the solar cell is <5 μm. Figure 11b shows the structure of the concentrator module [14]. The solar cell is fixed on a heat spreader with electric contacts. The sunlight is concentrated by Fresnel lenses and a tubular enclosure, which is a secondary concentrator, and is focused on the solar cell. Table 8 displays the main components of a concentrator

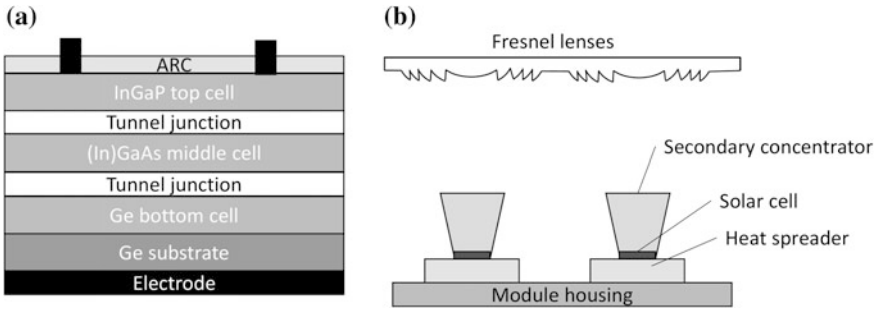

Fig. 11 **a** Structure of a GaAs solar cell, **b** structure of a concentrator PV module

Table 8 The components of a GaAs PV module

Components	Quantities	
	Weight (kg)	Ratio (wt%)
Fresnel lenses	46	16.2
Solar cell	~0.01	0.004
Support system	239	83.8
Total	285	100
Example: uModule (Arzon Solar LLC.)		

PV module with GaInP/GaAs/Ge solar cells. The example is the uModule, fabricated by Arzon Solar LCC., which is the world leading designer and manufacturer of commercial CPV systems. The module size is 511 cm in length and 216 cm in width and the total weight is 285 kg. The Fresnel lenses are usually constructed from poly-methyl-methacrylate (PMMA) and their weight is 46 kg. The number of solar cells in the module is 360. Because the size of the solar cells is so small, their total weight is only 0.01 kg (including the substrate) whereas 83.8 wt% of the PV module is contributed by the support system, which includes the cell compartment and shield.

3.5 CIGS PV Modules

CIGS is a I-III-VI_2 semiconductor material with high light absorption [15]. Like other thin-film solar cells, CIGS is advantageous because it can be deposited on flexible substrates. The other advantages of CIGS include high-temperature tolerance, good performance under low light intensities, light soaking effects, and shadow tolerance. It is manufactured by depositing a thin layer of copper, indium, gallium, and selenium on a glass substrate or stainless steel. The current market leader is Solar Frontier K.K., Japan. Figure 12 shows the structure of a CIGS PV module fabricated by Solar Frontier K.K. The fabrication process begins with the base electrode (Mo) formation on the glass substrate by sputtering. The absorber layer is fabricated by the selenization of sputtered metallic precursors, copper, gallium, and indium on the base electrode. The ZnS buffer layer is formed by chemical bath deposition. The TCO layer, which is boron-doped zinc oxide (BZO),

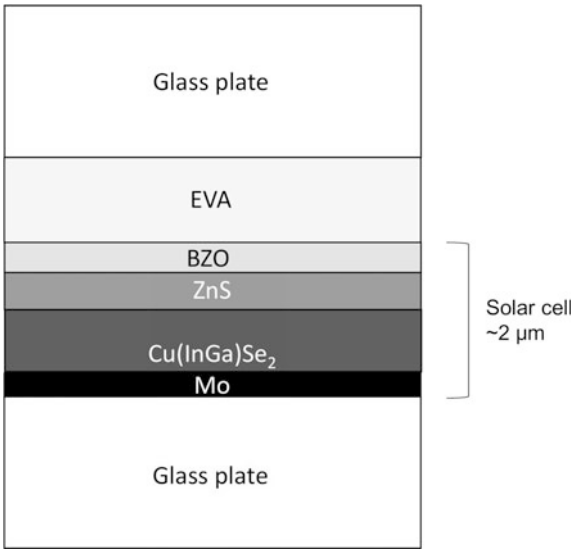

Fig. 12 Structure of a CIGS PV module

Table 9 The components of a CIGS PV module

Components	Quantities	
	Weight (kg)	Ratio (wt%)
Glass plate	16.8	84.0
Solar cell	~0.02	0.1
EVA	0.5	2.5
Junction box	0.3	1.5
Aluminum frame	2.4	12
Total	15	100
Example: CIS PV panel (Solar Frontier)		

Table 10 The PV power installations constructed by Solar Frontier K.K

Country	Location	Capacity (MW)
USA	California	82.5
USA	North Carolina	26[a]
Mexico	Cerro Prieto	1.5
France	Bessan	4.19
Spain	Almeria	1
Germany	Bochow	28.8
Germany	Eberswalde	5
Germany	Wildflecken	0.55
Germany	Kolitzheim	0.55
Germany	Hamburg	0.51
Germany	Schwabach	0.34
Saudi Arabia	Dhahran	10.5
Thailand	Phetchabun	3.3
Japan	Kansai International Airport	11.6
Japan	Niigata	1

[a]Under construction

is deposited by MOCVD. The thickness of a CIGS solar cell is only 1–2 μm. Because the CIGS module can be integrated by laser scribing, no ribbon is needed. After the solar cell fabrication, the front side is encapsulated in EVA and another glass plate. Table 9 displays the main components of a CIGS PV module. Because the module is bifacial, 84 wt% corresponds to the glass plate whereas the solar cells only contribute 0.1 wt%.

Solar Frontier K.K is a typical company that produces CIGS PV modules. Table 10 lists the PV power installations constructed by Solar Frontier K.K. Until 2015, more than 2 GW of PV power was installed and some solar power plants are still under construction. The biggest power plate, with a capacity of 82.5 MW, is located in California, USA.

4 Recycling Process

For PV module recycling, appropriate separation, and purification methods are necessary. A PV module contains more than one component and sometimes different components combine as alloys or compounds. Therefore, the PV module recycling process usually includes several separation processes, such as physical or chemical treatments. In Sect. 4, the different recycling processes used for different PV module types are discussed.

4.1 Recycling of Crystalline Silicon PV Modules

The fabrication process of crystalline silicon PV modules consists of: ingot growth, wafer slicing, solar cell fabricating, and module encapsulation. During the production steps from ingot to wafer, approximately 68 % of silicon feedstock is lost in the form of silicon-containing waste [16]. The recycling of silicon-containing waste, such as top, tail, edge, pot scrap, and broken wafer, is a mature technology. Even kerf-loss waste produced during wafer slicing can be recycled by physical and chemical methods [17, 18]. These recycling methods are not complicated because the composition of silicon-containing waste is simple. The major component of the waste is silicon with purity higher than 99 %. The only task is to remove the metal impurities. The recycling of silicon PV modules is more complicated because they consist of several components: solar cells, ribbon, glass, EVA, and back sheet.

The recycling method for crystalline silicon PV modules has several steps; the most difficult one is the removal of the encapsulated material. The solar cells inside the module are attached with EVA and the back sheet and they are not easily detachable from the module. Some separation methods have been suggested to detach the solar cells from the EVA. A chemical treatment step has been proposed for the decomposition of the EVA. Figure 13 shows the dissolution of the EVA and the back sheet in organic solvent [19]. However, processing time is an issue with this technique. The size of commercial modules is 180 cm in width and 120 cm in length. Dipping a module in a chemical solution requires several days or weeks to allow the chemical to penetrate the entire module and dissolve the EVA. Therefore, it is not suitable for large-sized modules. Regarding recycling capacity, the heat decomposition method is more suitable [20]. After removing the aluminum frame, the residual parts of the module are the glass plate, solar cells, EVA, and back sheet. The melting temperatures of the glass plate, solar cell, and ribbon are 800, 1420, and 700 °C, respectively. The cracking temperature of the EVA and the back sheet is in the range of 250–450 °C. Therefore, heating the module inside a furnace above 500 °C can burn out the EVA and back sheet. The remaining parts after heat decomposition are the glass plate, solar cells, and ribbons, as shown in Fig. 14.

Figure 15 shows the recycling process for crystalline silicon PV modules. First, the junction box and aluminum frame are disassembled from the module. After heat

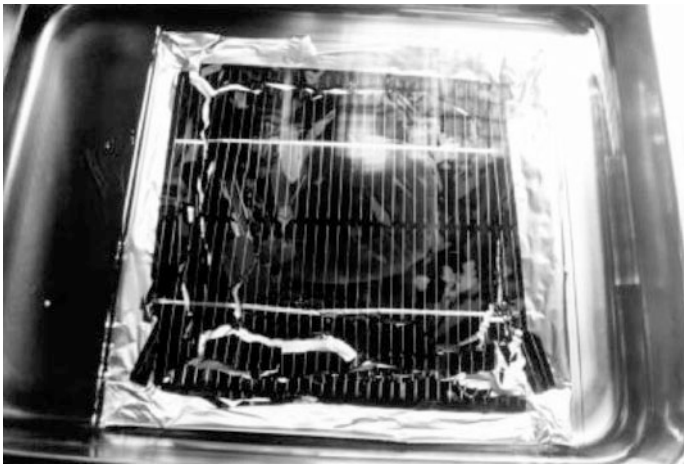

Fig. 13 Dissolution of EVA by organic solvent [19]

Fig. 14 Residual components of silicon module after heat decomposition

decomposition, the glass plate, solar cells, and ribbons can be separated. Broken glass and broken solar cells are sorted manually. This glass is clean because the temperature inside the furnace is not sufficiently high to diffuse impurities into the glass plate. Therefore, the glass can be reused for other products or be remelted to create a new glass plate for PV module application.

The components of a crystalline silicon solar cell are a silicon layer with different doping types, a conductive metal layer, and an antireflection coating layer (ARC).

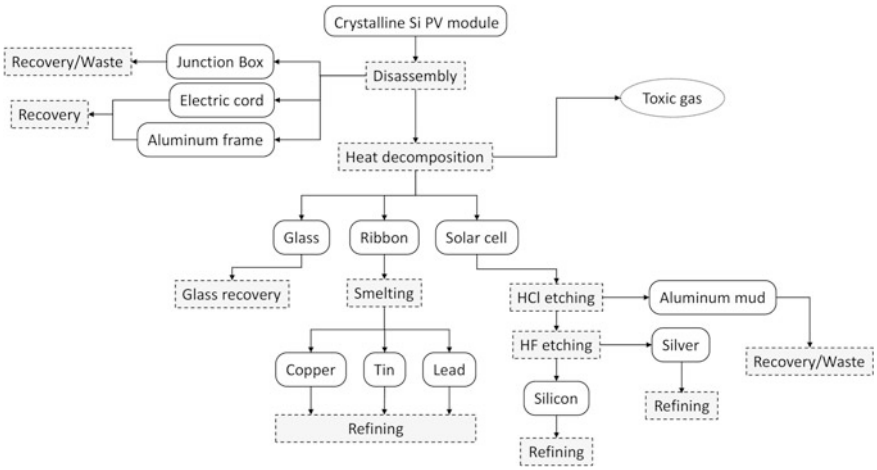

Fig. 15 The recycling process for crystalline silicon PV modules

For the decomposition of the solar cell, several chemical treatment steps are required. First, the solar cell is immersed in a hydrochloric acid solution and the aluminum rear conductive layer is decomposed. By collecting and filtrating the hydrochloric acid solution, an aluminum mud is obtained, which can be reused for steel refining applications. In the second step, the solar cell is dipped in a hydrofluoric acid solution to remove the ARC layer. The ARC layer is composed of silicon nitride (SiN_x) or, in some cases, silicon oxide (SiO_x), which are dissoluble in hydrofluoric acid solutions. Subsequently, the silver grid peels off from the solar cell surface. After the silver grid is collected and remelted at 980 °C, a piece of silver can be obtained. Silver is a valuable material and is widely used in the industry. After HF dipping, the remaining material is silicon with a p-n junction. The emitter layer on the silicon can be removed by acid etching or alkali etching; high-purity silicon material can be obtained after the final etching step [21]. However, considering the cost of the process and the price of silicon, using the silicon with the p-n junction in steel refining applications without the additional chemical etching step is more sensible [22].

The ribbon is obtained with high-temperature treatment and can be recycled. The ribbon is made of high-purity copper, with a skin of lead-tin alloy. The copper, lead, and tin can be separated by a refining process and provide high-purity raw materials.

4.2 Recycling of Noncrystalline Silicon PV Modules

The recycling method for silicon thin-film PV modules is simpler than that used for crystalline silicon PV modules. Figure 16 shows the recycling process of silicon thin-film PV modules. First, the junction box and aluminum frame are disassembled

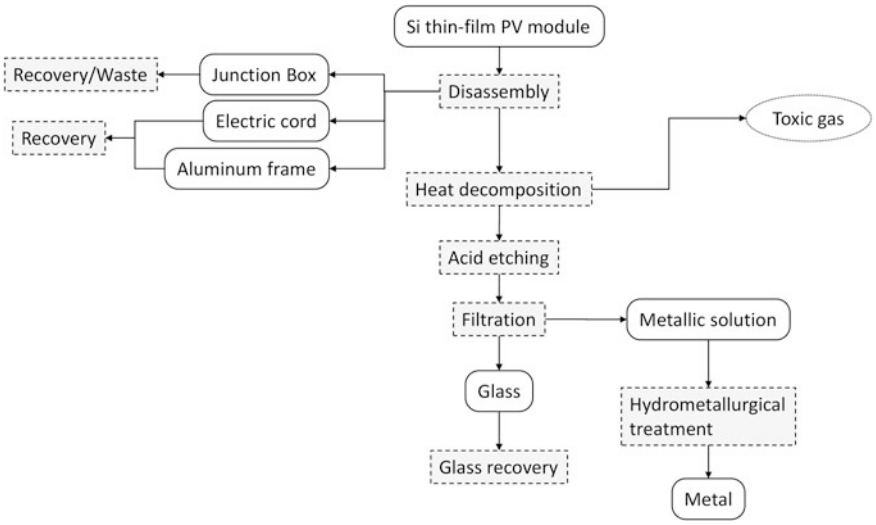

Fig. 16 The recycling process for silicon thin-film PV modules

from the module. The EVA and back sheet can be removed by heat decomposition. Because the solar cells are positioned directly on the glass when they are fabricated, the glass plate and solar cells are attached and cannot be separated in the heat decomposition step. Because the silicon thin-film solar cell is composed of microcrystalline or amorphous silicon, the acid solution can etch and remove the solar cells from the glass. After filtration, the glass can be recovered. The residual solution obtained from the filtration step contains metal ions. The metal solution can be refined by hydrometallurgical treatment and the metal can be recovered.

4.3 Recycling of CdTe PV Modules

Recycling is a necessary process for CdTe PV modules because cadmium is an environmental hazard. If a CdTe PV module is abandoned on the ground or buried underground, the leakage of cadmium may pollute the environment and cause biohazard problems. Figure 17 shows a possible recycling process for CdTe PV modules. The CdTe PV module uses two glass plates for encapsulation, which makes the burn out of the EVA compressed between the two glass plates difficult. On the other hand, the low vapor pressure of cadmium introduces the risk of losing the cadmium because of evaporation. Therefore, decomposing the EVA by chemical treatment is a better choice than thermal treatment. First, the junction box is disassembled from the module. The module is crushed into small pieces by a hammer mill. For a CdTe PV module, the contributing weight of glass and EVA is 94 wt% and $\sim$3 wt%, respectively. Therefore, sieving out the EVA flakes from the

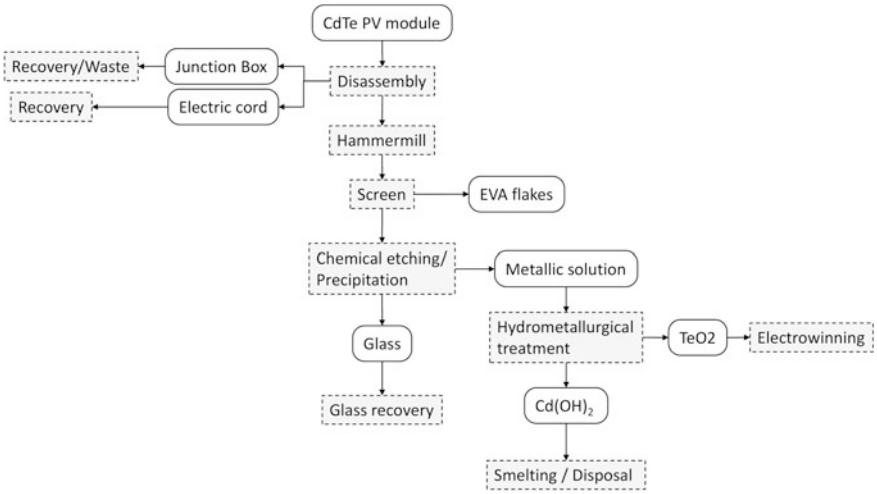

Fig. 17 The recycling process for CdTe PV modules

crushed module is suggested. Chemical etching removes the solar cell material from the surface of the glass. A precipitation step separates the chemical solution and the glass and the glass is recovered. Hydrometallurgical treatment can recover the cadmium and tellurium [23, 24].

In the hydrometallurgical treatment, sulfuric acid and peroxide are used to etch the CdTe. The chemical reactions are [25]:

$$\mathrm{CdTe_{(s)} + 3H_2SO_4 + 3H_2O_2 \rightarrow CdSO_{4(aq)} + Te(SO_4)_{2(aq)} + 6H_2O} \quad (1)$$

$$\mathrm{CdS_{(s)} + H_2SO_4 + H_2O_2 \rightarrow CdSO_{4(aq)} + S_{(s)} + 2H_2O} \quad (2)$$

A leaching step can remove the sulfur. The cadmium and tellurium dissolve in the solution. Adding caustic solution, such as sodium carbonate, to adjust the PH value can make the cadmium and tellurium precipitate [26].

$$\mathrm{CdSO_{4(aq)} + Na_2CO_{3(s)} \rightarrow CdCO_{3(s)} + Na_2SO_{4(aq)}} \quad (3)$$

$$\mathrm{Te(SO_4)_{2(aq)} + 2Na_2CO_{3(s)} \rightarrow TeO_{2(s)} + 2Na_2SO_{4(aq)} + CO_{2(g)}} \quad (4)$$

After filtration, the $CdCO_3$ and TeO_2 can be collected and reduced in a hydrogen furnace to regenerate CdTe [27]:

$$\mathrm{CdCO_3 + TeO_2 + 3H_2 \rightarrow Cd + Te + CO_2 + 3H_2O} \quad (5)$$

$$\mathrm{Cd + Te \rightarrow CdTe} \quad (\text{in } \mathrm{N_2} \text{ at } \sim 500\,^{\circ}\mathrm{C}) \quad (6)$$

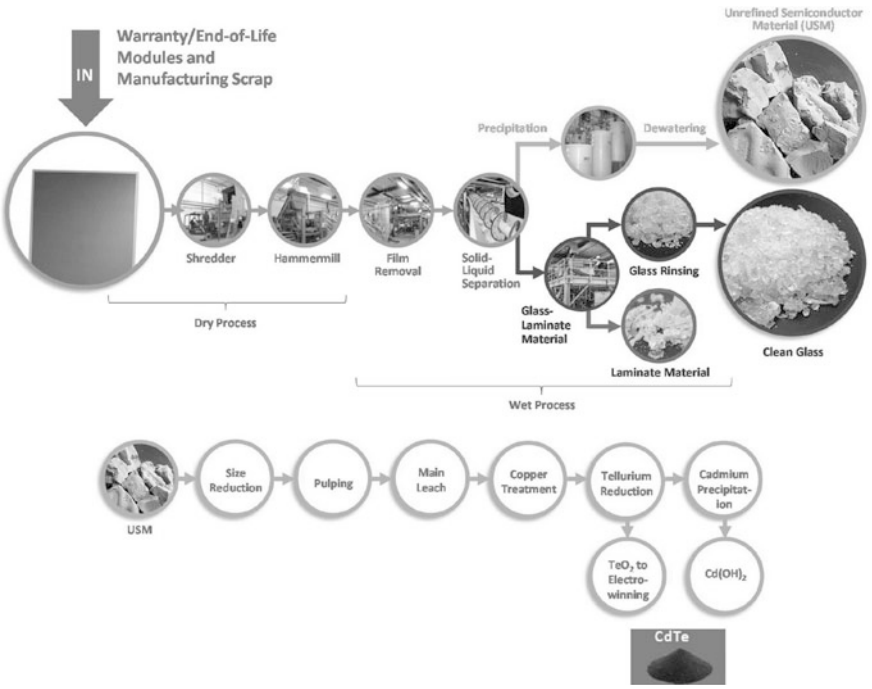

Fig. 18 The CdTe PV module recycling process of First Solar Inc. [27]

Another method exists for the recovery of the tellurium. TeO_2 can dissolve in the alkaline solution and be separated from $CdCO_3$. High-purity tellurium can be obtained by electrowinning [26].

$$TeO_{2(s)} + 2KOH \rightarrow K_2TeO_{3(aq)} + H_2O \tag{7}$$

$$K_2TeO_{3(aq)} + 4e^- + H_2O \rightarrow Te_{(s)} + 2KOH + O_2 \tag{8}$$

First Solar Inc. is the typical company to that produce CdTe PV modules. They have established a recycling system to recover the materials from end-of-life CdTd PV modules. Figure 18 shows the recycling process of First Solar Inc. [27], in which 95 % of the semiconductor materials and 90 % of the glass can be recovered and reused in new PV modules.

4.4 Recycling of III–V PV Modules

In this subsection, the recycling process of concentrator PV modules is discussed. Figure 19 shows the assembly drawing of a concentrator PV module. The displayed

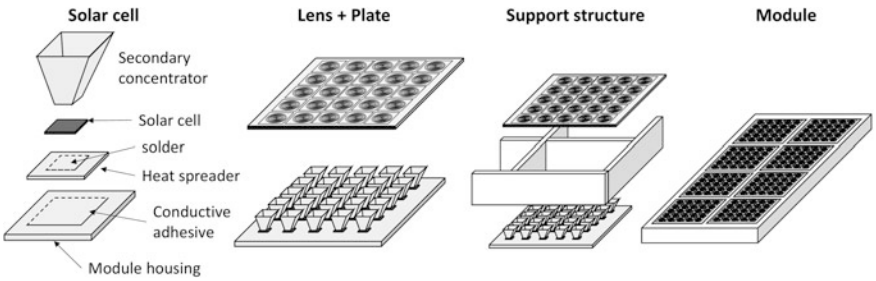

Fig. 19 The concentrator PV module assembly drawing

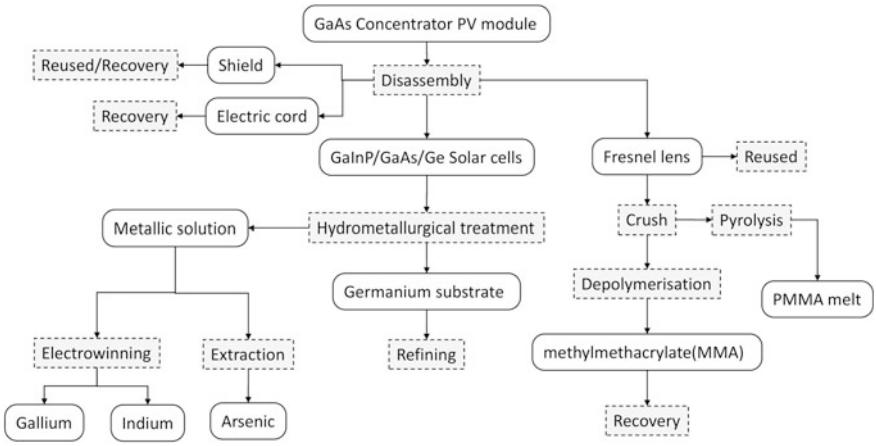

Fig. 20 The recycling process for concentrator PV modules

components are mechanically assembled to create the module. To recycle an end-of-life concentrator PV module, all units of the module are disassembled. Figure 20 shows the recycling process of a concentrator PV module. The support structure, module housing, and secondary concentrator are made of alloy. They can be directly reused in new concentrator PV modules. The Fresnel lens can be reused if it is still in a useable condition. If the Fresnel lens is damaged, it can be recovered by crushing and pyrolysis. The Fresnel lens is constructed from PMMA, which is a type of thermoplastic material. PMMA can melt at a temperature higher than 160 °C and be shaped into other forms for application. Another recovery process is depolymerization [28]. PMMA can be depolymerized by contact with molten lead at approximately 500 °C. The methyl methacrylate (MMA) monomer can be obtained with a purity of more than 98 %. GaAs solar cells are fabricated by MOCVD on germanium substrates. A chemical treatment, etching with an acid solution, can remove the solar cell layers from the substrate. The obtained germanium substrate can be refined to high purity and recovered.

In hydrometallurgical treatment, nitric acid can be used to etch the solar cell layer. The chemical reactions are [29]:

$$2GaAs + 8HNO_3 + H_2O \rightarrow 2Ga(NO_3)_3 + 2NO_2 + As_2O_3 + 5H_2 \quad (9)$$

Gallium and indium are rare elements and must be recovered. Gallium and indium compounds can be separated by precipitation, extraction, or ion exchange. After extracting these compounds, an electrowinning process can refine the gallium and indium to high purity. Arsenic is poisonous and constitutes a biohazard; however, treatment with an arsenic-containing solution is necessary. The arsenic-containing solution reacts with SO_2 gas and As_2O_3 is extracted from the reduction solution.

4.5 Recycling of CIGS PV Modules

The CIGS solar cell contains four elements: copper, indium, gallium, and selenium. Indium and gallium are rare elements and must be recovered for reuse. Figure 21 shows the recycling process for a CIGS PV module. First, the junction box and aluminum frame are disassembled from the module. The encapsulation material used in CIGS PV modules is EVA, which can decompose under high-temperature treatment. However, a heat decomposition process is not recommended because the vapor pressure of selenium can be as high as 10 kPa at the thermal decomposition temperature of EVA, 500 °C. The sublimation of selenium involves environmental pollution issues. Therefore, the temperature of the recycling process must be kept as low as possible. Decomposing the EVA by chemical treatment is a better choice than thermal treatment. The CIGS module can be crushed into small pieces by a hammer mill and the EVA flakes sieved out from the crushed module. Chemical

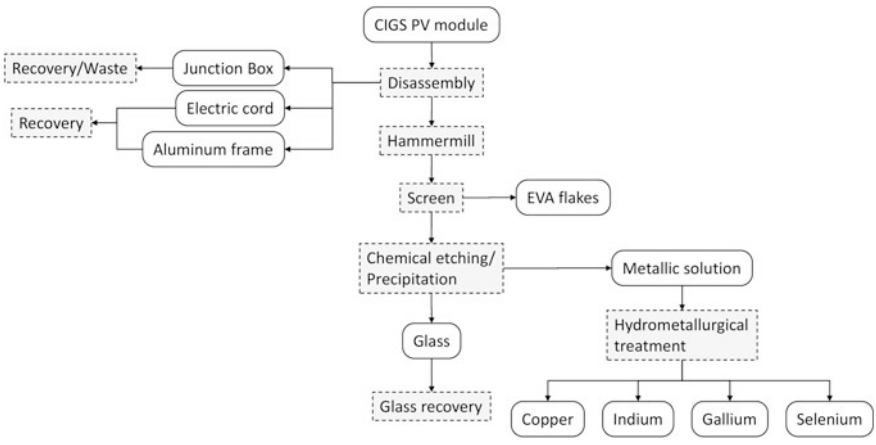

Fig. 21 The recycling process for CIGS PV modules

Table 11 The typical elements of PV module

Element	Purpose	Price (USD/kg)		2014 World production (metric ton)
		Past 5 years	2015	
Cadmium	CdTe	1.0–4.5	1.0–1.9	22,200
Aluminum	Frame, Electrode	1.5–2.8	1.5–1.9	49,300,000
Lead	Ribbon	1.6–2.9	1.6–2.2	5,460,000
Zinc	CIGS, TCO	1.6–2.6	1.6–2.4	13,300,000
Arsenic	GaAs	1.6–2.1	1.7–2.1	46,000
Copper	Ribbon, CIGS	4.8–10	4.8–6.4	18,700,000
Molybdenum	Electrode	8.5–39	8.5–20	266,000
Tin	Ribbon, TCO	14–33	14–19	296,000
Silicon	Substrate	18–75	18–20	250,000
Selenium	CIGS	32–166	32–51	2800
Tellurium	CdTe	100–349	100–127	300
Gallium	GaAs, CIGS	205–1075	205–240	170
Indium	CIGS, InGaP	390–830	390–705	820
Silver	Electrode	506–1620	512–649	26,100
Germanium	Substrate	925–2000	1800–1920	165

etching removes the solar cell material from the surface of the glass. A precipitation step separates the chemical solution and the glass and the glass is recovered. Hydrometallurgical treatment can recover the metal from the chemical solution [30–32].

5 Benefits of PV Module Recycling

There are two purposes for recycling end-of-life PV modules: (1) reduce the processing cost by recovering the valuable materials, (2) reduce the environmental effects from toxic waste [33–36]. Table 11 shows the typical elements inside the PV module.

5.1 Valuable Materials

5.1.1 Gallium, $_{31}$Ga

Gallium is a byproduct of aluminum and zinc processing [37]. Most gallium is extracted from the crude aluminum hydroxide solution of the Bayer process, which is used for producing alumina and aluminum. The abundance of gallium in the

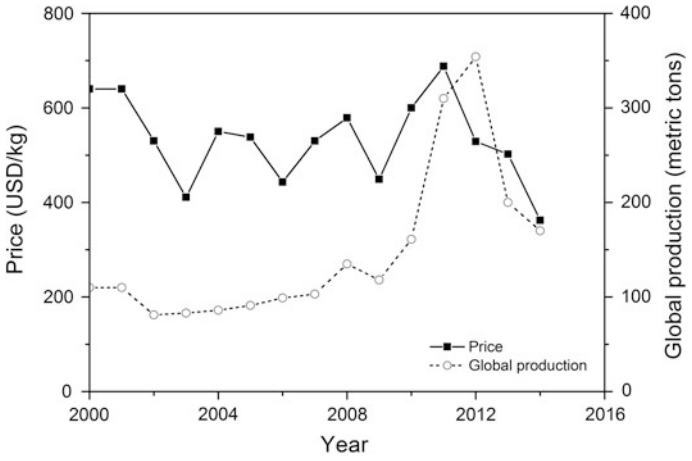

Fig. 22 The price and global production of gallium

Earth's crust is 19 ppmw, which is much higher than that of the rare element indium (0.25 ppmw). Because of the high cost of the extraction process, gallium is expensive. In 2014, the global production of refined gallium was 170 metric tons [38]. Gallium is widely used in electronic components, including integrated circuits and optoelectronics, such as laser diodes and light-emitting diodes (LEDs). In PV applications, it is the major component of GaAs concentrator solar cells and it is used in the GaInP top cell and the GaAs middle cell. The absorber layer of a CIGS solar cell also contains gallium. In 2015, the price of gallium is 205–240 USD/kg (Fig. 22).

5.1.2 Indium, $_{49}$In

Indium is a rare element with an abundance of only 0.25 ppmw in the Earth's crust. Indium is produced by leaching from slag and dust generated during zinc production [37]. In 2014, the global production of indium was 820 metric tons [38]. Indium is widely used in thin-film applications. Indium oxide and indium tin oxide are used as transparent conductive coatings applied to glass substrates in the construction of electroluminescent panels. Other applications of indium include LEDs, laser diodes, vacuum seal alloys, thermal conductors used in cryogenics, and ultra-high vacuum applications. In PV applications, indium is mainly employed in TCOs. In GaAs concentrator solar cells, indium is used in the GaInP top cell and the GaAs middle cell. The absorber layer of CIGS solar cells also contains indium. In 2015, the price of indium is 390–520 USD/kg (Fig. 23).

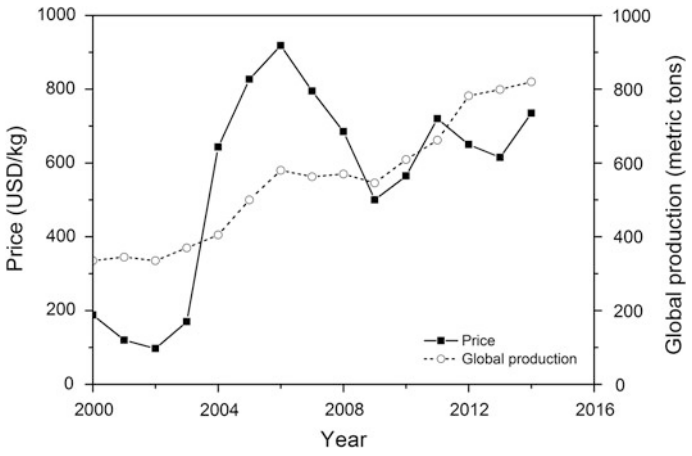

Fig. 23 The price and global production of indium

5.1.3 Silver, $_{47}$Ag

Silver is a precious metal. The abundance of silver in the Earth's crust is only 0.075 ppmw. Silver is produced as a byproduct of the electrolytic refining of copper, nickel, gold, and zinc [37]. It can be also produced by the Parkes process, which is a pyrometallurgical method for extracting silver from lead. In 2014, the global production of silver was 26,100 metric tons [38]. Silver is an important material for currency. Other applications include jewelry, silverware, air conditioners, water purification, dental fillings, photography, and electrical and electronic products. In PV applications, large quantities of silver are used as a conductive paste. For crystalline Si solar cell fabrication, the electrode material is silver because of its good electrical conductivity. Metallization pastes containing silver are the most expensive non-silicon materials used in crystalline Si solar cell fabrication. The cost of silver present in a solar cell is about 5.8 cents (1.3 cents/Wp). This means that each solar cell contains 0.13 g silver and there are 9.36 g silver inside a module containing 6 × 12 cells. The recycling of silver is the most beneficial stage of crystalline Si PV module recycling. The price of silver is 512–649 USD/kg in 2015 (Fig. 24).

5.1.4 Germanium, $_{32}$Ge

Germanium is very expensive owing to the shortage of raw materials and the complexity of its recovery and refinement [37]. The abundance of germanium in the Earth's crust is 1.5 ppmw. Germanium is recovered as a byproduct from sphalerite zinc ores. Another source of germanium is fly ash from coal power plants. In 2014, the global production of germanium was 165 metric tons [38]. The major end uses

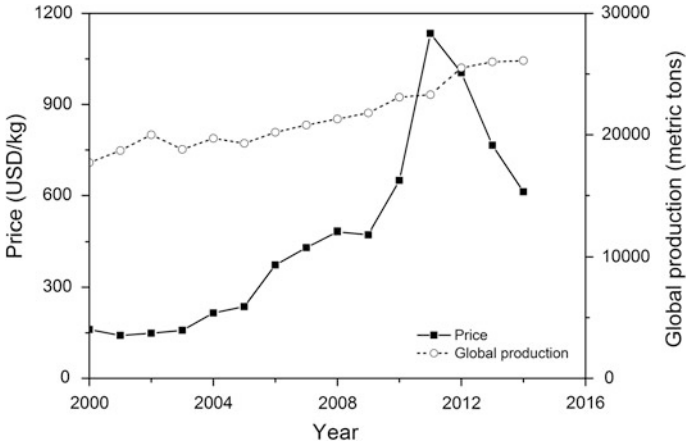

Fig. 24 The price and global production of silver

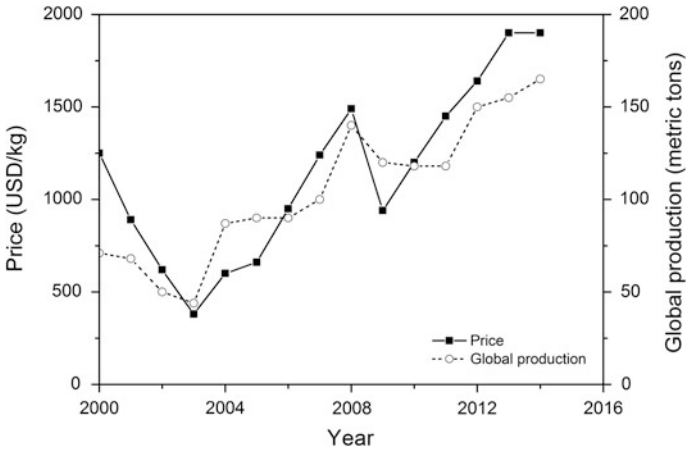

Fig. 25 The price and global production of germanium

for germanium are fiber-optic systems, infrared optics, polymerization catalysts, electronics, and PVs. Other applications include phosphors, metallurgy, and chemotherapy. In PV applications, germanium is used as the substrate for GaAs concentrator solar cells. The price of germanium in 2015 is 1800–1920 USD/kg (Fig. 25).

5.2 Environmental Effects

5.2.1 Cadmium, $_{48}$Cd

Cadmium is a toxic heavy metal that occurs naturally in the Earth's crust [37]. It is usually in the form of a mineral, combined with other elements. Cadmium is a common impurity in zinc ores. Most cadmium is extracted from zinc by vacuum distillation. The abundance of cadmium in the Earth's crust is 0.15 ppmw. In 2014, the global production of refined cadmium was 22,200 metric tons [38]. Cadmium is a common material for industrial usage, such as in batteries, pigments, plastics, and electroplatings. In PV applications, the major component of CdTe solar cells is cadmium. The price of cadmium in 2015 is 1–1.9 USD/kg.

Cadmium can enter the soil, water, and air from waste. Cadmium binds strongly to soil particles and does not breakdown in the environment. Organisms receive cadmium from the environment. The United States Department of Health and Human Services (DHHS) and the International Agency for Research on Cancer (IARC) have determined that cadmium and cadmium compounds are human carcinogens. Acute exposure to cadmium causes lung inflammation and chronic exposure induces lung cancer, osteomalacia, and proteinuria. The United States Environmental Protection Agency (EPA) determined that cadmium is a possible human carcinogen. The pollution limits and soil loading rates are regulated by the EPA [39]. The Ceiling Concentration Limit (CCL) for land-applied biosolids of cadmium is 85 mg/kg. The pollutant concentration limit (PCL) of cadmium is 39 mg/kg. The maximum contaminant level (MCL) of water is 0.005 mg/L, which is the highest level of a contaminant that is allowed in drinking water. The weight of cadmium in one CdTe PV module is approximately 15 g. If an end-of-life CdTe PV module is buried in the soil, 385 kg of soil will be contaminated and cannot be land applied and 3000 tons of drinking water will be contaminated and undrinkable. Therefore, the recycling of cadmium is necessary.

5.2.2 Arsenic, $_{33}$As

Arsenic is a toxic heavy metal and a natural element present in the Earth's crust [37]. In minerals, arsenic usually occurs in conjunction with sulfur and metals, and it can also exist as a pure elemental crystal. Most arsenic is obtained as a byproduct from the smelting of copper, lead, or gold ores. The abundance of arsenic in the Earth's crust is 1.8 ppmw. In 2014, the global production of refined arsenic was 46,000 metric tons [38]. The applications of arsenic include wood preservatives, agricultural insecticides, pesticides, herbicides, cotton desiccants, feed additives for poultry, and medicines. In PV applications, arsenic is used to fabricate GaAs solar cells. The price of arsenic in 2015 is 1.7–2.1 USD/kg.

Arsenic can enter the soil, water, and air from waste and cannot breakdown in the environment. Arsenic compounds can dissolve in water and ultimately result in

the soil or in sediments. The DHHS, IARC, and EPA have determined that inorganic arsenic is a known human carcinogen. Acute exposure to arsenic causes nausea, vomiting, diarrhea, encephalopathy, multi-organ effects, arrhythmia, and painful neuropathy. Chronic exposure to arsenic causes diabetes, hypopigmentation, hyperkeratosis, and cancer. The pollution limits and soil loading rates for arsenic are regulated by the EPA [39]. The CCL for land-applied biosolids of arsenic is 75 mg/kg, the PCL of arsenic is 41 mg/kg, and the MCL of drinking water is 0.01 mg/L. The weight of arsenic in one GaAs concentrator PV module is approximately 0.1 g. This amount can contaminate 10 tons of drinking water and make it undrinkable. Although the amount of arsenic in one waste module is small, the recycling of arsenic must be performed based on environmental considerations.

5.2.3 Lead, $_{82}$Pb

Lead is a toxic heavy metal that is extensively abundant in ores [37]. Galena, which contains an average of 5–60 % lead, is the most important lead mineral. The main method for the production of lead from ores is the sintering reduction process. The abundance of lead in the Earth's crust is 14 ppmw. In 2014, the global production of refined lead was 5,460,000 metric tons [38]. The applications of lead include building construction, lead-acid batteries, bullets and ammunition weights, fusible alloys, electrodes for electrolysis, and radiation shielding. Lead has been used in the solder for electronics for a long time. Regarding PV applications, the ribbon used inside the solar cell module is copper with a lead-tin skin. The silver paste used in the metallization process for crystalline silicon solar cells usually contains lead oxide. The price of lead in 2015 is 1.6–2.2 USD/kg.

Lead can enter the soil, water, and air from waste. Once lead enters the soil, it is usually attached to soil particles. The DHHS, IARC, and EPA have determined that inorganic lead and lead compounds are known human carcinogens. Acute exposure to lead causes brain dysfunction, nausea, and vomiting and chronic exposure induces anemia, encephalopathy, palsy, and nephropathy. The pollution limits and soil loading rates for lead are regulated by the EPA [39]. The CCL for land-applied biosolids of lead is 840 mg/kg, the PCL of lead is 300 mg/kg, and the MCL of drinking water is 0.015 mg/L. The weight of lead in one crystalline silicon PV module is approximately 40 g. Without recycling, lead waste can cause 130 kg of land contamination and render 2700 tons of drinking water contaminated and undrinkable.

5.2.4 Toxic Gas

In the recycling process of some types of PV modules, heat decomposition is chosen for removing the EVA and back sheet. EVA is the copolymer of ethylene and vinyl acetate. The chemical formula of EVA is $(C_2H_4)_n(C_4H_6O_2)_m$, which is composed only of carbon, hydrogen, and oxygen. The burning of EVA produces a

large amount of steam and carbon dioxide, which is an important greenhouse gas [40]. The incomplete combustion of EVA generates carbon monoxide and acetic acid. Carbon monoxide is a highly toxic gas for the human body whereas acetic acid is corrosive and can harm the skin.

Polyvinyl fluoride (PVF) is the most commonly used back sheet material for PV module encapsulation. The chemical formula of PVF is $(C_2H_3F)_n$, which is composed of carbon, hydrogen, and fluorine. The burning of PVF produces carbon dioxide, steam, and hydrofluoric acid [41]; the latter is a highly corrosive chemical and poison. In high temperature, hydrofluoric acid vapor is dangerous and must be handled very carefully. Fluoride plastics have good thermal resistance and burn very slowly. The intermediates of PVF during thermal decomposition include methane, ethane, propane, butane, ethylene, and benzene. Benzene is a human carcinogen and benzene exposure causes bone marrow failure.

6 Summary

The production and installation of a large number of PV modules worldwide requires that the recycling and recovery of PV modules must be considered. Solar technology is a clean energy regarding energy production, but it can produce a large amount of waste at the end of its life. The recycling of PV modules has been proven to be feasible. Valuable materials and rare elements can be recovered after refining. The toxic and harmful materials must be separated and properly managed. Most PV modules are installed in Europe and America; thus, most PV waste will also appear in these areas. In Europe, the association “PV Cycle” was established in 2008 and offers a network of PV waste collection and recycling solutions. While developing green energy, the protection of the environment should also be considered.

References

1. SEMI (2015) International technology roadmap for photovoltaic 2014 results, 6th edn. http://www.itrpv.net/Reports/Downloads/
2. McDonald NC, Pearce JM (2010) Producer responsibility and recycling solar photovoltaic modules. Energy Policy 38:7041–7047. doi:10.1016/j.enpol.2010.07.023
3. EPIA (2013) Global market outlook for photovoltaics 2013–2017, Brussels. http://www.fotovoltaica.com/fv-look.pdf
4. Wheeler NR, Bruckman LS, Ma J, Wang E, Wang CK, Chou I, Sun J, French RH (2013) Degradation pathway models for photovoltaics module lifetime performance. In: Proceedings of IEEE photovoltaic specialists conference (39th IEEE PVSC), Tampa, FL, USA, 16–21 June 2013, pp 3185–3190. doi:10.1109/PVSC.2013.6745130
5. Ndiaye A, Charki A, Kobi A, Kébé CMF, Ndiaye PA, Sambou V (2013) Degradations of silicon photovoltaic modules: a literature review. Sol Energy 96:140–151. doi:10.1016/j.solener.2013.07.005

6. Munoz MA, García MCA, Vela N, Chenlo F (2011) Early degradation of silicon PV modules and guaranty conditions. Sol Energy 85:2264–2274. doi:10.1016/j.solener.2011.06.011
7. Polverini D, Fidle M, Dunlop E, Zaaiman W (2013) Polycrystalline silicon PV modules performance and degradation over 20 years. Prog Photovoltaics Res Appl 21:1004–1015. doi:10.1002/pip.2197
8. Dhere NG, Shiradkar NS (2012) Fire hazard and other safety concerns of photovoltaic system. J Photonics Energy 2:022006. doi:10.1117/1.JPE.2.022006
9. Fraunhofer ISE (2014) Annual Report 2014/2015. https://www.ise.fraunhofer.de/en/press-and-media/annual-reports
10. Avrutin V, Izyumskaya N, Morkoç H (2011) Semiconductor solar cells: recent progress in terrestrial applications. Superlattices Microstruct 49:337–364. doi:10.1016/j.spmi.2010.12.011
11. Nakajima A, Gotoh M, Sawada T, Fukuda S, Yoshimi M, Yamamoto K, Nomura T (2009) Development of thin-film Si HYBRID solar module. Sol Energy Mater Sol Cells 93:1163–1166. doi:10.1016/j.solmat.2009.03.006
12. Masuko K, Shigematsu M, Hashiguchi T, Fujishima D, Kai M, Yoshimura N, Yamaguchi T, Ichihashi Y, Mishima T, Matsubara N, Yamanishi T, Takahama T, Taguchi M, Maruyama E, Okamoto S (2014) Achievement of more than 25 % conversion efficiency with crystalline silicon heterojunction solar cell. IEEE J Photovoltaic 4:1433–1435. doi:10.1109/JPHOTOV.2014.2352151
13. Sinha P (2013) Life cycle materials and water management for CdTe photovoltaics. Sol Energy Mater Sol Cells 119:271–275. doi:10.1016/j.solmat.2013.08.022
14. Garboushian V, Kinsey GS, Stone K, Crawford C, Gordon R (2009) Performance of Amonix multijunction arrays. In: Proceedings of SPIE—The International Society for Optical Engineering, San Diego, CA, USA, 2 Aug 2009, p 740703. doi:10.1117/12.826624
15. Reinhard P, Chirilă A, Blösch P, Pianezzi F, Nishiwaki S, Buechelers S, Tiwari AN (2013) Review of progress toward 20 % efficiency flexible CIGS solar cells and manufacturing issues of solar modules. IEEE J Photovoltaics 3:572–580. doi:10.1109/JPHOTOV.2012.2226869
16. Sarti D, Einhaus R (2002) Silicon feedstock for the multi-crystalline photovoltaic industry. Solar Energy Mat Solar Cells 72:27–40. doi:10.1016/S0927-0248(01)00147-7
17. Wang TY, Lin YC, Tai CY, Sivakumar R, Rai DK, Lan CW (2008) A novel approach for recycling of kerf loss silicon from cutting slurry waste for solar cell applications. J Cryst Growth 310:3403–3406. doi:10.1016/j.jcrysgro.2008.04.031
18. Want TY, Lin YC, Tai CY, Fei CC, Tseng MY, Lan CW (2009) Recovery of silicon from kerf loss slurry waste for photovoltaic applications. Prog Photovoltaics Res Appl 17:155–163. doi:10.1002/pip.863
19. Doi T, Tsuda I, Unagida H, Murata A, Sakuta K, Kurokawa K (2001) Experimental study on PV module recycling with organic solvent method. Solar Energy Mat Solar Cells 67:397–403. doi:10.1016/S0927-0248(00)00308-1
20. Wang TY, Hsiao JC, Du CH (2012) Recycling of materials from silicon base solar cell module. In: Proceedings of IEEE photovoltaic specialists conference (38th IEEE PVSC), Austin, Texas, USA, 3–8 June 2012, pp 2355–2358. doi:10.1109/PVSC.2012.6318071
21. Wang TY, Hsiao JC, Du CH, Chen SW (2012) The recycle process for crystalline silicon solar module. In: Proceedings of 27th European photovoltaic solar energy conference and exhibition (27th EUPVSC), Frankfurt, Germany, 24–28 Sept 2012, pp 4642–4644
22. Radxiemska EK, Piotr Ostrowski (2010) Chemical treatment of crystalline silicon solar cells as a method of recovering pure silicon from photovoltaic modules. Renew Energy 35:1751–1759. doi:10.1016/j.renene.2009.11.031
23. Kuvhař L, Drápala J, Luňáček J (1996) Purification methods of Cd, Te and CdTe and periodicity of segregation coefficients of admixtures. J Cryst Growth 161:94–103. doi:10.1016/0022-0248(95)00618-4
24. Fthenakis VM (2000) End-of-life management and recycling of PV modules. Energy Policy 28:1051–1058. doi:10.1016/S0301-4215(00)00091-4

25. Wang W, Fthenakis V (2005) Kinetics study on separation of cadmium from tellurium in acidic solution media using ion-exchange resins. J Hazard Mater B125:80–88. doi:10.1016/j.jhazmat.2005.02.013
26. Bohland J, Anisimov I, Dapkus T (1997) Economic recycling of CdTe photovoltaic modules. In: Proceedings of IEEE photovoltaic specialists conference (26th IEEE PVSC), Anaheim, USA, Sept 30–Oct 3 1997, pp 355–358. doi:10.1109/PVSC.1997.654101
27. Sinha P, Cossette M, Ménard JF (2012) End-of life CdTe PV recycling with semiconductor refining. In: Proceedings of 27th European photovoltaic solar energy conference and exhibition (27th EUPVSC), Frankfurt, Germany, 24–28 Sept 2012, pp 4653–4656
28. Popescu V, Vasile C, Brebu M, Popescu GL, Moldovan M, Prejmerean C, Stãnulet L, Rusu CT, Cojocaru I (2009) The characterization of recycled PMMA. J Alloy Compd 483:432–436. doi:10.1016/j.jallcom.2008.08.148
29. Lee HS, Nam CW (1998) A study on the extraction of gallium from gallium arsenide scrap. Hydrometallurgy 49:125–133. doi:10.1016/S0304-386X(98)00016-4
30. Zimmermann YS, Niewersch C, Lenz M, Kül ZZ, Corvini PFX, Schäffer A, Wintgens T (2014) Recycling of indium from CIGS photovoltaic cells: potential of combining acid-resistant nanofiltration with liquid-liquid extraction. Environ Sci Technol 48:13412–13418. doi:10.1021/es502695k
31. Marwede M, Berger W, Schlummer M, Maurer A, Reller A (2013) Recycling paths for thin-film chalcogenide photovoltaic waste—current feasible processes. Renew Energy 55:220–229. doi:10.1016/j.renene.2012.12.038
32. Gustafssom AMK, Foreman MRS, Ekberg C (2014) Recycling of high purity selenium from CIGS solar cell waste materials. Waste Manage 34:1775–1782. doi:10.1016/j.wasman.2013.12.021
33. Redlinger M, Eggert R, Woodhouse M (2015) Evaluating the availability of gallium, indium, and tellurium from recycled photovoltaic modules. Sol Energy Mater Sol Cells 138:58–71. doi:10.1016/j.solmat.2015.02.027
34. Fthenakis VM, Moskowitz PD (2000) Photovoltaics: environmental, health and safety issues and perspectives. Prog Photovoltaics Res Appl 8:27–38. doi:10.1002/(SICI)1099-159X(200001/02)8:1 <27::AID-PIP296> 3.0.CO;2-8
35. Marwede M, Reller A (2014) Estimation of life cycle material costs of cadmium telluride—and copper indium gallium diselenide—photovoltaic absorber materials based on life cycle material flows. J Ind Ecol 18:254–267. doi:10.1111/jiec.12108
36. Rocchetti L, Beolchini F (2015) Recovery of valuable materials from end-of-life thin-film photovoltaic panels: environmental impact assessment of different management options. J Clean Prod 89:59–64. doi:10.1016/j.jclepro.2014.11.009
37. Nordbeg M, Nordbeg GF, Fowler B, Friberg L (2011) Handbook on the toxicology of metals, 3rd edn. Academic Press
38. Kimball SM (2015) Mineral commodity summaries. Geological Survey, Reston, Virginia, U.S. doi:10.3133/70140094
39. Lu Q, He ZL, Stoffella PJ (2012) Land application of biosolids in the USA: a review. Appl Environ Soil Sci 2012:201462. doi:10.1155/2012/201462
40. Osayemwenre GO, Meyer EL (2014) Thermal decomposition of EVA composite encapsulant of single junction amorphous silicon photovoltaic (PV) module. J Ovonic Res 10:221–229
41. Chatfield DA (1983) The pyrolysis and nonflaming oxidative degradation of poly (vinylfluoride). J Polym Sci Polym Chem 21:1681–1691. doi:10.1002/pol.1983.170210611